DISSERTATION

SUBMITTED TO THE

COMBINED FACULTIES OF MATHEMATICS, ENGINEERING AND NATURAL SCIENCES OF

HEIDELBERG UNIVERSITY, GERMANY

FOR THE DEGREE OF

DOCTOR OF NATURAL SCIENCES

PUT FORWARD BY

JAN EBERHARDT

BORN IN: MANNHEIM, GERMANY

ORAL EXAMINATION: JULY 22, 2025

DISCOVERY AND DYNAMICAL CHARACTERIZATION OF EXOPLANETARY SYSTEMS WITH THE TRANSIT AND RADIAL VELOCITY METHODS

REFEREES:

PROF. DR. THOMAS HENNING

PROF. DR. MATTHIAS BARTELMANN

Remember to look up at the stars and not down at your feet.

— Stephen Hawking

Dedicated to my family.

ABSTRACT

This thesis is dedicated to the discovery and characterisation of exoplanet systems using the radial velocity- and transit methods. This study focuses on the detailed characterization of several Jovian mass planets discovered in warm orbits ($P > 10$ days) as part of the **W**arm g**I**a**N**ts with t**E**ss (WINE) collaboration, which aims to validate exoplanet discoveries made with the Transiting Exoplanet Survey Satellite (TESS). The physical and orbital properties of these exoplanets have significant implications for planet formation- and evolution theories.

Within the WINE collaboration, I studied five different exoplanets in four systems, TOI-2373 b, TOI-2416 b, TOI-2524 b as well as TOI-6695 b and c. The planets have been detected by TESS as candidates and later confirmed by myself and my collaboration with ground-based follow-up observations using the Fiber-fed Extended Range Optical Spectrograph (FEROS). TOI-2373 b, TOI-2416 b and TOI-2524 b orbit G-type solar analog stars on close orbits, with periods shorter than 15 days each, while TOI-6695 b and c orbit a late F-type star on wider orbits of ~ 80 and ~ 240 days. The planets presented in this thesis mark important discoveries, with TOI-2373 b, TOI-2416 b and TOI-2524 b residing in the transition region between hot and warm Jupiters, TOI-2373 b being the second most massive exoplanet known to orbit a solar analog star and TOI-2524 b having an inflated radius. The pair of planets in the TOI-6695 system is a rare case of two planets with a period ratio of close to 3, that is, close to the 3:1 resonance.

Beyond my work with the WINE collaboration, I studied the case of the young T-Tauri star TW Hya. In 2008, an exoplanet discovery was presented for TW Hya. The discovery was based on radial velocity observations with FEROS, which revealed a 3.57 day periodicity. Shortly after, this signal was suggested to be caused by a long-lived stellar spot instead of a planet. In this thesis, I present a detailed radial velocity and photometry analysis, including a spot-induced radial velocity model. I found no further evidence for an exoplanet, but instead attribute the radial velocity signal to a large polar spot, fueled by stellar accretion.

ZUSAMMENFASSUNG

Diese Arbeit ist der Entdeckung und Charakterisierung von Exoplanetensystemen mit Hilfe der Radialgeschwindigkeits- und Transitmethoden gewidmet. Diese Studie konzentriert sich auf die detaillierte Charakterisierung mehrerer Planeten mit jupiterähnlicher Masse, die im Rahmen der WINE-Kollaboration in warmen Umlaufbahnen ($P > 10$ Tage) entdeckt wurden, welche sich zum Ziel gesetzt hat, die mit TESS gemachten Entdeckungen von Exoplaneten zu validieren. Die physikalischen und orbitalen Eigenschaften dieser Exoplaneten haben erhebliche Auswirkungen auf die Theorien zur Planetenentstehung und -entwicklung.

Im Rahmen der WINE-Kollaboration habe ich fünf verschiedene Exoplaneten in vier Systemen untersucht, TOI-2373 b, TOI-2416 b, TOI-2524 b sowie TOI-6695 b und c. Die Planeten wurden von TESS als Kandidaten entdeckt und später von mir und meiner Kollaboration durch bodengestützte Nachbeobachtungen mit FEROS bestätigt. TOI-2373 b, TOI-2416 b und TOI-2524 b umkreisen sonnenanaloge Sterne vom G-Typ auf engen Bahnen mit Perioden von jeweils weniger als 15 Tagen, während TOI-6695 b und c einen späten Stern vom F-Typ auf breiteren Bahnen von ~ 80 und ~ 240 Tagen umkreisen. Die in dieser Arbeit vorgestellten Planeten stellen wichtige Entdeckungen dar: TOI-2373 b, TOI-2416 b und TOI-2524 b befinden sich im Übergangsbereich zwischen heißen und warmen Jupitern, wobei TOI-2373 b der zweitmassereichste bekannte Exoplanet ist, der einen sonnenanalogen Stern umkreist, und TOI-2524 b einen aufgeblähten Radius aufweist. Das Planetenpaar im System TOI-6695 ist ein seltener Fall von zwei Planeten mit einem Periodenverhältnis von annähernd 3, d. h. nahe der 3:1-Resonanz.

Neben meiner Arbeit mit der WINE-Kollaboration habe ich den Fall des jungen T-Tauri-Sterns TW Hya untersucht. Im Jahr 2008 wurde die Entdeckung eines Exoplaneten für TW Hya vorgestellt. Die Entdeckung basierte auf Radialgeschwindigkeitsbeobachtungen mit FEROS, die eine Periodizität von 3,57 Tagen zeigten. Kurz darauf wurde vermutet, dass dieses Signal von einem langlebigen stellaren Fleck und nicht von einem Planeten verursacht wird. In dieser Arbeit präsentiere ich eine detaillierte Analyse der Radialgeschwindigkeit und der Photometrie, einschließlich eines Modells zur Beschreibung der durch einen Fleck erzeugten Radialgeschwindigkeit. Ich habe keine weiteren Hinweise auf einen Exoplaneten gefunden, sondern führe das Radialgeschwindigkeitssignal auf einen großen polaren Fleck zurück, der durch stellare Akkretion hervorgebracht wird.

LIST OF PUBLICATIONS

Publications as first author:

[1] Jan Eberhardt et al. “Three Warm Jupiters around Solar-analog Stars Detected with TESS.” In: *AJ* 166.6, 271 (Dec. 2023), p. 271. DOI: `10.3847/1538-3881/ad06bc`. arXiv: `2402.17592 [astro-ph.EP]`.

[2] Jan Eberhardt et al. “A Massive Spot on the Stellar Surface of TW Hya.” In: *in prep.* (2025).

[3] Jan Eberhardt et al. “TOI-6695: A Pair of Near-resonant Massive Planets Observed with TESS from the WINE Survey.” In: *AJ* 169.6, 298 (June 2025), p. 298. DOI: `10.3847/1538-3881/adc44e`.

Publications as contributing author:

[1] Rafael Brahm et al. “Three Long-period Transiting Giant Planets from TESS.” In: *AJ* 165.6, 227 (June 2023), p. 227. DOI: `10.3847/1538-3881/accadd`. arXiv: `2304.02139 [astro-ph.EP]`.

[2] Ilaria Carleo et al. “Mass determination of two Jupiter-sized planets orbiting slightly evolved stars: TOI-2420 b and TOI-2485 b.” In: *A&A* 690, A18 (Oct. 2024), A18. DOI: `10.1051/0004-6361/202451313`. arXiv: `2408.05612 [astro-ph.EP]`.

[3] Samuel Gill et al. “Correction to: TOI-2447 b / NGTS-29 b: a 69-day Saturn around a Solar analogue.” In: *MNRAS* 533.1 (Sept. 2024), pp. 109–109. DOI: `10.1093/mnras/stae1804`. arXiv: `2405.07367 [astro-ph.EP]`.

[4] Samuel Gill et al. “TOI-2447 b / NGTS-29 b: a 69-day Saturn around a Solar analogue.” In: *MNRAS* 532.2 (Aug. 2024), pp. 1444–1458. DOI: `10.1093/mnras/stae1256`.

[5] N. Heidari et al. “Characterization of seven transiting systems, including four warm Jupiters from SOPHIE and TESS.” In: *A&A* 694, A36 (Feb. 2025), A36. DOI: `10.1051/0004-6361/202451519`. arXiv: `2412.08527 [astro-ph.EP]`.

[6] Melissa J. Hobson et al. “The WINE survey. A transiting 100-day exo-Saturn with a companion in the Habitable Zone.” In: *Bulletin of the American Astronomical Society*. Vol. 54. June 2022, p. 102.260.

[7] Matías I. Jones et al. "A long-period transiting substellar companion in the super-Jupiters to brown dwarfs mass regime and a prototypical warm-Jupiter detected by TESS." In: *A&A* 683, A192 (Mar. 2024), A192. DOI: `10.1051/0004-6361/202348147`. arXiv: `2401.09657 [astro-ph.EP]`.

[8] Toby Rodel et al. "NGTS-EB-7, an eccentric, long-period, low-mass eclipsing binary." In: *MNRAS* 537.1 (Feb. 2025), pp. 35–55. DOI: `10.1093/mnras/stae2799`. arXiv: `2501.04523 [astro-ph.SR]`.

[9] Romy Rodríguez Martínez et al. "Discovery and Characterization of an Eccentric, Warm Saturn Transiting the Solar Analog TOI-4994." In: *AJ* 169.2, 72 (Feb. 2025), p. 72. DOI: `10.3847/1538-3881/ad9b90`. arXiv: `2412.02769 [astro-ph.EP]`.

[10] Lizhou Sha et al. "Correction to: TESS spots a mini-neptune interior to a hot saturn in the TOI-2000 system." In: *MNRAS* 526.2 (Dec. 2023), pp. 2440–2440. DOI: `10.1093/mnras/stad2924`.

[11] Lizhou Sha et al. "TESS spots a mini-neptune interior to a hot saturn in the TOI-2000 system." In: *MNRAS* 524.1 (Sept. 2023), pp. 1113–1138. DOI: `10.1093/mnras/stad1666`. arXiv: `2209.14396 [astro-ph.EP]`.

[12] Marcelo Tala Pinto et al. "Three warm Jupiters orbiting TOI-6628, TOI-3837, and TOI-5027 and one sub-Saturn orbiting TOI-2328." In: *A&A* 694, A268 (Feb. 2025), A268. DOI: `10.1051/0004-6361/202452517`. arXiv: `2412.02069 [astro-ph.EP]`.

[13] Trifon Trifonov et al. "A New Third Planet and the Dynamical Architecture of the HD 33142 Planetary System." In: *AJ* 164.4, 156 (Oct. 2022), p. 156. DOI: `10.3847/1538-3881/ac7ce0`. arXiv: `2206.03899 [astro-ph.EP]`.

[14] Michaela Vítková et al. "TOI-4504: Exceptionally Large Transit Timing Variations Induced by Two Resonant Warm Gas Giants in a Three-planet System." In: *ApJL* 978.2, L22 (Jan. 2025), p. L22. DOI: `10.3847/2041-8213/ad9a53`. arXiv: `2412.05609 [astro-ph.EP]`.

ACKNOWLEDGMENTS

I would like to express my deep gratitude to the people that made this Thesis possible:

My supervisors Thomas Henning and Trifon Trifonov, who guided me through my time as a PhD candidate.

To Thomas, thank you for introducing me to my projects, the WINE collaboration and the TW Hya project. Thank you for all your support and encouragement! I'm also deeply grateful to have had the opportunity to travel to the amazing places I've visited during my PhD, fulfilling life-long dreams of seeing the cherry blossoms in Japan and the breathtaking night sky and nature in Patagonia.

To Trifon, thank you for always supporting me, for always taking the time to help me with either technical or scientific problems.

I would like to thank my Thesis committee members, Thomas, Trifon and Sabine Reffert. Our meetings and discussions were really helpful for guiding my projects into the right directions. Thanks to Thomas and Matthias Bartelmann for refereeing my Thesis, as well as to Sabine and Michael Hausmann for being part of my examination committee.

Thank you to my close collaborators of the WINE collaboration, Rafael Brahm, Andrés Jordán, Nestor Espinoza, Melissa Hobson, Marcelo Tala Pinto, Martin Schlecker, Lorena Acuña and Matías Jones and to my close collaborators at MPIA, Ralf Launhardt and Remo Burn.

I'm also grateful to Roland Gredel, who unbureaucratically made it possible for me to visit La Silla Observatory in Chile, which was an amazing experience.

Thank you to Christian Fendt and Nina Zhao, who were always available for administrative help with IMPRS.

I would like to thank the staff of Haus der Astronomie, Markus Pössel, Carolin Liefke, Markus Nielbock, Olaf Fischer, Sigrid Brümmer, Carmen Müllerthann, who supported me from the beginning of my studies.

To my office mates and friends at MPIA, Dominik, Lukas, Klaus, Taavet, David, Peter, Sophia, Julia, Rhys, Marten, Molly, Dhruv, Kruti, Anastasia, Nina, thank you for making the wonderful time at MPIA even better. I'm glad that you were all around me!

A big thank you to everyone who proofread my thesis, as a whole or in parts: Trifon, Melissa, Dominik, Martin, Benni, Julia, Thomas.

To my family, thank you very much for your unconditional love and support. Without you, I would never have been able to get to where I am today and I love you all!

Thank you to *André Miede*, who created the LaTeX template for this Thesis.

CONTENTS

LIST OF FIGURES

LIST OF TABLES

ACRONYMS

ASTEP	Antarctica Search for Transiting ExoPlanets
BIC	Bayesian Information Criterion
BIS	Bisector Inverse Span
BJD	Barycentric Julian Date
CCF	Cross Correlation Function
CERES	Collection of Elemental Routines for Echelle Spectra
CRIRES	CRyogenic InfraRed Echelle Spectrograph
CRX	ChRomatic indeX
CWT	Continuous Wavelet Transform
dLW	differential Line Width
ESM	Emission Spectroscopy Metric
FAP	False-Alarm-Probability
FEROS	Fiber-fed Extended Range Optical Spectrograph
FFI	Full Frame Image
FWHM	Full Width at Half Maximum
GASTLI	GAS gianT modeL for Interiors
GLS	Generalised Lomb Scargle
GP	Gaussian Process
GWS	Global Wavelet Spectrum
HARPS	High-Accuracy Radial-velocity Planetary Search
IAU	International Astronomical Union
LCOGT	Las Cumbres Observatory Global Telescope
MAST	Mikulski Archive for Space Telescopes
MCMC	Markov Chain Monte Carlo
MLP	Maximum Likelihood Periodogram
MMR	Mean Motion Resonance
NS	Nested Sampling
PFS	Planet Finder Spectrograph
QLP	Quick Look Pipeline
RM	Rossiter-McLaughlin
RV	Radial Velocity
SED	Spectral Energy Distribution

SERVAL	SpEctrum Radial Velocity AnaLyser
SPOC	Science Processing Operations Center
TESS	Transiting Exoplanet Survey Satellite
TGLC	TESS-Gaia-Light-Curve
TLS	Transit Least Squares
TPF	Target Pixel File
TSM	Transmission Spectroscopy Metric
TTV	Transit Timing Variation
WINE	**W**arm g**I**a**N**ts with t**E**ss

Part I

MOTIVATION AND INTRODUCTION

The main source used for the introductory chapters was The Exoplanet Handbook [137], unless stated otherwise. The figures were either created by me / pictures taken by me if no additional reference is given.

1 MOTIVATION

1.1 WHAT ARE EXOPLANETS?

The word *planet* comes from the greek word πλανήτης (planetes), meaning 'wanderer', alluding to their fast motion in the night sky, relative to the fixed apparent positions of the other stars. The planets *Mercury*, *Venus*, *Mars*, *Jupiter* and *Saturn* were correctly identified as planets by greek philiosphers, the *Earth* joined them during the Copernican Revolution, with the advent of the Heliocentric Model. The planet *Uranus* was discovered by the German-British astronomer William Herschel in 1781 and officially acknowledged as a planet by 1783. Due to deviations in the observed positions of Uranus from its predicted positions according to its estimated orbit, a new potential planet was postulated and its position independently calculated by the astronomers John Couch Adams and Urbain Le Verrier in the 1840's. German astronomer Johann Gottfried Galle was requested by Le Verrier to observe at the predicted position and discovered the planet later called *Neptune* in 1845. Similarly, observations of Neptune's orbit led to the discovery of *Pluto* in 1930 by American astronomer Clyde Tombaugh.

The Sun and the Moon were originally included as planets.

With the discoveries of more and more small objects similar to Pluto, the International Astronomical Union (IAU) revised the definition of a planet to distinguish them from smaller Solar System bodies. According to their 2006 definition [89], a planet

1. is in orbit around the Sun,
2. has sufficient mass for its self-gravity to overcome rigid body forces so that it assumes a hydrostatic equilibrium (nearly round) shape,
3. has cleared the neighbourhood around its orbit.

This definition keeps the eight known planets, while preventing bodies like the Moon, transneptunian objects like Pluto or asteroids like Ceres from being counted towards the planets.

Extrasolar planets or exoplanets are planets that are not part of the Solar System. There is no official definition for exoplanets from the IAU, but an analogous definition for most known exoplanets can be assumed, by replacing the Sun with their respective host object (mostly main-sequence stars, but also neutron stars and white dwarfs). However, this definition fails for planets without any host object, so called free-floating planets. Furthermore, the distinction between planets and brown dwarfs, a sort of intermediate object between planet and star, is difficult and ambiguous.

The current IAU working definition for exoplanets is [110]

1. Objects with true masses below the limiting mass for thermonuclear fusion of deuterium (currently calculated to be 13 Jupiter masses for objects of solar metallicity) that orbit stars, brown dwarfs or stellar remnants and that have a mass ratio with the central object below the L4/L5 instability ($M/M_{\text{central}} < 2/(25 + \sqrt{621}) \approx 1/25$) are "planets", no matter how they formed.
2. The minimum mass/size required for an extrasolar object to be considered a planet should be the same as that used in our Solar System, which is a mass sufficient both for self-gravity to overcome rigid body forces and for clearing the neighborhood around the object's orbit.

The first exoplanet detection dates back to 1992, when a system of planets was discovered orbiting the millisecond pulsar PSR B1257+12 [185], while the first planet orbiting a main-sequence star, 51 Peg, was discovered in 1995 with the radial velocity method [119]. In 2000, the first transit of an exoplanet was observed, when the star HD 209458 was observed photometrically [35], after a short-period planet was detected with the radial velocity method in 1999 [75].

Within the last three decades, more than 5 800 confirmed exoplanets have been detected with various methods, Table 2.2 listing the number of confirmed exoplanets for each method. The most successful method has proven to be the transit method, with more than 4 300 confirmed exoplanets. This is mainly due to the large Kepler/K2 [22, 82] and *TESS* [146] missions.

1.2 WHY STUDY EXOPLANETS?

The study of exoplanets is fueled by the desire to understand the formation of our own Solar System, as well as finding earthlike planets and the question of whether there is extraterrestrial life in the universe. The extensive search for exoplanets revealed various kinds of planets, some unknown in the Solar System. Most notable are the so called hot Jupiters, planets of jovian mass, that orbit their host star within a few days. Other new types of planets include super-Earths and mini-Neptunes.

Discoveries of the different kinds of planets, different type of host stars, as well as planetary systems in varying stages of their formation helps to better understand the formation histories of planets and to deepen our theories of planetary formation and evolution.

Table 2.1: Posterior distribution and priors for the parameters of the spot model.

DETECTION METHOD	PLANETS
Transit	4374
Radial Velocity	1119
Microlensing	239
Imaging	83
Transit Timing Variations	36
Eclipse Timing Variations	17
Orbital Brightness Modulations	9
Pulsar Timing Variations	8
Astrometry	5
Pulsation Timing Variations	2
Disk Kinematics	1
Total	5893

Table 2.2: Exoplanets detected by various methods `https://exoplanetarchive.ipac.caltech.edu`; Accessed 2025 May 15.

1.3 OUTLINE OF THE THESIS

In this thesis, I present the discoveries and dynamical characterization of five jovian mass planets in four systems, as well as an in-depth analysis on a 17-year old radial velocity signal from the young T-Tauri star TW Hya and its unclear origin.

In Chapter 2 of Part I, I give a short overview of the theories of orbital motion, the radial velocity and transit methods, as well as their intricacies and how they complement each other. Part II is based on the papers I worked on during my time as a PhD candidate, Chapter 3 being about the three warm giants TOI-2373 b, TOI-2416 b and TOI-2524 b, that orbit solar analogue stars, Chapter 4 about the planets TOI-6695 b and c, a near resonant pair of warm giants in a particularly rare orbital configuration. Chapter 5 deals with the analysis of the persistent radial velocity signal of TW Hya and the question of whether this signal is caused by a planetary companion or a stellar spot on the surface. Chapter 6 puts the results of the thesis into broader context and provides an outlook into the future of exoplanet research.

2

INTRODUCTION

2.1 ORBITAL MOTION

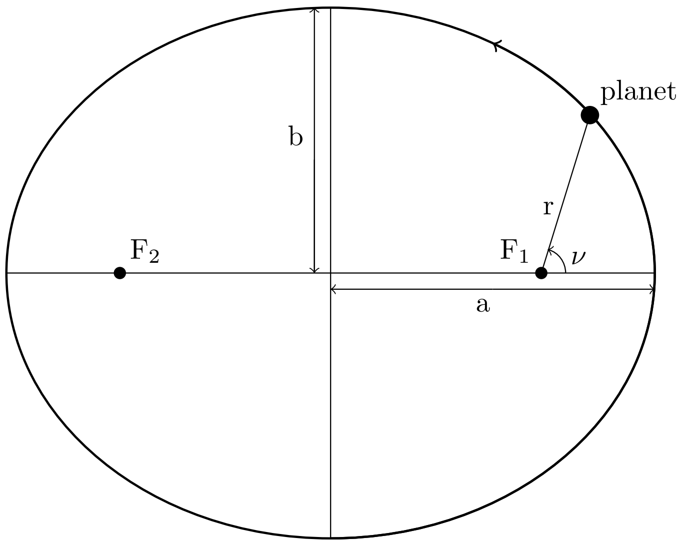

Figure 2.1: Elements of an elliptical orbit in 2-dimensions.

The orbital motion of planets was first described mathematically by German astronomer Johannes Kepler during the early 17th century in his *Astronomia Nova*. His work was based on that of his teacher, Tycho Brahe. Kepler described the motion of the planets in three laws.

Kepler's first law described the planets orbiting the Sun on elliptical orbits instead of purely circular ones. The Sun is located in one of the ellipse's focal points. Figure 2.1 shows a schematic view of the orbital elements of an elliptical orbit. The Sun is located in the focal point F_1. Illustrated are the semimajor and semiminor axes a and b, the radius vector r, as well as the true anomaly ν. The degree of ellipticity of an orbit, called the *numeric eccentricity*, e is given as

$$e = \sqrt{1 - \left(\frac{b}{a}\right)^2}. \tag{1}$$

Kepler's second law described that a connecting line between the Sun and a planet covered equal areas of the ellipse for a given time, independent of the planet's position on the orbit. In his third law, Kepler established a relation between the orbital period P and semimajor axis of the planetary orbit a.

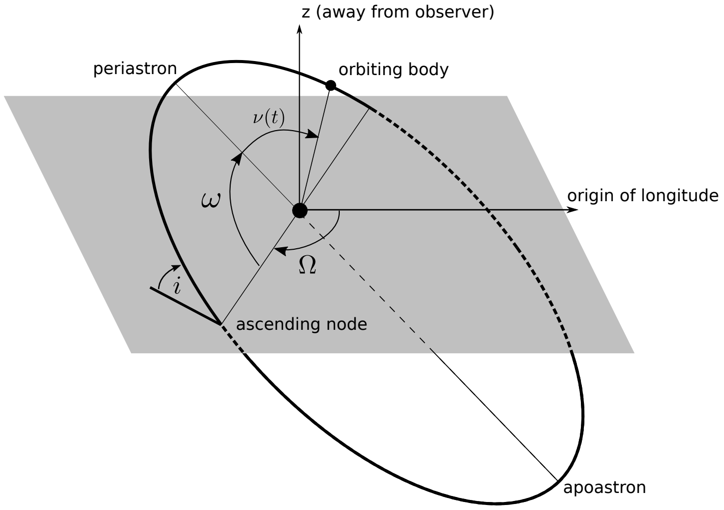

Figure 2.2: Schematic of an inclined elliptical orbit.

The orbital period of a planet orbiting its star with a semimajor axis of a is given as

$$P^2 = \frac{4\pi^2}{GM} a^3, \tag{2}$$

with $M = (M_* + M_p)$ being the sum of the stellar mass M_* and the planetary mass M_p and G being Newton's gravitational constant. This can be expressed in terms of the semimajor axis of the stellar orbit around the common barycenter a_*:

$$P^2 = \frac{4\pi^2}{GM'} a_*^3, \tag{3}$$

with $M' = \frac{M_p^3}{(M_*+M_p)^2}$.

2.2 SPECTROSCOPIC EXOPLANET DETECTION WITH THE RADIAL VELOCITY METHOD

To fully describe an orbit of a planet in three dimensions, a set of 7 parameters is necessary, namely the semimajor axis a, the numerical eccentricity e, the orbital period P, the time of periastron passage t_p, the orbital inclination i, the longitude of ascending node Ω, and the argument of periastron ω.

Figure 2.2 shows a schematic of a planetary orbit. The orbit is inclined about an angle of i, defined between 0° (face-on view) and 90° (edge-on view), with respect to the plane of reference (the plane perpendicular to the line of sight) and illustrates the angles ν between the planet and the periastron, ω between the periastron and the ascending node and Ω between the ascending node and the origin of longitide as a reference direction.

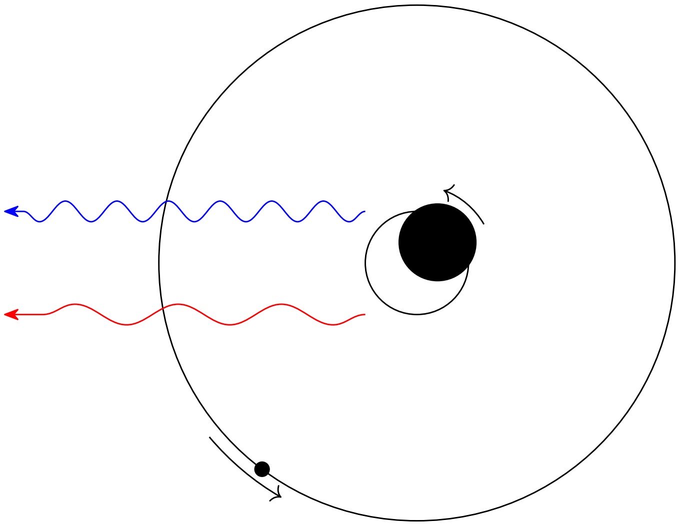

Figure 2.3: Doppler-shifted light of a star due to a planet on a circular orbit.

The motion of the star around the common center of mass on an orbit with semimajor axis a_* causes a Doppler shift in the spectrum of the star. This relative wavelength shift $\Delta\lambda/\lambda$ is proportional to the line-of-sight velocity, also called Radial Velocity (RV) $v_r = c\Delta\lambda/\lambda$, as illustrated in Figure 2.3, with c being the speed of light. By measuring this Doppler shift, the orbital elements of the star's orbit (and thus the planet's orbit) can be determined. The radial component of the star's velocity is given as

$$v_r = K[\cos(\omega + \nu) + e \cos\omega], \tag{4}$$

with the RV semi-amplitude

$$K = \left(\frac{2\pi G}{P}\right)^{1/3} \frac{M_p \sin i}{(M_* + M_p)^{2/3}} \frac{1}{(1-e^2)^{1/2}}. \tag{5}$$

To give examples from the Solar System, values for the RV semi-amplitude for Jupiter and Earth are $K_{jup} = 12.5$ m s^{-1} and $K_{earth} = 0.09$ m s^{-1}. While the shape of the RV curve is defined by e and ω, its amplitude K is what limits detections. A spectrograph has to achieve very high spectral resolutions, measurement precisions and stability to be able to detect terrestrial planets. A list of widely used spectrographs can be found in Table 2.1.

In addition to the Doppler shifts induced by planets, stellar activity produces changes in the stellar absorption lines, that influence the measurement of the star's line-of-sight velocity. As spectrographic precision steadily improves, these changes become detectable and need to be corrected for.

Table 2.1: Different spectrographs used or mentioned within the thesis.

INSTRUMENT	RESOLUTION	TELESCOPE	PRECISION	REF.
FEROS	48 000	MPG/ESO 2.2m	7.5 m/s	[100]
HARPS	120 000	ESO 3.6m	0.97 m/s	[118]
PFS	38 000	Magellan II 6.5m	1.2 m/s	[37–39]
CHIRON	27.4–136 000*	SMARTS-GSU 1.5m	1.0 m/s	[175]
CORALIE	60 000	Swiss LET 1.2m	3 m/s	[139]
ESPRESSO	140–190 000**	VLTI 4x UT 8.2m	0.097 m/s	[136]
CRIRES	100 000	VLT UT1 8.2m	5 m/s	[101, 102]
CRIRES+	50–100 000***	VLT UT3 8.2m	3 m/s	[47, 48]

* Resolutions of 27 400, 79 000, 95 000, and 136 000 are available for different observing modes. ** ESPRESSO offers resolutions of 140 000 in HR mode and 190 000 in UHR mode. *** The resolution for CRIRES+ is 50 000 for the 0.4″ slit and 100 000 for the 0.2″ slit.

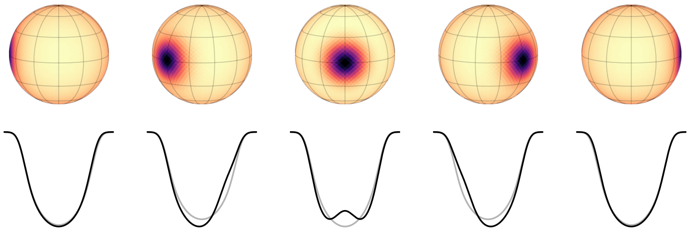

Figure 2.4: Line shape variation due to a spot on the stellar surface. Recreated after the `spotter` documentation (`https://spotter.readthedocs.io/en/latest/`).

2.2.1 *Know thy star, know thy planet*

Stars are dynamically very complex objects. Their atmospheric activity is mainly driven by their magnetic fields, convection and stellar oscillations, and can lead to significant noise in RV measurements. This noise, or 'jitter', is of the order of m/s, which can make detecting Earth-sized planets extremely challenging. In order to disentangle planetary signals from the noise, a careful and thorough understanding and modeling of the stellar activity is crucial.

Luckily, the stellar activity can be measured from the same spectra that are used to extract radial velocity measurements. Processes like star spots, prominences, flares, and faculae produce changes in the stellar absorption lines, that can be observed. Figure 2.4 shows an example of a spot that changes the shape of an absorption line. Since this skews the line to either side, it creates a net shift in radial velocity, which - depending on the size and longevity of the spot, as well as

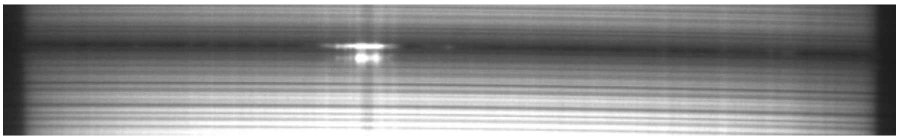

Figure 2.5: M8-class flare observed by the author on July 29, 2024 in the Ca II H and H_ϵ absorption lines of the solar spectrum. A sunspot can be seen as a dark vertical line across the continuum at the same position of the flare.

the rotational period of the star and the orbital period of the planet - can either disturb or mimic a planetary signal. Activity that changes the shape of lines is also called *photospheric activity*. It occurs mainly in the photoshpere, the outermost layer of the star. Other than by changing the shapes of absorption lines, stellar activity can also be seen as emission in the cores of spectral lines. Since this emission is produced in the thin layer above the photosphere, the chromosphere, this is also called *chromospheric activity*. Figure 2.5 shows a flare in the upper chromosphere of the Sun, observed on August 27, 2024. It can be seen as a bright spot in both the Ca II H and H_ϵ lines.

Photospheric activity can be measured with the help of the Cross Correlation Function (CCF) [see eg. 140, 141]. When extracting radial velocities from a stellar spectrum, the observed spectrum is cross correlated with a synthetic spectrum. The resulting CCF enables a precise determination of the center of the line, as well as a number of different measures of the line shape deformation. Activity indicators from the CCF include the Bisector Inverse Span (BIS), the Full Width at Half Maximum (FWHM), the differential Line Width (dLW), the ChRomatic indeX (CRX) and the contrast. Figure 2.6 shows a schematic of the FWHM and the line bisector of the CCF. The BIS is defined as the inverse slope between the upper and the lower part of the line bisector curve.

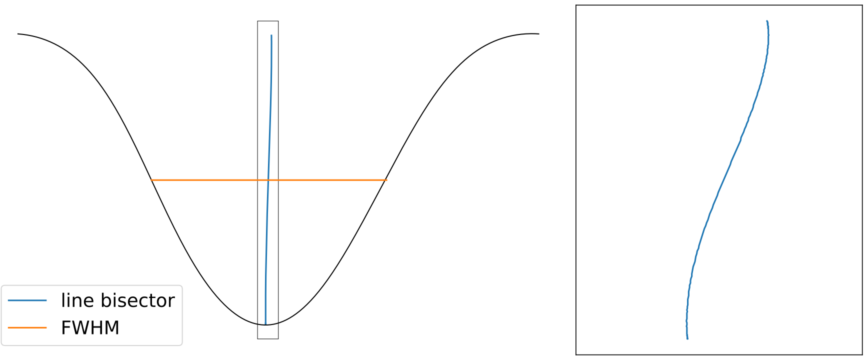

Figure 2.6: *Left:* Line bisector and FWHM activity indicators. *Right:* Zoom in on the line bisector.

Chromospheric activity is measured as the relative flux of an absorption line with respect to the continuum flux. A thin region around the core of the line is chosen to measure the stellar flux, while two flanking regions to either side are averaged for the mean continuum flux. Commonly used line indicators are H_{α}, Ca II H, Ca II K, Na II D1, Na II D2 and He I D3 [see eg. 19, 70].

By carefully studying the photospheric and chromospheric activity of the star, a better understanding of the nature of observed radial velocity measurements can be achieved. For example, studying the BIS can provide constraints on the stellar rotation period and correlating the BIS measurements with the radial velocity measurements can help to assign an observed signal to either a planet or a spot on the stellar surface.

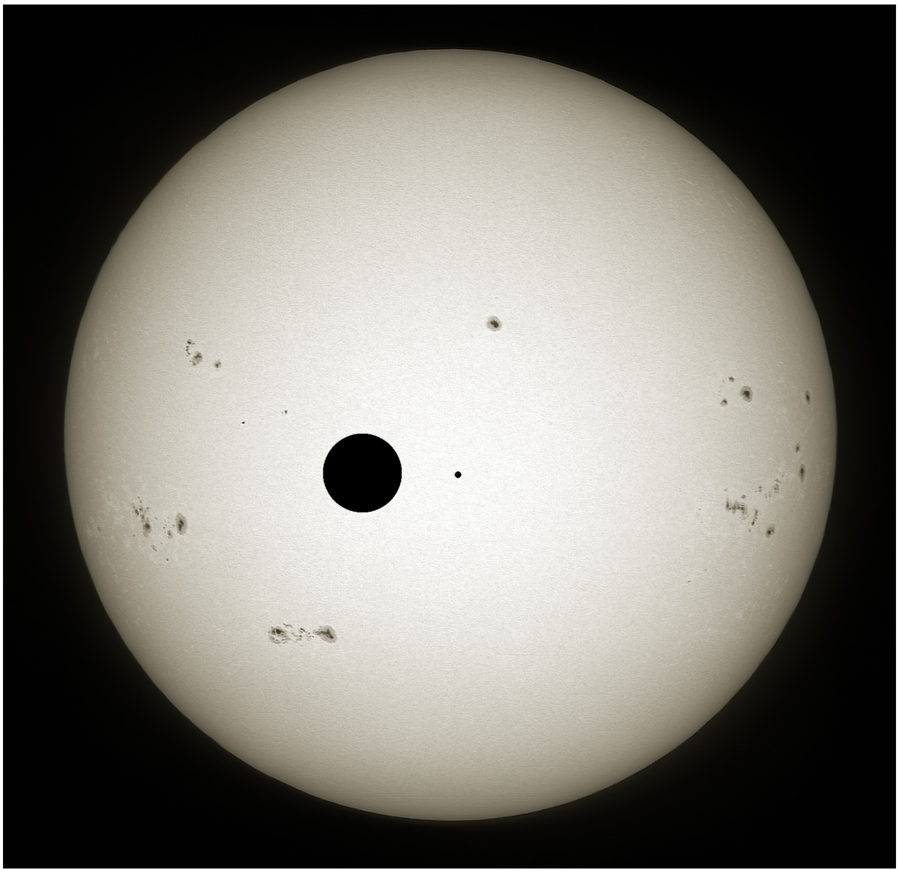

Figure 2.7: Simulated transit of Jupiter and Earth in front of the Sun. Dark disks of the size of Jupiter and Earth are overlaid to demonstrate the difficulties in detecting Earth-sized exoplanets.

2.3 PHOTOMETRIC DETECTION OF TRANSITING EXOPLANETS

A planet that transits in front of its host star, blocks out a fraction of the stellar light, resulting in a temporary decrease in the star's flux of the factor $\Delta F = (R_p/R_*)^2$. With a sufficiently sensitive instrument, this transit depth can be observed and used to model a transit light curve. The distance of the planet from the center of the star during transit is called the impact parameter $b = a/R_* \sin i$. For a transit to occur (at least partially), the impact parameter cannot be larger than $1 + R_p/R_*$. This leads for a randomly oriented orbit to a probability of

$$p \approx \frac{R_* + R_p}{a} \tag{6}$$

to be oriented in such a way that a transit can be observed from Earth.

As can be seen in Figure 2.7, detecting Earth-sized planets around stars similar to the Sun is much harder than giant planets, with transit depths of $(\Delta F)_{\mathrm{jup}} = 0.01$ and $(\Delta F)_{\mathrm{earth}} = 8.4 \times 10^{-5}$. Because of this, the search for Earth-sized exoplanets is much more promising around dwarf stars. A transit of an Earth-sized planet in front of a

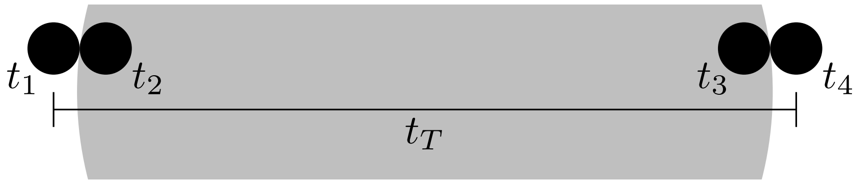

Figure 2.8: The four contact points of a transit t_1, t_2, t_3, and t_4. The time between t_1 and t_4 is the transit duration t_T.

hypothetical dwarf star with a radius of $R_{\text{dwarf}} = 0.1\,R_\odot$ would instead have a depth of $\Delta F = 0.008$, comparable to the transit of Jupiter in front of the Sun. A list of relevant photometric facilities and their precision is given in Table 2.2.

A planet transiting its host star goes through four contact points, t_1, when the planet's and star's limbs make contact for the first time, t_2, when the planet's disk is fully in front of the star, t_3, when the planet starts to cross the stellar limb again, and t_4, when the planet's disk loses contact with the stellar disk (demonstrated in Figure 2.8). The total transit duration $t_T = t_4 - t_1$ is given as

$$t_T = \frac{P}{\pi} \arcsin\left[\frac{R_*}{a}\left(\frac{[1 + (R_p/R_*)]^2 - b^2}{1 - \cos^2 i}\right)^{1/2}\right], \tag{7}$$

with the orbital period P, the stellar and planetary radii R_* and R_p, the semimajor axis a, orbital inclination i and impact parameter b. The phases of partial transit are called ingress ($t_1 \to t_2$) and egress ($t_3 \to t_4$).

Table 2.2: Relevant photometric facilities (both space missions and ground based sites).

FACILITY	DIAMETER	LOCATION	PRECISION	REF.
TESS	10 cm	Space (orbits Earth)	10^2 - 10^5 ppm*	[146]
Kepler	95 cm	Space (orbits the Sun)	20 ppm**	[22, 68, 82]
ASTEP	40 cm	East Antarctic Plateau	~ 1 000 ppm	[49, 71, 122], priv. comm.
LCOGT	1 m	Worldwide network	~ 1 000 ppm	[30], priv. comm.
Observatoire Moana	60 cm	El Sauce, Rio Hurtado, Chile	~ 1 000 ppm	priv. comm.

* Depending on the apparent magnitude of the target. ** For a magnitude 12 star, integrated over 6.5 hours.

2.3.1 *Transit Timing Variations*

By observing multiple transits, the orbital period of a planet can be very accurately determined. This can be used to predict upcoming transits. In systems with more than one planet, gravitational interactions between the planets can lead to a delayed or earlier transit, depending on the orbital position of the perturbing planet.

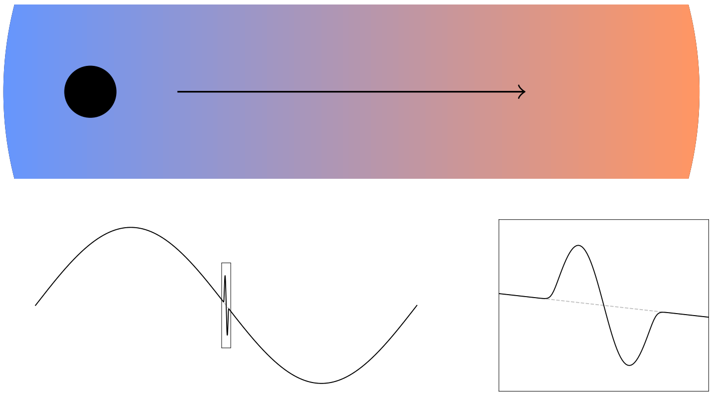

Figure 2.9: The principle of the Rossiter-McLaughlin effect. *Top:* Exoplanet transiting the host star. The star is colored to show the Doppler-shifted light; *Bottom left:* Full RV curve; *Bottom right:* Zoom in on the RV curve during the transit, showing the distortion due to the RM effect.

2.4 LIMITATIONS AND INTEROPERABILITY OF THE RV AND TRANSIT METHODS

As can be seen from Equation 5, the strength of an observed RV signal scales with the planetary mass. This, together with the aforementioned difficulties in correctly recognizing the signals from lower mass planets, creates an observation bias, as the RV method is more sensitive towards high-mass planets. In the same way, both the radial velocity and the transit method create an observation bias towards short-period planets. In the radial velocity method, signals of long-period planets can often only be accounted for with linear or quadratic trends and often provide only poor phase coverage. With the transit method, multiple transits of a planet are necessary to robustly determine their orbital period, or detect potential transit timing variations. The transit method itself is biased towards detecting planets with larger radii, due to the deeper resulting transits. These observational biases are responsible for the large number of known hot Jupiters.

While the strength of the RV signal increases with the planetary mass, there is a degeneracy between the planetary mass m_p and the orbital inclination i. It is generally unknown, whether a strong signal means a very high mass on an inclined orbit or a lower mass on an edge-on orbit. Therefore, from the radial velocity method alone, only the minimum mass $m_p \sin i$ can be directly determined.

For transiting exoplanets on the other hand, the inclination in general already has to be close to 90°, but can be directly determined from the model. This allows to break the degeneracy and to determine the true masses of exoplanets that are observed with both the transit as well as the radial velocity method. The estimation of both the true mass and the radius of the planet open up deeper studies of the planets, including the modelling of their internal compositions and their formation histories.

Observing the radial velocities of a transiting planet during the transit can provide additional information about the system. Similar to the radial velocity induced by a large spot, a transiting planet will, as it moves across the stellar disk, block out part of the Doppler-shifted light and lead to a deformation in the line shape, causing an additional net-shift in the observed radial velocities. This effect is called the Rossiter-McLaughlin (RM) effect [121, 148] and is illustrated in Figure 2.9. Due to the wavelength of the blocked-out light depending on the position of the planet on the stellar disk, the form of the in-transit RV curve can be used to determine the obliquity λ of the planetary orbit, relative to the stellar rotational axis.

The amplitude of the RM signal is given by

$$\Delta V \simeq \left(\frac{R_p}{R_*}\right)^2 \sqrt{(1-b^2)}\, v \sin i_*, \tag{8}$$

with the projected stellar rotational velocity $v \sin i_*$ and the stellar inclination denoted as i_* to differentiate from the planet's orbital inclination i. In the Solar System, values for Jupiter and Earth would be $(\Delta V)_{\mathrm{jup}} \approx 21\,\mathrm{m/s}$ and $(\Delta V)_{\mathrm{earth}} \approx 0.17\,\mathrm{m/s}$. Since the amplitude of the RM signal is directly proprtional to the transit depth, the observation of the RM effect for Earth-sized planets is difficult around Sun-like stars and becomes more accessible around dwarf stars.

Part II

RESEARCH PROJECTS

3

THREE WARM JUPITERS AROUND SOLAR-ANALOG STARS DETECTED WITH TESS

J. EBERHARDT, M. J. HOBSON, T. HENNING, T. TRIFONOV, R. BRAHM, N. ESPINOZA, A. JORDÁN, D. THORNGREN, R. BURN, F. I. ROJAS, P. SARKIS, M. SCHLECKER, M. TALA PINTO, K. BARKAOUI, R. P. SCHWARZ, O. SUAREZ, T. GUILLOT, A. H. M. J. TRIAUD, M. N. GÜNTHER, L. ABE, G. BOYLE, R. LEIVA, V. SUC, P. EVANS, N. DUNCKEL, C. ZIEGLER, B. FALK, W. FONG, A. RUDAT, A. SHPORER, S. STRIEGEL, D. WATANABE, J. M. JENKINS, S. SEAGER, J. N. WINN

This chapter is published in Eberhardt et al. [53]. As the leading author of this project, I did the majority of the analyses myself and wrote most of the text myself. R. Brahm wrote some parts in Section 3.2 as he was responsible for data acquisition and corresponded with external observers. D. Thorngren did the analysis of the heavy element mass and provided corresponding text in Section 3.3.4. R. Burn provided data for a planetary composition curve and added text to the discussion.

Abstract

We report the discovery and characterization of three giant exoplanets orbiting solar-analog stars, detected by the *TESS* space mission and confirmed through ground-based photometry and Radial Velocity (RV) measurements taken at La Silla observatory with *FEROS*. TOI-2373 b is a warm Jupiter orbiting its host star every ~ 13.3 days, and is one of the two most massive known exoplanet with a precisely determined mass and radius around a star similar to the Sun, with an estimated mass of $m_p = 9.3^{+0.2}_{-0.2}\,M_{jup}$, and a radius of $r_p = 0.93^{+0.2}_{-0.2}\,R_{jup}$. With a mean density of $\rho = 14.4^{+0.9}_{-1.0}\,\mathrm{g\,cm^{-3}}$, TOI-2373 b is among the densest planets discovered so far. TOI-2416 b orbits its host star on a moderately eccentric orbit with a period of ~ 8.3 days and an eccentricity of $e = 0.32^{+0.02}_{-0.02}$. TOI-2416 b is more massive than Jupiter with $m_p = 3.0^{+0.10}_{-0.09}\,M_{jup}$, however is significantly smaller with a radius of $r_p = 0.88^{+0.02}_{-0.02}, R_{jup}$, leading to a high mean density of $\rho = 5.4^{+0.3}_{-0.3}\,\mathrm{g\,cm^{-3}}$. TOI-2524 b is a warm Jupiter near the hot Jupiter transition region, orbiting its star every ~ 7.2 days on a circular orbit. It is less massive than Jupiter with a mass of $m_p = 0.64^{+0.04}_{-0.04}\,M_{jup}$, and is consistent with an inflated radius of $r_p = 1.00^{+0.02}_{-0.03}\,R_{jup}$, leading to a low mean density of $\rho = 0.79^{+0.08}_{-0.08}\,\mathrm{g\,cm^{-3}}$. The newly discovered exoplanets TOI-2373 b, TOI-2416 b, and TOI-2524 b have estimated equilibrium temperatures of 860^{+10}_{-10} K, 1080^{+10}_{-10} K, and 1100^{+20}_{-20} K, respectively, placing them in the sparsely populated transition zone between hot and warm Jupiters.

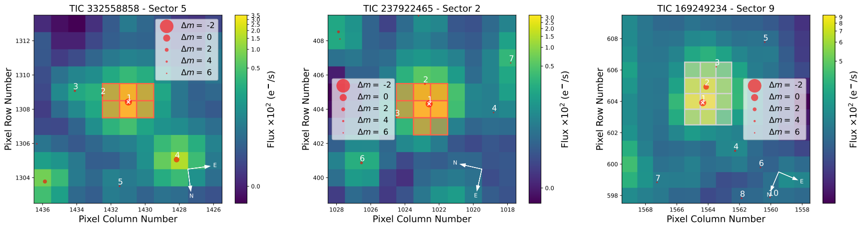

Figure 3.1: *TESS* TPFs of TOI-2373 (TIC 332558858; *left*), TOI-2416 (TIC 237922465; *middle*) and TOI-2524 (TIC 169249234; *right*), created using `tpfplotter`. Orange overlays show the apertures used to determine the flux (a white overlay indicates an automatically detected threshold aperture). Gaia DR2 catalog objects are shown as filled red circles sized according to their brightness relative to the target (marked with a white cross).

3.1 INTRODUCTION

The discovery of an exoplanet around a solar-type star Mayor and Queloz [119], was one of the great achievements of modern astronomy. To date, the field of exoplanetary science has rapidly progressed, leading to the detection of over 5400 exoplanets[1], discovered with various astronomical techniques, such as radial velocity (RV) measurements, transit photometry, and direct imaging. The continued study of exoplanets has provided valuable insights into the diversity and frequency of planetary systems in the Galaxy. With these systems showing a great diversity in physical and orbital characteristics, their study is fundamental for understanding planet formation and evolution. Especially interesting for testing theories of planet formation is the detection and characterization of hot and warm Jupiter-mass planets (see e.g. [40, 57]). Such massive planets in short-period orbits are easier to detect with the transit and RV methods than their long-period counterparts, which allow us to study their properties in depth. The orbits of hot Jupiters however, are influenced by tidal interactions with their host stars, leading to circularization on short timescales, erasing important information about their formation history. On the other hand, warm Jupiter planets are located at greater distances from their host stars, and are much more likely to maintain their postformation and migration orbital eccentricity, since the tidal interactions are weaker. Therefore, warm Jupiters provide an opportunity to study the past interaction with the protoplanetary disk during planet formation and migration.

With the **W**arm g**I**a**N**ts with t**E**ss (WINE) survey[2], we aim for the confirmation and characterization of warm gas giants first identified in photometric data obtained from the Transiting Exoplanet Survey Satellite (TESS) [146]. This survey uses various spectroscopic

---

[1] `http://exoplanet.eu`

[2] `https://sites.google.com/view/wine-exoplanets/home`

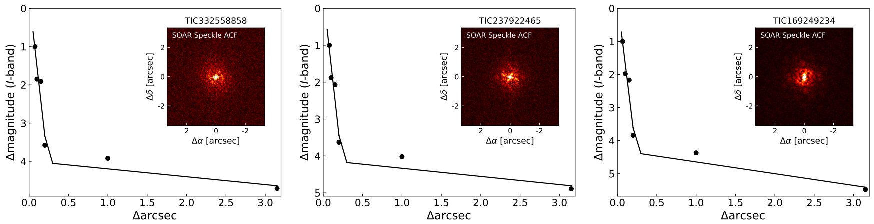

Figure 3.2: Speckle observations from HRCam at SOAR. The black points and solid curves represent the 5σ contrast curves. The insets show the speckle ACFs.

facilities to provide Doppler validation for *TESS* planet candidates. The WINE follow-up survey has been highly successful to date, having detected and characterized many giant planets (see e.g. [27, 28, 60, 79, 98, 104, 152, 177]), including a highly eccentric warm Jupiter [152] and multiple planet systems consistent with a pair of two warm Jupiters near Mean Motion Resonance (MMR) [23, 177, 178].

This work reports the discovery of three single, warm giant exoplanets as part of the WINE survey. The exoplanet companions are designated as TOI-2373 b, TOI-2416 b, and TOI-2524 b, and are found in the transition phase between hot and warm Jupiters and orbit around stars similar to the Sun. Adopting the definitions of [113] for solar analogs [3] and solar twins [4] a search in the TEPCAT catalog [161] reveals 276 exoplanets with known masses and radii orbiting solar analogs, of which only 25 orbit solar twins. Therefore, the newly discovered TESS planets provide valuable insights into the formation and evolution of planets around G dwarf stars similar to the Sun.

In Section 3.2, we present the photometric and spectroscopic observational data used for our analysis. Section 3.3 describes the derivation of the stellar parameters from FEROS spectra, as well our global analyses based on *TESS* photometry and FEROS precise Doppler measurements. Our results are discussed in Section 3.4, and finally, we provide a summary and conclusions of our work in Section 3.5.

3.2 OBSERVATIONS

3.2.1 TESS *photometry*

During the first year of the *TESS* mission, the targets TOI-2373, TOI-2416, and TOI-2524 were observed in the 30 minute cadence mode in the following Sectors: 2, 3, 4, 8 (TOI-2416); 5 (TOI-2373); and 9 (TOI-2524). These three systems were identified as candidates based on

---

[3] $4.04\,\mathrm{cm\,s^{-2}} < \log g < 4.84\,\mathrm{cm\,s^{-2}}$, $-0.3 < [\mathrm{Fe/H}] < 0.3$, $5472\,\mathrm{K} < T_{\mathrm{eff}} < 6072\,\mathrm{K}$

[4] $4.24\,\mathrm{cm\,s^{-2}} < \log g < 4.64\,\mathrm{cm\,s^{-2}}$, $-0.1 < [\mathrm{Fe/H}] < 0.1$, $5672\,\mathrm{K} < T_{\mathrm{eff}} < 5872\,\mathrm{K}$

the analysis of the `tesseract`[5] (F. I. Rojas et al. 2023 in preparation.) generated light curves, where we automatically search for individual transit-like features produced by giant planets [e.g. 152]. In the extended *TESS* mission these targets were observed with a 2 minute cadence in the following Sectors: 28, 29, 30, and 38 (TOI-2416); 31 (TOI-2373, TOI-2416); and 35, 45, and 46 (TOI-2524).

The Science Processing Operations Center (SPOC) [90] at NASA Ames Research Center processed the 2 min data for each of these targets to calibrate pixels, provide photometry, and conducted single and multisector transiting planet searches using an adaptive, noise-compensating matched filter [91–93]. The SPOC detected the transit signatures of TOI-2373, TOI-2416, and TOI-2524 on 2020 December 11, 2020 September 6, 2021 and December 9, respectively. An initial limb-darkened transit model was fitted [114] for the transit signatures, and a suite of diagnostic tests were conducted to help make or break the planetary nature of the signal [180]. The transit signatures all passed the diagnostic tests presented in the Data Validation reports. According to the difference image centroiding tests, the host star is located within $0.74(264)''$ of the transit signal source for TOI-2373, $0.51(258)''$ of the transit signal source for TOI-2416, and $0.898(2570)''$ of the transit signal source for TOI-2524. The SPOC failed to find additional transiting planet signatures in each case. The transit signatures for all three targets were also detected in searches of Full Frame Image (FFI) data by the Quick Look Pipeline (QLP) at MIT [83, 84] as community-provided *TESS* Objects of Interest (TOIs). The TESS Science Office (TSO) reviewed the vetting information and issued an alert on 2020 November 11 for TOI-2416 based on the SPOC detection. TOI-2373 and TOI-2524 were alerted as CTOIs by the WINE collaboration on 2020 October 23 and 2021 March 2, respectively.

We obtained the light curves for the 2 minute cadence data by querying the Mikulski Archive for Space Telescopes (MAST)[6]. We use the data calculated by the SPOC [90] at NASA Ames Research Center, which provides Simple Aperture Photometry (SAP) and systematics-corrected Presearch Data Conditioning (PDF) [159, 164, 165] photometry.

To account for possible contamination from other sources, we studied the Target Pixel File (TPF) plots, generated with `tpfplotter` [5], adopting a standard magnitude limit of $\Delta m = 6$. Figure 3.1 shows the TPF plots for the sectors in which the first transits of TOI-2373, TOI-2416, and TOI-2524 were detected. The TPF plots show the field around the target observed by *TESS* , overplotted with an aperture grid, showing the pixels used to determine the flux, as well as nearby Gaia DR2 sources. The remaining TPF plots for the three targets can be inspected in Figure A1, Figure A2, and Figure A3. Within the aper-

---

[5] `https://github.com/astrofelipe/tesseract`

[6] `https://mast.stsci.edu/portal/Mashup/Clients/Mast/Portal.html`

ture of TOI-2373 we found one other source (TIC 686510210), while the apertures of TOI-2416 and TOI-2524 each contained two additional sources (TIC 237922464 and TIC 650468769, and TIC 169249237 and TIC 169249240, respectively). We determined dilution factors for each 30 minute cadence *TESS* sector according to Espinoza, Kossakowski, and Brahm [61]. The 2 minute PDCSAP cadence data from MAST had already been corrected for contamination from nearby stars and instrumental systematics, thus no dilution correction was applied by our team.

3.2.2 *Ground-based photometry*

Due to the *TESS* cameras' relatively large pixel scale of $21''$ pixel^{-1}, nearby companions can contaminate the photometry. To confirm that the observed TESS signals were associated with the correct host stars, we used various ground-based facilities to observe TOI-2373, TOI-2416, and TOI-2524. The facilities are described in the following subsections.

3.2.2.1 *ASTEP*

Antarctica Search for Transiting ExoPlanets (ASTEP) [49, 71, 122] is a 40 cm telescope located on the East Antarctic Plateau. It features a FLI Proline 16800E 4k × 4k CCD camera with a $1^\circ \times 1^\circ$ field of view and a pixel scale of $0.93''$ pixel^{-1}. ASTEP observed a full transit of TOI-2416 b on 2021 June 28, which was not observed by *TESS*.

3.2.2.2 *LCOGT*

Las Cumbres Observatory Global Telescope (LCOGT) Network [30] is a worldwide network of $1\,\mathrm{m}$ telescopes, equipped with 4096 × 4096 SINISTRO cameras. The cameras have a pixel scale of $0.389''$ pixel^{-1}, resulting in a $26' \times 26'$ field of view. A full transit of TOI-2373 b on 2021 November 10 was observed by the telescopes located at South Africa Astronomical Observatory (SAAO), Teide and Cerro Tololo Inter-American Observatory (CTIO), with SAAO having observed the ingress, CTIO the egress and Teide the full transit. CTIO already observed a partial transit on 2021 September 3. All LCO science images were calibrated by the standard LCOGT `BANZAI` pipeline [120], and photometric measurements were extracted using `AstroImageJ` [36].

3.2.2.3 *Evans 0.36 m telescope at El Sauce*

El Sauce is a private observatory located in the Rio Hurtado province in Chile. TOI-2524 was observed with the Evans $0.36\,\mathrm{m}$ telescope on 2021 March 31, obtaining a full transit light curve with the R_c filter. The telescope is equipped with an STT 1603-3 CCD camera with 1536

× 1024 pixels with an image scale of 1.47″ pixel^{-1} when binned 2 × 2. The data were processed with the `AstroImageJ` package [36].

TOI-2416 was observed with the CDK24ND telescope on 2020 October 23, obtaining an egress. The CDK24ND system consists of a PlaneWave 0.61 m CDK (Corrected Dall-Kirkham) on a PlaneWave L-600 Direct-Drive mount using a Finger Lakes Instrumentation Pro-Line PL16803 CCD camera with no filter.

3.2.3 *Observatoire Moana*

Observatoire Moana (OM) is a global network of robotic telescopes. The station located at El Sauce Observatory (OM-ES), which consists of a 0.6 m CDK telescope coupled to an Andor iKon-L 936 deep depletion 2k × 2k CCD with a pixel scale of 0.67″ pixel^{-1}, was used on 2022 March 10 to obtain an egress for TOI-2524 using the Sloan r' filter. The adopted exposure time was of 33 seconds. This same station was used on 2021 November 9 to obtain an egress of TOI-2373 using the r' filter and exposure times of 50 s. The OM station located in SSO (OM-SSO), which consists of a 0.5 m RCOS Ritchey Chretien telescope coupled to an FLI ML16803 4k × 4k CCD with a pixel scale of 0.47″ pixel^{-1} operating with 2×2 binning, was used to obtain an ingress for TOI-2416 on 2021 October 30. The adopted exposure time was of 49 s and an Astrodon Exoplanet (Clear Blue Blocking) filter was used. Data for both OM stations were processed with a dedicated pipeline that performs the CCD reduction steps along with the computation of the aperture photometry for all stars in the field of view and the generation of the final light curve by selecting the optimal comparison stars.

3.2.4 *High-resolution imaging*

TOI-2373, TOI-2416, and TOI-2524 have all been observed as part of the SOAR *TESS* survey [191], in which high-resolution images of *TESS* planet candidate host stars have been acquired using speckle imaging with the high-resolution camera (HRCamera), mounted to the 4.1 m Southern Astrophysical Research (SOAR) telescope, located at Cerro Pachón, Chile [174]. These high-resolution images aided in the identification and rejection of false-positive *TESS* candidates.

TOI-2373 and TOI-2416 were observed on 2020 December 3, while TOI-2524 was observed on 2022 April 15. For all three targets, no nearby sources were identified within 3″. The contrast curves and auto-correlation functions (ACFs) are shown in Fig. 3.2.

Table 3.1: Stellar parameters for the three targets discussed in this work along with their 1σ uncertainties and floor uncertainties according to Tayar et al. [169] in parantheses.

PARAMETER	TOI-2373	TOI-2416	TOI-2524
$T_{\rm eff}$ (K)	5651 ± 80 (113)	5808 ± 80 (116)	5831 ± 80 (116)
[Fe/H] (dex)	0.3 ± 0.05	0.32 ± 0.05	0.06 ± 0.05
Distance (pc)	496 ± 10	542 ± 8	429 ± 11
Age (Gyr)	$5.9^{+1.7}_{-1.7}$ (1.2)	$4.9^{+1.2}_{-1.1}$ (1.0)	$6.7^{+1.7}_{-1.6}$ (1.3)
$v \sin i$ (km s^{-1})	2.7 ± 0.5	2.4 ± 0.5	2.2 ± 0.5
Mass ($M_\odot$)	$1.041^{+0.032}_{-0.028}$ (0.052)	$1.118^{+0.029}_{-0.027}$ (0.056)	$1.007^{+0.032}_{-0.029}$ (0.050)
$\log g$ (cm s^{-2})	$4.371^{+0.024}_{-0.023}$	$4.303^{+0.019}_{-0.020}$	$4.344^{+0.026}_{-0.025}$
Radius ($R_\odot$)	$1.102^{+0.019}_{-0.019}$ (0.044)	$1.236^{+0.018}_{-0.018}$ (0.049)	$1.119^{+0.024}_{-0.023}$ (0.045)
Luminosity ($L_\odot$)	$1.125^{+0.058}_{-0.046}$ (0.023)	$1.574^{+0.077}_{-0.061}$ (0.031)	$1.307^{+0.079}_{-0.065}$ (0.026)
ρ (g cm^{-3})	$1.096^{+0.083}_{-0.073}$	$0.835^{+0.049}_{-0.048}$	$1.013^{+0.083}_{-0.075}$
A_V (mag)	$0.097^{+0.075}_{-0.062}$	$0.097^{+0.070}_{-0.059}$	$0.130^{+0.089}_{-0.077}$

3.2.5 *FEROS Spectroscopy*

FEROS [100] is an echelle spectrograph mounted on the 2.2 m MPG/ESO[7] telescope at ESO's La Silla Observatory, Chile. FEROS is a highly efficient spectrograph with a resolving power of $R = 48\,000$, covering the visible wavelength range from ~ 350 to ~ 920 nm. FEROS's achievable RV precision is approximately 10 m s^{-1}, which makes it an ideal instrument for confirming the planetary nature of massive exoplanets discovered by *TESS* in the Southern Hemisphere. During the time from 2020 February to 2021 March, we obtained 16 FEROS spectra for TOI-2373, 17 for TOI-2416, and eight for TOI-2524. From these spectra we extracted the RV measurements and the stellar activity indicators BIS, Hα, He I, $\log R'_{\rm HK}$ and Na II using the Collection of Elemental Routines for Echelle Spectra (CERES) pipeline [25]. The FEROS RVs and stellar activity measurements for our targets are listed in Table A1.

3.3 ANALYSIS AND RESULTS

3.3.1 *Stellar Parameters*

The stellar parameters for the three studied targets have been estimated using a similar method to previous discoveries from the WINE survey (e.g. [27, 79, 152, 177]). We computed the atmospheric param-

---

[7] MPG = *Max-Planck-Gesellschaft* = Max Planck Society; ESO = European Southern Observatory.

eters of the three targets from the coadded FEROS spectra by using the `zaspe` package [26], which provides the effective temperature T_{eff}, surface gravity $\log g$, metallicity [Fe/H], and the projected rotational velocity $v \sin i$. `zaspe` determines these by comparing the coadded spectra with a grid of synthetic spectra that were generated from the ATLAS9 model atmospheres [34]. The parameters of the best-fit model atmosphere are adopted as the parameters of the observed star.

To determine the physical parameters of the stars, we followed the procedure described in Brahm et al. [27]. We used the Gaia DR2 parallaxes [65, 66] to convert broadband photometric measurements from publicly available catalogs into absolute magnitudes and compared them to synthetic magnitudes from the PARSEC stellar evolutionary models [29]. For the employed stellar models, we fixed the stellar metallicities to those we found with `zaspe`, while using the effective temperature from `zaspe` as a prior. We determined the age, mass, luminosity, density, and extinction using the `emcee` package [63] to sample the posterior distribution. We further obtained more precise values for T_{eff} and $\log g$ compared to the values obtained from `zaspe`. Table 3.1 lists the atmospheric and physical properties of TOI-2373, TOI-2416, and TOI-2524, alongside their 1σ uncertainties.

3.3.2 *Period search analysis*

We detrended the *TESS* transit light curves using the `wotan` package [78]. We chose a Gaussian Processes model with a Matern 3/2 kernel of size 5 days, while also taking dilution factors for each individual 30 minute *TESS* sector into account. After detrending the *TESS* light curves (see Sections 3.3.3.1 - 3.3.3.3), we performed a period search using the `transitleastsquares` (TLS) package [77]. The top panel of Figure 3.3 shows the results from the TLS analysis of the raw light curves after detrending, whereas the bottom panel shows the TLS analysis of the residuals after fitting of a best-fit transit model applied to the light curves. Figure 3.3 indicates we detected very significant TLS signals for the three targets at periods of ~ 13.3 days, ~ 8.3 days, and ~ 7.2 days indicated by dashed blue lines. No further significant signals were detected in the residuals from our best-fit transit model, which indicates only one transiting planet in each target could be detected with *TESS* .

We employed the Maximum Likelihood Periodogram (MLP) [15, 188] to inspect the FEROS RV and stellar activity measurements for significant periodic signals. Figure 3.4 shows the results for the available RV and activity data. The top two panels of Figure 3.4 show the power spectra for the RVs and the RV residuals from a one-planet Keplerian fit, respectively. The following panels show the periodograms of the stellar activity data, and the window function of the FEROS

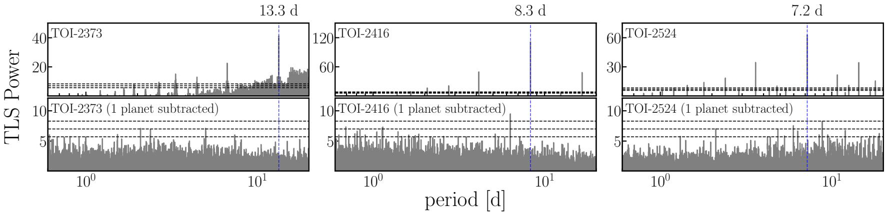

Figure 3.3: TLS analysis of TOI-2373, TOI-2416, and TOI-2524. The top panels show the TLS results of the raw light curves, the bottom panels show the TLS results after subtracting a photometric transit model. The dashed blue vertical lines show the transit signal periods. Dashed horizontal lines correspond to FAP levels of 10%, 1%, and 0.1%.

RVs in the bottom panel. The orbital periods of the planet candidates are indicated as dashed blue lines. We determined the maximum possible rotational periods of the host stars $P_{\rm rot}/\sin i = 2\pi R_\star/v \sin i$ and their 1σ uncertainties by using the stellar radii and projected rotational velocities from Table 3.1. Using our determined orbital inclinations of the systems, and assuming orbits and stellar spins are aligned, we removed the dependency on the inclination and found rotational periods of $P_{\rm rot} = 20.63^{+0.01}_{-0.01}$ days, $26.04^{+0.01}_{-0.06}$ days, and $25.71^{+0.01}_{-0.02}$ d for TOI-2373, TOI-2416, and TOI-2524, respectively. The orbital periods of all three planet candidates reside outside the uncertainties of their host stars' rotational periods.

3.3.3 *Global Modelling*

For the combined analyses of the RV and photometry data for TOI-2373, TOI-2416, and TOI-2524, we used the `Exo-Striker`[8] [176] exoplanet toolbox. `Exo-Striker` employs the `batman` package [105] for light-curve transit models, and the formalism in Lee and Peale [112] for RV models. For posterior analysis, the `Exo-Striker` uses the Nested Sampling (NS) algorithm [158] in conjunction with the `dynesty` package [162]. The NS setup in this work is similar to that adopted in Trifonov et al. [177]. We run 100 "live-points" per parameter using a "dynamic" NS scheme. The priors for the parameters were estimated from consecutive NS runs, starting from parameters derived from TLS and MLP runs.

In the NS scheme, the orbital elements, transit, and RV data parameters, and transit light-curve parameters were modeled simultaneously. The fitted parameters are namely the RV semiamplitude K, the orbital period P, the eccentricity e, the argument of periastron ω, the orbital inclination i, the time of midtransit t_0, and the relative semimajor axis and planetary radius $a/R_\star$ and $r/R_\star$. As well, we adopt quadratic limb-darkening coefficients u_1 and u_2 for the light-

---

[8] https://github.com/3fon3fonov/exostriker

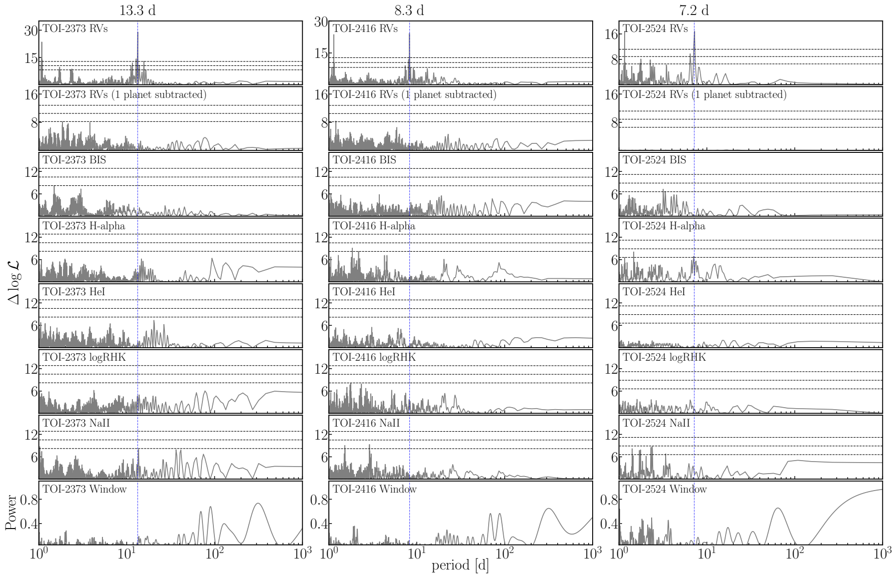

Figure 3.4: Maximum likelihood periodogram analysis of TOI-2373, TOI-2416, and TOI-2524. The top two panels show the periodograms of the RV data, before and after subtracting a Keplerian model, and the following panels show the periodograms of stellar activity indicators and the RV window function. Shown as dashed blue vertical lines are the transit signal periods. Dashed horizontal lines correspond to FAP levels of 10%, 1%, and 0.1%.

curve data. Additional parameters in our NS modeling are the transit and RV data offsets, and jitter parameters. The latter are added in quadrature to the instrumental data uncertainties to account for the unknown variance of the data, while we optimize the maximum $-\ln\mathcal{L}$ function of our combined model. From the resulting posterior probability distribution, we derive posteriors of the mass m_p, semimajor axis a_p, radius r_p, mean density ρ_p, and equilibrium temperature T_{eq} for each planet.

For each target, we tested two competing models, a circular fit (i.e., $e = 0$, while ω is undefined and forced to 0°) and a more complex, full Keplerian fit allowing eccentric orbits. We compared the competing models based on their Bayesian log-evidence $\ln\mathcal{Z}$ from the results of the NS fitting, computing $\Delta\ln\mathcal{Z}$ as $\ln\mathcal{Z}_{ecc} - \ln\mathcal{Z}_{circ}$. This model comparison was based on Trotta [179]. Two models are not considered distinguishable if their Bayesian log-evidence difference satisfies $\Delta\ln\mathcal{Z} \lesssim 2$. For $\Delta\ln\mathcal{Z} > 2$, a model is moderately favored over another, while a difference of $\Delta\ln\mathcal{Z} > 5$ indicates a strongly favored model. Below, we introduce each target analysis results individually, whereas Table 3.2 summarizes the relevant physical and orbital parameter estimates for TOI-2373, TOI-2416, and TOI-2524. The complete list of posterior estimates and $\ln\mathcal{Z}$ parameters are given in Tables A2 - A4.

3.3.3.1 *TOI-2373*

Our model comparison resulted in a difference of $\Delta \ln \mathcal{Z} = 16.71$, thus favoring the eccentric model strongly against the circular model. Our final estimates show that TOI-2373 b is a warm Jupiter with a mass of $m_p = 9.3^{+0.2}_{-0.2}\,M_{jup}$, a radius of $r_p = 0.93^{+0.2}_{-0.2}\,R_{jup}$, an orbital eccentricity of $e = 0.112^{+0.007}_{-0.009}$, and a bulk density of $\rho_p = 14.4^{0.92}_{-1.0}\,\mathrm{g\,cm^{-3}}$. It orbits its host star with an orbital period of $P = 13.34$ days corresponding to a distance of $a_p = 0.11$ au. The planetary equilibrium temperature is $T_{eq} = 860^{+10}_{-10}$ K.

Figure A4 shows a time series of the photometric and RV data, along with the residuals underneath. The top panel shows the *TESS* light curves for Sectors 5 and 31, together with the transit model shown as a solid gray line. In both sectors, two transits are detected. The bottom panel shows the FEROS RV measurements and the Keplerian model as a gray line. Figure 3.5 shows the *TESS* photometry (top left), ground-based photometry (top right), and FEROS RV measurements (bottom) phase folded with the orbital period of 13.3 days.

Table 3.2: Median values of the relevant physical and orbital parameters for TOI-2373 b, TOI-2416 b, and TOI-2524 b alongside their 1σ uncertainties.

PARAMETER	TOI-2373 b	TOI-2416 b	TOI-2524 b
P (d)	$13.33668^{+0.00001}_{-0.00001}$	$8.275479^{+0.000009}_{-0.000009}$	$7.18585^{+0.00001}_{-0.00001}$
e	$0.112^{+0.007}_{-0.009}$	$0.32^{+0.02}_{-0.02}$	0 (fixed)
i (degrees)	$89.2^{+0.6}_{-0.2}$	$90.0^{+0.6}_{-0.6}$	$89.4^{+0.4}_{-0.4}$
m (M_{jup})	$9.3^{+0.2}_{-0.2}$	$3.00^{+0.10}_{-0.09}$	$0.64^{+0.04}_{-0.04}$
r (R_{jup})	$0.93^{+0.02}_{-0.02}$	$0.88^{+0.02}_{-0.02}$	$1.00^{+0.02}_{-0.03}$
a (au)	$0.112^{+0.001}_{-0.001}$	$0.0831^{+0.0007}_{-0.0007}$	$0.0730^{+0.0007}_{-0.0007}$
ρ ($\mathrm{g\,cm^{-3}}$)	$14.4^{+0.9}_{-1.0}$	$5.4^{+0.3}_{-0.3}$	$0.79^{+0.08}_{-0.08}$
T_{eq} (K)	860^{+10}_{-10}	1080^{+10}_{-10}	1100^{+20}_{-20}

3.3.3.2 *TOI-2416*

As a result of our Bayesian log-evidence-based comparison, the eccentric model is very strongly favored against the circular model ($\Delta \ln \mathcal{Z} = 27.84$). TOI-2416 b is a warm Jupiter with a mass of $m_p = 3.00^{+0.10}_{-0.09}\,M_{jup}$, a radius of $r_p = 0.88^{+0.02}_{-0.02}\,R_{jup}$, an orbital eccentricity of $e = 0.32^{+0.02}_{-0.02}$ and a bulk density of $\rho_p = 5.4^{+0.3}_{-0.3}\,\mathrm{g\,cm^{-3}}$. It orbits its host star at a distance of $a_p = 0.08$ au corresponding to an orbital period of $P = 8.28$ days. Its equilibrium temperature is $T_{eq} = 1080^{+10}_{-10}$ K.

Figure A5 shows a time series of the photometric and RV data along with the residuals underneath. The top panel shows the *TESS* light curves for Sectors 2, 3, 4, 8, 28, 29, 30, 31 and 38 together with the transit model shown as solid gray line. In all sectors, two to three transits can be observed. The bottom panel shows the FEROS RV measurements and the Keplerian model as a gray line. Figure 3.6 shows the *TESS* photometry (top left), ground-based photometry (top right), and FEROS RV measurements (bottom) phase folded with the orbital period of 8.3 days.

3.3.3.3 *TOI-2524*

Considering a difference of $\Delta \ln \mathcal{Z} = -2.23$, the circular model is moderately favored against the eccentric model. Therefore, we chose to adopt the simpler circular model as our final result. TOI-2524 b is a warm giant with a mass of $m_p = 0.64^{+0.04}_{-0.04}\,M_{jup}$, a radius of $r_p = 1.00^{+0.02}_{-0.03}\,R_{jup}$ and a bulk density of $\rho_p = 0.79^{+0.08}_{-0.08}\,\mathrm{g\,cm^{-3}}$. It orbits its host star at a distance of $a_p = 0.07\,\mathrm{au}$ corresponding to an orbital period of $P = 7.19\,\mathrm{days}$. Its equilibrium temperature is $T_{eq} = 1100^{+20}_{-20}\,\mathrm{K}$.

Figure A6 shows a time series of the photometric and RV data along with the residuals underneath. The top panel shows the *TESS* light curves for Sectors 9, 35, 45, and 46 together with the transit model shown as solid gray line. In all sectors, two to four transits can be observed. The bottom panel shows the FEROS RV measurements and the Keplerian model as a gray line. Figure 3.7 shows the *TESS* photometry (top left), ground-based photometry (top right), and FEROS RV measurements (bottom) phase folded with the orbital period of 7.2 days.

3.3.4 *Heavy element mass*

Following [173], we determined the bulk metallicity fraction Z_p for TOI-2373 b, TOI-2416 b, and TOI-2524 b as well as the anomalous heating efficiency ϵ for TOI-2416 b and TOI-2524 b. The estimation of the planetary metallicity is based on an Markov Chain Monte Carlo inversion of a planet evolution model [see 173], using the planetary mass, bulk metallicity, age, and log anomalous heating fraction as parameters. The priors are either taken from observations (mass and age) or based on a mass-metallicity relation [for metallicity; 171] and equilibrium temperature [for heating; 172]. The model uses these parameters to compute a radius which it compares to the observed radius. The anomalous heating efficiency is defined as the logarithm of the heat injected into a planet as a fraction of the incident stellar flux [172]. It is a parameterization of an unknown mechanism transporting energy from irradiation to the interior of the planet and causing the planet to inflate (see Sect. 3.4).

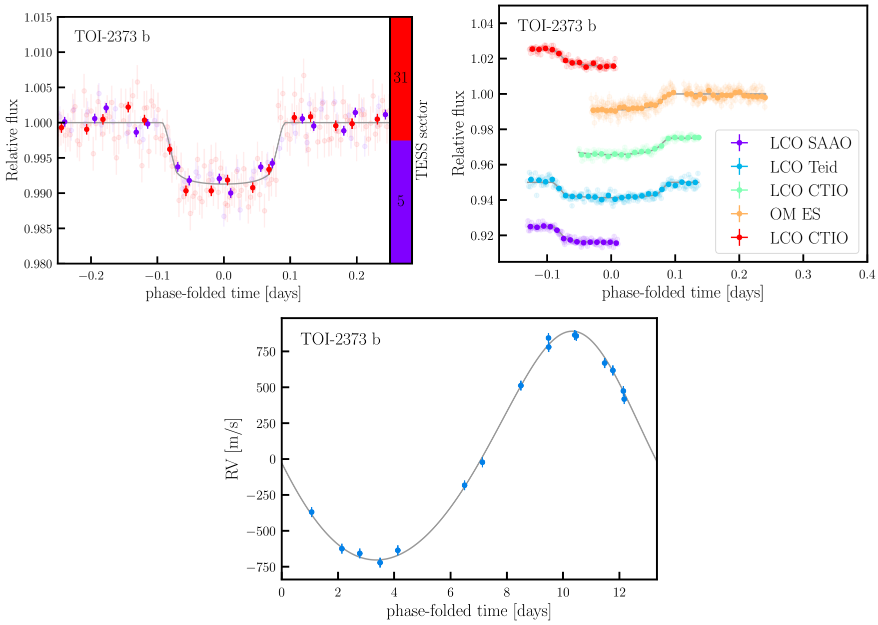

Figure 3.5: Phase plots for TOI-2373 b. *Top left*: phase-folded light curves for all TESS sectors. Faint points correspond to the unbinned data, the strong points to binned data. *Top right*: phase-folded light curves of the photometry from the ground-based facilities. Individual data sets are offset for better visibility. LCO CTIO observed two different transits and thus appears twice. *Bottom*: phase-folded radial velocities.

We found bulk metallicities of $Z_p = 0.11^{+0.06}_{-0.05}$, $Z_p = 0.36^{+0.03}_{-0.03}$, and $Z_p = 0.24^{+0.03}_{-0.03}$ for TOI-2373 b, TOI-2416 b, and TOI-2524 b, respectively. As well, we estimated heating efficiencies of $\epsilon = 0.34^{+0.012}_{-0.018}\%$ and $\epsilon = 0.40^{+0.014}_{-0.021}\%$ for TOI-2416 b and TOI-2524 b, respectively. TOI-2373 b has an equilibrium temperature of 860^{+10}_{-10} K and is therefore too cold for any anomalous heating.

3.4 DISCUSSION

Figures 4.8 - 4.11 show the three targets presented in this work in the context of all known transiting exoplanets orbiting solar analog stars, including the solar system planets. The planets have been selected from the TEPCAT catalog [161] to match the following selection criteria on the host stars: 4.3 dex $< \log g <$ 4.6 dex, $-0.1 < [\mathrm{Fe/H}] < 0.4$, and 5600 K $< T_{\mathrm{eff}} <$ 5900 K. Figure 3.8 shows a mass-separation diagram, with the exoplanets color coded according to their equilibrium temperatures. TOI-2373 b, TOI-2416 b, and TOI-2524 b are shown as big color-coded stars. The three planets, while all having similar semi-major axes, cover a wide range of masses, with TOI-2373 b being one of the two most massive known planets around a solar analog, featur-

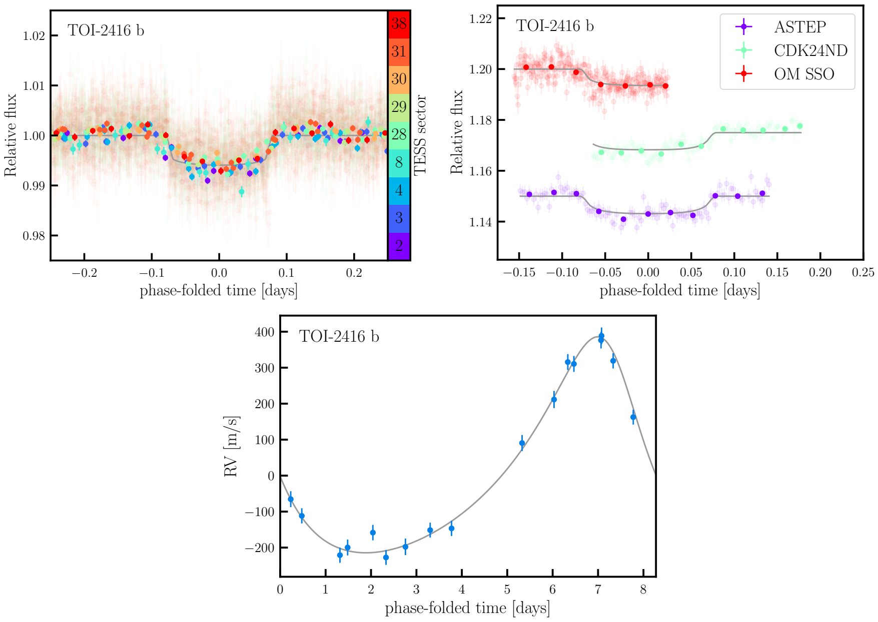

Figure 3.6: Same as Figure 3.5, but for TOI-2416 b.

ing a mass of $m_p = 9.3^{+0.2}_{-0.2} M_{jup}$, the other being CoRoT-27 b with a mass of $m_p = 10.39 \pm 0.55 M_{jup}$[133].

Figure 3.9 shows the same set of planets according to their orbital eccentricities and orbital separations. TOI-2373 b and TOI-2416 b have rather eccentric orbits compared to most known hot Jupiters orbiting similar stars. In the regime of warm Jupiters, there are planets with very highly eccentric orbits, however, this regime is only sparsely sampled with known exoplanets. Warm Jupiters with high eccentricities include TOI-2179 b ($e = 0.575$) [152], CoRoT-20 b ($e = 0.59$) [142, 144], Kepler-1656 b ($e = 0.838$) [8, 24], Kepler-1657 b ($e = 0.496$) [74], and K2-287 b ($e = 0.478$) [21, 97]. Understanding the orbital eccentricity demographics is important for constraining formation and migration models, as different evolutionary tracks predict different distributions.

Figure 3.10 shows all known exoplanets around Solar analog-stars, including the solar system giant planets, in a mass-radius diagram, allowing for study of their bulk densities. Shown in dashed lines are nominal density curves corresponding to 0.1, 0.3, 1, 3, and 10 $\mathrm{g\,cm^{-3}}$, while exoplanet composition models from Emsenhuber et al. [58], Mordasini et al. [126], and Zeng et al. [189] are shown as solid lines of varying colors. For the latter model, we fitted their synthetic planet population with orbital periods shorter than 30 days and masses larger than 100 M_{earth} using the same functional form as Mordasini et al. [126]

$$r(m) = \frac{b}{1 + \left|\frac{\log_{10}(m/M_0)}{w}\right|^{p}} \tag{9}$$

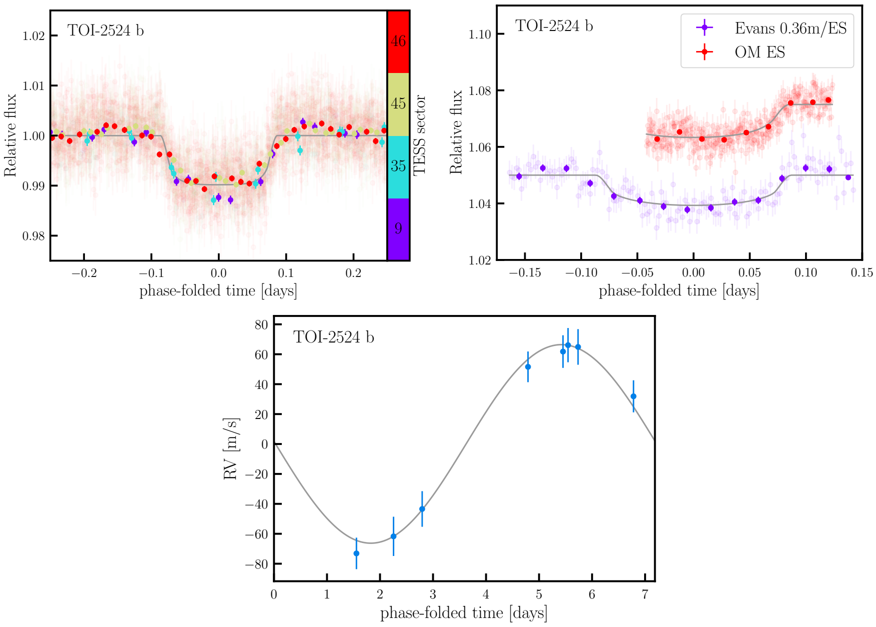

Figure 3.7: Same as Figure 3.5, but for TOI-2524.

and found $b = 1.061 \pm 0.002\,R_{jup}$, $M_0 = 3.85 \pm 0.10\,M_{jup}$, $w = 2.0 \pm 0.2$, and $p = 2.5 \pm 0.2$. The error of the fit was determined by bootstrapping their sample and taking the standard deviations of the resulting fit parameters. In Figure 3.10, we show as a shaded region the moving standard deviation of the synthetic data with respect to the fit. This visualizes the predicted scatter, which is larger at lower planetary masses.

While TOI-2524 b closely follows the model predictions, TOI-2373 b and TOI-2416 b are denser, containing either more massive cores, or consisting of a larger fraction of heavy elements in their envelopes. Hot Jupiters have frequently been observed to be inflated [43], although the exact mechanisms creating these puffy planets are still not entirely understood [109, 150, 153]. Observed inflated hot Jupiters span a temperature range of $1300\,K < T_{eq} < 1500\,K$, and have a mean observed radius of $1.1 \pm 0.1\ R_{jup}$.

However, the radius inflation effect is predicted to exist for planets with $T > 1000$ K [43, 124]. Therefore, for consistency we include anomalous heating in our model of TOI-2524 b, which has an equilibrium temperature of 1100 ± 20 K. Although this planet has a lower density than the other planets presented in this paper, it does not appear to be significantly inflated. Another possible explanation for TOI-2524 b's lower density compared to TOI-2373 b and TOI-2416 b might be a lower abundance of heavy elements, which could be associated to the host star's relatively low metallicity of [Fe/H] = $+0.06 \pm 0.05$. Assuming a similarly low abundance of heavy elements in the protoplanetary disk as in the star, would result in an equally low abundance of heavy elements in the planet; however, the correlation be-

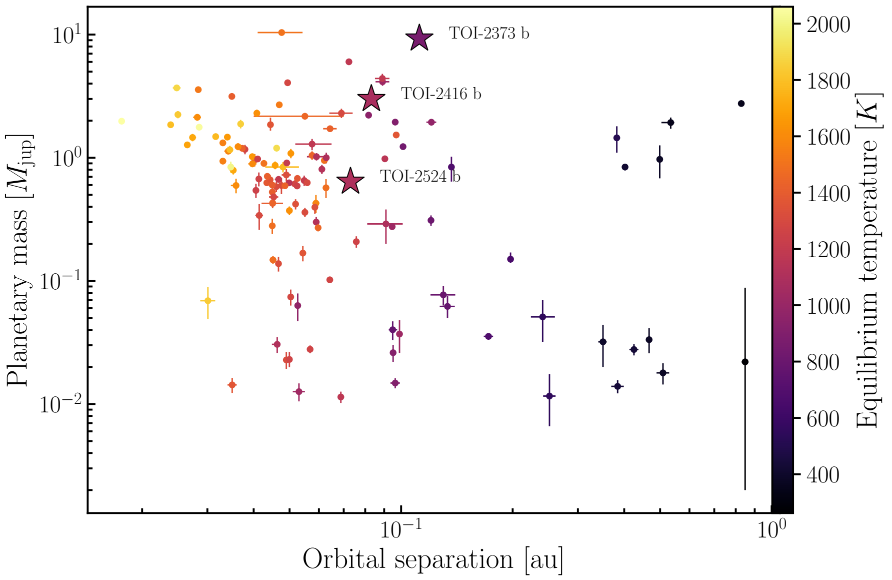

Figure 3.8: Mass-separation diagram for planets around solar-analog stars (definition according to [113], see Section 3.1). The new planets TOI-2373 b, TOI-2416 b, and TOI-2524 b are shown as big stars.

tween stellar metallicity and heavy element content is unclear [124, 171]. The low heavy element content of the planet could be also associated to formation/migration history.

Both TOI-2373 and TOI-2416 have higher metallicities and host denser exoplanets. The comparison to evolved, synthetic planets modeled by Emsenhuber et al. [58] shown in Figure 3.10 reveals that they are not necessarily reproduced naturally by core accretion formation models. TOI-2373 b has a bulk metallicity of $Z_p = 0.11^{+0.06}_{-0.05}$. A planet as massive as TOI-2373 b could possibly have formed either by core-accretion or by gravitational instability [151] and should have the same metallicity as the host star. Postformation accretion of metals could explain its high amount of heavy elements [33, 69, 88, 111, 125, 156]. TOI-2416 is a warm super-Jupiter and has an even higher bulk metallicity of $Z_p = 0.36^{+0.03}_{-0.03}$. This is an unusually high amount of metals and makes it a rare case. While it is still unclear how such a planet can form, similar planets, including CoRoT-10 b ($m = 2.75\,M_{\rm jup}$ and $Z_p \approx 0.23$), HATS-17 b ($m = 1.34\,M_{\rm jup}$ and $Z_p \approx 0.46$), HAT-P-20 b ($m = 7.25\,M_{\rm jup}$ and $Z_p \approx 0.29$) and Kepler-419 b ($m = 2.5\,M_{\rm jup}$ and $Z_p \approx 0.25$) have been presented by Thorngren et al. [171]. Combined with the existing sample of dense exoplanets, this poses a challenge to planet formation and evolution or, alternatively, interior structure models.

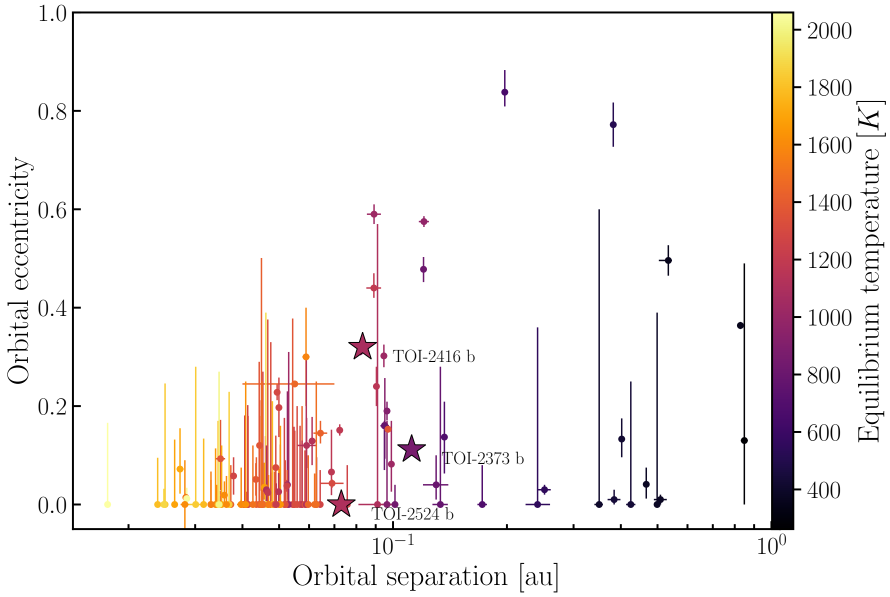

Figure 3.9: Mass-separation diagram for planets around solar-analog stars (definition according to [113], see Section 3.1). Shown as big stars are the new planets TOI-2373 b, TOI-2416 b, and TOI-2524 b.

3.5 SUMMARY AND CONCLUSION

We report the discovery and characterization of three giant exoplanets orbiting stars similar to the Sun, first identified as candidates using data from the *TESS* mission and confirmed with RV measurements with *FEROS*. TOI-2373 b is a warm Jupiter with an orbital period of ~ 13.3 days, an estimated mass of $m_p = 9.3^{+0.6}_{-0.2}\,M_{jup}$ and a radius of $r_p = 0.93^{+0.2}_{-0.2}\,R_{jup}$. With a mean density of $\rho = 14.4^{+0.9}_{-1.0}\,g\,cm^{-3}$, TOI-2373 b is among the densest planets discovered so far and presents a challenge to current theories of planet formation and evolution. TOI-2416 b is a planet with a short period of ~ 8.3 days, a mass of $m_p = 3.0^{+0.10}_{-0.09}\,M_{jup}$ and a small radius of $r_p = 0.88^{+0.02}_{-0.02}\,R_{jup}$, also resulting in an anomalously high mean density of $\rho = 5.4^{+0.3}_{-0.4}\,g\,cm^{-3}$. TOI-2524 b is a low-density warm Jupiter near the hot Jupiter transition region with a period of ~ 7.2 days. For TOI-2524 b we estimated a mass of $m_p = 0.64^{+0.04}_{-0.04}\,M_{jup}$ and a radius of $r_p = 1.00^{+0.02}_{-0.03}\,R_{jup}$, leading to a mean density of $\rho = 0.79^{+0.08}_{-0.08}\,g\,cm^{-3}$, similar to that of Saturn.

The newly discovered exoplanets TOI-2373 b, TOI-2416 b, and TOI-2524 b have estimated equilibrium temperatures of 860^{+10}_{-10} K, 1010^{+10}_{-10} K, and 1100^{+20}_{-20} K, respectively, placing them in the sparsely populated transition region between hot and warm Jupiters. This is further supported by Rice et al. [145], who empirically defined the boundary between hot and warm Jupiters based on orbital alignment or misalignment, using the relative size of the orbit $a/R_\star$, with hot Jupiters satisfying $a/R_\star < 11$ and warm Jupiters satisfying $a/R_\star > 11$. With

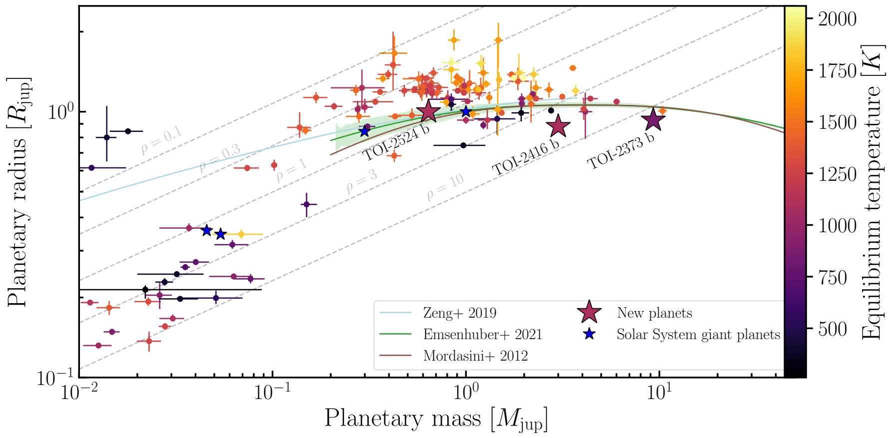

Figure 3.10: Mass-radius diagram for planets around Solar-analog stars. Shown as blue stars are the solar System giant planets, whereas the new planets TOI-2373 b, TOI-2416 b, and TOI-2524 b are shown as colored stars. Shown as solid lines are exoplanet composition models based on [58, 126, 189] and fixed densities of ρ = 0.1, 0.3, 1.0, 3.0, and 1.0 $\mathrm{g\,cm^{-3}}$ are shown as dashed gray lines. The shaded area around the fit to the data of Emsenhuber et al. [58] marks the moving standard deviation of the synthetic planets.

orbital sizes of $a_p/R_\star = 23.1$, $a_p/R_\star = 14.4$, and $a_p/R_\star = 14.3$ for TOI-2373 b, TOI-2416 b, and TOI-2524 b, respectively, these targets reside in the transition region.

While we do not have measurements for the three targets' RVs during the planets' transits, we can estimate the amplitudes of the Rossiter-McLaughlin (RM) effect [121, 148] to be 12.9, 10.4, and 22.8 $\mathrm{m\,s^{-1}}$, respectively, which can be measured by high-resolution spectrographs.

Rice et al. [145] showed that warm Jupiters tend to be in spin-orbit alignment, whereas hot Jupiters tend not to be aligned. Attia et al. [13] find the same tendency, with longer-period planets being more aligned than closer-in planets. These findings are also consistent with Huang, Wu, and Triaud [85], who come to the conclusion that hot Jupiters form separately from other gas giants, while warm Jupiters tend to form via disk migrations, explaining their coplanar orbits. As transiting planets, TOI-2373 b, TOI-2416 b, and TOI-2524 b are well suited to estimate the sky-projected spin-orbit alignment of their host stars through RM observations, aiding in constraining the formation scenarios of these systems.

4

TOI-6695: A PAIR OF NEAR-RESONANT MASSIVE PLANETS OBSERVED WITH TESS FROM THE WINE SURVEY

J. EBERHARDT, T. TRIFONOV, T. HENNING, M. TALA PINTO, R. BRAHM, A. JORDÁN, N. ESPINOZA, M. I. JONES, M. J. HOBSON, F. I. ROJAS, M. SCHLECKER, L. ACUÑA, R. BURN, G. BOYLE, R. LEIVA, J. MCCORMAC, N. DUNCKEL, D. DRAGOMIR, J. D. CRANE, S. SHECTMAN, J. K. TESKE, D. OSIP, A. F. GUPTA, S. ULMER-MOLL, F. BOUCHY, M. LENDL, D. GANDOLFI, G. R. RICKER, J. M. JENKINS, S. SEAGER, J. N. WINN

This chapter is published in Eberhardt et al. [55]. As the leading author of this project, most analyses were done by myself and most of the text was written by me. Some parts of Section 4.2 were written by R. Brahm, M. Jones, A. Gupta, D. Dragomir, who were responsible for data acquisition. R. Burn provided data for a compostion curve and carried out the simulation of synthetic 3:1 planet pairs and added text to the discussion. L. Acuña helped with text for the internal modelling with GASTLI.

ABSTRACT

We present the discovery and characterization of a pair of warm Jovian-mass exoplanets orbiting the Sun-like star TOI-6695, based on *TESS* transits and precise Radial Velocity (RV) measurements obtained with FEROS, HARPS, CHIRON, CORALIE, and PFS. The transiting exoplanet TOI-6695 b has an orbital period of ~80.4 days, a radius of $0.85\,\mathrm{R_{jup}}$, and a mass of $0.21\,\mathrm{M_{jup}}$.The outer planet has a minimum mass of $1.45\,\mathrm{M_{jup}}$ and an orbital period of about 242.4 days, confidently constrained by the Doppler time-series data. The TOI-6695 exoplanet system exhibits transit-timing variations due to the dynamical interaction of the planets, which reside near a 3:1 mean-motion resonance. We modeled the TOI-6695 system's orbital and dynamical configuration by performing self-consistent N-body fits of *TESS* photometry, ground-based photometry from Observatoire Moana, and precise RV data, all of which are consistent with the presence of a warm Jovian-mass duo of exoplanets.

4.1 INTRODUCTION

The first discovery of an exoplanet around a Solar-type star by Mayor and Queloz [119] using radial velocity (RV) measurements marked one of the major milestones in modern astronomy and astrophysics.

Since the discovery of the hot Jupiter 51 Peg b in 1995, the field of exoplanetary science progressed rapidly, revealing over 5 800 known exoplanets [1], discovered with a variety of astronomical techniques, such as Doppler RV measurements, transit photometry (e.g. HD 209458) [35, 75], microlensing (e.g. OGLE 2005-BLG-390Lb) [17] and direct imaging (e.g. β Pic b) [107], which are by far the most effective exoplanet detection methods. The ongoing study of exoplanets has contributed significant insights into the diversity and abundance of planetary systems within the Galaxy. As these systems vary greatly in physical and orbital characteristics, their study is of fundamental importance for the understanding of planet formation and evolution. Especially, the detection and characterization of hot ($P < 10\,\mathrm{d}$) and warm ($10\,\mathrm{d} < P < 300\,\mathrm{d}$) Jupiter-mass planets provides an ideal testing ground for studying theories of planet formation (see e.g. [40, 57]).

Hot and warm Jovian exoplanets have relatively short orbital periods, making them easy to detect with the RV and transit methods and to study their properties in detail. The orbits of hot Jupiters are subject to tidal interactions with their host stars, which result in a rapid circularisation process and a loss of information regarding the formation history of the planets. Warm Jupiters, however, orbit their stars at greater distances and are much more likely to maintain their original orbital eccentricities (see [40] and references therein) and stellar obliquities (see [3] and references therein), given the weaker tidal interactions. Therefore, the study of warm Jupiters offers a unique opportunity to understand the past interaction with the proto-planetary disk during the planetary formation and migration stage.

The aim of the **W**arm g**I**a**N**ts with t**E**ss (WINE) survey is the discovery and orbital and physical characterization of warm giants revealed by the Transiting Exoplanet Survey Satellite (TESS) [146], using precise Doppler follow-up observations. The WINE follow-up survey has been highly successful to date, having detected and characterized a significant number of warm giant planets (e.g. HD 1397 b [27], TOI-150 b and TOI-163 b [104], HD 213885 b [60], TOI-677 b [98], TOI-481 b and TOI-892 b [28], TOI-2179 b [152], TOI-216 [41], TOI-2202 [177], TOI-201 [79], TOI-199 [80], TOI-2373, TOI-2416 and TOI-2524 [53], TIC 279401253 [23], TOI-2525 [178], TOI-2529 and TIC 279401253 [96], TOI-2328, TOI-3837, TOI-5027 and TOI-6628 [168], TOI-4504 [182]), including two warm Jupiters on highly eccentric orbits (TOI-2179 b, TOI-6628 b) and multiple systems consisting of pairs of warm giants near mean motion resonance (MMR; TOI-2202, TIC 279401253, TOI-2525), as well as a warm Jupiter with the strongest Transit Timing Variation (TTV) reported to date (TOI-4504).

---

[1] `https://exoplanetarchive.ipac.caltech.edu/`; 2024 December 16

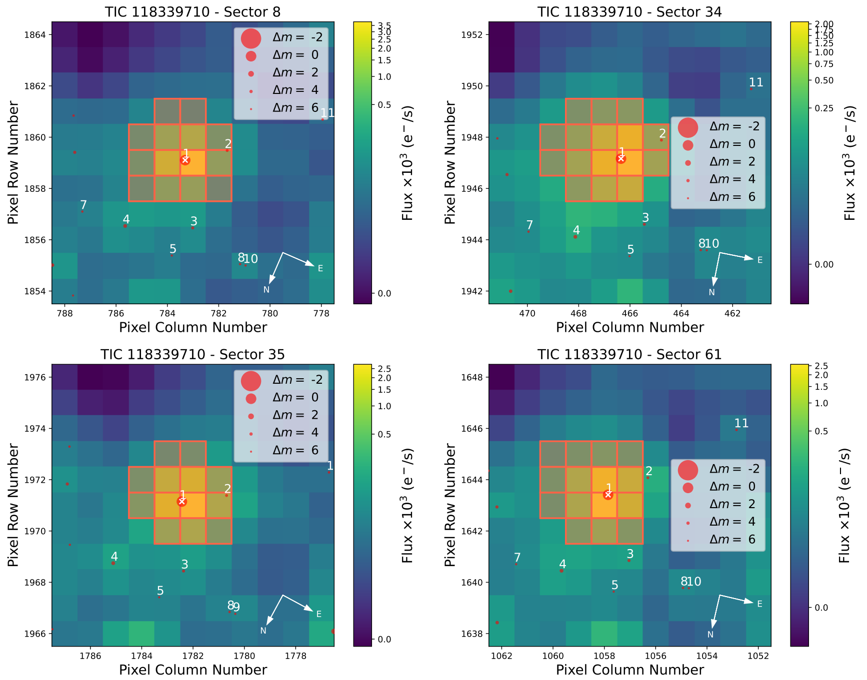

Figure 4.1: *TESS* Target Pixel Files (TPF) of TOI-6695 (TIC 118339710), created using `tpfplotter`. Orange overlays show the aperture used to determine the flux (a white overlay indicates an automatically detected threshold aperture). Gaia DR2 catalog objects are shown as filled red circles sized according to their brightness relative to the target (marked with a white cross).

In this work, we report the discovery and dynamical characterization of a system of two warm giants orbiting the late F dwarf star TOI-6695 as part of the WINE survey. TOI-6695 is very similar to the Sun, with $T_{\text{eff}} = 6400$ K, [Fe/H] = 0.2 dex, $\log g = 4.2 \log \text{cms}^{-2}$, $M_* = 1.34\,M_\odot$ and $R_* = 1.52\,R_\odot$. Apart from its higher temperature, the stellar parameters are consistent with so-called Solar analogs, defined to satisfy $4.04 \log \text{cm}\,\text{s}^{-2} < \log g < 4.84 \log \text{cm}\,\text{s}^{-2}$, $-0.3 <$ [Fe/H] < 0.3, $5\,472\,\text{K} < T_{\text{eff}} < 6\,072\,\text{K}$ [113]. The planets TOI-6695 b and c orbit their host star on low eccentricity orbits and are close to a 3:1 MMR. Therefore, the newly discovered *TESS* planets provide invaluable insights into both the history of their system and the theories of planetary formation and evolution.

In Section 4.2, we present the photometric and spectroscopic observational data obtained for TOI-6695 and which we use to characterize the orbital and physical parameters of the TOI-6695 pair of exoplanets. Section 4.3 describes the derivation of the stellar parameters from HARPS spectra and Gaia DR3 data. In Section 4.4, we introduce our data analysis and our global orbital analyses based on *TESS* photometry and our RV measurements. Our results are discussed in Section 4.5, and finally, we provide a summary and conclusions of our work in Section 4.6.

4.2 OBSERVATIONS

4.2.1 *Photometric data*

4.2.1.1 *TESS photometry*

TOI-6695 was first observed in sector 8 by *TESS* during its primary mission, and data are available with a cadence of 30 minutes. We identified the target as a candidate based on an analysis of the light curve generated by `tesseract`[2] from *TESS* Full Frame Images (FFI), where we automatically search for individual transit-like features produced by giant planets (e.g. [152]). During the extended mission, TOI-6695 was observed in sectors 34, 35, and 61 and data are available with a cadence of 2 minutes.

The 2-minute cadence light curves were provided by the Mikulski Archive for Space Telescopes (MAST)[3]. We selected the data processed by the Science Processing Operations Center (SPOC) [90]. The SPOC data products include both simple aperture photometry (SAP) and systematics-corrected Pre-search Data Conditioning photometry (PDCSAP) [159, 164, 165].

We examined the Target Pixel File (TPF) plots, visualized with `tpfplotter` [5] to identify possible contamination from nearby sources. Figure 4.1 shows the four TPF frames of TOI-6695 for sectors 8, 34, 35, and 61. These images show the field surrounding the target, overplotted with an aperture grid that indicates the pixels that were used to determine the flux, as well as nearby Gaia DR2 sources. Within the aperture of TOI-6695, we found that the TIC 118339698 faint source contaminates the flux from TOI-6695. Therefore, for *TESS* sector 8, we determined the dilution factor according to [61] as 0.98, which we used to correct the light curves for contribution. The dilution factor is defined as $D = \frac{1}{1+\sum_n F_n/F_T}$, with F_n being the flux of contaminating sources in the aperture and F_T being the out-of-transit flux of the target. The 2-minute PDCSAP cadence data for sectors 34, 35, and 61 from MAST had already been corrected for contamination from nearby stars and instrumental systematics. Thus, no dilution correction was applied for the flux time series collected in these sectors.

4.2.1.2 *Ground-based photometry at Observatoire Moana*

The pixel scale of the *TESS* cameras is large (21″ per pixel), making photometric measurements often contaminated by nearby sources. To identify possible false positive scenarios, as well as to confirm the predicted timing of the transit, we used ground-based photometry from a robotic network of telescopes named Observatoire Moana. Specifically, we used two stations of the network installed at the El Sauce Ob-

---

[2] https://github.com/astrofelipe/tesseract

[3] https://mast.stsci.edu/portal/Mashup/Clients/Mast/Portal.html

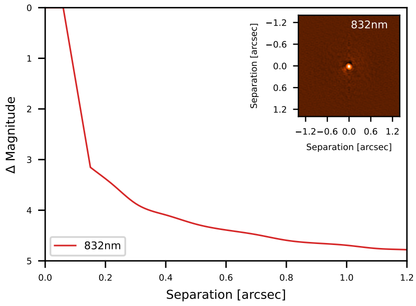

Figure 4.2: Speckle observations for TOI-6695 with NESSI. The red curve represents the 5σ contrast curve. The inset shows the reconstructed image of the star.

servatory in Rio Hurtado, Chile. These stations are known as OMES-CDK600 and OMES-RiDK500. OMES-CDK600 is a 0.6m CDK telescope coupled to an Andor iKon-L 936 deep depletion 2k × 2k CCD with a pixel scale of $0.67''$ per pixel. OMES-RiDK500 is a 0.5m Riccardi Dall-Kirkham telescope coupled to an Andor iKon-L 936 deep depletion 2k × 2k CCD with a pixel scale of $0.79''$ per pixel. We used OMES-CDK600 and OMES-RiDK500 on the night of 2024 March 5 to monitor the same transit event of TOI-6695. We adopted an exposure time of 6s and 12s for OMES-CDK600 and OMES-RiDK500, respectively, and used an r' filter in both cases. OM-ES data is processed with an automated custom-made pipeline [59, 178].

4.2.1.3 *Speckle imaging*

The NN-Explore Exoplanet Stellar Speckle Imager (NESSI) [154] was used to observe TOI-6695 on April 18 2022. We obtained a 1-minute sequence of diffraction-limited 40 ms exposures in the 832 nm filter on the red camera. These exposures were processed following Howell et al. [81] to produce a reconstructed image of the star, which we show in Figure 4.2 alongside the 5σ contrast limits for separations from $0.2''$ to $1.2''$. The NESSI data rule out the presence of blended companions or foreground or background sources down to a magnitude limit of $\Delta m_{832\mathbf{nm}} = 3.38$ at $0.2''$ and $\Delta m_{832\mathbf{nm}} = 4.78$ at $1.2''$.

4.2.2 *Spectroscopic data*

TOI-6695 was observed with the spectroscopic instruments HARPS, CHIRON, PFS, CORALIE, FEROS, and TRES. In the following, we give details to the individual spectra for all instruments, except TRES, since they are only preliminary vetting data and don't contribute significantly to the analysis, so we didn't include them.

4.2.2.1 *FEROS*

The Fiber-fed Extended Range Optical Spectrograph (FEROS) [100] is an echelle spectrograph mounted on the 2.2 meter MPG/ESO[4] telescope at ESO's La Silla Observatory, Chile. FEROS is a highly efficient spectrograph with a resolving power of $R = 48\,000$, covering the visible wavelength range from $\sim 350\,\text{nm}$ to $\sim 920\,\text{nm}$. FEROS's achievable RV precision is approximately $10\,\text{m}\,\text{s}^{-1}$, which is sufficient for validating massive exoplanets detected by *TESS* in the southern hemisphere. From 2020 March 1 to 2022 May 5, we obtained 16 FEROS spectra for TOI-6695. From these spectra we extracted the RV measurements and stellar activity indicators Bisector Inverse Span (BIS) [140], H_α [19], He I, $\log R'_{HK}$ [51, 129] and Na II [70], using the Collection of Elemental Routines for Echelle Spectra (CERES) pipeline [25]. The FEROS RVs and stellar activity measurements for our target are listed in Table B2. The RVs have a mean error of $11.3\ \text{m}\,\text{s}^{-1}$, and an r.m.s. of $40.3\ \text{m}\,\text{s}^{-1}$. Due to the high RV scatter and 5 out of the 16 RVs being outliers, we chose not to use the FEROS data for our analysis.

4.2.2.2 *HARPS*

We performed observations of TOI-6695 with the HARPS spectrograph [118] installed at the 3.6 m telescope at La Silla. We obtained 53 spectra between 2020 March 18, and 2024 March 15 and processed the spectra using the CERES pipeline [25], providing both RVs as well as BIS, $H\alpha$, Ca II, Na II and He I [70] activity indicators. The HARPS measurements are listed in Table B3. The RVs have a mean error of $4.0\ \text{m}\,\text{s}^{-1}$, and an r.m.s. of $46.3\ \text{m}\,\text{s}^{-1}$.

4.2.2.3 *CHIRON*

TOI-6695 was observed with the CHIRON spectrograph [175] at the Small and Moderate Aperture Research Telescope System (SMARTS) [166] 1.5 m telescope at CTIO. We obtained a total of 33 spectra between 2020 December 1, and 2023 May 4. We used the slit mode ($R \sim 80\,000$) with an exposure time between 1200 and 1800s, leading to a typical SNR per pixel of $\sim 25-35$, and $\sim$ 10-20 $\text{m}\,\text{s}^{-1}$ 1-σ RV uncertainties at a wavelength of $\sim$ 550 nm [175]. The data were automatically processed and reduced by the Yale pipeline [132], and the RVs were obtained using the pipeline described in Jones et al. [95]. The RVs have a mean error of $14.6\ \text{m}\,\text{s}^{-1}$, and an r.m.s. of $26.2\ \text{m}\,\text{s}^{-1}$.

4.2.2.4 *CORALIE*

TOI-6695 was observed with the CORALIE spectrograph [139] at the Swiss 1.2m Euler telescope at La Silla by both the WINE and

---

[4] MPG = *Max-Planck-Gesellschaft* = Max Planck Society; ESO = European Southern Observatory.

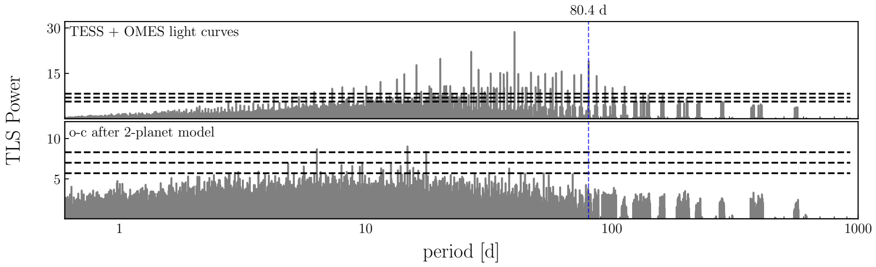

Figure 4.3: TLS power spectrum periodogram of TOI-6695. The top panel shows the results of the detrended and normalized *TESS* and OMES light curves. The bottom panel shows the residual TLS power after subtracting the full photodynamical model. The dashed blue line represents the orbital period of the transiting planet candidate, whereas dashed horizontal lines indicate the TLS signal detection efficiency [SDE; 78] power levels of 5.7, 7.0, and 8.3, which correspond to false-alarm-probability (FAP) levels of 10%, 1%, and 0.1%.

Swiss teams. In total, 18 spectra were obtained between 2020 January 20, and 2022 May 27, with a median exposure duration of 1200s. CORALIE is a fiber-fed echelle spectrograph with a $2''$ science fiber and a secondary fiber with a Fabry-Perot for simultaneous wavelength calibration. It has a spectral resolution of R = 60 000. RVs are extracted using the standard CORALIE DRS by cross-correlating the spectra with a binary G2V template [16, 135]. The BIS, FWHM, and other line-profile diagnostics were also computed via the CORALIE DRS, as was the H_α index for each spectrum to check for possible variation in stellar activity. The resulting RVs and activity indicators are listed in Table B5. The RVs have a mean error of 20.0 $\mathrm{m\,s^{-1}}$, and an r.m.s. of 27.4 $\mathrm{m\,s^{-1}}$.

4.2.2.5 *PFS*

We observed TOI-6695 with the Planet Finder Spectrograph (PFS) [37–39], which is mounted on the 6.5 m Magellan II (Clay) Telescope at Las Campanas Observatory in Chile. PFS is a slit-fed echelle spectrograph with a wavelength coverage of 391—734 nm. Wavelength calibration is achieved via an iodine gas cell, which also allows characterization of the instrumental profile. We used a $0.3''$ slit and obtained 16 spectra on 11 epochs, observed through iodine, between 2020 December 22, and 2022 January 23, with exposure times of 900 or 1200 seconds. Any contiguous spectra were binned together into a single epoch. We also obtained a high-SNR, iodine-free template observation. The radial velocities were extracted using a custom IDL pipeline that flat fields, removes cosmic rays, and subtracts scattered light, following the prescriptions of Marcy and Butler [116] and Butler and Marcy [32]. The mean internal precision achieved is 2.49 $\mathrm{m\,s^{-1}}$ and the r.m.s. is 17.6 $\mathrm{m\,s^{-1}}$. The radial velocities are presented in Table B6.

4.3 STELLAR PARAMETERS

Table 4.1: Stellar parameters of TOI-6695.

PARAMETER	VALUE	REF.
Names	TIC 118339710, TOI-6695	[130, 163]
	5701679002245319296	[64, 67]
RA (J2000)	$08^h\ 38^m\ 17.2895456952^s$	[64, 67]
DEC (J2000)	$-23^\circ\ 33'\ 00.826834104''$	[64, 67]
distance [pc]	282.670 ± 0.967	[64, 67]
T [mag]	10.354	[130, 163]
B [mag]	11.351	[130, 163]
V [mag]	10.768	[130, 163]
J [mag]	9.816	[130, 163]
H [mag]	9.599	[130, 163]
K [mag]	9.512	[130, 163]
Spectral type	F5V - G0V	[134]
$T_{\rm eff}$ [K]	6400 ± 100	this work
$\log g$ [cm s^{-2}]	4.202 ± 0.015	this work
$R_\star$ [$R_\odot$]	$1.517^{+0.023}_{-0.022}$	this work
$M_\star$ [$M_\odot$]	$1.338^{+0.023}_{-0.022}$	this work
$L_\star$ [$L_\odot$]	3.47 ± 0.18	this work
$\rho_\star$ [kg m^{-3}]	540^{+26}_{-25}	this work
[Fe/H] [dex]	0.2 ± 0.05	this work
$v \sin i$ [km s^{-1}]	6.7 ± 0.3	this work
Age [Gyr]	2.1 ± 0.3	this work
A_V [mag]	0.28 ± 0.07	this work

We followed the procedure initially presented in Brahm et al. [27] to determine the stellar atmospheric and physical parameters. This is a two-step iterative process. The first step consists of the comparison of the observed co-added HARPS spectra to a library of synthetic spectra [34] using the `zaspe` code [26]. This procedure allows us to estimate the atmospheric parameters of the star ($T_{\rm eff}$, $\log g$, [Fe/H], and $v \sin i$). The second step involves a Spectral Energy Distribution (SED) fit to public available broad-band magnitudes of the star. The model in this case corresponds to synthetic magnitudes of the PARSEC stellar evolutionary models transformed to apparent magnitudes using the Gaia DR3 parallax [66]. In this step we fix the metallicity of the models to the value obtained with `zaspe` and we use the $T_{\rm eff}$ obtained with `zaspe` as a prior. This procedure allows us to estimate the age of the star, along with its mass and radius, which can be used to obtain a more precise value for the $\log g$ than the one reported by `zaspe`. In the next iteration with `zaspe` we fix the log g value to the one obtained with the SED fit. The iterations end when reaching convergence in $T_{\rm eff}$ and [Fe/H] of two consecutive `zaspe` runs.

We find that TOI-6695 is a late F-type star ($T_{\rm eff} = 6400 \pm 100$ K) in the main sequence with a mass of 1.34 ± 0.02 $M_\odot$ and a radius of 1.52 ± 0.02 $R_\odot$. It is metal rich ([Fe/H] = 0.20 ± 0.05) and has a projected rotational velocity of $v \sin i = 6.7 \pm 0.3$ km s^{-1}. The stellar parameters and observational properties of TOI-6695 are presented in Table 4.1.

4.4 ANALYSIS AND RESULTS

4.4.1 *Period search analysis in* TESS

We detrended the 30-minute FFI cadence *TESS* light curve for sector 8 as well as the pre-processed 2-minute cadence light curves provided by MAST by using the `wotan` package [78]. For this purpose, we apply a Gaussian Process (GP) model with a Matern 3/2 kernel of size 5 days.

After detrending the 30-minute cadence light curve, we performed a period search on all light curves using the `transitleastsquares` (TLS) package [77]. The top panel of Figure 4.3 shows the TLS power of the *TESS* and OMES light curves of TOI-6695, and the bottom panel shows the TLS results of the residual light curves after subtracting the two-planet N-body model. The top panel shows many significant signals, most prominent at $P = 40.2$ days, which we could determine to be the harmonics and subharmonics of the orbital period of the planetary candidate $P_b = 80.4$ days, which is shown as a dashed blue line. The bottom panel shows that subtracting a model for both planets removes the signal and leaves the residual periodogram with no additional significant signals.

4.4.2 *Period search analysis in RV data*

Following the initial transit candidate discovery, we observed TOI-6695 with various spectroscopic instruments to confirm the planetary nature of the transit signals, as well as to disentangle the correct orbital period of the transiting planet. Figure 4.4 shows the Maximum Likelihood Periodogram (MLP) [15, 188] for the RV data. The top three panels show the likelihood of the combined HARPS, CHIRON, PFS, and CORALIE RVs after subtracting a model with only planet c, after subtracting a model with only planet b, and the residual periodogram after subtracting the combined two-planet model. The following five panels show the periodograms of the BIS, Hα, HeI, log $R'_{\rm HK}$, and NaII activity indicators obtained from the HARPS RVs; the bottom panel shows the window function of the combined RVs. Analogous to Figure 4.3, dashed blue lines represent the orbital periods of the plane-

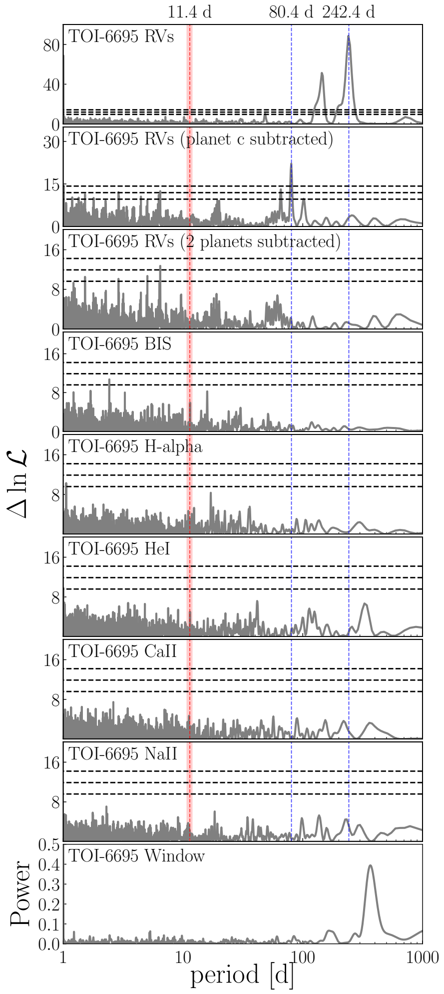

Figure 4.4: MLP periodograms for RV and stellar activity data of TOI-6695. The top four panels show the periodograms of the raw and residual RVs after subtracting Keplerian models, panels 5 to 9 show the periodograms of the stellar activity indicators and the bottom panel shows the RV window function. Dashed blue lines indicate the planetary orbital periods, and the red dashed line and shaded region correspond to the assumed stellar rotational period. Dashed horizontal lines correspond to FAP levels of 10%, 1%, and 0.1%.

tary candidates, and the red dashed line corresponds to the assumed rotational period of TOI-6695. We determined the maximum possible rotational period of TOI-6695 as $P_{\mathrm{rot}}/\sin i = 2\pi R_{\star}/v \sin i$ by using the stellar radius and projected rotational velocity from Table 4.1. A periodogram inspection of the *TESS* light curves did not provide any evidence for rotational modulation. Assuming an orbital alignment of the stellar spin to the orbit of TOI-6695 b, we found a rotational period of $P_{\mathrm{rot}} = 11.4^{+0.5}_{-0.6}$ days, which is indicated as a red dashed line and shaded region in Figure 4.4. In the base RV periodogram, instead of the 40.2 days signal, a new 241.3 days signal can be seen, which is not present in the TLS analysis. After subtracting a Keplerian model with the same period, the residual periodogram showed a significant signal at $P = 80.4$ days. A combined 2-planet Keplerian model with both signals left no significant signals in the residuals. Neither signal has a counterpart in the stellar activity periodogram, and neither signal coincides with the stellar rotational period. Due to the unfavorable situation that the three transits that were observed by *TESS* are equally spaced, as well as the close proximity to the 3:1 mean motion resonance commensurability, it required several models and the observation of our predicted transit on 2024 March 5 (see Section 4.2.1.2) to be convinced of the periods for our model.

4.4.3 *Joint transit and RV orbital fitting*

We performed a combined RV and transit photometry orbital analysis of TOI-6695 by using an N-body model included in the `Exo-Striker`[5] [176] exoplanet toolbox. The `Exo-Striker` employs the `batman` package [105] for transit lightcurve models, and the RV model formalism in Lee and Peale [112]. For the posterior analysis, the `Exo-Striker` utilizes the Nested Sampling (NS) algorithm in combination with the `dynesty` package [162]. The NS configuration in this work is similar to the one used in Trifonov et al. [177]. We used 100 "live-points" per fitted parameter with a "dynamic" NS sampler approach (see [162] for details). The priors for the parameters were determined through a series of consecutive NS runs, starting with initial values derived from the TLS and MLP signal vetting analyses. We simultaneously modeled the N-body osculating orbital parameters for the TOI-6695 system, and the nuisance RV data parameters and transit light-curve parameters, deriving posteriors from the NS results.

The parameters we fitted for each planet in the model were the RV semi-amplitude K, the orbital period P, and mean longitude λ valid for BJD = 2458525.6 (slightly before the first *TESS* mid-transit event). Instead of the eccentricity e and longitude of periastron ω we chose to use the $e \sin \omega$, $e \cos \omega$ parameterization. The transit model parameters are shared with these from the RV model but also include the

---

[5] `https://github.com/3fon3fonov/exostriker`

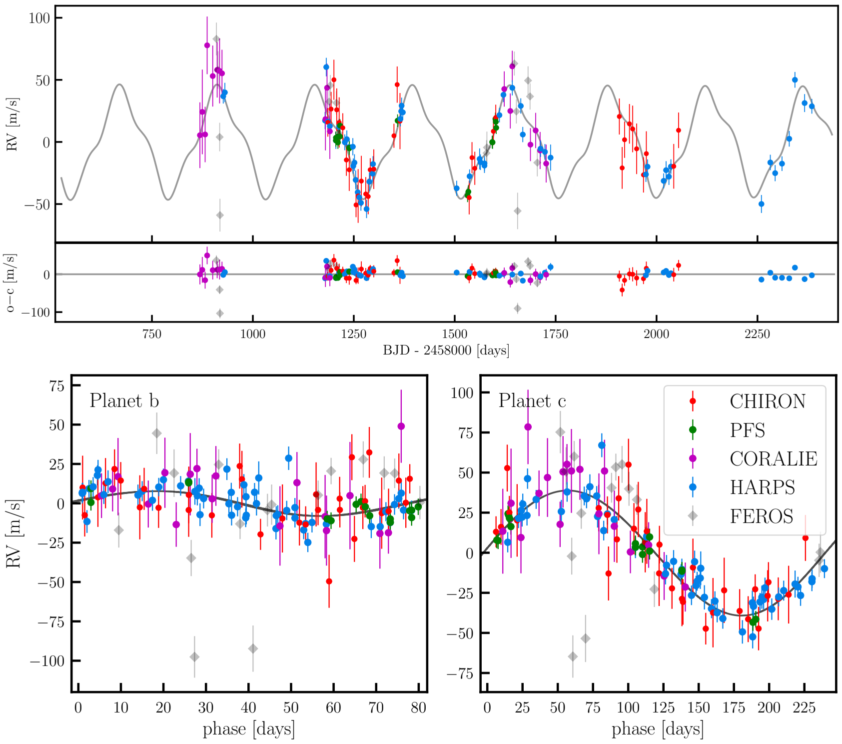

Figure 4.5: Radial velocity time series (top panel) and phase-folded plots of the planetary signals (TOI-6695 b bottom left; TOI-6695 c bottom right). In addition to the RVs from HARPS, CHIRON, PFS, and CORALIE, FEROS data are overlayed as greyed-out diamonds, to show their general agreement with our model, but also their overall poor quality.

orbital inclination i, time of mid-transit t_0, and the relative to the stellar radius semimajor axis $a/R_\star$ and planetary radius $r/R_\star$. Transit model parameters are quadratic limb-darkening coefficients u_1 and u_2 separately for *TESS* and Moana. Additionally, we fit the transit and RV data offsets and jitter parameters RV_{offset}, RV_{jitter}, $\text{transit}_{\text{offset}}$ and $\text{transit}_{\text{jitter}}$ for the different instruments. From the posterior probability distribution, we derived posteriors for the orbital eccentricity e, the argument of periastron ω, mean anomaly MA, planetary mass m_p (or minimum dynamical mass m_p for TOI-6695 c), semi major axis (a_p), radius (r_p), mean density (ρ_p), and equilibrium temperature (T_{eq}) for both planets. Since no transits were detected in the light curves for TOI-6695 c, we only modeled the transit parameters (t_0, $a/R_\star$, $r/R_\star$, r_p, and ρ_p) for the transiting planet, TOI-6695 b. An estimate of transit times for TOI-6695 c based on RV data, finds the planet transiting either during the *TESS* window or between *TESS* observations.

The results from our NS posteriors revealed that TOI-6695 b is a warm Saturn with a mass of $m_b = 0.21^{+0.01}_{-0.01}\,M_{\text{jup}}$, a radius of $r_b = 0.85^{+0.02}_{-0.02}\,R_{\text{jup}}$, an orbital eccentricity of $e_b = 0.040^{+0.006}_{-0.007}$ and a bulk density of $\rho_b = 0.41^{+0.04}_{-0.04}\,\text{g}\,\text{cm}^{-3}$. It orbits the host star at a distance of $a_b = 0.402$ au, corresponding to an orbital period of $P_b = 80.389$ days and an equilibrium temperature of $T_{eq} = 599^{+8}_{-8}$ K. TOI-6695 c is a warm Jupiter with a minimum dynamical mass of $m_c = 1.45^{+0.03}_{-0.03}\,M_{\text{jup}}$ and an orbital eccentricity of $e_c = 0.022^{+0.006}_{-0.007}$. The distance to its host star is $a_c = 0.838$ au, corresponding to an orbital period of 242.4 days and an equilibrium temperature of $T_{eq} = 415^{+6}_{-5}$ K. In our model, we fixed the inclination of TOI-6695 c to 90° and $\Delta\Omega$ to 0°, so the mutual inclination comes only from the difference $\Delta i = i_b - i_c$. Our NS result estimates are listed in Table 4.2 for the relevant orbital and derived parameters, as well as in Table B1 for the fitted nuisance parameters; the radial velocity and transit offsets and jitters, alongside the quadratic limb-darkening coefficients.

Figure 4.5 shows the available RV data alongside the RV part of our N-body model. The top panel shows the full RV time series, whereas the bottom panels show the phase-folded RVs for TOI-6695 b, and c, respectively. HARPS data is shown as blue points, CHIRON as red, PFS as green, and CORALIE as purple. Due to the many outliers and large overall scatter, we did not include the FEROS data for our analysis and chose to only include them as greyed-out diamonds for completeness and to show that they are generally consistent with our model.

Figure 4.6 shows the photometric part of our joint N-body model with the individual transit events shown phase-folded with a period of 80.438 days, corresponding to a transit duration of 10.81

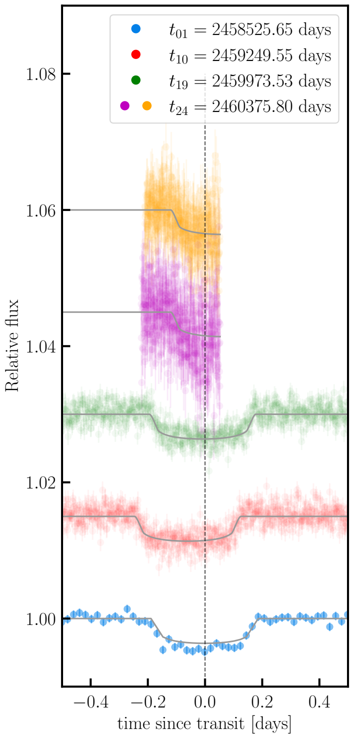

Figure 4.6: Individual transits for TOI-6695. `blue:` *TESS* sector 8; `red:` *TESS* sector 34; `green:` *TESS* sector 61; `purple/orange:` ground-based data from OM-ES.

hours, derived from a fit to the data with a static period. The blue data represent sector 8 of the *TESS* light curves, the red data corresponds to sector 34, and the green data to sector 61. Purple and orange data show the ingress observed at the El Sauce Observatory of the Observatoire Moana network in two separate bands. The individual transits are offset and are shown relative to the mid-transit time of the first detected transit, marked as a dashed line, showing Transit Timing Variation (TTV) caused by the outer planet. Our photodynamical model already incorporates the TTVs and the individual transit times are shown in the figure. The transit in sector 8 (blue data) shows a slightly anomalous depth. We inspected the light curve generated by `tesseract`, as well as the light curve generated by the *TESS* Quick Look Pipeline (QLP) [106] and the TESS-Gaia-Light-Curve (TGLC) pipeline [72]. Figure B1 shows a comparison between tesseract, QLP and TGLC pipelines. The transit depth was largely consistent in all data reductions. The RV fit does not support this transit event being a caused by another planet, thus we attribute it to unexplained systematics.

Table 4.2: Nested Sampling priors, posteriors, and the optimum $-\ln\mathcal{L}$ orbital parameters of the two-planet system derived by joint N-body modeling of *TESS* and Moana transit photometry and RV data taken with CORALIE, HARPS, PFS and CHIRON. The adopted priors, listed in the right-most columns, are uniform (flat) priors, assigning equal probability to all values within the allowed ranges.

	MEDIAN AND $1-\sigma$		MAX. $-\ln\mathcal{L}$		ADOPTED PRIORS	
PARAMETER	PLANET b	PLANET c	PLANET b	PLANET c	PLANET b	PLANET c
K [m s^{-1}]	$8.0^{+0.6}_{-0.6}$	$39.0^{+0.7}_{-0.6}$	7.9	39.0	$\mathcal{U}(5, 30)$	$\mathcal{U}(35, 45)$
P [days]	$80.389^{+0.003}_{-0.005}$	$242.4^{+0.4}_{-0.3}$	80.385	242.7	$\mathcal{U}(80.22, 80.96)$	$\mathcal{U}(239, 249)$
$e\sin(\omega)$	$0.028^{+0.007}_{-0.005}$	$-0.016^{+0.004}_{-0.004}$	0.037	-0.014	$\mathcal{U}(-0.1, 0.1)$	$\mathcal{U}(-0.1, 0.1)$
$e\cos(\omega)$	$-0.030^{+0.007}_{-0.019}$	$-0.01^{+0.01}_{-0.02}$	-0.025	-0.01	$\mathcal{U}(-0.1, 0.1)$	$\mathcal{U}(-0.1, 0.1)$
λ [deg]	$86.2^{+0.8}_{-2.2}$	139^{+2}_{-2}	86.8	141	$\mathcal{U}(45, 135)$	$\mathcal{U}(0, 360)$
i [deg]	$90.62^{+0.02}_{-0.02}$	90	90.64	90	$\mathcal{U}(89, 91)$	(fixed)
e	$0.040^{+0.006}_{-0.007}$	$0.022^{+0.006}_{-0.007}$	0.044	0.015	(derived)	(derived)
ω [deg]	137^{+26}_{-12}	-121^{+22}_{-69}	124	-111	(derived)	(derived)
M_0 [deg]	307^{+12}_{-26}	261^{+72}_{-23}	323	252	(derived)	(derived)
m_p [$M_{\mathrm{Jup.}}$]	$0.21^{+0.01}_{-0.01}$	$1.45^{+0.03}_{-0.03}$	0.20	1.45	(derived)	(derived)
r_p [$R_{\mathrm{Jup.}}$]	$0.85^{+0.02}_{-0.02}$	...	0.75	...	(derived)	...
ρ_p [g cm^{-3}]	$0.41^{+0.04}_{-0.04}$	...	0.60	...	(derived)	...
a_p [au]	$0.402^{+0.002}_{-0.002}$	$0.838^{+0.005}_{-0.005}$	0.402	0.839	(derived)	(derived)
$T_{\mathrm{eq.}}$ [K]	599^{+8}_{-8}	415^{+6}_{-5}	599	415	(derived)	(derived)

The orbital elements are in the Jacobi frame and are valid for epoch BJD = 2458400.0. The derived planetary posterior parameters of a, and m are calculated taking into account the stellar parameter uncertainties. The value listed for the mass m_p of planet c is the minimum dynamical mass m. We fixed $\Delta\Omega = 0$, thus, the mutual inclination in the model comes from the difference between $i_b - i_c$.

4.4.4 *Dynamical modelling*

Both planets TOI-6695 b, and c, orbit their host star on low eccentricity orbits. We studied the overall dynamics of the planetary system by using a numerical scheme similar to the one used for TOI-2202 [177] and TOI-2525 [178]. From the full set of samples, we randomly chose 1 000 and integrated them for 10 Myr using the Wisdom-Holman N-body integrator [also known as MVS, 184], which is implemented within the `Exo-Striker` toolbox. We adopted a numerical time step of 1 day, sufficiently sampling orbital time scales in the system. An integration time of 10 Myr corresponds to ~ 45 million orbits of TOI-6695 b, allowing us to derive robust conclusions about the system's stability and dynamics.

We monitored both the planetary semi-major axes and their orbital eccentricities evolve over the integrated time and rejected orbital configurations as unstable if either a_b or a_c deviated more than 10% of their initial value or if e_b or e_c became too large and led to crossing orbits. Figure 4.7 shows excerpts of 10 000 years of evolution for

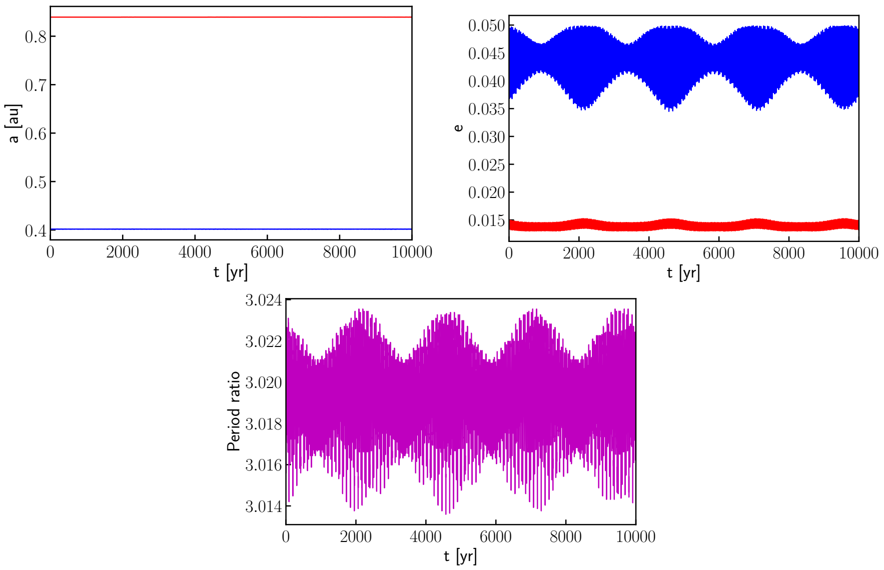

Figure 4.7: The top left figure shows the orbital evolution of the planetary semi-major axes from the best fit. The top right plot shows the evolution of the orbital eccentricities; `blue`: TOI-6695 b; `red`: TOI-6695 c. The bottom panel shows the evolution of the period ratio between the two massive planets.

the semi-major axes (left) and orbital eccentricities (right) of our best fit configuration. We find all samples to be long-term stable for 10 Myr in both semi-major axes and eccentricities. With a period ratio of ~ 3.02, we examined the characteristic resonance angles of the 3:1 mean motion resonance configuration;

$$\begin{aligned} \theta_1 &= \lambda_b - 3\lambda_c - 2\varpi_c && (10)\\ \theta_2 &= \lambda_b - 3\lambda_c + \varpi_b - \varpi_c && (11)\\ \theta_3 &= \lambda_b - 3\lambda_c + 2\varpi_b, && (12) \end{aligned}$$

with the planetary longitudes of periastron $\varpi_{b,c} = \Omega_{b,c} + \omega_{b,c}$ and the mean longitides $\lambda_{b,c}$= $M_{0b,c} + \varpi_{b,c}$, as well as the secular apsidal angle $\Delta\omega$, which is defined as:

$$\Delta\omega = \omega_c - \omega_b, \qquad (13)$$

and indicates whether the system is dominated by secular interactions if this angle librates around a fixed angle. We found all resonance angles circulating between $0 - 360^\circ$, indicating that the system is not in an actual MMR configuration.

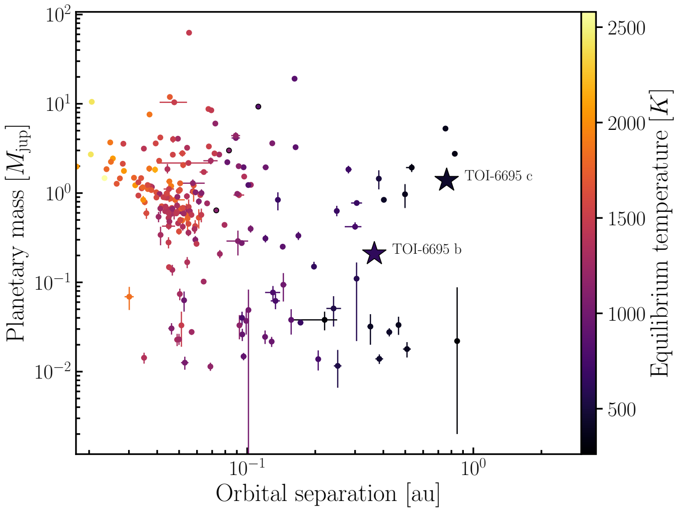

Figure 4.8: Mass-separation diagram for planets around Sun-like stars (definition according to Lehmann et al. [113], see Section 4.1, modified to include TOI-6695 b). The position of TOI-6695 b, and TOI-6695 c are shown as star symbols.

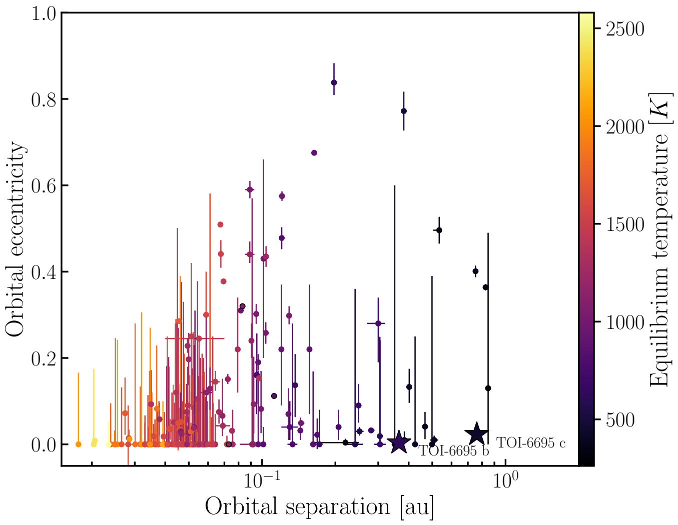

Figure 4.9: Same as of Figure 4.8, but for eccentricity against separation.

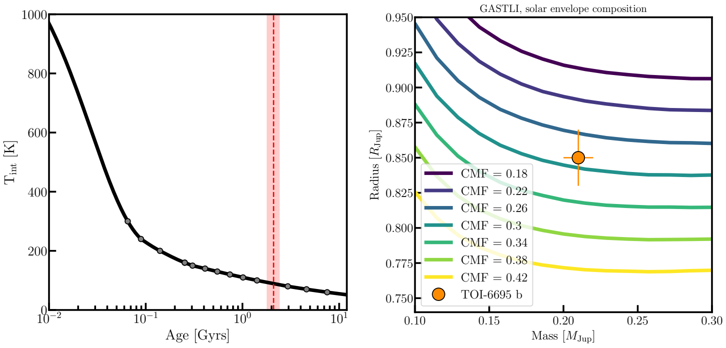

Figure 4.10: Thermal evolution for TOI-6695 b of the internal temperature and mass-radius-diagrams for varying core-mass-fractions, generated using GASTLI. We assumed a core mass fraction CMF = 0.30 and a solar envelope composition to compute the thermal evolution of TOI-6695 b. TOI-6695 b's age of 2.1 ± 0.3 Gyr (shown as red dashed line and shaded region) is consistent with an internal temperature $T_{\rm int} = 50 - 150$K. Thus, we adopted a value of 100 K for our mass-radius relations. Given its mass, radius and age, TOI-6695 b could present a CMF = 0.25 to 0.35 with a solar composition (see text).

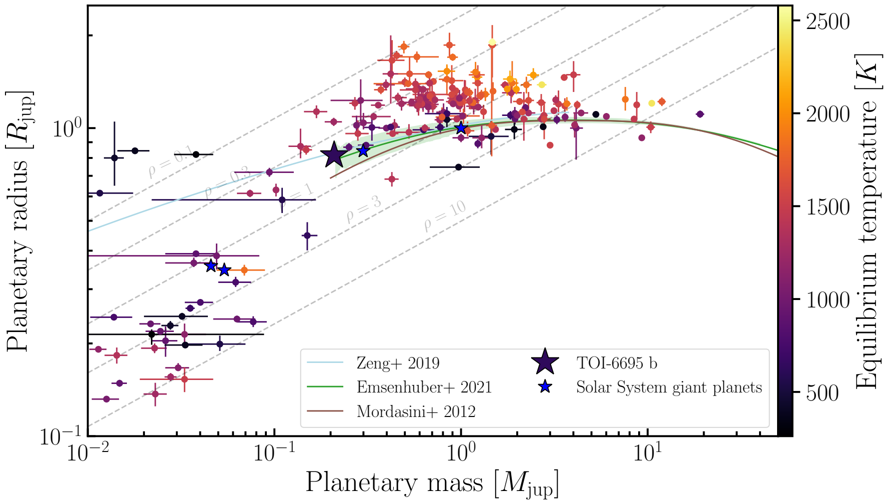

Figure 4.11: Mass-radius diagram for the same sample of planets as in Figure 4.8 and Figure 4.9. Marked as blue star symbols are the Solar system giant planets, whereas TOI-6695 b is shown as a colored star symbol. Solid lines represent exoplanet composition models derived from the theoretical frameworks of Emsenhuber et al. [58], Mordasini et al. [126], and Zeng et al. [189]. Dashed grey lines indicate fixed densities of ρ = 0.1, 0.3, 1.0, 3.0, and 1.0 g cm^{-3}. The shaded region surrounding the fit to the data from Emsenhuber et al. [58] illustrates the moving standard deviation of their synthetic planets, which arises from variations in core sizes and envelope metallicities (assumed to match stellar values).

4.4.5 *Interior modelling*

We used the GAS gianT modeL for Interiors (GASTLI) [1, 2][6] to investigate the interior composition of TOI-6695 b. GASTLI is a Python package specifically developed to model the internal structure volatile-rich exoplanets. It generates mass-radius and thermal evolution relationships (radius-age diagrams). In our analysis, the planetary interior is divided in two distinct layers: a core and an envelope. The core is assumed to contain a 1:1 mass ratio of rocks and water, while the envelope is composed of hydrogen, helium (H/He), and water, with water serving as a proxy for metals.

Our first step is to calculate a thermal evolution curve to estimate the internal (or intrinsic) temperature, $T_{\rm int}$, based on the age of TOI-6695 b. The left panel of Figure 4.10 shows an age-$T_{\rm int}$ diagram, from which we constrained the internal temperature $T_{\rm int} = 50 - 150$ K, according to an age of 2.1 Gyr. Thus, we adopted a representative value of $T_{\rm int}$ = 100 K to generate a mass-radius diagram (Figure 4.10, right panel). This diagram explores how the planet's radius varies with different core-mass fractions (CMF), assuming a fixed solar composition for the envelope.

From our analysis, we determined that TOI-6695 b has a bulk metal mass fraction of approximately 0.30, meaning that 30% of its total mass is composed of heavy elements. This is notably higher than Saturn's estimated bulk metal mass fraction of about 0.20, despite TOI-6695 b being slightly less massive. The higher metal content of TOI-6695 b aligns with the predictions of the core accretion model of planet formation, which suggests a positive correlation between planetary mass and bulk metallicity. Additionally, this result is consistent with observed trends for both Solar System giants and other exoplanets [171].

4.5 DISCUSSION

Figure 4.8 to Figure 4.11 put the planets discussed in this work in the broader context of all known transiting exoplanets orbiting stars with similar characteristics, including the Solar System giant planets. The exoplanet properties displayed in these figures were selected from the TEPCAT catalogue [161], based on the properties of their host stars: $-0.3 < [\mathrm{Fe/H}] < 0.3$; $4.04\,\mathrm{cm\,s^{-2}} < \log g < 4.84\,\mathrm{cm\,s^{-2}}$; $5472\,\mathrm{K} < T_{\rm eff} < 6500\,\mathrm{K}$.

Figure 4.8 shows the planetary masses (projected mass $m \sin i$ for TOI-6695 c) plotted against the orbital separation, with the planets discussed in this work shown as big stars. As evident, TOI-6695 b, and c are located in the sparsely populated long-period region of warm giant demographics. Analogously, Figure 4.9 shows the same planets in

---

[6] `https://github.com/lorenaacuna/GASTLI`

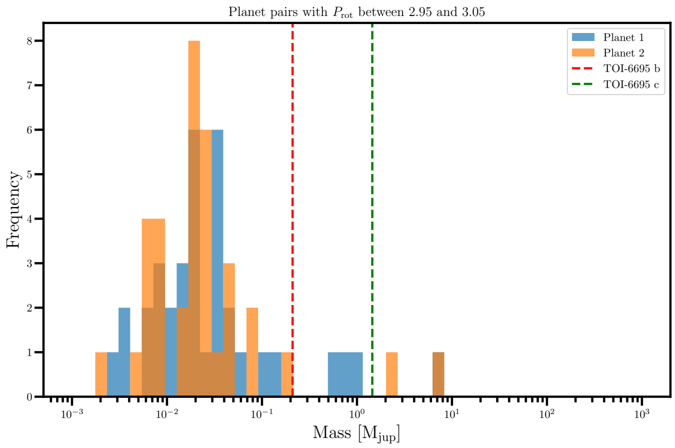

Figure 4.12: Mass-distribution for planet pairs with a period ratio close to 3. The masses of TOI-6695 b, and TOI-6695 c are shown as dashed lines.

an eccentricity-separation diagram, with the low-eccentricity planets TOI-6695 b, and c shown as big stars. Figure 4.11 shows a mass-radius diagram that contains the Solar System giant planets as blue stars in addition to TOI-6695 b. This allows us to study the bulk densities for the planets, showing composition models based on Emsenhuber et al. [58], Mordasini et al. [126], and Zeng et al. [189] as solid lines of varying colors. TOI-6695 b is consistent with the predictions by the displayed exoplanet composition models. With a projected rotational velocity of $v \sin i = 6.7$ km s^{-1}, the transiting planet TOI-6695 b becomes an interesting target to measure the Rossiter-McLaughlin (RM) [121, 148]. The estimated amplitude of the signal is 17.5 m s^{-1}, which can be measured by high-resolution instruments.

TOI-6695 b and c have a period ratio of 3.02, which is very close to a 3:1 mean motion resonance configuration. This is a rare configuration with only 34 known examples [7], such as 55 Cnc b & c [94, 190] and HD 60532 b & c [7, 108], as well as other systems close to the 3:1 MMR configuration without being in resonance, such as GJ 163 [20], HD 31527 [138], TOI-560 [56], K2-254 [115], Kepler-168, Kepler-180, Kepler-284, Kepler-359, Kepler-373 [149], and Kepler-430 [62]. Figure 4.12 shows the mass-distribution of those 34 pairs of exoplanets. Most of the known planets among these 34 pairs are sub-Neptunes. TOI-6695 b and c are among only a handful of giant planets in such a configuration. Similarly, this rarity is supported by simulations from Emsenhuber et al. [58] using a core accretion model of planet formation with disk evolution, N-body interactions, migration, and gas accretion [57]. Around Solar mass stars, 4 giant planet ($M > 20\,M_{\oplus}$) pairs in 3:1 mean motion resonances were obtained out of 1000 systems where 675 planets with masses above 20 Earth masses formed

---

[7] `https://exoplanetarchive.ipac.caltech.edu/`; chosen to satisfy $2.95 < P_{\mathrm{rat}} < 3.05$

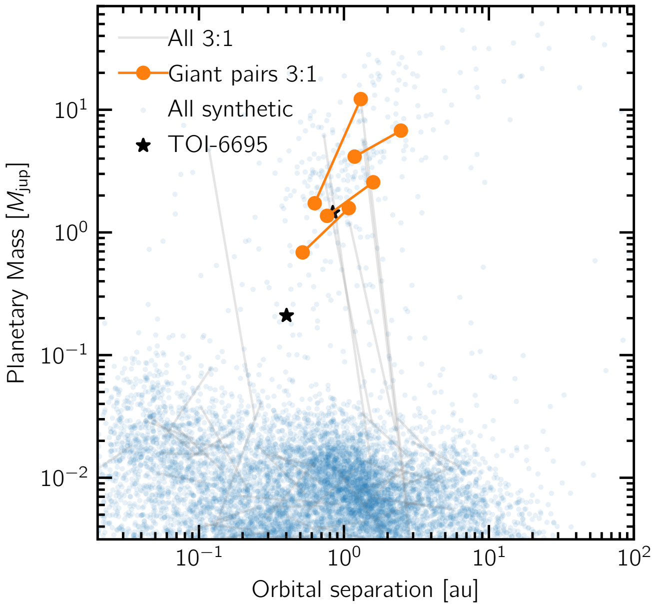

Figure 4.13: Mass-separation diagram for synthetic planets with neighboring planet pairs close to 3:1 mean motion resonance marked. The data is drawn from the 50 embryo simulations of Emsenhuber et al. [58]. Giant planet pairs are found after excluding planets below 50 Earth masses from the systems.

overall. For comparison, 34 pairs are close to a 2:1 mean motion resonance, and 2 pairs close to 3:2. The resulting 3:1 pairs are visualized on a distance against mass diagram in Fig. 4.13. As for the pair of planets around TOI-6695, the inner synthetic planet of the 3:1 period ratio pair is typically of lower mass than the outer. In the simulations, this is due to the inside-out opening of a gap in the gas disk (aided by planetary accretion itself) which first halts growth of the inner planets. In other words, owing to its position closer to the bulk of the disk gas mass, which is expected at around 30 au, the outer planet can accrete most of the gas accretion flux and prevent growth of the inner planet. Studying the dynamics and occurrences of resonantly coupled pairs of planets helps to understand the formation of planetary systems, and maybe even the formation of the Solar System. According to the "Grand Tack" model [183], Jupiter initially moved towards the Sun, until it reached a 2:3 resonance with Saturn, before reversing its migration [117] and moving together with Saturn away from the Sun again.

4.6 SUMMARY

We report the discovery and characterization of a system of two giant exoplanets orbiting a Sun-like star. The inner planet, TOI-6695 b was identified as a transiting planet candidate based on observations by *TESS* and later confirmed by RV follow-up observations with FEROS, HARPS, CHIRON, PFS, and CORALIE. Based on these RV observations, a second non-transiting planet, TOI-6695 c has been identified. TOI-6695 b is a Saturn-mass planet with a mass of $m_b = 0.21^{+0.01}_{-0.01}\,M_{jup}$ and a planetary radius of $r_b = 0.85^{+0.02}_{-0.02}\,R_{jup}$. It orbits the host star with an orbital period of ~ 80.4 days on a low eccentric orbit with an eccentricity of 0.04. Its bulk metal mass fraction is about 0.3. TOI-6695 c is a warm Jupiter with a minimum dynamical mass of $m_c = 1.45^{+0.03}_{-0.03}\,M_{jup}$ orbiting its host star every 242 days on an orbit with an eccentricity of 0.022. The estimated equilibrium temperatures of TOI-6695 b, and c are 599 ± 8 K and 415^{+5}_{-6} K, respectively. TOI-6695 b and c are in a rare orbital configuration close to the 3:1 mean motion resonance and are among the most massive planets of this extended subsample of Solar analogs.

5

A MASSIVE SPOT ON THE STELLAR SURFACE OF TW HYA

J. EBERHARDT, A. MÜLLER, R. LAUNHARDT, T. HENNING, T. TRIFONOV

This chapter is based on Eberhardt et al. [54], a manuscipt in preparation. A. Müller started this study, but never finished it. I took it over as my third PhD project, repeated his analyses with newer data, conducted my own additional analyses and wrote the text myself, based on his notes.

Abstract

At a period of 3.57 d, TW Hya exhibits periodic fluctuations in its radial velocity. A planetary companion orbiting at 0.04 au was proposed to be the source of this signal, however the claim was quickly questioned. In order to provide a solid response to the question of whether TW Hya is orbited by a planetary companion or if the observed signals are due to rotational modulation of stellar surface features, we look for spectroscopic and photometric indicators in radial velocity data obtained with FEROS and HARPS as well as photometric data obtained with TESS. We discover a correlation with the bisector inverse span and a clear evolution in both amplitude and phase from the radial velocities. A spot with a temperature difference of $\Delta T \approx 400$ K, located at a latitude of $\theta = 71°$, and a size of $\sim 30\%$ of the visible hemisphere can be used to model the observed radial velocity changes. The rotational modulation of a massive spot near the rotational axis is the source of the reported 3.57 d period in the radial velocity data of TW Hya for more than 19 years.

5.1 INTRODUCTION

TW Hya is a young, close-by T Tauri star that is surrounded by a relatively massive disk [18] that appears nearly face-on ($i_{\mathrm{disk}} \approx 4 - 10°$ [170]). Recent high-spatial resolution studies have shown that the disk contains complex structures that are indicative of continuing planet formation, including rings, gaps, and possible spiral patterns (e.g [193]). Disk mass measurements based on long-term observations of accretion [76] estimate that the disk will live another 3.8 Myr, while age estimates of TW Hya range from 3 to 15 Myr (see [160] and references therein). The stellar parameters for TW Hya are listed in Table 5.1.

Table 5.1: Stellar parameters for TW Hya and their 1-σ uncertainties.

PARAMETER	VALUE	REF.
d [pc]	59.98±0.15	[14]
Age [Myr]	8±3	[160]
Sp. type	K7 + M2	[42]
	M0.5	[160, 181]
M [$M_\odot$]	0.58±0.09	[181]
$\log g$ [cgs]	4.46±0.13	[181]
T_{eff} [K]	3800±100	[160]
	3870±40	[181]
B [kG]	3.60±0.04	[45]
R [$R_\odot$]	1.22±0.24	[181]
	1.3±0.6	this work
$v \sin i$ [km/s]	3±1	[44]
	7±2	[181]
i [deg]	18±10	[4]
	11±4	this work

Setiawan et al. [155] reported changes in radial velocity (RV) with a period of 3.57 d ($K = 196\,\mathrm{m/s}$). According to their analysis, a $m_p \sin i = 1.2 \pm 0.4\,M_{\mathrm{jup}}$ planetary companion orbiting at a distance of 0.04 au is responsible for the observed periodicity. Huélamo et al. [86] rejected this conclusion, arguing that a spot at latitude 54°, covering 7% of the stellar surface, could account for the observed variations. The authors based their results on five epochs of CRyogenic InfraRed Echelle Spectrograph (CRIRES) RVs in the H-band, which were inconsistent with the amplitude of the optical FEROS RVs. The presence of spots on the surface is to be expected due to the strong poloidal magnetic field (e.g. [44]). However, a spectropolarimetric survey in the near-IR by Donati et al. [45] found only low brightness contrast on the surface with respect to the quiet photosphere, likely attributed to a variability in the magnetic activity. Another possible explanation for the long-term stable RV signal could be an unresolved stellar companion, forming a spectroscopic binary system with a 3.57 d period. Such a system could induce RV as well as bisector (BIS) variations and could be a reason for TW Hya's historically spectral type, with Debes et al. [42] even suggesting a composite spectrum.

The aim of this work is to analyze a large spectroscopic data set in order to provide solid and conclusive evidence for the origin of the observed RV period. Our paper is structured as follows. We describe the observations and their reduction in Section 5.2. Section 5.3 presents the analysis of the RV data, while Section 5.4 presents the characteristics of the proposed spot which could cause the observed fluctuations. Section 5.6 and Section 5.5, respectively, discuss a statistical comparison of three models and an analysis of the existing *TESS* photometric data. A summary of our results is discussed in Section 5.7.

5.2 OBSERVATIONS

5.2.1 *Spectroscopic data*

5.2.1.1 *FEROS*

From March 2005 to March 2024, we collected 188 high-resolution spectra with the Fiber-fed Extended Range Optical Spectrograph (FEROS)[100], covering a total baseline of 19 years. FEROS is an echelle spectrograph that is mounted on the 2.2 m MPG/ESO telescope, located at La Silla Observatory in Chile. With a resolving power of $R = 48\,000$, FEROS covers the full visible spectrum from ~ 350 nm to ~ 920 nm, reaching an approximate RV precision of 7.5 m/s. From the spectra, we extracted the radial velocity measurements and the stellar activity indicators BIS, FWHM [140], H_α [19], He I, $\log R'_{HK}$ [51, 129], Na II [70], Ca II and S_MW. We reduced the spectra with the CERES pipeline [25] and obtained the RV and activity data by cross-correlating the spectra with a mask between the range of 378 nm to 680 nm and fitting a gaussian to the resulting cross-correlation function. We binned the reduced RV and stellar activity data into hourly bins, resulting in a total of 184 individual measurements.

5.2.1.2 *HARPS*

We obtained a total of 34 spectra with the High-Accuracy Radial-velocity Planetary Search (HARPS) spectrograph [118], between April 2005 and May 2009. HARPS has a spectral resolving power of $R = 120\,000$ and can achieve a precision of 1 m/s. We reduced the HARPS data with the SpEctrum Radial Velocity AnaLyser (SERVAL) pipeline [187] and extracted the radial velocity measurements as well as the stellar activity data for BIS, contrast, FWHM, H_α, CRX, dLW, Na D1 and Na D2. The RV, dLW and CRX data were extracted with a maximum likelihood approach, while the other data were extracted with the HARPS DRS pipeline. As for the FEROS data, we binned the HARPS data into hourly averages, resulting in a total of 32 measurements (31 for BIS, contrast and FWHM). The HARPS RV and stellar activity data is listed in Table C5.

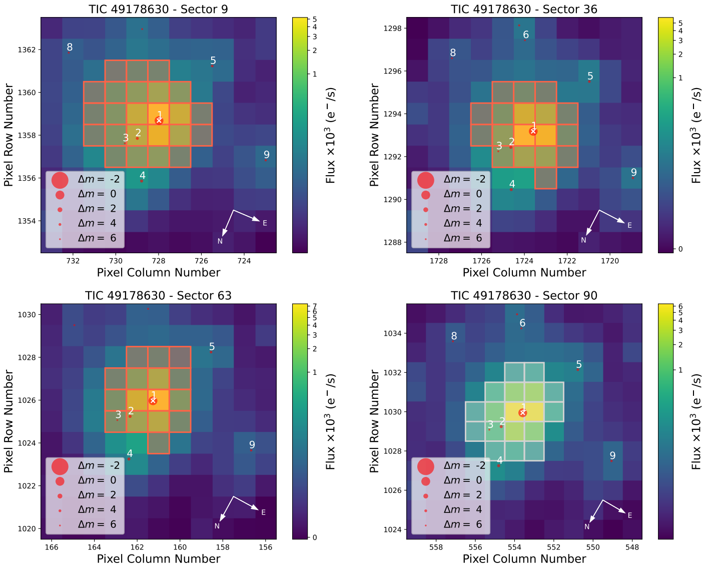

Figure 5.1: *TESS* Target Pixel Files (TPF) of TW Hya (TIC 49178630), created using `tpfplotter`. Orange overlays show the aperture used to determine the flux (a white overlay indicates an automatically detected threshold aperture). Gaia DR2 catalog objects are shown as filled red circles sized according to their brightness relative to the target (marked with a white cross).

5.2.2 *Photometric data*

5.2.2.1 *TESS photometry*

TESS has observed TW Hya in four sectors during its lifetime so far. During its primary mission, TW Hya was observed in sector 9 in March 2019, and in sectors 36, 63 and 90 during the extended mission in March 2021, March 2023 and March 2025, respectively. We generated the light curves for these sectors from the *TESS* FFI using the `tesseract`[1] package.

We examined the Target Pixel Files (TPF), visualized with `tpfplotter` [5] to identify possible contamination from nearby sources. Figure 5.1 shows the four TPF frames of TW Hya for sectors 9, 36, 63, and 90. These images show the field surrounding the target, overplotted with an aperture grid that indicates the pixels that were used to determine the flux, as well as nearby Gaia DR2 sources. In the *TESS* aperture, two nearby sources can be identified (TIC 49178625 and TIC 49178623, labelled 2 and 3, respectively). As the *TESS* data show no transits, the dilution of these sources doesn't have to be corrected for[2].

---

[1] https://github.com/astrofelipe/tesseract

[2] Dilution from contaminating sources can lead to wrong interpretations of the transit depth and therefore a planet's radius.

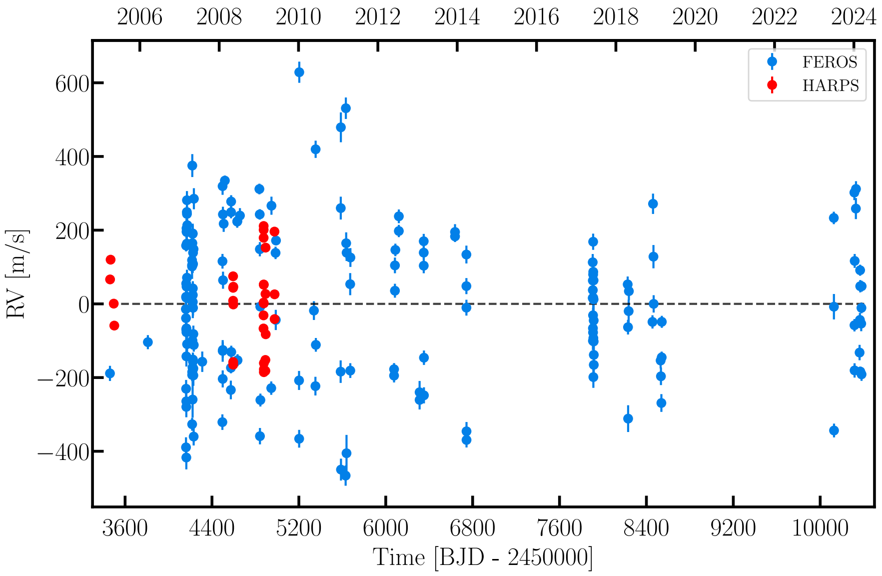

Figure 5.2: Time series of FEROS (*blue*) and HARPS (*red*) radial velocity measurements for TW Hya.

5.3 RADIAL VELOCITIES

Figure 5.2 shows the FEROS and HARPS radial velocity measurements. We analysed the data with the MLP [15, 188], shown in Figure 5.3, as well as Figure C1 and Figure C2. Figure 5.3 shows the periodograms for various models. The first panel shows the periodogram of the combined raw RV measurements for FEROS and HARPS, the second panel shows the periodogram of the residuals after subtracting the spot model (see Section 5.4) from the FEROS RVs. The third, fourth and fifth panels show the periodograms of the combined FEROS and HARPS data after subtracting a stellar activity GP, Keplerian and GP+Keplerian model, respectively (see Section 5.6). The last panel shows the window function of the combined datasets. In the raw RV periodogram, a strong significant peak at a period of 3.57 d and a weaker but still significant peak at a period of 1.38 d can be identified. As can be seen in the other panels, the power of the weaker signal decreases or vanishes completely after subtracting any model with a period of 3.57 d. We therefore attribute the 1.38 d signal to an alias of the 3.57 d period.

5.3.1 *Periodogram, amplitude and phase evolution*

Since the 3.57 d RV signal has been present in the data since 2005, and attributed to both a planet and a stellar spot in 2008 [86, 155], we constructed the Generalised Lomb Scargle (GLS) [186] periodogram evolution of the signal for increasing number of observations. The stacked periodogram is shown in Figure 5.4. The main panel shows

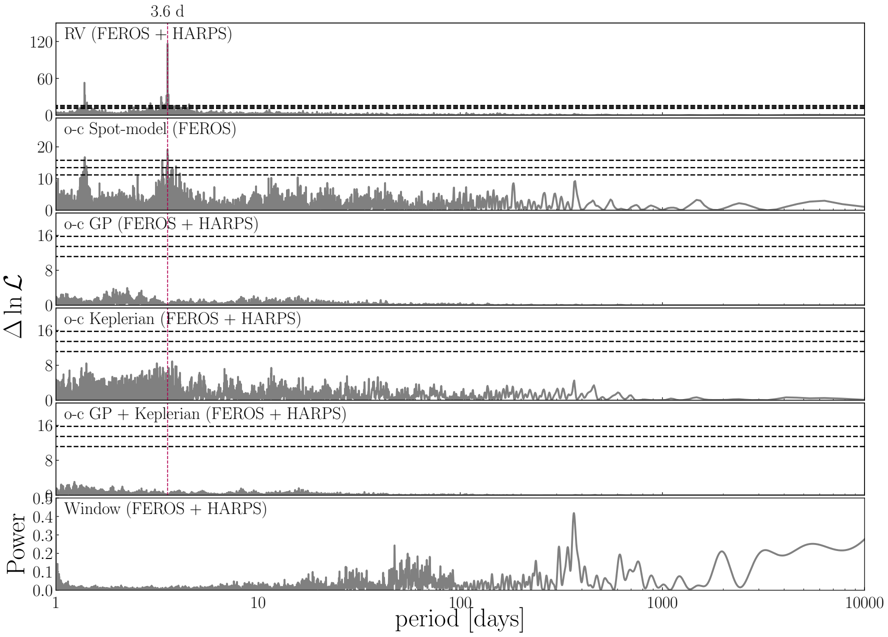

Figure 5.3: Maximum likelihood periodograms for the RV residuals of various models. The strong 3.57 d signal is shown as a dashed red vertical line. Horizontal dashed lines indicate FAP levels of 10%, 1% and 0.1%, from bottom to top.

the power for periods between 3.4 days and 3.7 days, computed for an increasing number of RV observations, with a step size of 2 data points. The additional panels show the evolution of the power of the 3.57 d period and the corresponding False-Alarm-Probability (FAP). As can be seen, while the power steadily increases, the signal itself only starts to appear after the first 25 data points as a broad peak and gets significantly more precise after ~ 60 data points. The power of the signal linearly increases until ~ 80 data points, after which it starts to decrease again. The FAP decreases roughly linearly until ~ 130 data points, at which point it starts to increase again. A signal produced by a massive companion would not show this behavior. The power of the signal would stay constant, independent of the number of epochs and the FAP would linearly decrease.

To further investigate the evolution of the signal, we binned the measurements using a range of time intervals. Starting from 4 days, we increased the bin size in steps of 4 days, up to a maximum of 1 600 days, resulting in a total of 2 662 bins across all bin sizes, covering the whole baseline. We filtered only bins with at least 5 data points and fit a sine function to the data, storing the amplitude and phase of the best fit, as well as the mean of the Barycentric Julian Date (BJD) values of the bin as the associated time. Figure 5.5 shows the evolution of both the the RV amplitude (left) and the phase (right) over time for varying bin sizes. We adopted an arbitrary reliability level of 100

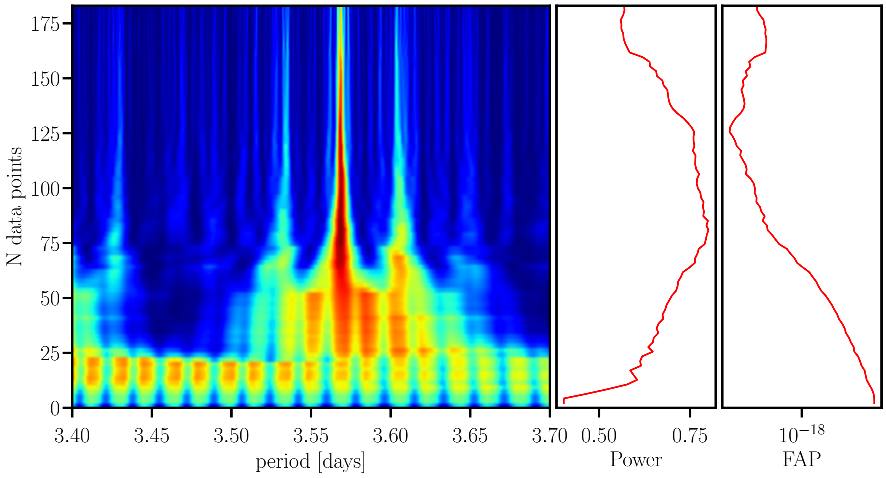

Figure 5.4: Evolution of the GLS periodogram of the FEROS RVs with increasing amounts of data. The evolution of the power and FAP are shown as red curves.

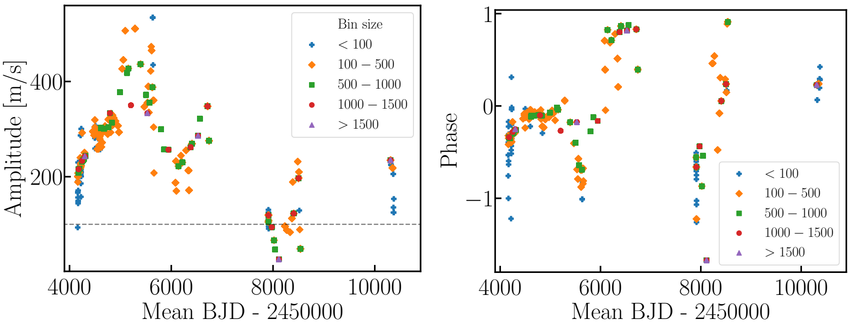

Figure 5.5: Amplitude (*left*) and phase (*right*) evolution of a sine function fit to RV data in bins of variable sizes. The dashed line in the amplitude diagram marks an arbitrarily chosen reliability level of 100 m/s.

m/s, below which we considered a fit non-converging. For both the amplitude, as well as the phase of the RV signal, a significant change over time is clearly visible on a timescale of ≈ 2000 days. If caused by a planetary companion of TW Hya, both the RV amplitude and phase would stay constant, indicating a stellar origin of the signal.

5.3.2 *RV correlation with activity*

Figure C1 and Figure C2 show the periodograms for the FEROS and HARPS RV and activity data, respectively. In the second panel of Figure C1, a weak signal can be identified in the BIS activity at the period of 3.57 d. To examine the influence of magnetic activity on the radial velocity, we inspected the correlation of the FEROS and HARPS BIS measurements with the radial velocities. Figure 5.6 shows correlation diagrams for FEROS BIS against RV (left) and HARPS BIS

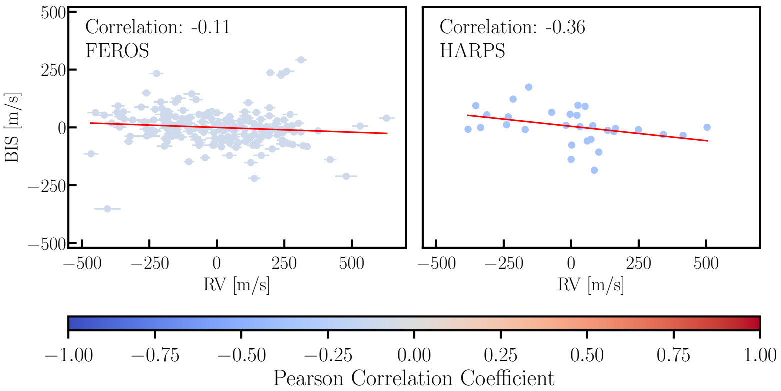

Figure 5.6: Correlation between the FEROS RVs and BIS (*left*) and HARPS RVs and BIS (*right*). The data is colored according to the Pearson correlation coefficients and a red line indicates a linear fit. A complete corner plot, showing the correlations for all FEROS activity data is shown in Figure C3.

against RV (right). To quantify their correlation, we computed the Pearson correlation coefficient for FEROS ($r = -0.11$) and HARPS ($r = -0.36$). This shows a weak negative correlation of the FEROS RVs and BIS data, and a moderate negative correlation for HARPS. A correlation between the radial velocity and bisector data is consistent with the signal being present in the FEROS BIS periodogram[3]. A weak negative correlation between the RVs and BIS data is consistent with a line shape change induced by the rotational modulation of a big spot on the stellar surface viewed from low inclinations.

5.4 SPOT MODEL

In order to determine a spot model that could replicate the observed radial velocities, we used the `spotter`[4] tool. Using the stellar parameters from Table 5.1 and adopting the observed RV signal as the rotational period of TW Hya, we set up a star with uniform intensity and radius $R_* = 1.22\,R_\odot$, a rotational period of $P = 3.57$ d, an intermediate inclination $i = 7°$ and limb darkening parameters of $u_1 = 0.171$ and $u_2 = 0.613$, derived from Eastman, Gaudi, and Agol [52]. From this star, we subtracted a circular spot with radius r_{spot}, sharpness sh_{spot}, contrast[5] C, located at the stellar latitude and longitude θ_{spot} and λ_{spot}. `spotter` computes the radial velocity from the integrated flux of the visible stellar surface.

---

[3] In the HARPS BIS periodogram, no significant peak at 3.57 d is present, but an overall increased power can be seen at around 1.3 and 3 d.

[4] https://github.com/lgrcia/spotter

[5] The contrast of a spot is defined as $C = 1 - \frac{I_{\text{spot}}}{I_{\text{phot}}}$, with I_{spot} and I_{phot} being the intensities of the spot and the stellar photosphere, respectively.

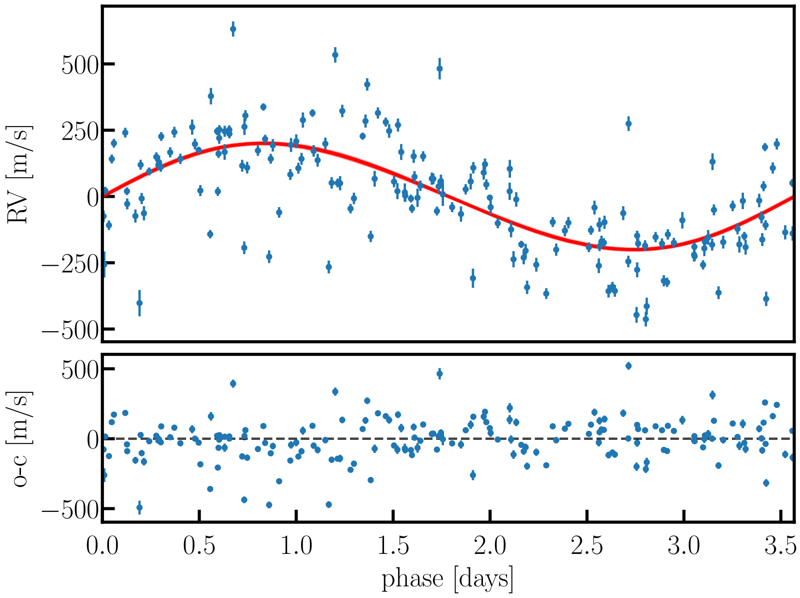

Figure 5.7: *Top:* 250 random samples of the spot-model plotted as red curves over the FEROS RVs. *Bottom:* RV residuals after subtracting the best-fit model.

To fit a spot model to the RV data, we phase-folded them with $P = 3.57$ d and performed a Markov Chain Monte Carlo (MCMC) analysis using the `emcee` package [63]. We kept the rotational period and the limb-darkening coefficients fixed and let the inclination and stellar radius as well as the spot parameters vary. For the variable parameters, we used flat priors to derive posterior distributions. Our MCMC setup consisted of 45 walkers and a total of 25 000 steps. From the resulting 900 000 samples, we discarded the first 5 000 as burn-in.

Figure 5.7 shows the FEROS RV data with 250 curves drawn from random samples of our spot model. Table 5.2 lists the parameters of our best spot model, the fixed stellar parameters, as well as the posterior distributions of the spot parameters and the adopted prior bounds. We find that a large spot, located at a latitude of $\sim 78°$ and covering $\sim 35\%$ of the visible hemisphere, including the entire polar region can reliably create a radial velocity signal that matches the observed data. From our model, we find that the star is viewed under a low inclination of $i \sim 10°$, which is consistent with the literature value listed in Table 5.1. From the best-fit spot contrast, we derived the temperature difference between the photosphere and the spot in two different ways. From all samples, we derived the temperature difference $\Delta T = 558^{+464}_{-195}$ K by calculating $\Delta T = T_{\text{eff}} - T_{\text{eff}}(1-C)^{1/4}$. We further determined the temperature difference directly from synthetic PHOENIX spectra [87]. For a stellar temperature of $T_{\text{eff}} = 3\,870$ K and a range of spot temperatures of $T_{\text{spot}} = 2\,870 - 3\,770$ K, we inte-

Table 5.2: Median and $1-\sigma$ uncertainties of the posterior distribution and uniform priors for the parameters of the spot model.

PARAMETER	POSTERIOR	PRIORS
R [$R_\odot$]	$1.3^{+0.6}_{-0.4}$	$\mathcal{U}$(0.1, 4.0)
P [days]	3.569	fixed
i [deg]	11^{+4}_{-3}	$\mathcal{U}$(0, 20)
u_1	0.171	fixed
u_2	0.613	fixed
θ_{spot} [deg]	71^{+5}_{-6}	$\mathcal{U}$(60, 90)
λ_{spot} [deg]	$-0.1^{+0.7}_{-0.6}$	$\mathcal{U}$(-5, 5)
r_{spot} [rad]	$0.8^{+0.2}_{-0.2}$	$\mathcal{U}$(0.0, 1.5)
sh_{spot}	153^{+103}_{-109}	$\mathcal{U}$(0, 300)
C	$0.5^{+0.2}_{-0.1}$	$\mathcal{U}$(0, 1)
A_{PV}	$0.04^{+0.02}_{-0.01}$	derived
ΔT	558^{+464}_{-195}	derived
	280^{+259}_{-99}	derived$^{(a)}$

(a): Derived by calculating the contrast from the flux ratio of synthetic spectra for the stellar temperature and a range of spot temperatures and comparing to the contrast posterior.

grated the synthetic spectra over the FEROS wavelength range. From the resulting intensities, we calculated the spot contrasts and fitted a polynomial to the discrete points. We then cross-matched the MCMC contrast posterior with the best-fit curve to determine a temperature difference of $\Delta T = 280^{+259}_{-99}$ K. This is illustrated in Figure C5.

While the original model of a large spot by Huélamo et al. [86] reported a latitude of $\theta \approx 54°$, the higher latitude of $\theta > 70°$ is supported by Donati et al. [44] who estimated a latitude of around 80°, consistent to their findings of a strong polar magnetic field of ≈ 3 kG.

5.5 PHOTOMETRY

Due to its large size, the spot should have a significant impact on the photometry of the star. Since the combination of spot latitude and stellar inclination show the spot over the full orbital period, the spot causes a net decrease of the flux over the full rotation, the amplitude of the sinusoidal flux signal (for a perpetually visible spot) depending on the exact values of those parameters. Figure 5.9 shows the simulated light curve of TW Hya, relative to the brightness of the unspotted surface, based on our spot model. The best-fit model is shown as a solid black line, 250 random samples as light grey lines

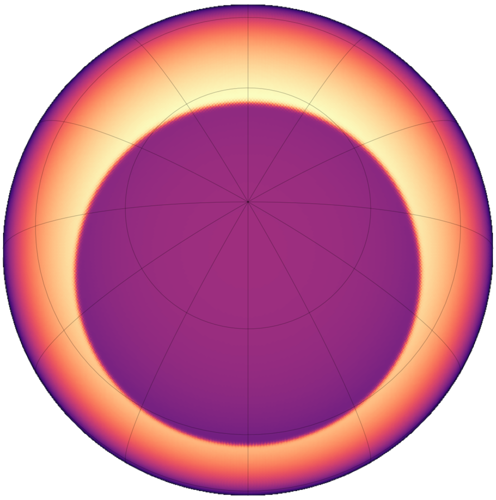

Figure 5.8: Visual representation of the spot covering the polar region of TW Hya.

and the unspotted flux as a dashed grey line. For the relative photometric variation, we find an amplitude of $A_{\mathrm{pv}} = 0.04^{+0.002}_{-0.001}$.

Figure 5.10, Figure C6 and Figure C7 show the *TESS* light curves for sectors 9, 36 and 63, respectively, with the top panels showing the flux relative to the mean flux and the bottom panels showing the flux after detrending with a time window of width 2.4 hours. The light curves each cover a time span of 24 days and show significant brightness fluctuations. Such brightness fluctuations are typical for T Tauri stars. A main driver of such fluctuations is variable accretion [see e.g. 31, 192]. TW Hya shows strong variable poleward accretion from the surrounding disk [45, 76], which in turn can create a large spot in the polar region.

Even after the thorough detrending of the *TESS* photometry, the scatter of the flux measurements is still comparable to the amplitude of the photometry variability of our spot models. We inspected the individual light curves in two ways, using a GLS periodogram approach and a Continuous Wavelet Transform (CWT) analysis in combination with a Global Wavelet Spectrum (GWS), providing a time-resolved power spectrum, as well as an averaged periodogram analysis. Figure 5.11 shows the GLS periodograms for *TESS* sectors 9, 36, 63 and 90, while Figure C9 shows the wavelet analysis results. The CWT scalogram shows the time resolved power for each period. Both the GLS periodograms and the wavelet analyses show peaks at or close to the 3.57 d signal.

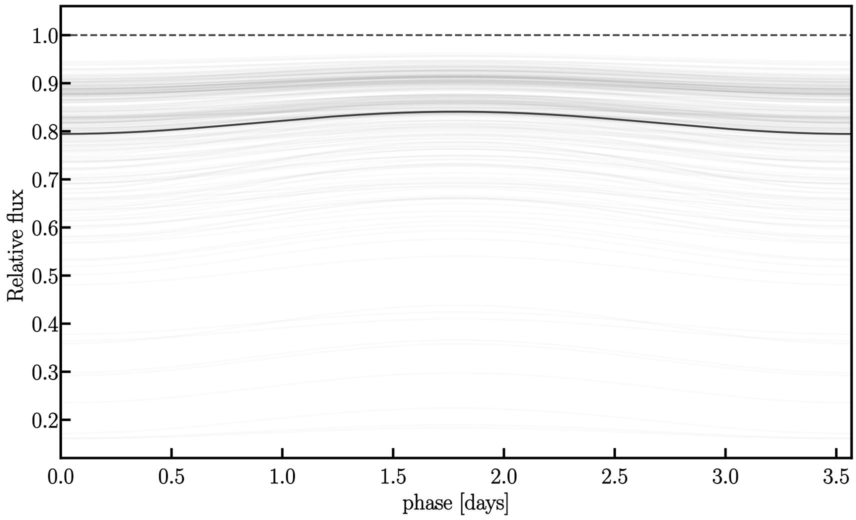

Figure 5.9: Photometric variation of the flux of the spotted star from our model. The best-fit parameter model is shown as a solid black line, while 250 random sample curves are shown as grey lines. The flux of the unspotted star is shown as a dashed black line.

5.6 KEPLERIAN MODELLING AND GAUSSIAN PROCESS

Even though the spot model manages to recreate the radial velocity signal, it still leaves a significant signal in the residual periodogram. To thoroughly test the spot vs. planet hypotheses, we performed NS [158] analyses for three distinct models. The first model consists of a quasi-periodic gaussian process with a rotational kernel, to model the RVs solely based on stellar activity. The parameters were the radial velocity offsets and jitter for FEROS and HARPS, as well as the hyperparameters amplitude, timescale, period and factor. The jitter is added in quadrature to the RV uncertainties, to account for unknown instrumental, atmospheric or stellar noise. As initial values, we chose an amplitude of $40\,000\,\mathrm{m}^2/\mathrm{s}^2 = (200\,\mathrm{m/s})^2 \approx K^2$, a timescale of 2000 days, corresponding to the amplitude and phase modulation of the RV signal, a rotational period of 3.57 days and a factor of 0.5, as a measure of the aggressiveness of the GP. Our second model is a simple Keplerian, presenting the planet hypothesis. In addition to the RV offset and jitter parameters, we optimized the RV semi-amplitude K, the orbital period P, the orbital eccentricity e, as well as the argument of periastron ω and the mean anomaly MA. The third model is a combination of the GP and Keplerian models, where we optimized the full range of orbital elements and GP hyperparameters.

We performed our nested sampling, by using the `Exo-Striker`[6] [176] toolbox, which utilizes the `dynesty` [162] package. Similar to

---

[6] https://github.com/3fon3fonov/exostriker

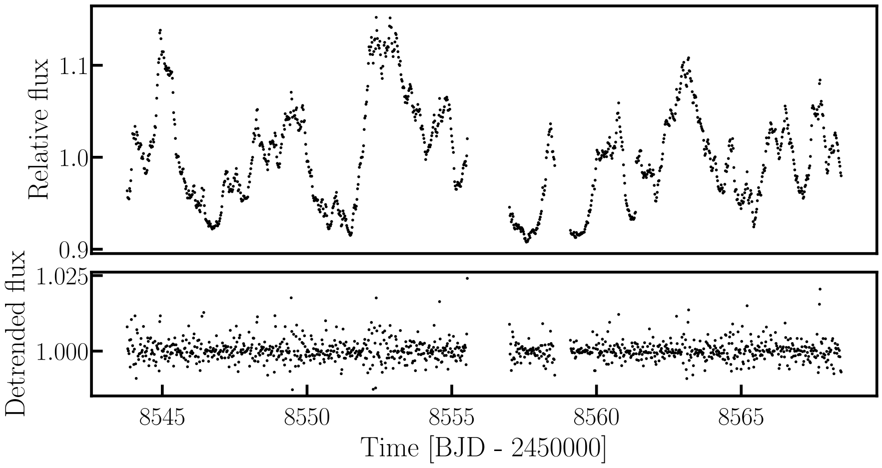

Figure 5.10: *Top:* Photometric flux of TW Hya against the time, relative to the mean flux, observed by *TESS* in sector 9. *Bottom:* Photometric flux detrended with a time-window of width 0.1 days.

the approach in Trifonov et al. [177], we used 100 live points for our dynamic NS, while optimizing the $-\ln \mathcal{L}$ function of our models. The results for our models are listed in Table 5.3.

Table 5.3: Median and $1-\sigma$ uncertainties for the parameters of the model comparison for a GP, Keplerian and GP+Keplerian model, along with their priors ($\mathcal{U}$– uniform and $\mathcal{J}$– Jeffrey's).

PARAMETER	GP	KEPLERIAN	GP + KEPLERIAN	PRIORS
BIC	2674.14	2729.23	2732.46	–
ΔBIC	–	55.09	58.32	–
$RV_{offset;F}$ [m/s]	9^{+139}_{-138}	-4^{+11}_{-11}	-26^{+137}_{-205}	$\mathcal{U}(-1500, 1500)$
$RV_{offset;H}$ [m/s]	-16^{+143}_{-140}	14^{+4}_{-4}	-51^{+140}_{-206}	$\mathcal{U}(-1500, 1500)$
$RV_{jitter;F}$ [m/s]	91^{+8}_{-7}	141^{+8}_{-7}	93^{+7}_{-7}	$\mathcal{J}(1, 150)$
$RV_{jitter;H}$ [m/s]	12^{+4}_{-3}	22^{+4}_{-3}	12^{+4}_{-3}	$\mathcal{J}(1, 45)$
K [m/s]	–	185^{+6}_{-6}	173^{+37}_{-51}	$\mathcal{U}(100, 300)$
P [d]	–	3.5684^{+6e-05}_{-7e-05}	$3.56882^{+0.0004}_{-0.0003}$	$\mathcal{U}(3.4, 3.7)$
e	–	$0.05^{+0.03}_{-0.03}$	$0.07^{+0.04}_{-0.03}$	$\mathcal{U}(0, 0.2)$
ω [deg]	–	221^{+35}_{-51}	196^{+50}_{-42}	$\mathcal{U}(90, 360)$
MA [deg]	–	319^{+51}_{-35}	317^{+40}_{-55}	$\mathcal{U}(120, 480)$
Amplitude [m^2/s^2]	86772^{+82623}_{-35840}	–	$98178^{+100422}_{-57508}$	$\mathcal{U}(0, 250000)$
Timescale [d]	2066^{+2591}_{-1042}	–	3664^{+3680}_{-2312}	$\mathcal{U}(0, 10000)$
P_{GP} [d]	$3.569^{+0.001}_{-0.001}$	–	$3.573^{+0.001}_{-0.003}$	$\mathcal{U}(3.4, 3.7)$
Factor	$0.2^{+0.3}_{-0.2}$	–	$0.3^{+0.3}_{-0.2}$	$\mathcal{U}(0, 1)$
m [M_{jup}]	–	$0.97^{+0.03}_{-0.03}$	$0.9^{+0.2}_{-0.3}$	(derived)
a [au]	–	$0.0381349^{+8e-07}_{-8e-07}$	$0.038132^{+6e-06}_{-6e-06}$	(derived)

The GP-only model successfully recovered both the timescale of 2066^{+2591}_{-1042} days and the rotational period of $P_{GP} = 3.569 \pm 0.001$ days. Figure 5.12 shows the gaussian process model overplotted

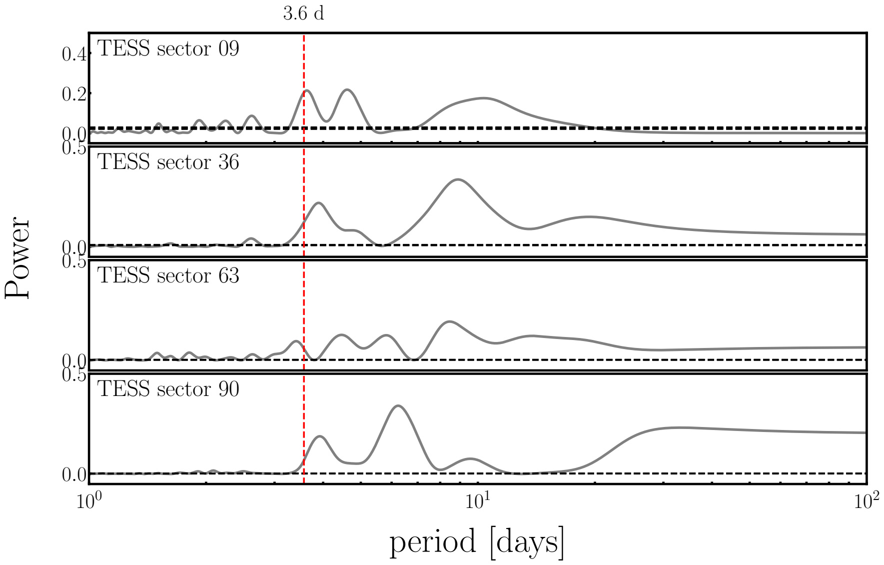

Figure 5.11: GLS periodograms for the four available *TESS* sectors of TW Hya. The 3.57 d signal is shown as a red dashed line.

with the FEROS and HARPS RV data, the posterior distribution is shown in Figure C10. The third panel of Figure 5.3 shows the periodogram of the residuals after subtracting the GP model, leaving no significacnt signal. From the Keplerian model, we found a planet of $m_p \sin i = 0.97 \pm 0.03\,M_{jup}$ on a near circular orbit at a semimajor axis of $a = 0.04$ au. Figure 5.13 shows the RV data, phase-folded with the period of $P = 3.569$ d with the Keplerian model shown as a black curve. The posterior distribution is shown in Figure C11. As for the GP model, the Keplerian model residual periodogram shows no significant peaks, although a direct comparison with the 3.57 d signal shows lingering insignificant power around the 3.57 and 1.38 d periods. The combined GP+Keplerian model returned comparable results as the other models. The posterior distribution for the full parameters of this model are shown in Figure C12. The periodogram again shows no significant peaks left.

From each models best likelihood $\mathcal{L}$, we calculated the Bayesian Information Criterion (BIC) values, to directly quantify the quality of our models. The BIC is defined as $\mathrm{BIC} = k \ln n - 2 \ln \mathcal{L}$, with the number of free parameters k and the number of measurements n. When comparing two models, a strong statistical evidence in favor of the model with the lower BIC is given when $\Delta\mathrm{BIC} > 10$ [99].

To test the models involving a planetary Keplerian, we calculated the BIC differences with respect to the GP model. With differences of $(\Delta\mathrm{BIC})_{\mathrm{Kepler,GP}} = \mathrm{BIC}_{\mathrm{Kepler}} - \mathrm{BIC}_{\mathrm{GP}} = 55.09$ and $(\Delta\mathrm{BIC})_{\mathrm{GP+Kepler,GP}} = 58.32$, both models involving a Keplerian show an extremely significant evidence in favor of the GP-only model.

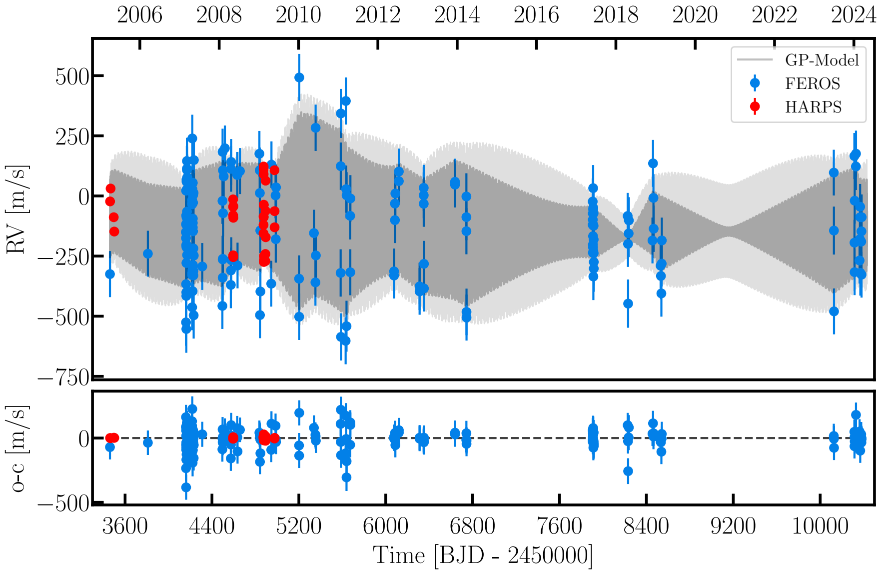

Figure 5.12: FEROS (*blue*) and HARPS (*red*) radial velocity data with the gaussian process model shown as a grey line. The $1-\sigma$-uncertainty is shown as a light grey shaded region.

5.7 CONCLUSION AND DISCUSSION

In this work, we presented an extensive analysis of 216 optical FEROS and HARPS radial velocity measurements, spanning a baseline of 19 years in addition to four sectors of TESS photometry. Our aim was to provide insights and a conclusive answering of the origin of the 3.57 d radial velocity signal. This signal has been present in the data for almost 20 years. We found a weak negative correlation between the radial velocity and BIS measurements, a strong indicator of stellar activity at the observed period. To further investigate this, we conducted a number of experiments, including a spot model to reproduce the observed radial velocities. Our spot model produced a large cool spot ($\Delta T \approx 400$ K), covering $\sim 30\%$ of the visible hemisphere of TW Hya on a high latitude of $\sim 71°$, which can accurately reproduce the observed signal. An inspection of the stacked RV periodogram showed a decrease in the significance of the 3.57 d period, which would not be the case for a purely planetary signal. The spot we propose is similar to the one found in the polar region of the M dwarf TOI-3884 [6], which was discovered from the shape of the in-transit flux, as the planet TOI-3884 b passes on an inclined orbit in front of the spot. Donati et al. [46] and Morin et al. [127] find that fast rotating low-mass M dwarfs generate strong, long-lived poloidal magnetic fields. This is consistent with the strong polar accretion of TW Hya, transporting material from the inner disk to its polar regions (see e.g. [45, 76, 157]).

We found a clear evolution and $\sim 2\,000$ d modulation (equivalent to $5-6$ years) of the amplitude and phase of the RV signal, poten-

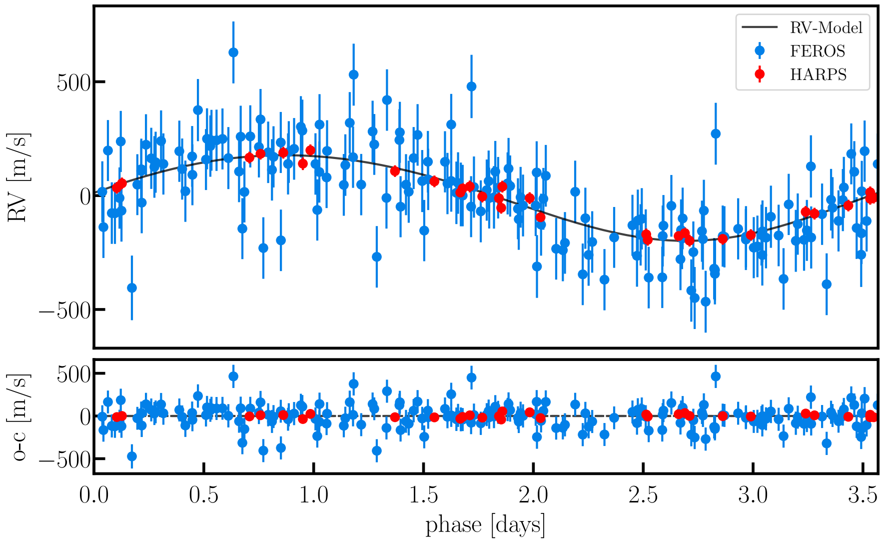

Figure 5.13: FEROS (*blue*) and HARPS (*red*) radial velocity data, phase-folded with the period of 3.569. The Keplerian model from the best parameters of the MCMC is shown as a black curve.

tially showing the magnetic cycle of TW Hya, comparable to the 11 year solar cycle. A planetary companion, or even a binary companion to TW Hya would produce a radial velocity signal with constant amplitude and phase, unless interacting with the accretion disk and thus leading to unstable orbits. However, with the inner cavity of TW Hya's accretion disk lying at 4 au [123, 193], such an interaction is unlikely. A binary companion of TW,Hya could potentially contribute to the formation of such a cavity [11], depending on the mass ratio and the resulting separation of the stars [128, 143], although it might not be solely responsible given the large size of the cavity [143, 167]. However, it would produce a positive correlation between RV and BIS data, and can therefore be ruled out.

We studied periodograms for both stellar activity and TESS photometry, finding significant evidence for stellar activity in multiple indicators, like H-alpha, FWHM, contrast and Na D2 on longer timescales of $\sim 20-200$ days, showing the dynamically active nature of TW Hya. The periodograms of the TESS, as well as their wavelet analyses revealed photometric activity around the observed period of $3-4$ days, as well as on slightly longer timescales of $6-10$ days, which can be explained by waves in the accretion disk [147]. The activity at the $3-4$ day period could be explained by either photometric modulation due to the large spot, or brightness fluctuations in the disk at the corotation radius.

To present a more quantitative direct comparison between the planetary and activity-driven models for the RV variations, we performed nested sampling analyses of three different models: A Gaussian Process (GP) only model, a simple Keplerian model and a combination of both models. With the Keplerian models, we managed to reproduce the planet claimed by Setiawan et al. [155]. However, consistent with our other results, a statistical comparison of the individual Bayesian Information Criterion (BIC) values provided strong evidence for the stellar activity-only GP model, rejecting any Keplerian component.

6

SUMMARY AND OUTLOOK

6.1 SUMMARY

In Chapter 3 and Chapter 4, I studied transiting exoplanets as part of the WINE collaboration. The WINE collaboration focuses on radial velocity follow-up and validation of TESS candidates. The main scope of the collaboration are "warm" giants, i.e. planets that orbit their host stars with orbital periods longer than 10 days or planets with equilibrium temperatures smaller than $\sim 1\,000$ K. These definitions are somewhat arbitrary and some of the targets of the collaboration and also two targets described in this Thesis orbit their host star on closer orbits.

In Chapter 3, myself and my collaboration report the discovery of three exoplanets, orbiting solar analog stars. These are stars with surface gravity, metallicity and effective temperature similar to those of the Sun [113]. Out of all $\sim 6\,000$ known exoplanets with well determined masses and radii, only 276 orbit solar analogs. The planets TOI-2373 b, TOI-2416 b and TOI-2524 b were first discovered by TESS and followed up with FEROS radial velocities. With orbital periods of $P = 13.3$ d, $P = 8.3$ d and $P = 7.2$ d, respectively, the planets reside right in the transition zone between hot and warm giants, with TOI-2416 b and TOI-2524 b technically being considered hot giants.

For all three planets, I detrended the TESS light curves, performed Transit Least Squares (TLS) and MLP period searches and carried out a joint photometric and Keplerian model. I precisely estimated the masses and radii and subsequently their mean densities. Out of the three planets, TOI-2373 b stands out in particular with a high mass of $m_p = 9.3\,M_{jup}$, a radius of $r_p = 0.93\,R_{jup}$ and a mean density of $\rho_p = 14.4\,\mathrm{gcm}^{-3}$, making it one of the densest known exoplanets and the second most massive exoplanet known orbiting solar analog stars. TOI-2416 b and TOI-2524 b have masses of $m_p = 3.0\,M_{jup}$ and $m_p = 0.64\,M_{jup}$ and radii of $r_p = 0.88\,R_{jup}$ and $r_p = 1.0\,R_{jup}$, respectively, leading to a dense TOI-2416 with $\rho_p = 5.4\,\mathrm{gcm}^{-3}$ and an inflated TOI-2524 with $\rho_p = 0.79\,\mathrm{gcm}^{-3}$. A heavy element mass estimation based on [173] showed large bulk metallicity fractions of $Z_p = 0.11$, $Z_p = 0.36$ and $Z_p = 0.24$ for TOI-2373 b, TOI-2416 b and TOI-2524 b, respectively.

In Chapter 4, I studied a system of two exoplanets, orbiting the late F-type star TOI-6695. TESS observed a transit in sector 8 and 724 days later another one in sector 34. Our collaboration observed the target with FEROS and HARPS and found a period of ~ 240 days in the RV periodogram, corresponding to 1/3 of the time between the two transiting events. Initially attributing the transits to a planet with an orbital period of 240 days, we took more RV data, including CHIRON, PFS and CORALIE data and found a second signal of ~ 80 days. As the period ratio between these signals is almost exactly 3:1, there was an ambiguity about which signal corresponds to each transit. Analogously to the analysis in Chapter 3, I detrended the TESS light curves and performed combined models. Due to a difference in transit depths, I suggested a system of two single-transiting exoplanets, when a third transit by TESS was observed another 723 days later in sector 61. The dual single-transiter model was inconsistent with the new transit, but either the 80 day or 240 day planet would have been able to cause the transit. To correctly attribute the transit to one of the planets, I predicted transits for the shorter period planet. On 2024 March 5, we observed a transit ingress at the predicted time with two telescopes of the Observatoire Moana El Sauce in Chile, confirming the transits to be caused by the inner planet, TOI-6695 b.

TOI-6695 b is a warm giant with a mass of $m_b = 0.21\,M_{jup}$ and a radius of $r_b = 0.85\,R_{jup}$, comparable to Saturn. Since we didn't observe a transit for TOI-6695 c, its true mass and its radius remain unknown. TOI-6695 c has a minimum dynamical mass of $m_c \sin i = 1.45\,M_{jup}$. Despite having a period ratio of almost exactly 3:1, the planets are not in a dynamically coupled mean motion resonance. Out of all exoplanets discovered to date, only 34 pairs of planets close to a 3:1 resonance are known. Most of these are lower mass sub-Neptunes and TOI-6695 b and c among the six most massive planets of this subsample.

For Chapter 5, I took on a long-running project about the young T Tauri star TW Hya. From FEROS radial velocity observations, a signal with a period of 3.57 day was detected by Setiawan et al. [155]. They claimed that the signal was caused by a Jupiter-mass planet. Huélamo et al. [86] presented an alternate explanation, based on near-infrared CRIRES radial velocity observations. They noticed inconsistent semi-amplitudes for the optical and infrared data, which they attributed to a stellar spot. Their argumentation, however, was based on only five data points, of which the reduction at the time was only poorly understood, even by CRIRES operators themselves. As a result, the planet hypothesis was never fully ruled out, but the spot was widely accepted.

To settle this debate, I conducted a thorough radial velocity and photometry analysis, based on almost 20 years of FEROS and HARPS RV baseline and four individual TESS light curves. I studied the periodograms of both the RV data and light curves, as well as stellar activity. I correlated the BIS measurements to the RV data to confirm a weak correlation and constructed a spot model that reliably recreates the observed periodic modulation to the RVs. My model showed a large polar spot at a latitude of 71°, covering $\sim 30\%$ of TW Hya's visible hemisphere, with a temperature difference of ≈ 400 K. In addition to the spot itself, my model returned estimates for the radius and inclination of TW Hya, namely $R = 1.3\,R_\odot$ and $i = 11°$. Despite the large spot, the low inclination of TW Hya leads to the spot being visible during the full rotation of the star, resulting in a photometric variability of only 4%, only slightly larger than the scatter of the TESS data.

I examined the evolution of the amplitude and phase of the RV signal and found a modulation of about ~ 2000 days. To directly compare the planet hypothesis to a stellar activity hypothesis, I computed competitive models for a quasiperiodic gaussian process with rotational kernel, a Keplerian model and a combination of both. While the Keplerian model found the same planetary parameters as Setiawan et al. [155], a comparison of their BIC values showed strong evidence for the simple gaussian process model. This model recovered both the stellar rotational period of 3.57 days, as well as the 2000 day amplitude and phase modulation. A periodogram and wavelet analysis of the TESS photometry revealed periodic activity at about $3-4$ days. TW Hya shows strong polar accretion from the surrounding disk, which can lead to the formation and maintenance of a large spot.

During the work on this Thesis I have learned how to analyse and model radial velocity and transit data for a variety of different systems. These included transiting planets, orbital dynamics, potential single-transiting planets and uncertain cases of stellar activity. I further learned how to extract transit timing variations from a transit model and to model stellar activity with gaussian processes and surface spots.

6.2 OUTLOOK

The results presented in this Thesis provide a solid groundwork for further research. While the definition of "warm" and "hot" giants is somewhat arbitrary, a statistical correlation between the orbital separation of a star and planet and the spin-orbit alignment, the angle between the axis of rotation of an exoplanet host star and the angular momentum vector of the planetary orbit, has been observed. Rice et al. [145] and Attia et al. [13] noticed a trend that the orbits of planets orbiting their host stars on wider orbits tend to be aligned to the stars rotational axis, whereas such an alignment is rarely present for close-in planets. Studying the spin-orbit alignment of planets within this transition zone can be useful for probing this trend. The spin-orbit alignment of planetary orbits can be determined by observing the Rossiter-McLaughlin (RM) effect. The shape of the RM radial velocity curve depends on the sky-projected alignment of the planet's path during transit to the rotational axis of the star.

As transiting exoplanets with successful radial velocity follow-up, TOI-2373 b, TOI-2416 b, TOI-2524 b and TOI-6695 b are excellent targets to observe the RM effect. Using Equation 8, I calculated the expected amplitudes for all four planets. Their expected amplitudes are $\Delta V = 12.90$ m/s, $\Delta V = 10.43$ m/s, $\Delta V = 22.82$ m/s and $\Delta V = 17.49$ m/s, respectively. With a sufficient dense sampling during their transit duration, using a high-precision spectrograph like ESPRESSO or potentially HARPS, these signals can be detected and allow the direct inference of the spin-orbit alignment.

Table 6.1 and Table 6.2 list the next 20 (5 for TOI-6695 b) transits, with both their BJD as well as their UTC time stamps. Table 6.2 also lists the next 5 transits for TOI-6695 c, predicted based on the root[1] of the radial velocity curve and the observed orbital period. Even though no transits for TOI-6695 c were observed, predicted transits during the available TESS sectors fall in between observation gaps. A detection of a transit during one of the predicted times would allow us to determine both the true mass and the radius of TOI-6695 c as well as density estimations and interior modelling. A non-detection during one or more of the predicted times would mean the planet is passing above or below the star and would help constrain the mutual inclinations of the orbits.

Table 6.1: Predicted transit times for TOI-2373 b, TOI-2416 b, and TOI-2524 b.

Transit	TOI-2373 b		TOI-2416 b		TOI-2524 b	
	BJD	UTC	BJD	UTC	BJD	UTC
1	2460822.24832	2025-05-26 17:57	2460810.78537	2025-05-15 06:50	2460815.93340	2025-05-20 10:24
2	2460835.58500	2025-06-09 02:02	2460819.06085	2025-05-23 13:27	2460823.11925	2025-05-27 14:51
3	2460848.92168	2025-06-22 10:07	2460827.33633	2025-05-31 20:04	2460830.30510	2025-06-03 19:19
4	2460862.25836	2025-07-05 18:12	2460835.61181	2025-06-09 02:41	2460837.49095	2025-06-10 23:46
5	2460875.59504	2025-07-19 02:16	2460843.88729	2025-06-17 09:17	2460844.67680	2025-06-18 04:14
6	2460888.93172	2025-08-01 10:21	2460852.16277	2025-06-25 15:54	2460851.86265	2025-06-25 08:42
7	2460902.26840	2025-08-14 18:26	2460860.43824	2025-07-03 22:31	2460859.04850	2025-07-02 13:09
8	2460915.60508	2025-08-28 02:31	2460868.71372	2025-07-12 05:07	2460866.23435	2025-07-09 17:37
9	2460928.94176	2025-09-10 10:36	2460876.98920	2025-07-20 11:44	2460873.42020	2025-07-16 22:05
10	2460942.27844	2025-09-23 18:40	2460885.26468	2025-07-28 18:21	2460880.60605	2025-07-24 02:32
11	2460955.61512	2025-10-07 02:45	2460893.54016	2025-08-06 00:57	2460887.79190	2025-07-31 07:00
12	2460968.95180	2025-10-20 10:50	2460901.81564	2025-08-14 07:34	2460894.97775	2025-08-07 11:27
13	2460982.28848	2025-11-02 18:55	2460910.09112	2025-08-22 14:11	2460902.16360	2025-08-14 15:55
14	2460995.62516	2025-11-16 03:00	2460918.36660	2025-08-30 20:47	2460909.34945	2025-08-21 20:23
15	2461008.96184	2025-11-29 11:05	2460926.64208	2025-09-08 03:24	2460916.53530	2025-08-29 00:50
16	2461022.29852	2025-12-12 19:09	2460934.91756	2025-09-16 10:01	2460923.72115	2025-09-05 05:18
17	2461035.63520	2025-12-26 03:14	2460943.19304	2025-09-24 16:37	2460930.90700	2025-09-12 09:46
18	2461048.97188	2026-01-08 11:19	2460951.46851	2025-10-02 23:14	2460938.09285	2025-09-19 14:13
19	2461062.30856	2026-01-21 19:24	2460959.74399	2025-10-11 05:51	2460945.27870	2025-09-26 18:41
20	2461075.64524	2026-02-04 03:29	2460968.01947	2025-10-19 12:28	2460952.46455	2025-10-03 23:08

---

[1] $K = 0$ m/s.

Table 6.2: Predicted transit times for TOI-6695 b and TOI-6695 c.

Transit	TOI-6695 b		TOI-6695 c	
	BJD	UTC	BJD	UTC
1	2460858.13400	2025-07-01 15:12	2460917.73300	2025-08-30 05:35
2	2460938.52300	2025-09-20 00:33	2461160.13300	2026-04-29 15:11
3	2461018.91200	2025-12-09 09:53	2461402.53300	2026-12-28 00:47
4	2461099.30100	2026-02-27 19:13	2461644.93300	2027-08-27 10:23
5	2461179.69000	2026-05-19 04:33	2461887.33300	2028-04-25 19:59

TOI-2373 b and TOI-2416 b show unusually high amounts of heavy elements, presenting challenges to planet formation theories. If the 9.3 M_{jup} TOI-2373 b formed via either core-accretion or gravitational instability, its metallicity would be comparable to that of its host star. A direct spectroscopic observation of its atmosphere would provide invaluable insight into its interior composition. With an even higher bulk metallicity, TOI-2416 b would greatly benefit from atmospheric observations as well. Figure 6.1 shows the Transmission Spectroscopy Metric (TSM) and Emission Spectroscopy Metric (ESM) [103] for TOI-2373 b, TOI-2416 b, TOI-2524 b and TOI-6695 b, as well as for planets from the updated PlanetS catalogue [131]. The TSM and ESM provide a metric to gauge the suitability of a planet for either transit spectroscopy or emission spectroscopy, respectively. Planets are deemed suitable for transit spectroscopy, if their TSM is above the threshold of 90 (10 for planets with radii smaller than 1.5 $R_\oplus$) and for emission spectroscopy, if their ESM exceeds the threshold of 7.5. With TSM values of 1.26, 3.59, 34.17 and 42.26, neither of the four planets is particularly suitable for transit spectroscopy, but TOI-2373 b, TOI-2416 b and TOI-2524 b exceed the ESM threshold, having values of 9.42, 11.44 and 20.95, respectively, making them good targets for emission spectroscopy. Only TOI-6695 b is unsuitable for atmospheric spectroscopy, showing an ESM of 3.59.

The analyses on TW Hya's persistent radial velocity signal presented in this Thesis provide compelling arguments against a planetary companion and I instead come to the conclusion that the signal is indeed caused by a large polar spot. To further cement this result, an even more sophisticated modelling of the stellar activity, or a model linking photometry with radial velocity (e.g. FENRIR [73]) could be better suited to model the signal. A careful extraction of radial velocity, correcting stellar activity by either template matching (e.g. [9, 12]) or line-by-line extraction [10, 50] could provide cleaner data.

Due to the low quality of the initial CRIRES data and the lack of simultaneously taken RV data in visual and infrared, considering the demonstrated amplitude variability, a simultaneous multiwavelength high precision radial velocity observation with a sufficiently dense

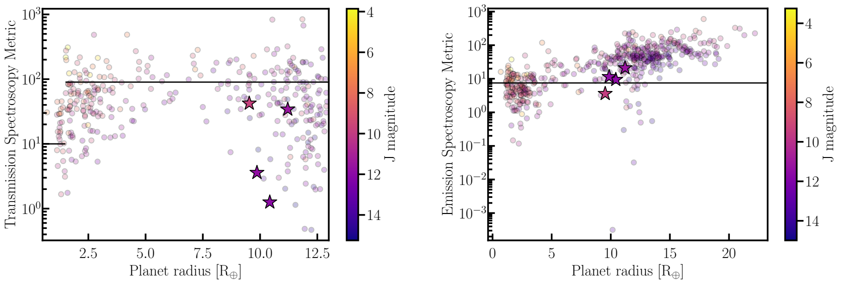

Figure 6.1: TSM (*left*) and ESM (*right*) for planets within the updated PlanetS catalogue as transparent circles and the transiting planets studied in this work, shown as filled stars. The planets are colored according to the their host stars magnitude in the J band. Thresholds for suitability of transit- and emission spectroscopy of 90 and 7.5, respectively, are shown as solid lines.

phase coverage could provide the smoking gun evidence. Observations like these could be carried out with facilities like CARMENES or HARPS + NIPRS. A planetary signal would show no significant amplitude difference between wavelengths, while a stellar spot would show a difference in amplitude, corresponding to the wavelength dependent spot contrast.

As already briefly touched upon, a more in depth study of TW Hya's disk could provide a better understanding of its short-term photometric variability, its magnetic activity and orbital dynamics.

Part III

APPENDIX

A

APPENDIX FOR CHAPTER 3

In this appendix, we show additional plots, including TPF plots for all *TESS* sectors used within this work, and additional time-series plots of the photometric and RV data, as well as tables containing our FEROS RV measurements, and the full results of our analysis. Table A1 lists the RV and stellar activity data obtained with the FEROS instrument for all three targets and Table A2, Table A3, and Table A4 list the results for all fit parameters and both tested models from the Nested Sampling (NS) for TOI-2373, TOI-2416, and TOI-2524, respectively. Figure A1, Figure A2, and Figure A3 show the TPF plots for the *TESS* sectors used for our analysis but not shown before. Figure A4, Figure A5, and Figure A6 show time-series plots of the photometric and RV data for TOI-2373, TOI-2416, and TOI-2524, respectively. These plots are complementary to Figure 3.5, Figure 3.6, and Figure 3.7.

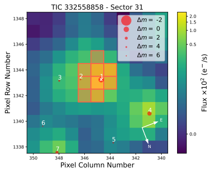

Figure A1: TPF plot for Sector 31 for TOI-2373

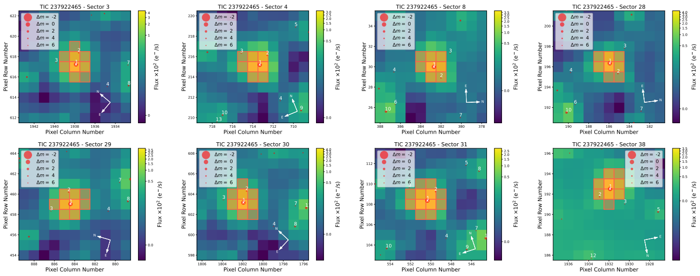

Figure A2: TPF plots for Sectors 3, 4, 8, 28-31, and 38 for TOI-2416

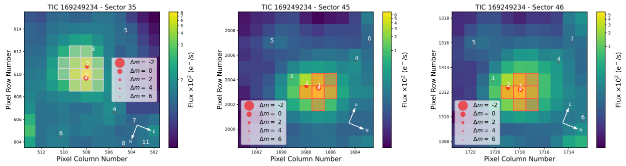

Figure A3: TPF plots for Sectors 35, 45, and 46 for TOI-2524

Table A1: FEROS radial velocity and stellar activity measurements along with their $1-\sigma$ uncertainties.

BJD	RV ($\mathrm{m\,s^{-1}}$)	σ_{RV}	BIS ($\mathrm{m\,s^{-1}}$)	σ_{BIS}	H-Alpha	$\sigma_{\mathrm{H-Alpha}}$	$\log R'_{\mathrm{HK}}$	$\sigma_{\log R'_{\mathrm{HK}}}$	FWHM	He I	$\sigma_{\mathrm{He\,I}}$	Na II	$\sigma_{\mathrm{Na\,II}}$
TOI-2373													
2458905.55535	-898.0	9.9	1	15	0.1469	0.0047	-4.8448	0.0899	-3	0.4994	0.0102	0.2507	0.0075
2458911.54656	603.9	10.2	-9	15	0.1215	0.0042	-4.9407	0.1573	-8	0.4950	0.0100	0.2507	0.0075
2458913.53698	492.4	11.1	-22	15									
2458917.53471	-800.8	11.1	-22	15	0.1239	0.0046	-4.9716	0.1593	-20	0.5223	0.0112	0.2246	0.0077
2458919.52262	-812.4	13.0	-28	18	0.1473	0.0054	-4.6186	0.1356	-31	0.4980	0.0124	0.2221	0.0092
2458922.52825	-198.7	12.9	-36	18	0.1402	0.0050	-4.6925	0.1965	-38	0.5245	0.0124	0.2123	0.0089
2458927.53614	297.6	10.5	-49	15	0.1249	0.0038	-4.6071	0.1995	-48	0.4944	0.0093	0.2226	0.0066
2458931.50776	-833.7	10.7	-29	15	0.1320	0.0042	-4.7896	0.1572	-29	0.4797	0.0097	0.2439	0.0071
2459188.62842	-359.0	9.4	28	14	0.1368	0.0040	-4.9199	0.0648	27	0.5253	0.0092	0.2607	0.0068
2459190.62923	335.4	8.8	-36	13	0.1290	0.0035	-5.0861	0.0809	-36	0.5046	0.0085	0.2492	0.0061
2459191.61001	667.0	10.1	-06	15	0.1434	0.0047	-5.0645	0.0990	-6	0.5054	0.0102	0.2600	0.0079
2459192.59836	681.3	11.3	-91	16	0.1273	0.0052	-5.0354	0.1301	-83	0.5048	0.0116	0.2423	0.0088
2459207.63706	241.4	9.9	-18	15	0.1283	0.0040	-5.0056	0.0963	-21	0.5201	0.0095	0.2297	0.0069
2459260.58094	440.9	12.6	-1	18	0.1619	0.0060	-	-	-11	0.5083	0.0132	0.2408	0.0098
2459272.56488	687.6	10.7	-06	15	0.1516	0.0050	-5.1569	0.1731	-4	0.5182	0.0110	0.2662	0.0080
2459276.55084	-545.6	11.8	-30	17	0.1437	0.0050	-5.4864	0.6791	-31	0.4872	0.0113	0.2166	0.0082
TOI-2416													
2458920.53485	274.7	11.7	-38	16	0.1318	0.0049	-5.0250	0.2500	-4	0.4995	0.0108	0.2129	0.0079
2458924.51734	-199.3	10.1	4	15	0.1111	0.0039	-4.7267	0.1015	2	0.5152	0.0101	0.1961	0.0066
2458928.50695	170.7	14.7	26	19	0.1159	0.0064	-5.3012	0.7261	26	0.5068	0.0149	0.2122	0.0112
2458929.55344	347.7	13.4	42	18	0.1318	0.0060	-	-	43	0.5034	0.0135	0.2076	0.0099
2459188.60699	-261.9	9.6	2	14	0.1201	0.0035	-5.1144	0.2002	2	0.5148	0.0089	0.2043	0.0059
2459189.62117	-268.3	8.4	-14	13	0.1018	0.0029	-4.9003	0.0747	-14	0.5030	0.0077	0.2131	0.0051
2459190.59374	-192.3	8.2	-3	13	0.1251	0.0033	-5.2681	0.1344	-3	0.4965	0.0080	0.1992	0.0051
2459192.61798	49.7	11.7	0.0	17	0.1260	0.0054	-4.7975	0.0836	-1	0.5009	0.0126	0.2380	0.0090
2459194.62382	278.1	9.6	13	14	0.1168	0.1168	-4.7863	0.0793	13	0.5120	0.0097	0.2110	0.0062
2459207.6163	-187.6	9.5	-22	14	0.1078	0.0035	-5.3027	0.2413	-23	0.5119	0.0090	0.2065	0.0060
2459211.61738	121.7	8.4	-1	13	0.1088	0.0032	-5.0988	0.1003	-1	0.4938	0.0077	0.2006	0.0053
2459213.60256	-240.6	11.7	24	16	0.1132	0.0043	-4.9743	0.1494	25	0.5145	0.0111	0.2095	0.0078
2459260.56028	335.5	13.2	-31	18	0.1584	0.0060	-4.6841	0.1229	-34	0.4982	0.0132	0.1797	0.0094
2459264.52873	-238.8	12.9	-29	18	0.1326	0.0055	-	-	-28	0.4775	0.0125	0.2039	0.0090
2459270.52139	-152.7	9.4	-5	14	0.1139	0.0033	-5.0822	0.1685	-7	0.5005	0.0086	0.2153	0.0057
2459276.51409	269.6	11.6	-26	16	0.1119	0.0044	-4.6902	0.1068	-25	0.4835	0.0108	0.2187	0.0079
2459278.5535	-106.3	11.5	-9	16	0.1217	0.0044	-5.5500	0.9654	-9	0.4950	0.0110	0.2018	0.0073
TOI-2524													
2459209.77377	52.6	11.0	17	14	0.1193	0.0038	-5.0542	0.1871	18	0.5158	0.0091	0.2650	0.0067
2459212.77926	-85.4	9.5	9	13	0.1207	0.0036	-4.9892	0.0982	13	0.5210	0.0085	0.2870	0.0064
2459216.77064	53.8	10.5	19	14	0.1277	0.0046	-5.0112	0.0925	23	0.5050	0.0104	0.2672	0.0077
2459223.86138	49.5	9.9	-2	14	0.1210	0.0036	-4.9228	0.0840	-15	0.5081	0.0086	0.2657	0.0064
2459263.78018	-74.0	12.3	29	15	0.1354	0.0047	-4.8204	0.0888	29	0.4997	0.0104	0.3056	0.0083
2459278.69207	-55.7	11.0	-4.3	14	0.1361	0.0039	-5.2602	0.2095	-42	0.5039	0.0089	0.2918	0.0071
2459280.68823	39.3	9.2	2	13	0.1118	0.0031	-5.1824	0.1390	22	0.5040	0.0083	0.2941	0.0060
2459282.6783	19.6	9.7	-1	13	0.1086	0.0034	-4.9126	0.0715	-6	0.5022	0.0086	0.3096	0.0065

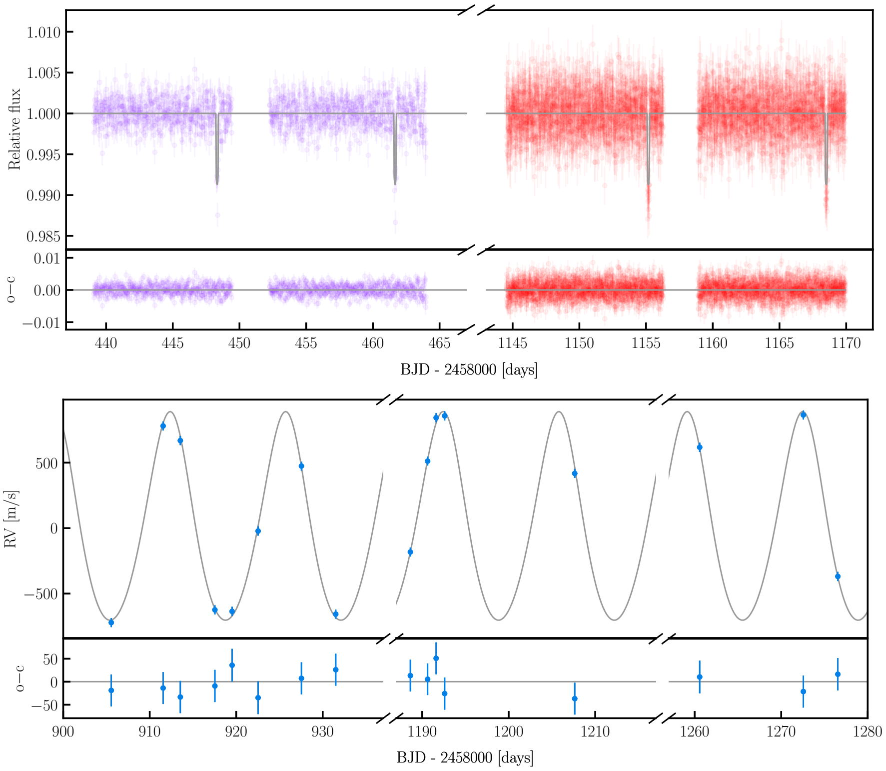

Figure A4: Time series of TOI-2373. *Top*: photometric time series. *Bottom*: RV time series.

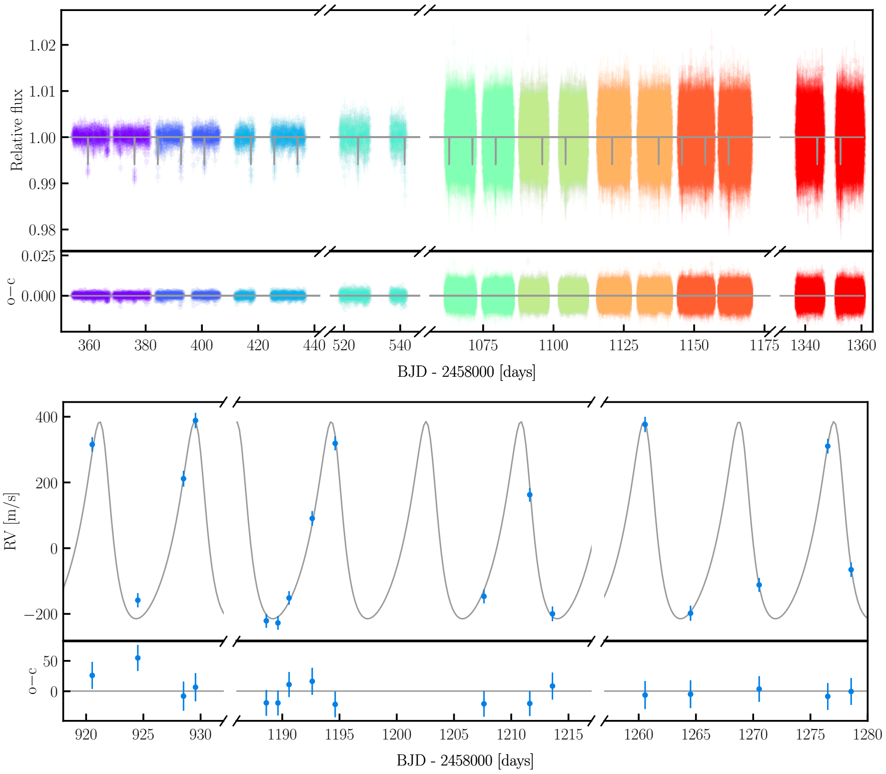

Figure A5: Time series of TOI-2416. *Top*: photometric time series. *Bottom*: RV time series.

Table A2: Results from the NS run for TOI-2373. Listed are likelihood parameters, priors, posteriors and derived parameters for both a circular and eccentric model. $\Delta\ln\mathcal{Z}$ is defined as $\ln\mathcal{Z}_{\mathrm{ecc}}$ - $\ln\mathcal{Z}_{\mathrm{circ}}$. *TESS* sector numbers are denoted as "TX" for transit offset and jitter parameters.

PARAMETER		CIRCULAR MODEL		ECCENTRIC MODEL	
		POSTERIOR	PRIOR	POSTERIOR	PRIOR
$\ln\mathcal{Z}$		24 878.63		24 895.34	
$\Delta\ln\mathcal{Z}$			16.71		
$\mathrm{RV}_{\mathrm{offset}}$	$\mathrm{m\,s^{-1}}$	4632^{+36}_{-36}	$\mathcal{U}(4500.0, 4800.0)$	4596^{+8}_{-8}	$\mathcal{U}(4500.0, 4700.0)$
$\mathrm{RV}_{\mathrm{jitter}}$	$\mathrm{m\,s^{-1}}$	149^{+27}_{-24}	$\mathcal{U}(50.0, 200.0)$	36^{+15}_{-9}	$\mathcal{U}(-20.0, 100.0)$
K	$\mathrm{m\,s^{-1}}$	778^{+47}_{-47}	$\mathcal{U}(600.0, 900.0)$	784^{+10}_{-10}	$\mathcal{U}(650.0, 850.0)$
P	days	$13.33669^{+0.00002}_{-0.00002}$	$\mathcal{U}(13.25, 13.4)$	$13.33668^{+0.00001}_{-0.00001}$	$\mathcal{U}(13.25, 13.4)$
e		0	fixed	$0.112^{+0.007}_{-0.009}$	$\mathcal{U}(0.0, 0.22)$
ω	degrees	–	undefined	15^{+7}_{-6}	$\mathcal{U}(-90.0, 360.0)$
i	degrees	$88.6^{+0.2}_{-0.2}$	$\mathcal{U}(82.0, 92.0)$	$89.2^{+0.6}_{-0.2}$	$\mathcal{U}(85.0, 92.0)$
t_0	days	$2458448.325^{+0.002}_{-0.002}$	$\mathcal{U}(2458448.0, 2458449.0)$	$2458448.326^{+0.001}_{-0.001}$	$\mathcal{U}(2458448.0, 2458449.0)$
$a/R_\star$		$21.9^{+0.8}_{-0.8}$	$\mathcal{U}(0.0, 30.0)$	$23.1^{+0.6}_{-0.5}$	$\mathcal{U}(0.0, 30.0)$
$r/R_\star$		$0.0897^{+0.0009}_{-0.0010}$	$\mathcal{U}(0.0, 0.15)$	$0.0867^{+0.0009}_{-0.0009}$	$\mathcal{U}(0.0, 0.15)$
$\mathrm{transit}_{\mathrm{offset,T5}}$		$0.00014^{+0.00004}_{-0.00004}$	$\mathcal{U}(-0.001, 0.001)$	$0.00012^{+0.00003}_{-0.00003}$	$\mathcal{U}(-0.001, 0.001)$
$\mathrm{transit}_{\mathrm{offset,T31}}$		$0.00031^{+0.00004}_{-0.00004}$	$\mathcal{U}(-0.001, 0.001)$	$0.00031^{+0.00002}_{-0.00003}$	$\mathcal{U}(-0.001, 0.001)$
$\mathrm{transit}_{\mathrm{offset,LCO-SAAO}}$		$0.0000^{+0.0001}_{-0.0001}$	$\mathcal{U}(-0.001, 0.001)$	$0.00006^{+0.00009}_{-0.00008}$	$\mathcal{U}(-0.001, 0.001)$
$\mathrm{transit}_{\mathrm{offset,LCO-Teid}}$		$0.00121^{+0.00008}_{-0.00008}$	$\mathcal{U}(-0.001, 0.001)$	$0.00131^{+0.00006}_{-0.00005}$	$\mathcal{U}(-0.001, 0.001)$
$\mathrm{transit}_{\mathrm{offset,LCO-CTIO1}}$		$0.00007^{+0.00010}_{-0.00010}$	$\mathcal{U}(-0.001, 0.001)$	$-0.00005^{+0.00007}_{-0.00007}$	$\mathcal{U}(-0.001, 0.001)$
$\mathrm{transit}_{\mathrm{offset,LCO-CTIO2}}$		$0.00026^{+0.00010}_{-0.00010}$	$\mathcal{U}(-0.001, 0.001)$	$0.00027^{+0.00008}_{-0.00008}$	$\mathcal{U}(-0.001, 0.001)$
$\mathrm{transit}_{\mathrm{offset,OM-ES}}$		$-0.0002^{+0.0001}_{-0.0001}$	$\mathcal{U}(-0.001, 0.001)$	$-0.00014^{+0.00009}_{-0.00012}$	$\mathcal{U}(-0.001, 0.001)$
$\mathrm{transit}_{\mathrm{jitter,T5}}$		$0.000994^{+0.000005}_{-0.000009}$	$\mathcal{U}(-0.01, 0.01)$	$0.000988^{+0.000007}_{-0.000008}$	$\mathcal{U}(-0.01, 0.01)$
$\mathrm{transit}_{\mathrm{jitter,T31}}$		$0.000993^{+0.000005}_{-0.000010}$	$\mathcal{U}(-0.01, 0.01)$	$0.000987^{+0.000009}_{-0.000015}$	$\mathcal{U}(-0.01, 0.01)$
$\mathrm{transit}_{\mathrm{jitter,LCO-SAAO}}$		$0.000993^{+0.000005}_{-0.000010}$	$\mathcal{U}(-0.01, 0.01)$	$0.00097^{+0.00002}_{-0.00002}$	$\mathcal{U}(-0.01, 0.01)$
$\mathrm{transit}_{\mathrm{jitter,LCO-Teid}}$		$0.0009989^{+0.0000008}_{-0.0000015}$	$\mathcal{U}(-0.01, 0.01)$	$0.000996^{+0.000002}_{-0.000003}$	$\mathcal{U}(-0.01, 0.01)$
$\mathrm{transit}_{\mathrm{jitter,LCO-CTIO1}}$		$0.000995^{+0.000003}_{-0.000007}$	$\mathcal{U}(-0.01, 0.01)$	$0.000990^{+0.000006}_{-0.000008}$	$\mathcal{U}(-0.01, 0.01)$
$\mathrm{transit}_{\mathrm{jitter,LCO-CTIO2}}$		$0.000996^{+0.000003}_{-0.000006}$	$\mathcal{U}(-0.01, 0.01)$	$0.000990^{+0.000006}_{-0.000010}$	$\mathcal{U}(-0.01, 0.01)$
$\mathrm{transit}_{\mathrm{jitter,OM-ES}}$		$0.0009^{+0.0001}_{-0.0003}$	$\mathcal{U}(-0.01, 0.01)$	$0.00007^{+0.00054}_{-0.00005}$	$\mathcal{U}(-0.01, 0.01)$
$u_{1,\mathrm{TESS}}$		$0.2^{+0.2}_{-0.1}$	$\mathcal{U}(0.0, 1.0)$	$0.2^{+0.1}_{-0.1}$	$\mathcal{U}(0.0, 1.0)$
$u_{2,\mathrm{TESS}}$		$0.3^{+0.2}_{-0.2}$	$\mathcal{U}(0.0, 1.0)$	$0.5^{+0.2}_{-0.2}$	$\mathcal{U}(0.0, 1.0)$
$u_{1,\mathrm{LCO-SAAO}}$		$0.2^{+0.1}_{-0.1}$	$\mathcal{U}(0.0, 1.0)$	$0.31^{+0.07}_{-0.09}$	$\mathcal{U}(0.0, 1.0)$
$u_{2,\mathrm{LCO-SAAO}}$		$0.3^{+0.2}_{-0.2}$	$\mathcal{U}(0.0, 1.0)$	$0.3^{+0.2}_{-0.1}$	$\mathcal{U}(0.0, 1.0)$
$u_{1,\mathrm{LCO-Teid}}$		$0.2^{+0.1}_{-0.1}$	$\mathcal{U}(0.0, 1.0)$	$0.28^{+0.06}_{-0.07}$	$\mathcal{U}(0.0, 1.0)$
$u_{2,\mathrm{LCO-Teid}}$		$0.3^{+0.2}_{-0.2}$	$\mathcal{U}(0.0, 1.0)$	$0.3^{+0.1}_{-0.1}$	$\mathcal{U}(0.0, 1.0)$
$u_{1,\mathrm{LCO-CTIO}}$		$0.5^{+0.1}_{-0.2}$	$\mathcal{U}(0.0, 1.0)$	$0.55^{+0.07}_{-0.08}$	$\mathcal{U}(0.0, 1.0)$
$u_{2,\mathrm{LCO-CTIO}}$		$0.3^{+0.2}_{-0.2}$	$\mathcal{U}(0.0, 1.0)$	$0.3^{+0.1}_{-0.1}$	$\mathcal{U}(0.0, 1.0)$
$u_{1,\mathrm{OM-ES}}$		$0.5^{+0.2}_{-0.2}$	$\mathcal{U}(0.0, 1.0)$	$0.2^{+0.2}_{-0.1}$	$\mathcal{U}(0.0, 1.0)$
$u_{2,\mathrm{OM-ES}}$		$0.2^{+0.3}_{-0.2}$	$\mathcal{U}(0.0, 1.0)$	$0.4^{+0.2}_{-0.2}$	$\mathcal{U}(0.0, 1.0)$
m	M_{jup}	$9.3^{+0.6}_{-0.6}$		$9.3^{+0.2}_{-0.2}$	
r	R_{jup}	$0.96^{+0.02}_{-0.02}$		$0.93^{+0.02}_{-0.02}$	
a	au	$0.112^{+0.001}_{-0.001}$		$0.112^{+0.001}_{-0.001}$	
ρ	$\mathrm{g\,cm^{-3}}$	13^{+1}_{-1}		$14.4^{+0.9}_{-1.0}$	
T_{eq}	K	860^{+10}_{-10}		860^{+10}_{-10}	

Table A3: Results from the NS run for TOI-2416. Listed are likelihood parameters, priors, posteriors and derived parameters for both a circular and eccentric model. $\Delta\ln\mathcal{Z}$ is defined as $\ln\mathcal{Z}_{\mathrm{ecc}}$ - $\ln\mathcal{Z}_{\mathrm{circ}}$. *TESS* sector numbers are denoted as "TX" for transit offset and jitter parameters.

PARAMETER		CIRCULAR MODEL		ECCENTRIC MODEL	
		POSTERIOR	PRIOR	POSTERIOR	PRIOR
$\ln\mathcal{Z}$		326,957.01		326,984.85	
$\Delta\ln\mathcal{Z}$			27.84		
$\mathrm{RV}_{\mathrm{offset}}$	$\mathrm{m\,s^{-1}}$	22190^{+18}_{-17}	$\mathcal{U}(22100.0, 22250.0)$	22145^{+6}_{-6}	$\mathcal{U}(22100.0, 22250.0)$
$\mathrm{RV}_{\mathrm{jitter}}$	$\mathrm{m\,s^{-1}}$	99^{+9}_{-9}	$\mathcal{U}(0.0, 120.0)$	21^{+7}_{-5}	$\mathcal{U}(-20.0, 100.0)$
K	$\mathrm{m\,s^{-1}}$	285^{+27}_{-27}	$\mathcal{U}(150.0, 400.0)$	296^{+8}_{-8}	$\mathcal{U}(150.0, 400.0)$
P	days	$8.275478^{+0.000010}_{-0.000010}$	$\mathcal{U}(8.24, 8.3)$	$8.275479^{+0.000009}_{-0.000009}$	$\mathcal{U}(8.24, 8.3)$
e		0	fixed	$0.32^{+0.02}_{-0.02}$	$\mathcal{U}(0.0, 0.5)$
ω	degrees	–	undefined	30^{+5}_{-5}	$\mathcal{U}(-90.0, 360.0)$
i	degrees	$89.8^{+0.2}_{-0.3}$	$\mathcal{U}(80.0, 90.0)$	$90.0^{+0.6}_{-0.6}$	$\mathcal{U}(80.0, 92.0)$
t_0	days	$2458359.4885^{+0.0010}_{-0.0008}$	$\mathcal{U}(2458359.0, 2458360.0)$	$2458359.4884^{+0.0009}_{-0.0009}$	$\mathcal{U}(2458359.0, 2458360.0)$
$a/R_{\star}$		$17.5^{+0.1}_{-0.2}$	$\mathcal{U}(0.0, 45.0)$	$14.4^{+0.4}_{-0.5}$	$\mathcal{U}(0.0, 45.0)$
$r/R_{\star}$		$0.0734^{+0.0007}_{-0.0007}$	$\mathcal{U}(0.0, 0.25)$	$0.0732^{+0.0008}_{-0.0008}$	$\mathcal{U}(0.0, 0.25)$
$\mathrm{transit}_{\mathrm{offset,T2}}$		$0.00025^{+0.00003}_{-0.00003}$	$\mathcal{U}(-0.001, 0.001)$	$0.00023^{+0.00003}_{-0.00003}$	$\mathcal{U}(-0.001, 0.001)$
$\mathrm{transit}_{\mathrm{offset,T3}}$		$0.00027^{+0.00004}_{-0.00004}$	$\mathcal{U}(-0.001, 0.001)$	$0.00026^{+0.00005}_{-0.00004}$	$\mathcal{U}(-0.001, 0.001)$
$\mathrm{transit}_{\mathrm{offset,T4}}$		$0.00025^{+0.00004}_{-0.00004}$	$\mathcal{U}(-0.001, 0.001)$	$0.00026^{+0.00004}_{-0.00005}$	$\mathcal{U}(-0.001, 0.001)$
$\mathrm{transit}_{\mathrm{offset,T8}}$		$0.00030^{+0.00008}_{-0.00007}$	$\mathcal{U}(-0.001, 0.001)$	$0.00030^{+0.00007}_{-0.00007}$	$\mathcal{U}(-0.001, 0.001)$
$\mathrm{transit}_{\mathrm{offset,T28}}$		$0.00029^{+0.00003}_{-0.00003}$	$\mathcal{U}(-0.001, 0.001)$	$0.00030^{+0.00003}_{-0.00003}$	$\mathcal{U}(-0.001, 0.001)$
$\mathrm{transit}_{\mathrm{offset,T29}}$		$0.00028^{+0.00003}_{-0.00003}$	$\mathcal{U}(-0.001, 0.001)$	$0.00027^{+0.00003}_{-0.00003}$	$\mathcal{U}(-0.001, 0.001)$
$\mathrm{transit}_{\mathrm{offset,T30}}$		$0.00030^{+0.00003}_{-0.00003}$	$\mathcal{U}(-0.001, 0.001)$	$0.00030^{+0.00003}_{-0.00003}$	$\mathcal{U}(-0.001, 0.001)$
$\mathrm{transit}_{\mathrm{offset,T31}}$		$0.00032^{+0.00003}_{-0.00003}$	$\mathcal{U}(-0.001, 0.001)$	$0.00033^{+0.00003}_{-0.00003}$	$\mathcal{U}(-0.001, 0.001)$
$\mathrm{transit}_{\mathrm{offset,T38}}$		$0.00030^{+0.00003}_{-0.00003}$	$\mathcal{U}(-0.001, 0.001)$	$0.00031^{+0.00003}_{-0.00003}$	$\mathcal{U}(-0.001, 0.001)$
$\mathrm{transit}_{\mathrm{offset,ASTEP}}$		$0.0011^{+0.0002}_{-0.0002}$	$\mathcal{U}(-0.001, 0.001)$	$0.0011^{+0.0002}_{-0.0003}$	$\mathcal{U}(-0.001, 0.001)$
$\mathrm{transit}_{\mathrm{offset,CDK24ND}}$		$0.0020^{+0.0002}_{-0.0003}$	$\mathcal{U}(-0.001, 0.001)$	$0.0020^{+0.0002}_{-0.0002}$	$\mathcal{U}(-0.001, 0.001)$
$\mathrm{transit}_{\mathrm{offset,OM-SSO}}$		$-0.0034^{+0.0002}_{-0.0002}$	$\mathcal{U}(-0.001, 0.001)$	$-0.0034^{+0.0002}_{-0.0002}$	$\mathcal{U}(-0.001, 0.001)$
$\mathrm{transit}_{\mathrm{jitter,T2}}$		$-0.00088^{+0.00004}_{-0.00004}$	$\mathcal{U}(-0.01, 0.01)$	$-0.00086^{+0.00174}_{-0.00006}$	$\mathcal{U}(-0.01, 0.01)$
$\mathrm{transit}_{\mathrm{jitter,T3}}$		$-0.00097^{+0.00194}_{-0.00006}$	$\mathcal{U}(-0.01, 0.01)$	$-0.00098^{+0.00004}_{-0.00004}$	$\mathcal{U}(-0.01, 0.01)$
$\mathrm{transit}_{\mathrm{jitter,T4}}$		$0.00109^{+0.00006}_{-0.00217}$	$\mathcal{U}(-0.01, 0.01)$	$0.00112^{+0.00004}_{-0.00004}$	$\mathcal{U}(-0.01, 0.01)$
$\mathrm{transit}_{\mathrm{jitter,T8}}$		$-0.0002^{+0.0009}_{-0.0005}$	$\mathcal{U}(-0.01, 0.01)$	$-0.0003^{+0.0009}_{-0.0005}$	$\mathcal{U}(-0.01, 0.01)$
$\mathrm{transit}_{\mathrm{jitter,T28}}$		$0.00000^{+0.00007}_{-0.00007}$	$\mathcal{U}(-0.01, 0.01)$	$0.00001^{+0.00010}_{-0.00009}$	$\mathcal{U}(-0.01, 0.01)$
$\mathrm{transit}_{\mathrm{jitter,T29}}$		$-0.00001^{+0.00009}_{-0.00008}$	$\mathcal{U}(-0.01, 0.01)$	$-0.00000^{+0.00010}_{-0.00010}$	$\mathcal{U}(-0.01, 0.01)$
$\mathrm{transit}_{\mathrm{jitter,T30}}$		$-0.00000^{+0.00009}_{-0.00009}$	$\mathcal{U}(-0.01, 0.01)$	$0.00000^{+0.00009}_{-0.00010}$	$\mathcal{U}(-0.01, 0.01)$
$\mathrm{transit}_{\mathrm{jitter,T31}}$		$-0.00002^{+0.00010}_{-0.00009}$	$\mathcal{U}(-0.01, 0.01)$	$-0.0000^{+0.0001}_{-0.0001}$	$\mathcal{U}(-0.01, 0.01)$
$\mathrm{transit}_{\mathrm{jitter,T38}}$		$0.00005^{+0.00009}_{-0.00008}$	$\mathcal{U}(-0.01, 0.01)$	$0.00001^{+0.00009}_{-0.00009}$	$\mathcal{U}(-0.01, 0.01)$
$\mathrm{transit}_{\mathrm{jitter,ASTEP}}$		$-0.0018^{+0.0003}_{-0.0003}$	$\mathcal{U}(-0.01, 0.01)$	$0.0018^{+0.0002}_{-0.0002}$	$\mathcal{U}(-0.01, 0.01)$
$\mathrm{transit}_{\mathrm{jitter,CDK24ND}}$		$0.0022^{+0.0002}_{-0.0002}$	$\mathcal{U}(-0.01, 0.01)$	$0.0022^{+0.0002}_{-0.0002}$	$\mathcal{U}(-0.01, 0.01)$
$\mathrm{transit}_{\mathrm{jitter,OM-SSO}}$		$0.0030^{+0.0002}_{-0.0059}$	$\mathcal{U}(-0.01, 0.01)$	$-0.0030^{+0.0002}_{-0.0002}$	$\mathcal{U}(-0.01, 0.01)$
$u_{1,\mathrm{TESS}}$		$0.2^{+0.1}_{-0.1}$	$\mathcal{U}(0.0, 1.0)$	$0.27^{+0.10}_{-0.12}$	$\mathcal{U}(0.0, 1.0)$
$u_{2,\mathrm{TESS}}$		$0.2^{+0.2}_{-0.1}$	$\mathcal{U}(0.0, 1.0)$	$0.1^{+0.2}_{-0.1}$	$\mathcal{U}(0.0, 1.0)$
$u_{1,\mathrm{ASTEP}}$		$0.4^{+0.1}_{-0.2}$	$\mathcal{U}(0.0, 1.0)$	$0.4^{+0.2}_{-0.2}$	$\mathcal{U}(0.0, 1.0)$
$u_{2,\mathrm{ASTEP}}$		$0.6^{+0.2}_{-0.2}$	$\mathcal{U}(0.0, 1.0)$	$0.6^{+0.3}_{-0.4}$	$\mathcal{U}(0.0, 1.0)$
$u_{1,\mathrm{CDK24ND}}$		$0.6^{+0.2}_{-0.2}$	$\mathcal{U}(0.0, 1.0)$	$0.6^{+0.2}_{-0.2}$	$\mathcal{U}(0.0, 1.0)$
$u_{2,\mathrm{CDK24ND}}$		$0.6^{+0.2}_{-0.2}$	$\mathcal{U}(0.0, 1.0)$	$0.6^{+0.3}_{-0.3}$	$\mathcal{U}(0.0, 1.0)$
$u_{1,\mathrm{OM-SSO}}$		$0.2^{+0.2}_{-0.1}$	$\mathcal{U}(0.0, 1.0)$	$0.14^{+0.14}_{-0.10}$	$\mathcal{U}(0.0, 1.0)$
$u_{2,\mathrm{OM-SSO}}$		$0.3^{+0.2}_{-0.2}$	$\mathcal{U}(0.0, 1.0)$	$0.4^{+0.3}_{-0.2}$	$\mathcal{U}(0.0, 1.0)$
m	M_{jup}	$3.1^{+0.3}_{-0.3}$		$3.00^{+0.10}_{-0.09}$	
r	R_{jup}	$0.88^{+0.02}_{-0.02}$		$0.88^{+0.02}_{-0.02}$	
a	au	$0.0831^{+0.0007}_{-0.0007}$		$0.0831^{+0.0007}_{-0.0007}$	
ρ	$\mathrm{g\,cm^{-3}}$	$5.5^{+0.6}_{-0.6}$		$5.4^{+0.3}_{-0.4}$	
T_{eq}	K	1080^{+10}_{-10}		1080^{+10}_{-10}	

Table A4: Results from the NS run for TOI-2524. Listed are likelihood parameters, priors, posteriors and derived parameters for both a circular and eccentric model. $\Delta\ln\mathcal{Z}$ is defined as $\ln\mathcal{Z}_{\mathrm{ecc}}$ - $\ln\mathcal{Z}_{\mathrm{circ}}$. *TESS* sector numbers are denoted as "TX" for transit offset and jitter parameters.

Parameter		Circular Model		Eccentric Model	
		Posterior	Prior	Posterior	Prior
$\ln\mathcal{Z}$		148,587.37		148,585.14	
$\Delta\ln\mathcal{Z}$		-2.23			
$\mathrm{RV}_{\mathrm{offset}}$	$\mathrm{m\,s^{-1}}$	9434^{+3}_{-3}	$\mathcal{U}(9400.0, 9450.0)$	9436^{+6}_{-4}	$\mathcal{U}(9400.0, 9450.0)$
$\mathrm{RV}_{\mathrm{jitter}}$	$\mathrm{m\,s^{-1}}$	-0^{+5}_{-5}	$\mathcal{U}(-10.0, 30.0)$	8^{+7}_{-4}	$\mathcal{U}(-10.0, 30.0)$
K	$\mathrm{m\,s^{-1}}$	67^{+4}_{-4}	$\mathcal{U}(45.0, 90.0)$	67^{+4}_{-6}	$\mathcal{U}(45.0, 90.0)$
P	days	$7.18585^{+0.00001}_{-0.00001}$	$\mathcal{U}(7.185, 7.187)$	$7.18585^{+0.00002}_{-0.00003}$	$\mathcal{U}(7.185, 7.187)$
e		0	fixed	$0.06^{+0.03}_{-0.03}$	$\mathcal{U}(0.0, 0.5)$
ω	degrees	–	undefined	101^{+130}_{-92}	$\mathcal{U}(-90.0, 360.0)$
i	degrees	$89.4^{+0.4}_{-0.4}$	$\mathcal{U}(85.0, 92.0)$	$90.2^{+0.4}_{-0.5}$	$\mathcal{U}(85.0, 92.0)$
t_0	days	$2458550.155^{+0.002}_{-0.001}$	$\mathcal{U}(2458550.0, 2458550.3)$	$2458550.156^{+0.003}_{-0.002}$	$\mathcal{U}(2458550.0, 2458550.3)$
$a/R_\star$		$14.3^{+0.2}_{-0.3}$	$\mathcal{U}(5.0, 30.0)$	$14.5^{+0.9}_{-0.4}$	$\mathcal{U}(5.0, 30.0)$
$r/R_\star$		$0.092^{+0.001}_{-0.001}$	$\mathcal{U}(0.0, 0.15)$	$0.0928^{+0.0011}_{-0.0007}$	$\mathcal{U}(0.0, 0.15)$
$\mathrm{transit}_{\mathrm{offset,T9}}$		$0.00022^{+0.00006}_{-0.00006}$	$\mathcal{U}(-0.001, 0.001)$	$0.00021^{+0.00006}_{-0.00005}$	$\mathcal{U}(-0.001, 0.001)$
$\mathrm{transit}_{\mathrm{offset,T35}}$		$0.00044^{+0.00004}_{-0.00005}$	$\mathcal{U}(-0.001, 0.001)$	$0.00042^{+0.00004}_{-0.00005}$	$\mathcal{U}(-0.001, 0.001)$
$\mathrm{transit}_{\mathrm{offset,T45}}$		$0.00030^{+0.00003}_{-0.00003}$	$\mathcal{U}(-0.001, 0.001)$	$0.00028^{+0.00002}_{-0.00002}$	$\mathcal{U}(-0.001, 0.001)$
$\mathrm{transit}_{\mathrm{offset,T46}}$		$0.00030^{+0.00003}_{-0.00002}$	$\mathcal{U}(-0.001, 0.001)$	$0.00029^{+0.00003}_{-0.00002}$	$\mathcal{U}(-0.001, 0.001)$
$\mathrm{transit}_{\mathrm{offset,El-Sauce}}$		$0.0008^{+0.0003}_{-0.0004}$	$\mathcal{U}(-0.001, 0.001)$	$0.0011^{+0.0003}_{-0.0002}$	$\mathcal{U}(-0.001, 0.001)$
$\mathrm{transit}_{\mathrm{offset,OM-ES}}$		$0.0014^{+0.0002}_{-0.0002}$	$\mathcal{U}(-0.001, 0.001)$	$0.0014^{+0.0002}_{-0.0002}$	$\mathcal{U}(-0.001, 0.001)$
$\mathrm{transit}_{\mathrm{jitter,T9}}$		$-0.00131^{+0.00006}_{-0.00006}$	$\mathcal{U}(-0.02, 0.02)$	$-0.00130^{+0.00007}_{-0.00006}$	$\mathcal{U}(-0.02, 0.02)$
$\mathrm{transit}_{\mathrm{jitter,T35}}$		$0.00254^{+0.00008}_{-0.00512}$	$\mathcal{U}(-0.02, 0.02)$	$-0.0025^{+0.0051}_{-0.0001}$	$\mathcal{U}(-0.02, 0.02)$
$\mathrm{transit}_{\mathrm{jitter,T45}}$		$0.00002^{+0.00010}_{-0.00009}$	$\mathcal{U}(-0.02, 0.02)$	$0.0000^{+0.0001}_{-0.0001}$	$\mathcal{U}(-0.02, 0.02)$
$\mathrm{transit}_{\mathrm{jitter,T46}}$		$0.0000^{+0.0001}_{-0.0002}$	$\mathcal{U}(-0.02, 0.02)$	$0.00002^{+0.00008}_{-0.00011}$	$\mathcal{U}(-0.02, 0.02)$
$\mathrm{transit}_{\mathrm{jitter,El-Sauce}}$		$0.0037^{+0.0004}_{-0.0077}$	$\mathcal{U}(-0.02, 0.02)$	$0.0038^{+0.0002}_{-0.0002}$	$\mathcal{U}(-0.02, 0.02)$
$\mathrm{transit}_{\mathrm{jitter,OM-ES}}$		$0.0019^{+0.0003}_{-0.0039}$	$\mathcal{U}(-0.02, 0.02)$	$0.0020^{+0.0003}_{-0.0004}$	$\mathcal{U}(-0.02, 0.02)$
$u_{1,\mathrm{TESS}}$		$0.13^{+0.08}_{-0.08}$	$\mathcal{U}(0.0, 1.0)$	$0.15^{+0.09}_{-0.07}$	$\mathcal{U}(0.0, 1.0)$
$u_{2,\mathrm{TESS}}$		$0.5^{+0.2}_{-0.2}$	$\mathcal{U}(0.0, 1.0)$	$0.31^{+0.08}_{-0.08}$	$\mathcal{U}(0.0, 1.0)$
$u_{1,\mathrm{El-Sauce}}$		$0.5^{+0.1}_{-0.1}$	$\mathcal{U}(0.0, 1.0)$	$0.44^{+0.10}_{-0.10}$	$\mathcal{U}(0.0, 1.0)$
$u_{2,\mathrm{El-Sauce}}$		$0.6^{+0.3}_{-0.3}$	$\mathcal{U}(0.0, 1.0)$	$0.5^{+0.2}_{-0.2}$	$\mathcal{U}(0.0, 1.0)$
$u_{1,\mathrm{OM-ES}}$		$0.5^{+0.1}_{-0.1}$	$\mathcal{U}(0.0, 1.0)$	$0.6^{+0.2}_{-0.2}$	$\mathcal{U}(0.0, 1.0)$
$u_{2,\mathrm{OM-ES}}$		$0.7^{+0.2}_{-0.2}$	$\mathcal{U}(0.0, 1.0)$	$0.5^{+0.2}_{-0.2}$	$\mathcal{U}(0.0, 1.0)$
m	M_{jup}	$0.64^{+0.04}_{-0.04}$		$0.64^{+0.06}_{-0.04}$	
r	R_{jup}	$1.00^{+0.03}_{-0.03}$		$1.01^{+0.02}_{-0.02}$	
a	au	$0.0730^{+0.0007}_{-0.0007}$		$0.0730^{+0.0007}_{-0.0007}$	
ρ	$\mathrm{g\,cm^{-3}}$	$0.79^{+0.08}_{-0.09}$		$0.76^{+0.08}_{-0.08}$	
T_{eq}	K	1100^{+20}_{-20}		1100^{+20}_{-20}	

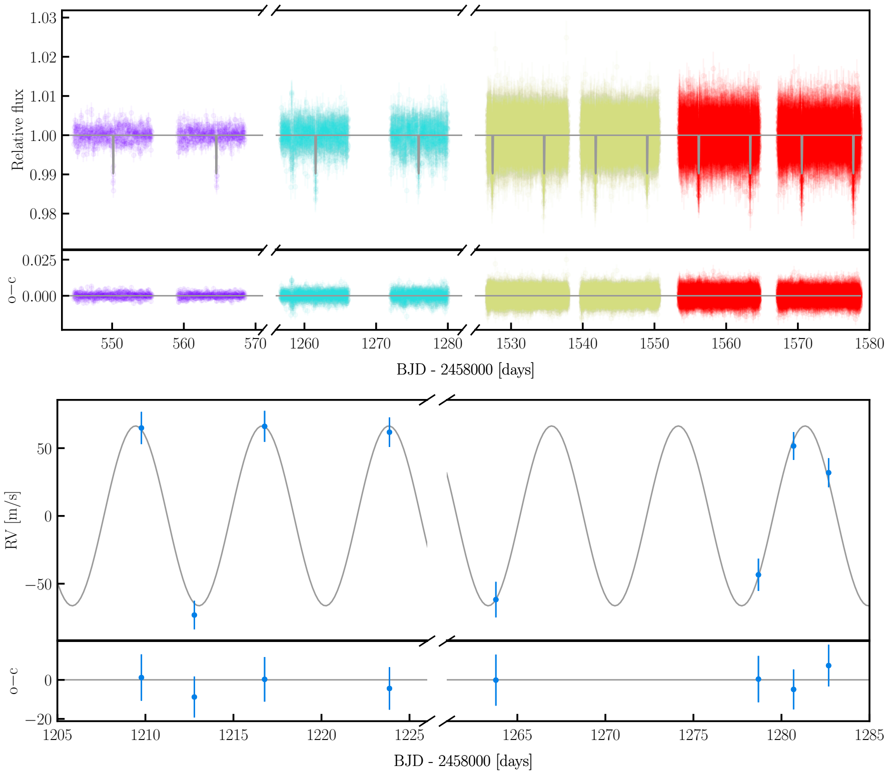

Figure A6: Time series of TOI-2524. *Top*: photometric time series. *Bottom*: RV time series.

B

APPENDIX FOR CHAPTER 4

In this appendix, we present an additional figure and additional tables. Figure B1 shows a comparison between the transit of TOI-6695 b in *TESS* sector 8 with the tesseract pipeline, Quick Look Pipeline and the Tess-Gaia-Light-Curve pipeline. Table B1 is a continuation of Table 4.2 and lists the relevant offset and jitter parameters for both the spectroscopic radial velocities and the photometric transit light curves. It also lists the quadratic limb-darkening coefficients for both the *TESS* and OMES light curves.

Table B2 to Table B6 list the radial velocity and stellar activity measurements for FEROS, HARPS, CHIRON, CORALIE and PFS, along with their 1σ uncertainties.

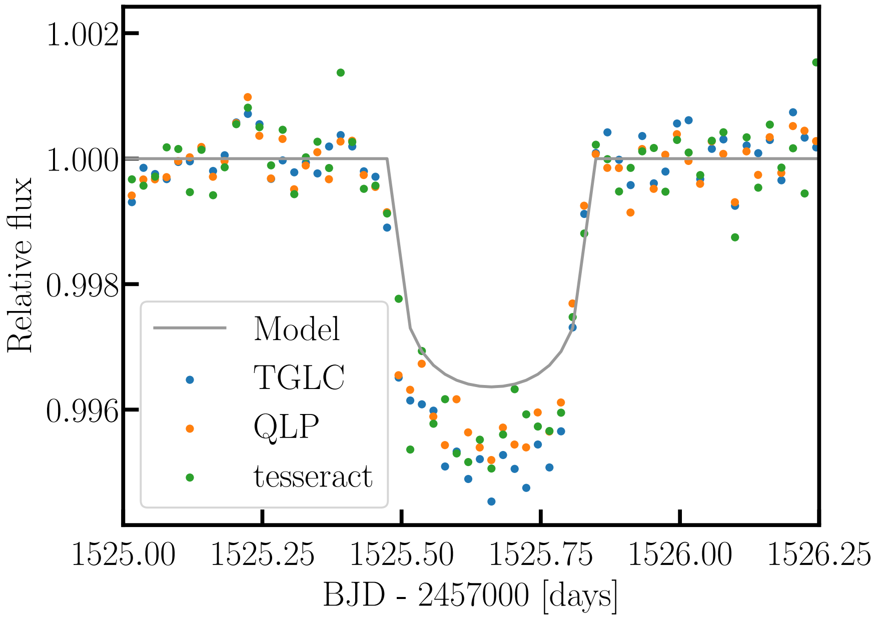

Figure B1: Transit of TOI-6695 b in *TESS* sector 8 with the TGLC pipeline (`blue`), the QLP pipeline (`orange`) and the tesseract pipeline (`green`).

Table B1: Results from the nested sampling run for TOI-6695. Listed are priors and posteriors for the RV and transit offsets and jitter parameters, as well as the quadratic limb-darkening coefficients.

	Median and $1-\sigma$		Max. $-\ln\mathcal{L}$		Adopted priors	
parameter	planet b	planet c	planet b	planet c	planet b	planet c
$RV_{off.}$ HARPS [$m\,s^{-1}$]	…	$-33.4^{+0.6}_{-0.7}$	…	-33.4	…	$\mathcal{U}(-45, -15)$
$RV_{off.}$ CHIRON [$m\,s^{-1}$]	…	21498^{+2}_{-2}	…	21494	…	$\mathcal{U}(21470, 21530)$
$RV_{off.}$ PFS [$m\,s^{-1}$]	…	-4^{+1}_{-1}	…	-3	…	$\mathcal{U}(-20, 20)$
$RV_{off.}$ CORALIE [$m\,s^{-1}$]	…	135^{+2}_{-2}	…	134	…	$\mathcal{U}(100, 170)$
$RV_{jitt.}$ HARPS [$m\,s^{-1}$]	…	$5.9^{+0.4}_{-0.4}$	…	5.1	…	$\mathcal{U}(0.1, 20)$
$RV_{jitt.}$ CHIRON [$m\,s^{-1}$]	…	$4.5^{+0.7}_{-0.7}$	…	3.8	…	$\mathcal{U}(0.1, 20)$
$RV_{jitt.}$ PFS [$m\,s^{-1}$]	…	$5.0^{+0.6}_{-0.7}$	…	4.5	…	$\mathcal{U}(0.1, 20)$
$RV_{jitt.}$ CORALIE [$m\,s^{-1}$]	…	$2.6^{+0.5}_{-0.6}$	…	2.6	…	$\mathcal{U}(0.1, 20)$
$transit_{off.}$ T8	…	$0.00005^{+0.00002}_{-0.00002}$	…	0.00003	…	$\mathcal{U}(-0.001, 0.001)$
$transit_{off.}$ T34	…	$0.000094^{+0.000008}_{-0.000008}$	…	0.000097	…	$\mathcal{U}(-0.001, 0.001)$
$transit_{off.}$ T35	…	$0.000111^{+0.000007}_{-0.000007}$	…	0.000110	…	$\mathcal{U}(-0.001, 0.001)$
$transit_{off.}$ T61	…	$0.000090^{+0.000007}_{-0.000006}$	…	0.000092	…	$\mathcal{U}(-0.001, 0.001)$
$transit_{off.}$ OM-ES 1	…	$0.0010^{+0.0001}_{-0.0001}$	…	0.00098	…	$\mathcal{U}(-0.001, 0.001)$
$transit_{off.}$ OM-ES 2	…	$0.0008^{+0.0001}_{-0.0001}$	…	-0.0008	…	$\mathcal{U}(-1, 2)$
$transit_{jitt.}$ T8	…	$0.00030^{+0.00002}_{-0.00002}$	…	0.00028	…	$\mathcal{U}(0, 0.001)$
$transit_{jitt.}$ T34	…	$0.00017^{+0.00003}_{-0.00002}$	…	0.00011	…	$\mathcal{U}(0, 0.001)$
$transit_{jitt.}$ T35	…	$0.00017^{+0.00002}_{-0.00002}$	…	0.00017	…	$\mathcal{U}(0, 0.001)$
$transit_{jitt.}$ T61	…	$0.00017^{+0.00004}_{-0.00003}$	…	0.00015	…	$\mathcal{U}(0, 0.001)$
$transit_{jitt.}$ OM-ES 1	…	$0.0022^{+0.0002}_{-0.0002}$	…	0.0020	…	$\mathcal{U}(0, 0.003)$
$transit_{jitt.}$ OM-ES 2	…	$0.0001^{+0.0002}_{-0.0002}$	…	0.00008	…	$\mathcal{U}(-0.2, 0.2)$
u_1 *TESS*	…	$0.41^{+0.03}_{-0.04}$	…	0.31	…	$\mathcal{U}(0, 1)$
u_2 *TESS*	…	$0.39^{+0.11}_{-0.07}$	…	0.36	…	$\mathcal{U}(0, 1)$
u_1 OM-ES	…	$0.4^{+0.1}_{-0.1}$	…	0.3	…	$\mathcal{U}(0, 1)$
u_2 OM-ES	…	$0.26^{+0.06}_{-0.07}$	…	0.22	…	$\mathcal{U}(0, 1)$

The orbital elements are in the Jacobi frame and are valid for epoch BJD = 2458400.0. The adopted priors are listed in the right-most columns and their meanings are $\mathcal{U}$ – Uniform.

Table B2: FEROS radial velocity and bisector measurements, along with their $1-\sigma$ uncertainties.

BJD	RV ($m\,s^{-1}$)	σ_{RV}	BIS ($m\,s^{-1}$)	σ_{BIS}	H-Alpha	$\sigma_{H-Alpha}$	Ca II	$\sigma_{Ca\,II}$	S_MW	σ_{S_MW}	log RHK	$\sigma_{\log RHK}$	Na II	$\sigma_{Na\,II}$	He I	$\sigma_{He\,I}$
2458909.692	209.3	13.2	30.0	12.0	0.117	0.003	0.116	0.009	0.144	0.011	-5.08	0.09	0.368	0.006	0.497	0.007
2458913.750	184.3	15.1	65.0	13.0	0.124	0.004	0.132	0.014	0.162	0.016	-4.95	0.10	0.380	0.007	0.500	0.008
2458917.775	130.3	11.5	-40.0	11.0	–	–	–	–	–	–	–	–	–	–	–	–
2458918.566	67.4	13.2	8.0	12.0	0.106	0.003	0.125	0.008	0.154	0.010	-5.00	0.07	0.362	0.006	0.494	0.007
2459188.770	158.8	9.3	33.0	10.0	0.101	0.002	0.126	0.004	0.155	0.007	-4.99	0.05	0.362	0.004	0.503	0.005
2459191.815	171.9	8.4	11.0	9.0	0.105	0.002	0.118	0.003	0.146	0.006	-5.06	0.05	0.378	0.003	0.500	0.004
2459206.765	157.8	9.4	65.0	10.0	0.108	0.002	0.116	0.004	0.144	0.006	-5.08	0.05	0.372	0.004	0.507	0.005
2459212.693	133.6	10.6	31.0	11.0	0.111	0.003	0.124	0.005	0.152	0.007	-5.01	0.05	0.374	0.005	0.509	0.006
2459578.779	117.4	10.4	48.0	11.0	–	–	–	–	–	–	–	–	–	–	–	–
2459579.760	121.9	12.8	44.0	12.0	0.106	0.003	0.136	0.008	0.166	0.010	-4.92	0.06	0.374	0.006	0.510	0.007
2459647.709	189.5	9.7	46.0	10.0	0.121	0.002	0.116	0.006	0.144	0.008	-5.08	0.07	0.387	0.004	0.498	0.005
2459652.727	150.9	9.7	-3.0	10.0	0.112	0.002	0.095	0.008	0.120	0.010	-5.34	0.15	0.371	0.004	0.500	0.005
2459655.777	70.8	14.7	-168.0	12.0	0.136	0.004	0.167	0.046	0.200	0.051	-4.75	0.21	0.385	0.007	0.510	0.008
2459681.680	175.8	11.5	44.0	11.0	0.114	0.002	0.111	0.025	0.138	0.028	-5.13	0.27	0.366	0.005	0.499	0.006
2459686.609	163.0	10.6	46.0	11.0	–	–	–	–	–	–	–	–	–	–	–	–
2459704.609	109.7	11.1	84.0	11.0	0.125	0.003	0.134	0.014	0.164	0.017	-4.93	0.10	0.358	0.005	0.511	0.006

Table B3: HARPS radial velocity and stellar activity measurements along with their $1-\sigma$ uncertainties.

BJD	RV	σ_{RV}	BIS	σ_{BIS}	H-Alpha	$\sigma_{H-Alpha}$	log RHK	$\sigma_{\log RHK}$	FWHM	He I	$\sigma_{He\,I}$	Ca II	$\sigma_{Ca\,II}$	S_MW	σ_{S_MW}	Na II	$\sigma_{Na\,II}$
2458926.641	3.4	2.8	0.047	0.003	0.1033	0.0009	-5.48	0.13	10.082	0.502	0.002	0.085	0.003	0.113	0.006	0.395	0.002
2458930.660	6.5	5.8	0.032	0.009	0.1056	0.0020	–	–	10.063	0.502	0.005	0.009	0.009	0.031	0.011	0.389	0.004
2459178.862	-16.2	4.6	0.054	0.006	0.1051	0.0015	–	–	10.071	0.506	0.004	0.013	0.005	0.035	0.007	0.408	0.003
2459181.842	26.9	5.4	0.046	0.005	0.1065	0.0014	–	–	10.062	0.505	0.003	0.062	0.004	0.089	0.006	0.400	0.003
2459185.812	-17.0	4.1	0.044	0.005	0.1046	0.0014	–	–	10.048	0.502	0.003	0.059	0.004	0.085	0.006	0.405	0.003
2459190.699	-20.7	3.8	0.034	0.005	0.1028	0.0014	–	–	10.037	0.498	0.003	0.063	0.004	0.090	0.006	0.399	0.003
2459205.698	-32.2	4.4	0.041	0.005	0.1214	0.0015	–	–	10.107	0.501	0.003	0.043	0.004	0.068	0.006	0.406	0.003
2459213.715	-21.3	3.9	0.052	0.005	0.1021	0.0013	-5.62	0.19	10.051	0.501	0.003	0.080	0.004	0.107	0.006	0.403	0.003
2459213.729	-20.7	3.1	0.050	0.004	0.1019	0.0012	-5.34	0.10	10.063	0.501	0.003	0.092	0.004	0.121	0.006	0.401	0.003
2459227.799	-33.6	3.8	0.055	0.004	0.1040	0.0012	–	–	10.084	0.500	0.003	0.061	0.004	0.088	0.006	0.396	0.002
2459238.657	-37.4	4.3	0.040	0.006	0.1072	0.0017	–	–	10.071	0.490	0.004	0.052	0.005	0.078	0.007	0.393	0.003
2459247.710	-37.2	4.7	0.048	0.005	0.1029	0.0014	–	–	10.074	0.495	0.003	0.044	0.005	0.070	0.007	0.403	0.003
2459248.735	-52.7	3.3	0.040	0.004	0.1025	0.0011	-5.34	0.09	10.082	0.500	0.003	0.092	0.003	0.121	0.006	0.400	0.002
2459251.703	-50.0	4.4	0.034	0.005	0.1048	0.0014	–	–	10.120	0.497	0.003	0.059	0.005	0.085	0.007	0.409	0.003
2459254.665	-63.9	5.6	0.066	0.007	0.1038	0.0019	–	–	10.091	0.498	0.004	0.039	0.007	0.064	0.009	0.414	0.004
2459259.674	-73.9	3.0	0.056	0.005	0.1043	0.0013	–	–	10.092	0.496	0.003	0.046	0.004	0.071	0.007	0.396	0.003
2459263.707	-78.0	3.1	0.047	0.004	0.1033	0.0012	–	–	10.075	0.499	0.003	0.045	0.004	0.070	0.006	0.399	0.002
2459267.713	-82.4	3.8	0.036	0.005	0.1028	0.0014	–	–	10.051	0.503	0.003	0.049	0.005	0.075	0.007	0.408	0.003
2459296.652	-58.9	3.4	0.044	0.005	0.1043	0.0012	–	–	10.101	0.503	0.003	0.032	0.005	0.056	0.007	0.406	0.002
2459297.655	-51.2	3.8	0.025	0.006	0.1052	0.0015	–	–	10.062	0.501	0.003	0.032	0.006	0.056	0.008	0.413	0.003
2459365.476	-14.8	3.2	0.051	0.005	0.1049	0.0012	–	–	10.077	0.493	0.003	0.013	0.005	0.036	0.007	0.401	0.002
2459367.493	-8.7	4.0	0.024	0.006	0.1027	0.0013	–	–	10.024	0.496	0.003	0.006	0.006	0.028	0.008	0.397	0.003
2459368.495	-4.1	4.0	0.060	0.006	0.1036	0.0013	–	–	10.091	0.493	0.003	0.021	0.007	0.044	0.009	0.402	0.003
2459371.498	-9.5	3.6	0.068	0.005	0.1020	0.0012	–	–	10.062	0.498	0.003	0.044	0.007	0.069	0.009	0.400	0.002
2459504.855	-70.7	3.3	0.050	0.005	0.1035	0.0012	–	–	10.096	0.499	0.003	0.058	0.004	0.084	0.006	0.411	0.002
2459536.840	-61.0	2.1	0.037	0.003	0.1047	0.0009	–	–	10.070	0.500	0.002	0.083	0.002	0.111	0.005	0.399	0.002
2459563.772	-49.7	3.6	0.037	0.005	0.1074	0.0012	–	–	10.072	0.492	0.003	0.036	0.004	0.060	0.006	0.412	0.002
2459573.672	-52.4	2.9	0.032	0.004	0.1043	0.0011	–	–	10.065	0.496	0.003	0.066	0.003	0.093	0.006	0.399	0.002
2459573.805	-50.6	2.6	0.050	0.004	0.1033	0.0010	–	–	10.058	0.497	0.002	0.057	0.004	0.083	0.006	0.394	0.002
2459610.763	-11.8	2.9	0.049	0.003	0.1019	0.0010	–	–	10.066	0.495	0.002	0.066	0.003	0.092	0.006	0.391	0.002
2459620.714	4.6	2.9	0.045	0.003	0.1041	0.0009	-5.61	0.17	10.086	0.499	0.002	0.080	0.003	0.108	0.006	0.395	0.002
2459642.684	10.2	3.3	0.057	0.004	0.1028	0.0011	–	–	10.062	0.496	0.003	0.054	0.004	0.080	0.006	0.398	0.002
2459663.691	-4.4	3.4	0.044	0.005	0.1031	0.0011	–	–	10.083	0.497	0.003	0.065	0.005	0.092	0.007	0.397	0.002
2459668.657	-27.4	3.4	0.056	0.005	0.1029	0.0012	–	–	10.024	0.494	0.003	0.048	0.005	0.073	0.007	0.402	0.003
2459712.517	-38.8	4.2	0.044	0.006	0.1068	0.0013	–	–	10.080	0.493	0.003	0.032	0.006	0.056	0.008	0.405	0.003
2459723.503	-41.3	3.7	0.047	0.005	0.1045	0.0011	–	–	10.094	0.498	0.003	0.039	0.005	0.063	0.007	0.392	0.002
2459973.677	-59.5	3.3	0.042	0.004	0.1054	0.0011	–	–	10.071	0.498	0.003	0.042	0.003	0.066	0.006	0.404	0.002
2459977.673	-53.3	2.9	0.057	0.004	0.1047	0.0010	–	–	10.066	0.496	0.002	0.066	0.003	0.093	0.006	0.401	0.002
2460017.685	-64.7	3.2	0.036	0.004	0.1044	0.0010	–	–	10.085	0.501	0.002	0.045	0.003	0.070	0.005	0.394	0.002
2460035.539	-53.2	2.8	0.046	0.003	0.1057	0.0009	–	–	10.066	0.497	0.002	0.058	0.003	0.085	0.005	0.395	0.002
2460281.834	-49.9	3.5	0.046	0.006	0.1082	0.0014	–	–	10.027	0.501	0.003	0.043	0.004	0.068	0.006	0.401	0.003
2460293.811	-58.5	4.0	0.058	0.006	0.1070	0.0014	–	–	10.053	0.495	0.003	0.031	0.004	0.055	0.006	0.398	0.003
2460310.764	-50.8	2.9	0.064	0.004	0.1047	0.0010	–	–	10.068	0.498	0.003	0.064	0.003	0.091	0.005	0.391	0.002
2460328.742	-30.8	3.7	0.030	0.006	0.1056	0.0014	–	–	10.062	0.495	0.003	0.057	0.004	0.083	0.007	0.393	0.003
2460342.809	16.7	3.7	0.056	0.004	0.1054	0.0011	–	–	10.076	0.494	0.003	0.042	0.004	0.067	0.006	0.391	0.002
2460384.693	-4.7	3.0	0.047	0.003	0.1056	0.0010	–	–	10.096	0.495	0.003	0.052	0.004	0.077	0.006	0.392	0.002

Table B4: Processed CHIRON radial velocity and bisector measurements along with their $1-\sigma$ uncertainties.

BJD	RV ($\mathrm{m\,s^{-1}}$)	σ_{RV}	BIS ($\mathrm{m\,s^{-1}}$)	σ_{BIS}
2459185.837	21512.5	13.2	-44.0	25.0
2459193.827	21520.5	13.7	-15.0	17.0
2459200.793	21529.2	14.4	4.0	17.0
2459207.745	21516.1	14.9	19.0	19.0
2459213.793	21502.3	21.4	-2.0	22.0
2459222.755	21479.5	16.0	30.0	22.0
2459231.647	21486.4	11.9	55.0	20.0
2459238.726	21480.1	14.6	3.0	24.0
2459255.609	21444.1	10.2	39.0	19.0
2459260.754	21444.9	16.1	-6.0	28.0
2459268.676	21466.2	17.3	42.0	33.0
2459279.664	21462.0	12.5	21.0	28.0
2459285.708	21464.7	9.4	-13.0	34.0
2459290.695	21476.9	16.0	14.0	29.0
2459299.558	21488.7	13.5	42.0	28.0
2459349.520	21525.4	12.4	42.0	27.0
2459357.469	21552.3	19.9	63.0	26.0
2459364.484	21548.7	11.8	56.0	26.0
2459491.878	21502.5	43.1	134.0	49.0
2459535.828	21447.8	13.5	16.0	17.0
2459542.839	21476.2	15.3	26.0	16.0

Table B5: CORALIE radial velocity and activity measurements along with their $1-\sigma$ uncertainties, rounded to significant digits.

BJD	RV ($\mathrm{m\,s^{-1}}$)	σ_{RV}	FWHM ($\mathrm{m\,s^{-1}}$)	σ_{FWHM}	BIS ($\mathrm{m\,s^{-1}}$)	σ_{BIS}	contrast	$\sigma_{\mathrm{contrast}}$	H_{α}	$\sigma_{\mathrm{H}_{.}}$	Na	σ_{Na}	Ca	σ_{Ca}	BERV	weight
2458868.867	139.1	26.3	10163.9	14.4	5.3	37.3	30.075935	0.000001	0.190	0.005	0.328	0.005	0.145	0.016	7.93	1
2458874.715	158.0	34.0	10143.2	14.3	16.9	48.1	30.412710	0.000001	0.200	0.006	0.321	0.006	0.173	0.019	5.96	1
2458881.749	139.7	22.2	10245.8	14.5	81.8	31.4	29.813853	0.000001	0.198	0.004	0.341	0.004	0.097	0.011	3.05	1
2458886.753	211.5	23.1	10233.4	14.5	10.5	32.6	29.662468	0.000001	0.191	0.005	0.346	0.004	0.048	0.011	1.02	1
2458900.580	186.8	24.4	10208.6	14.4	-25.5	34.6	29.817047	0.000001	0.193	0.005	0.336	0.005	0.093	0.013	-4.18	1
2458911.601	191.8	22.2	10178.3	14.4	-19.9	31.3	29.796913	0.000001	0.195	0.004	0.331	0.004	0.120	0.011	-8.49	1
2458917.554	190.9	26.0	10225.1	14.5	-84.9	36.8	29.431163	0.000001	0.196	0.005	0.333	0.005	0.186	0.013	-10.54	1
2458923.584	189.0	18.8	10157.4	14.4	21.8	26.6	29.581695	0.000001	0.188	0.004	0.324	0.004	0.156	0.009	-12.67	1
2459179.798	152.1	25.1	10165.3	14.4	43.0	35.5	30.089368	0.000001	0.208	0.005	0.333	0.005	0.092	0.013	22.41	1
2459183.792	177.3	19.3	10095.8	14.3	56.9	27.3	29.749666	0.000001	0.185	0.004	0.330	0.004	0.128	0.010	21.95	1
2459190.733	142.2	22.1	10243.0	14.5	162.2	31.3	29.821387	0.000001	0.190	0.005	0.344	0.005	0.111	0.012	21.01	1
2459622.765	176.4	14.0	10134.5	14.3	20.7	19.8	29.799852	0.000001	0.194	0.003	0.334	0.003	0.050	0.006	-1.25	1
2459637.720	158.7	13.9	10128.5	14.3	8.8	19.7	30.099597	0.000001	0.195	0.004	0.341	0.004	0.120	0.006	-7.09	1
2459642.596	194.6	12.4	10154.0	14.4	49.9	17.5	30.128359	0.000001	0.189	0.003	0.336	0.003	0.126	0.005	-8.66	1
2459687.593	131.6	13.0	10153.0	14.4	51.5	18.4	29.805901	0.000001	0.184	0.004	0.330	0.003	0.112	0.005	-21.00	1
2459700.540	143.0	14.0	10170.7	14.4	51.8	19.8	29.908795	0.000001	0.191	0.004	0.331	0.003	0.127	0.006	-22.36	1
2459711.541	126.9	14.7	10167.6	14.4	19.1	20.8	29.973974	0.000001	0.195	0.004	0.339	0.004	0.155	0.007	-22.72	1
2459726.548	116.3	15.1	10137.2	14.3	33.1	21.3	29.851747	0.000001	0.195	0.004	0.338	0.003	0.116	0.009	-21.99	1

Table B6: PFS radial velocity along with their $1-\sigma$ uncertainties and activity measurements.

BJD	RV ($\mathrm{m\,s^{-1}}$)	σ_{RV}	S-index	H-Alpha	counts	T_{exp}
2459205.721	0.00	2.46	-1.0000	0.02750	1506	900
2459205.732	-2.14	2.30	-1.0000	0.02724	1508	900
2459210.734	0.88	2.60	-1.0000	0.02739	1194	900
2459210.745	-3.81	2.55	-1.0000	0.02762	1347	900
2459215.754	0.97	2.56	-1.0000	0.02719	1249	900
2459215.765	9.81	2.53	-1.0000	0.02714	1197	900
2459238.731	-8.55	2.59	-1.0000	0.02723	1215	900
2459238.742	-7.95	2.46	-1.0000	0.02766	1416	900
2459358.471	13.76	2.35	-1.0000	0.02702	1785	1200
2459531.815	-46.48	2.86	-1.0000	0.02659	1365	1201
2459533.829	-43.48	2.56	-1.0000	0.02765	1924	1200
2459592.815	-3.48	2.33	-1.0000	0.02800	1764	1200
2459593.729	-3.70	2.71	-1.0000	0.02758	1135	1201
2459600.774	15.12	2.41	-1.0000	0.02781	1353	1200
2459601.783	12.77	2.43	-1.0000	0.02731	1447	1200
2459602.803	8.02	2.14	-1.0000	0.02757	1685	1200

C

APPENDIX FOR CHAPTER 5

In this appendix, we list the radial velocity and stellar activity data for TW Hya, as well as show additional plots.

Table C1 to Table C4 llist the FEROS radial velocity and stellar activity data, Table C5 lists the HARPS radial velocity and stellar activity data.

Figure C1 and Figure C2 show the full sets of FEROS and HARPS maximum likelihood periodograms. Figure C3 and Figure C4 show the corner plots for the correlation of the FEROS RV and activity data, as well as the posterior distribution of our spot model, respectively. Figure C6, Figure C7 and Figure C8 show the additional photometric time seriesfor *TESS* sectors 36, 63 and 90, respectively. Figure C9 shows the wavelet analysis for all four *TESS* sectors. Figure C10, Figure C11 and Figure C12 show the posterior distributions for our nested sampling of the GP, Keplerian and GP+Keplerian models, respectively.

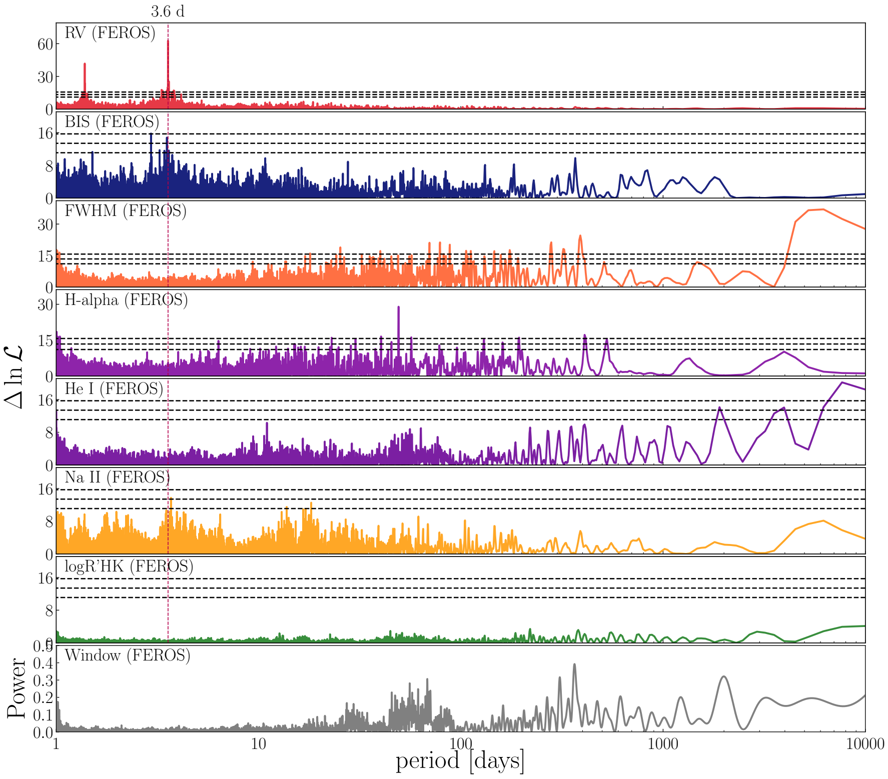

Figure C1: Full set of maximum likelihood periodograms for FEROS radial velocity and activity measurements of TW Hya.

Table C1: FEROS radial velocity and activity data along with their $1-\sigma$ uncertainties. (1)

BJD	RV	σ_{RV}	BIS	σ_{BIS}	H_{α}	$\sigma_{\mathrm{H}_{,}}$	Ca II	$\sigma_{\mathrm{Ca\,II}}$	He I	$\sigma_{\mathrm{He\,I}}$	Na II	$\sigma_{\mathrm{Na\,II}}$	log R′HK	$\sigma_{\log \mathrm{R'HK}}$
2453460.758534	-188.654	20.550	2.500	7.000	3.220	0.898	-0.546	0.147	0.259	0.153	0.062	0.182	-0.041	0.012
2453809.760654	-103.900	19.100	-148.000	8.000	-1.507	0.667	-1.046	0.132	0.035	0.155	0.006	0.194	-0.083	0.012
2454159.618028	-14.200	27.300	-77.000	11.000	2.097	0.829	-0.220	0.146	0.029	0.148	0.007	0.181	-0.016	0.011
2454160.734649	-38.800	19.900	53.000	9.000	-0.360	0.733	0.234	0.161	-0.015	0.148	-0.034	0.181	0.017	0.011
2454160.907381	-389.300	27.200	19.000	11.000	-1.284	0.667	-0.992	0.136	-0.003	0.149	0.045	0.181	-0.078	0.012
2454161.557409	19.200	20.800	5.000	11.000	-2.183	0.596	1.163	0.195	-0.057	0.147	-0.090	0.181	0.077	0.012
2454161.651215	158.200	15.800	7.000	9.000	-2.144	0.592	1.521	0.194	-0.039	0.148	-0.082	0.181	0.098	0.011
2454161.912219	-230.300	23.900	-17.000	11.000	-1.862	0.627	-0.942	0.142	0.033	0.150	0.047	0.181	-0.074	0.012
2454162.574011	16.900	30.200	-62.000	11.000	-1.599	0.632	-1.662	0.117	-0.019	0.148	-0.038	0.180	-0.140	0.012
2454162.798489	55.100	24.100	14.000	10.000	-0.396	0.686	-1.482	0.117	-0.048	0.147	-0.046	0.180	-0.122	0.011
2454162.901916	-69.200	28.800	-54.000	11.000	-0.498	0.679	-1.680	0.122	-0.073	0.147	-0.029	0.180	-0.142	0.012
2454163.612980	-264.400	27.700	23.000	10.000	0.704	0.753	-1.375	0.118	-0.007	0.147	-0.000	0.181	-0.112	0.011
2454163.810792	-279.500	28.200	88.000	10.000	1.674	0.829	-0.992	0.127	0.033	0.148	0.037	0.181	-0.078	0.011
2454163.860128	-416.900	32.200	53.000	11.000	1.615	0.835	-1.196	0.124	0.019	0.147	0.058	0.180	-0.096	0.011
2454164.612755	-142.500	27.500	126.000	11.000	1.743	0.844	-0.525	0.133	-0.012	0.147	0.043	0.181	-0.040	0.011
2454164.791409	-76.900	24.700	120.000	11.000	1.863	0.860	0.437	0.162	0.046	0.148	0.015	0.181	0.030	0.011
2454164.835468	-66.500	26.800	56.000	11.000	1.689	0.851	0.401	0.160	0.037	0.148	0.022	0.181	0.028	0.011
2454165.621110	205.100	26.100	-93.000	10.000	2.467	0.872	-0.393	0.140	0.064	0.147	0.026	0.181	-0.029	0.011
2454165.771149	195.900	23.100	-19.000	9.000	2.499	0.865	0.263	0.158	0.174	0.153	0.043	0.181	0.019	0.011
2454165.847311	46.900	26.800	-121.000	10.000	2.054	0.831	-0.060	0.152	0.170	0.153	0.022	0.181	-0.004	0.011
2454168.539766	163.500	19.100	35.000	11.000	2.447	0.849	2.946	0.246	0.056	0.150	-0.036	0.182	0.173	0.012
2454168.667545	194.700	20.400	50.000	10.000	1.618	0.780	1.512	0.196	0.045	0.150	-0.043	0.181	0.097	0.011
2454168.793574	249.300	16.600	-16.000	9.000	1.382	0.751	1.505	0.197	0.060	0.150	-0.040	0.181	0.097	0.011
2454169.547271	281.300	24.800	-74.000	9.000	0.879	0.771	0.113	0.160	0.063	0.146	0.037	0.180	0.008	0.011
2454169.669306	244.000	25.800	-71.000	9.000	0.614	0.741	-0.603	0.136	0.055	0.147	0.028	0.180	-0.046	0.011
2454169.800210	71.100	21.600	-86.000	9.000	1.200	0.738	0.153	0.155	0.017	0.147	-0.033	0.180	0.011	0.011
2454170.754411	-109.300	26.600	38.000	9.000	0.033	0.703	-1.704	0.110	-0.054	0.144	-0.013	0.180	-0.144	0.011
2454171.773803	18.900	14.600	-4.000	9.000	0.057	0.681	1.589	0.185	-0.033	0.149	-0.123	0.181	0.102	0.011
2454171.885813	16.800	14.600	-84.000	9.000	-0.323	0.667	3.145	0.298	-0.053	0.149	-0.122	0.181	0.182	0.014
2454172.598575	213.500	16.000	-3.000	11.000	-2.601	0.548	4.800	0.275	-0.129	0.149	-0.133	0.181	0.254	0.011
2454216.500483	105.300	21.700	50.000	9.000	1.037	0.752	0.346	0.157	0.100	0.152	-0.011	0.182	0.024	0.011
2454216.560798	118.500	21.600	27.000	8.000	1.339	0.757	-0.249	0.141	0.111	0.151	0.005	0.182	-0.018	0.011
2454216.688855	101.400	33.600	-30.000	10.000	0.900	0.739	-1.552	0.114	0.059	0.151	0.041	0.181	-0.129	0.011
2454217.500280	-326.700	17.600	-61.000	8.000	-1.168	0.620	-1.768	0.106	-0.087	0.146	-0.074	0.181	-0.151	0.011
2454217.641016	-192.900	17.300	12.000	8.000	-1.555	0.596	-1.284	0.116	-0.139	0.146	-0.089	0.182	-0.104	0.011
2454217.732511	-184.700	22.400	48.000	9.000	-1.474	0.631	-1.294	0.120	-0.093	0.145	-0.025	0.182	-0.105	0.011
2454218.715881	375.300	31.100	-15.000	11.000	-0.620	0.676	-1.563	0.120	-0.057	0.146	-0.075	0.182	-0.130	0.012
2454219.697668	164.700	30.000	-121.000	12.000	-1.444	0.579	-0.578	0.142	-0.019	0.148	-0.097	0.182	-0.044	0.011
2454220.479201	-99.500	18.600	44.000	11.000	-0.497	0.623	2.118	0.198	-0.010	0.149	-0.091	0.183	0.131	0.011
2454220.730737	-172.600	21.400	13.000	11.000	-0.235	0.653	1.834	0.191	0.017	0.150	-0.060	0.182	0.115	0.011
2454221.734657	-259.600	49.100	-37.000	13.000	1.105	0.780	-2.084	0.116	-0.010	0.148	0.002	0.182	-0.184	0.013
2454222.471867	105.700	21.900	-60.000	9.000	-1.629	0.653	-1.024	0.125	0.021	0.148	-0.026	0.182	-0.081	0.011
2454222.604355	190.000	23.500	1.000	10.000	-1.756	0.627	-0.304	0.141	0.046	0.149	-0.063	0.182	-0.022	0.011
2454222.698220	191.200	26.400	-36.000	11.000	-1.793	0.646	0.000	0.157	0.056	0.148	-0.041	0.182	0.000	0.011
2454223.481322	5.000	43.700	20.000	16.000	-2.566	0.554	0.192	0.176	0.030	0.149	-0.067	0.183	0.014	0.012
2454223.599239	24.100	19.600	-15.000	10.000	-1.945	0.587	1.005	0.163	0.042	0.150	-0.082	0.182	0.067	0.010
2454223.705713	42.000	19.500	-40.000	11.000	-1.482	0.615	2.043	0.203	0.081	0.151	-0.058	0.183	0.127	0.011
2454224.483676	-151.000	18.900	-34.000	9.000	0.000	0.660	1.273	0.177	0.098	0.150	-0.023	0.183	0.083	0.011
2454224.578806	-156.400	19.300	-31.000	10.000	0.113	0.656	1.794	0.189	0.104	0.152	-0.034	0.183	0.113	0.011
2454224.673158	-177.900	19.200	-28.000	11.000	0.348	0.672	2.942	0.228	0.111	0.151	-0.035	0.183	0.172	0.011

Table C2: FEROS radial velocity and activity data along with their $1-\sigma$ uncertainties. (2)

BJD	RV	σ_{RV}	BIS	σ_{BIS}	H_{α}	$\sigma_{\mathrm{H}_{\alpha}}$	Ca II	$\sigma_{\mathrm{Ca\,II}}$	He I	$\sigma_{\mathrm{He\,I}}$	Na II	$\sigma_{\mathrm{Na\,II}}$	log R′HK	$\sigma_{\log \mathrm{R'HK}}$
2454225.496697	-10.700	21.000	-23.000	11.000	-0.437	0.603	1.447	0.182	-0.046	0.149	-0.103	0.183	0.093	0.011
2454225.595422	108.500	18.500	30.000	11.000	-0.019	0.627	2.343	0.200	-0.002	0.150	-0.100	0.183	0.142	0.010
2454225.696302	138.800	19.600	0.000	11.000	-0.052	0.638	2.489	0.211	0.053	0.151	-0.091	0.183	0.150	0.011
2454228.496582	-175.200	24.300	53.000	10.000	-0.126	0.728	-0.318	0.140	-0.047	0.148	-0.007	0.183	-0.024	0.011
2454228.612286	-194.200	28.200	-81.000	11.000	-0.240	0.706	-0.156	0.147	-0.060	0.148	-0.026	0.182	-0.011	0.011
2454228.694330	-81.800	22.800	-40.000	11.000	-0.233	0.695	0.245	0.156	-0.068	0.148	-0.040	0.183	0.017	0.011
2454230.469001	148.600	24.900	-78.000	10.000	3.073	0.901	-0.504	0.139	-0.007	0.148	-0.058	0.182	-0.038	0.011
2454231.474076	-360.100	24.100	1.000	8.000	2.948	0.861	-0.976	0.124	0.018	0.147	0.110	0.182	-0.077	0.011
2454232.465817	-111.600	18.100	9.000	8.000	2.471	0.854	0.108	0.149	-0.053	0.146	-0.054	0.182	0.008	0.011
2454233.466398	285.300	28.600	-20.000	12.000	1.334	0.814	0.016	0.160	0.011	0.147	-0.087	0.183	0.001	0.012
2454310.506116	-157.000	27.700	-8.000	11.000	-2.108	0.606	-0.844	0.146	0.080	0.150	0.000	0.185	-0.066	0.012
2454495.865417	-320.900	21.100	-38.000	9.000	-4.089	0.522	1.347	0.178	0.046	0.154	0.117	0.192	0.087	0.011
2454496.826944	115.600	19.900	41.000	9.000	-4.905	0.473	0.955	0.177	0.053	0.154	-0.003	0.191	0.064	0.011
2454497.775577	319.400	23.500	-79.000	10.000	-3.603	0.537	2.431	0.241	0.205	0.159	0.043	0.192	0.147	0.012
2454498.646328	-127.700	29.400	39.000	10.000	-1.699	0.688	0.190	0.161	0.123	0.155	0.074	0.191	0.013	0.011
2454498.879130	-203.600	23.100	82.000	8.000	-1.544	0.682	-0.401	0.136	0.072	0.155	0.068	0.191	-0.030	0.011
2454499.814635	-125.100	21.000	74.000	9.000	-2.547	0.539	-0.432	0.133	-0.031	0.155	-0.053	0.191	-0.032	0.010
2454500.738088	242.800	20.800	-55.000	10.000	-1.560	0.587	1.247	0.189	-0.026	0.154	-0.051	0.192	0.082	0.011
2454501.806346	64.200	23.200	-40.000	8.000	-1.244	0.695	0.010	0.151	0.191	0.159	0.043	0.191	0.001	0.011
2454507.847581	217.400	22.000	14.000	8.000	-4.171	0.534	0.972	0.188	0.134	0.154	0.159	0.192	0.065	0.012
2454518.782527	334.500	13.700	-83.000	6.000	–	–	–	–	–	–	–	–	–	–
2454573.660512	-233.600	25.300	32.000	8.000	1.798	0.824	0.504	0.172	0.309	0.164	0.079	0.194	0.035	0.011
2454574.594987	-173.400	15.000	2.000	7.000	2.330	0.918	1.973	0.235	0.194	0.159	0.024	0.194	0.123	0.013
2454575.710578	248.700	16.500	32.000	8.000	3.114	0.970	0.353	0.181	0.027	0.151	0.026	0.194	0.025	0.012
2454576.517842	277.700	17.200	7.000	8.000	0.658	0.717	-1.061	0.126	-0.088	0.152	-0.061	0.193	-0.084	0.011
2454577.576507	-130.500	17.000	18.000	8.000	1.336	0.714	0.384	0.157	-0.066	0.153	-0.090	0.194	0.027	0.011
2454632.463646	223.300	16.700	29.000	7.000	0.196	0.766	-0.363	0.144	0.081	0.151	0.032	0.196	-0.027	0.011
2454633.502696	224.500	13.300	-32.000	8.000	-0.009	0.705	0.271	0.147	-0.163	0.151	-0.073	0.196	0.019	0.010
2454635.471736	-152.900	16.200	46.000	9.000	-2.119	0.603	1.405	0.189	-0.051	0.154	-0.060	0.197	0.091	0.011
2454657.514176	239.600	20.200	-12.000	9.000	0.985	0.737	-0.046	0.154	0.009	0.154	-0.039	0.197	-0.003	0.011
2454836.676928	311.700	14.400	-20.000	8.000	-3.482	0.484	0.155	0.157	0.005	0.163	-0.075	0.202	0.011	0.011
2454839.753894	242.800	14.200	-24.000	7.000	-4.467	0.515	1.750	0.228	0.113	0.161	0.023	0.203	0.111	0.013
2454840.816727	148.300	19.300	-63.000	8.000	-2.104	0.636	0.526	0.186	0.302	0.167	0.060	0.202	0.036	0.012
2454841.805684	-359.000	22.200	47.000	7.000	-0.858	0.638	-2.644	0.093	-0.085	0.156	0.057	0.201	-0.251	0.012
2454844.729686	-7.400	10.700	12.000	8.000	-2.507	0.534	3.710	0.247	-0.108	0.161	-0.105	0.203	0.208	0.011
2454845.829825	-261.000	17.500	149.000	8.000	-1.974	0.602	0.186	0.160	-0.007	0.161	0.017	0.203	0.013	0.011
2454945.718171	-228.600	18.200	78.000	8.000	-1.881	0.637	-0.040	0.160	0.101	0.167	0.036	0.205	-0.003	0.012
2454947.756894	266.386	24.550	-70.941	8.500	-1.060	0.627	-1.573	0.124	0.023	0.165	0.004	0.205	-0.131	0.012
2454985.539499	138.400	16.900	16.000	8.000	-4.035	0.457	-0.683	0.132	-0.052	0.163	-0.082	0.207	-0.052	0.011
2454987.493895	-43.600	27.400	-7.000	9.000	0.402	0.691	-0.817	0.133	0.107	0.166	0.050	0.207	-0.063	0.011
2454989.556779	171.900	12.600	-14.000	9.000	-4.031	0.470	2.693	0.212	-0.215	0.161	-0.180	0.208	0.160	0.011
2455201.814519	-207.800	25.800	110.000	10.000	4.507	0.942	2.932	0.265	0.359	0.179	0.040	0.215	0.172	0.013
2455202.809522	-366.000	24.100	93.000	9.000	2.770	0.794	0.218	0.167	0.194	0.173	0.021	0.214	0.015	0.012
2455203.874410	628.600	28.700	40.000	9.000	4.682	0.945	0.861	0.191	0.348	0.179	0.057	0.214	0.058	0.012
2455338.641294	-18.200	25.500	69.000	14.000	1.172	0.779	6.084	0.449	0.197	0.180	-0.059	0.218	0.303	0.016
2455352.581395	-223.200	25.300	233.000	10.000	1.933	0.790	2.228	0.231	0.313	0.180	-0.007	0.218	0.137	0.012
2455354.464218	419.500	23.400	-139.000	9.000	-2.056	0.613	1.302	0.201	0.343	0.179	0.012	0.218	0.085	0.012
2455356.519392	-111.200	18.600	5.000	11.000	1.735	0.742	4.847	0.320	0.117	0.176	-0.097	0.219	0.256	0.013
2455584.800064	-183.900	30.600	-4.000	8.000	0.454	0.741	-1.306	0.122	0.227	0.183	0.076	0.221	-0.106	0.011
2455585.815950	259.900	31.000	3.000	8.000	-1.946	0.662	-0.802	0.139	0.317	0.184	0.090	0.221	-0.062	0.012

Table C3: FEROS radial velocity and activity data along with their $1-\sigma$ uncertainties. (3)

BJD	RV	σ_{RV}	BIS	σ_{BIS}	H_α	$\sigma_{\mathrm{H}_\alpha}$	Ca II	$\sigma_{\mathrm{Ca\,II}}$	He I	$\sigma_{\mathrm{He\,I}}$	Na II	$\sigma_{\mathrm{Na\,II}}$	log R′HK	$\sigma_{\log \mathrm{R'HK}}$
2455586.822958	479.100	40.500	-211.000	9.000	-1.921	0.663	1.194	0.203	0.631	0.197	0.151	0.222	0.078	0.012
2455587.838596	-449.700	29.700	64.000	9.000	-0.857	0.688	-0.031	0.154	0.272	0.184	0.058	0.222	-0.002	0.011
2455630.714510	-466.000	27.500	-114.000	9.000	-2.516	0.616	1.537	0.225	0.352	0.186	0.072	0.223	0.099	0.013
2455632.681290	530.931	29.150	5.789	9.500	-2.958	0.545	0.803	0.171	0.322	0.187	0.089	0.223	0.055	0.011
2455635.679824	164.600	29.500	-43.000	9.000	-3.354	0.582	-0.777	0.137	0.246	0.182	0.080	0.223	-0.060	0.011
2455638.809703	-405.300	49.700	-352.000	11.000	-1.498	0.658	-2.568	0.105	0.056	0.175	0.057	0.223	-0.241	0.013
2455639.645137	138.800	22.500	-220.000	10.000	-2.814	0.549	0.558	0.160	0.151	0.182	0.025	0.223	0.038	0.011
2455672.639141	53.500	30.000	-51.000	9.000	-0.904	0.692	-0.505	0.141	0.273	0.185	0.073	0.223	-0.038	0.011
2455673.625930	-181.000	20.000	69.000	10.000	-0.321	0.713	4.039	0.278	0.192	0.184	0.054	0.225	0.223	0.012
2455674.600293	125.800	25.500	-152.000	9.000	-0.501	0.768	0.580	0.172	0.150	0.176	0.102	0.223	0.040	0.011
2456076.545662	-194.700	18.500	38.000	8.000	-1.482	0.678	-0.559	0.134	-0.000	0.182	0.081	0.225	-0.042	0.011
2456076.622831	-177.400	16.700	17.000	8.000	-1.271	0.680	0.354	0.151	0.026	0.183	0.064	0.225	0.025	0.010
2456084.584966	35.700	18.900	-7.000	9.000	0.034	0.802	2.654	0.260	0.190	0.186	0.121	0.226	0.158	0.013
2456084.632460	104.400	21.300	-6.000	9.000	0.226	0.867	2.667	0.268	0.302	0.186	0.180	0.226	0.159	0.013
2456088.590233	146.400	17.000	65.000	10.000	0.915	0.755	2.292	0.210	-0.059	0.183	-0.017	0.226	0.140	0.011
2456120.492556	197.700	16.600	236.000	9.000	–	–	–	–	–	–	–	–	–	–
2456120.551003	237.600	18.600	226.000	10.000	-3.504	0.583	2.258	0.249	-0.051	0.180	0.014	0.226	0.138	0.013
2456311.711042	-239.800	30.600	-11.000	8.000	-3.145	0.620	-1.545	0.111	0.174	0.193	0.062	0.226	-0.129	0.011
2456311.828349	-260.600	25.900	-8.000	8.000	-2.614	0.662	-1.166	0.117	0.176	0.190	0.076	0.225	-0.093	0.011
2456349.651325	170.000	19.900	-18.000	8.000	5.179	1.090	-0.826	0.123	0.068	0.187	0.133	0.226	-0.064	0.010
2456349.717512	139.000	18.600	-29.000	8.000	5.586	1.145	-0.346	0.143	0.090	0.187	0.111	0.226	-0.026	0.011
2456349.859867	103.600	20.500	67.000	8.000	5.849	1.157	0.194	0.167	0.110	0.183	0.109	0.227	0.014	0.012
2456351.562123	-248.200	21.800	-30.000	8.000	4.477	1.018	-1.321	0.117	0.066	0.193	0.029	0.226	-0.107	0.011
2456351.766103	-146.100	19.600	-22.000	7.000	3.581	0.930	-1.453	0.111	0.031	0.189	0.034	0.226	-0.120	0.011
2456637.787317	183.100	15.300	3.000	9.000	-4.508	0.523	1.301	0.184	-0.225	0.185	-0.080	0.227	0.085	0.011
2456637.848151	195.100	21.200	85.000	13.000	-4.419	0.520	2.471	0.236	-0.237	0.184	-0.093	0.227	0.149	0.012
2456742.549468	133.900	24.200	-77.000	9.000	9.511	1.251	-0.761	0.125	-0.010	0.191	0.118	0.226	-0.059	0.010
2456742.621717	48.200	21.800	-48.000	9.000	10.339	1.327	0.270	0.151	0.089	0.194	0.122	0.226	0.019	0.011
2456742.736696	-10.300	21.500	-76.000	9.000	10.938	1.419	0.885	0.185	0.214	0.196	0.124	0.226	0.059	0.012
2456743.629984	-345.800	25.200	67.000	10.000	6.403	1.117	-0.608	0.137	-0.045	0.191	0.072	0.226	-0.046	0.011
2456743.728884	-369.300	20.300	65.000	8.000	6.558	1.114	-0.742	0.133	-0.029	0.190	0.065	0.226	-0.057	0.011
2457905.528638	15.900	16.600	-44.000	9.000	-1.942	0.521	-0.355	0.135	-0.155	0.146	-0.117	0.180	-0.026	0.010
2457905.654184	112.900	22.400	-56.000	11.000	-1.758	0.536	0.295	0.198	-0.115	0.145	-0.077	0.181	0.021	0.014
2457906.573405	37.400	19.800	-47.000	9.000	-1.285	0.575	1.384	0.193	0.000	0.149	-0.006	0.180	0.090	0.011
2457906.640291	63.300	20.600	-14.000	10.000	-1.316	0.573	1.653	0.230	0.021	0.147	-0.017	0.180	0.105	0.013
2457907.523376	-100.300	24.800	-17.000	9.000	-0.335	0.658	-1.913	0.107	-0.059	0.146	0.012	0.179	-0.166	0.011
2457907.619865	-66.100	26.200	-77.000	9.000	-0.361	0.665	-1.770	0.117	-0.018	0.148	0.006	0.179	-0.151	0.012
2457908.508188	-77.600	21.400	-1.000	10.000	0.817	0.711	0.905	0.184	-0.003	0.147	-0.020	0.180	0.061	0.012
2457908.630108	-31.000	20.600	65.000	11.000	0.920	0.733	3.240	0.283	0.007	0.149	-0.034	0.181	0.187	0.013
2457909.471522	79.700	20.500	-66.000	9.000	-0.809	0.625	0.153	0.154	-0.038	0.148	-0.014	0.180	0.011	0.011
2457909.591973	168.600	22.000	-38.000	10.000	-1.054	0.599	-0.167	0.151	-0.071	0.147	-0.023	0.180	-0.012	0.011
2457910.469208	86.900	26.300	28.000	9.000	-0.588	0.678	-1.737	0.110	-0.045	0.147	0.043	0.180	-0.147	0.011
2457910.602992	16.600	32.700	-56.000	10.000	-0.370	0.675	-1.810	0.114	-0.036	0.148	0.026	0.180	-0.155	0.012
2457911.493856	-92.900	31.100	145.000	9.000	0.624	0.731	-1.474	0.116	-0.030	0.146	0.059	0.180	-0.122	0.011
2457911.607290	-198.700	29.200	56.000	10.000	1.047	0.757	-0.831	0.133	-0.023	0.145	0.040	0.180	-0.064	0.011
2457913.475586	63.800	29.700	3.000	10.000	2.339	0.901	-0.335	0.141	-0.055	0.147	0.041	0.180	-0.025	0.011
2457913.631153	12.100	34.200	-9.000	11.000	1.985	0.870	-1.247	0.137	-0.092	0.145	0.045	0.181	-0.101	0.012
2457914.474973	-102.000	21.600	18.000	9.000	1.431	0.758	-1.415	0.116	-0.110	0.145	-0.034	0.179	-0.116	0.011
2457914.609604	-45.000	26.000	-1.000	10.000	1.692	0.785	-1.899	0.112	-0.134	0.145	-0.017	0.179	-0.164	0.012
2457915.475135	-165.500	24.300	-38.000	8.000	1.839	0.805	-1.912	0.107	-0.079	0.147	0.033	0.179	-0.166	0.011

Table C4: FEROS radial velocity and activity data along with their $1-\sigma$ uncertainties. (4)

BJD	RV	σ_{RV}	BIS	σ_{BIS}	H_α	$\sigma_{\mathrm{H}_\alpha}$	Ca II	$\sigma_{\mathrm{Ca\,II}}$	He I	$\sigma_{\mathrm{He\,I}}$	Na II	$\sigma_{\mathrm{Na\,II}}$	$\log \mathrm{R'HK}$	$\sigma_{\log \mathrm{R'HK}}$
2457915.593476	-138.400	26.800	19.000	9.000	1.636	0.791	-1.804	0.111	-0.076	0.147	0.025	0.179	-0.154	0.011
2458227.647548	52.900	21.400	25.000	9.000	0.321	0.680	-1.565	0.117	-0.169	0.145	-0.018	0.182	-0.130	0.011
2458230.623887	-63.200	19.900	-66.000	9.000	0.803	0.679	0.258	0.155	-0.052	0.150	0.027	0.183	0.018	0.011
2458231.623693	-311.400	36.300	32.000	9.000	2.119	0.815	-1.225	0.123	0.036	0.149	0.215	0.183	-0.099	0.011
2458236.584835	-19.700	31.000	38.000	9.000	-3.291	0.519	-2.073	0.107	-0.051	0.148	0.025	0.183	-0.183	0.012
2458238.584646	34.500	24.200	32.000	10.000	-2.813	0.511	-1.345	0.121	-0.094	0.148	-0.050	0.183	-0.110	0.011
2458455.839211	-48.900	18.000	53.000	10.000	3.973	0.958	3.221	0.233	-0.029	0.151	0.093	0.187	0.186	0.011
2458460.842625	271.600	27.600	56.000	9.000	1.758	0.804	-2.140	0.104	-0.040	0.149	0.012	0.185	-0.190	0.012
2458464.844576	128.100	31.600	-39.000	8.000	1.424	0.767	-2.654	0.094	-0.031	0.147	0.052	0.184	-0.252	0.012
2458466.828294	0.000	23.500	63.000	9.000	1.283	0.816	-0.867	0.134	0.033	0.151	0.012	0.185	-0.067	0.011
2458530.892307	-153.700	21.300	109.000	9.000	-3.460	0.516	-1.404	0.121	-0.099	0.149	-0.016	0.185	-0.115	0.011
2458533.808837	-196.500	23.900	32.000	8.000	-4.264	0.456	-1.986	0.105	-0.023	0.151	0.024	0.184	-0.173	0.011
2458537.814030	-269.000	24.100	24.000	9.000	2.255	0.764	-1.611	0.114	0.034	0.154	0.011	0.185	-0.135	0.011
2458540.771128	-145.200	15.700	8.000	9.000	-3.253	0.510	2.474	0.223	-0.011	0.153	0.007	0.186	0.149	0.011
2458541.812102	-48.700	16.300	-21.000	9.000	-5.098	0.408	0.522	0.158	0.006	0.155	-0.061	0.185	0.036	0.011
2460125.506295	233.200	16.900	-9.000	9.000	0.189	0.599	-0.424	0.145	-0.110	0.147	-0.165	0.179	-0.032	0.011
2460126.476780	-7.700	34.500	-47.000	7.000	2.088	0.778	-2.478	0.097	0.004	0.145	0.071	0.177	-0.230	0.012
2460127.482301	-343.600	18.700	37.000	8.000	1.617	0.734	0.900	0.183	0.063	0.148	-0.004	0.179	0.060	0.012
2460314.745846	302.100	20.500	18.000	9.000	-13.365	0.038	-4.150	0.145	-1.119	0.209	0.637	0.618	-0.506	0.033
2460315.733818	-57.950	16.800	-11.000	9.000	0.574	0.653	1.077	0.171	-0.050	0.150	-0.044	0.180	0.071	0.011
2460316.771681	-180.600	19.400	42.500	9.000	-0.119	0.632	-1.197	0.118	-0.145	0.147	-0.056	0.179	-0.096	0.011
2460317.774387	116.500	18.900	107.000	13.000	-1.033	0.579	3.000	0.254	-0.194	0.150	-0.225	0.180	0.175	0.012
2460328.747185	258.600	28.600	243.000	10.000	0.745	0.662	-1.691	0.116	-0.114	0.146	-0.077	0.180	-0.143	0.012
2460329.705450	311.900	21.000	292.000	10.000	3.001	0.823	2.143	0.220	-0.015	0.150	-0.058	0.181	0.132	0.012
2460362.790822	-132.100	20.900	-42.000	12.000	1.060	0.642	1.235	0.203	-0.190	0.148	-0.186	0.181	0.081	0.012
2460365.778282	-43.500	19.000	-131.000	10.000	0.986	0.653	-0.263	0.144	-0.105	0.149	-0.143	0.181	-0.019	0.011
2460367.784617	91.300	15.000	6.000	9.000	3.719	0.838	1.935	0.224	-0.069	0.148	-0.120	0.182	0.121	0.012
2460368.756791	47.900	16.700	-68.000	10.000	1.793	0.697	3.631	0.249	-0.082	0.150	-0.097	0.183	0.205	0.011
2460369.704152	-183.700	13.500	-61.000	9.000	0.038	0.592	1.814	0.186	-0.203	0.148	-0.218	0.181	0.114	0.010
2460377.835807	-53.600	20.600	25.000	10.000	1.762	0.688	-0.626	0.148	-0.171	0.147	-0.104	0.181	-0.048	0.012
2460379.841887	-10.900	14.600	-70.000	10.000	2.458	0.762	2.682	0.239	-0.077	0.149	-0.127	0.182	0.160	0.012
2460380.814654	-191.200	17.700	-48.000	9.000	1.972	0.725	-0.475	0.139	-0.181	0.146	-0.102	0.181	-0.036	0.011
2460381.809297	47.900	14.800	47.000	9.000	1.943	0.706	1.377	0.188	-0.200	0.147	-0.165	0.182	0.089	0.011

Table C5: HARPS radial velocity and activity data along with their $1-\sigma$ uncertainties.

BJD	RV	σ_{RV}	BIS	σ_{BIS}	contrast	$\sigma_{\mathrm{contrast}}$	FWHM	σ_{FWHM}	H_α	$\sigma_{\mathrm{H}_\alpha}$	CRX	σ_{CRX}	dLW	σ_{dLW}	Na D1	$\sigma_{\log \mathrm{Na\,D1}}$	Na D2	$\sigma_{\log \mathrm{Na\,D2}}$
2453461.778055	66.367	2.187	-76.329	-0.743	-1.457	0.150	-107.801	95.542	3.093	0.015	-39.365	34.670	5.697	2.079	-0.075	0.003	-0.050	0.003
2453466.589591	119.931	2.912	-12.887	-0.108	6.346	0.228	-56.434	96.056	4.126	0.015	19.854	25.709	-37.946	3.164	-0.063	0.004	-0.089	0.004
2453495.613608	0.641	3.137	96.166	0.982	0.311	0.168	-247.196	94.148	-10.332	0.014	92.636	190.128	16.501	1.709	-0.104	0.005	-0.092	0.005
2453500.578384	-58.917	3.051	-9.168	-0.071	-2.509	0.139	-366.687	92.953	1.508	0.020	0.000	90.198	10.123	2.835	-0.053	0.005	-0.078	0.005
2454594.519307	74.847	3.980	-106.663	-1.046	2.252	0.187	77.731	97.397	2.074	0.025	33.221	159.847	-15.831	3.676	0.024	0.006	-0.001	0.007
2454594.647689	43.612	2.978	-51.280	-0.492	1.832	0.183	147.357	98.093	3.160	0.020	-22.656	92.894	-14.694	2.714	0.014	0.005	0.000	0.005
2454594.737171	8.460	5.637	-58.806	-0.568	2.418	0.189	245.611	99.076	2.643	0.033	-41.507	175.859	-12.177	4.807	0.015	0.009	-0.010	0.009
2454595.483439	-157.739	3.638	45.830	0.479	-0.026	0.164	-90.574	95.714	-0.467	0.023	75.931	239.757	-5.604	2.037	-0.001	0.006	-0.031	0.006
2454595.630901	-165.081	4.063	122.445	1.245	0.353	0.168	-1.278	96.607	-0.623	0.024	54.314	247.727	-3.547	2.306	-0.048	0.006	-0.035	0.007
2454596.502900	-1.625	4.185	3.494	0.055	2.478	0.189	-29.613	96.324	-1.753	0.026	-16.502	245.704	-20.046	2.718	-0.048	0.007	-0.056	0.007
2454596.642711	46.466	4.315	-18.020	-0.160	2.663	0.191	-125.888	95.361	-0.239	0.027	-56.965	187.353	-20.827	2.935	0.044	0.007	0.030	0.007
2454874.618158	-66.808	4.517	65.535	0.676	0.784	0.172	-20.507	96.415	0.000	0.028	3.825	200.793	-3.875	2.747	0.060	0.008	0.054	0.008
2454874.772043	-31.213	3.535	57.134	0.592	-0.999	0.155	27.501	96.895	0.222	0.024	-63.293	167.407	0.081	1.633	0.094	0.006	0.092	0.007
2454874.887588	3.411	3.539	91.202	0.932	-0.340	0.161	1.278	96.633	-0.981	0.022	12.622	122.983	2.945	2.874	0.096	0.006	0.100	0.007
2454875.615060	179.333	3.904	-30.656	-0.286	0.026	0.165	-114.047	95.479	-2.456	0.023	-38.240	82.989	-2.912	2.231	0.000	0.007	0.012	0.007
2454875.769093	200.867	4.797	0.666	0.027	-4.081	0.124	-49.485	96.125	-3.246	0.028	-95.600	188.510	18.659	3.187	0.040	0.008	0.054	0.008
2454875.892436	211.315	4.666	-34.300	-0.323	-3.206	0.132	-1.566	96.604	-3.106	0.025	-45.271	141.447	21.970	2.665	0.002	0.007	0.062	0.008
2454876.618080	52.579	6.087	-4.570	-0.025	-2.875	0.136	108.914	97.709	0.320	0.033	-103.419	112.870	20.179	3.335	0.087	0.010	0.166	0.010
2454876.766053	51.893	4.985	-184.748	-1.827	-2.667	0.138	146.325	98.083	1.540	0.031	149.563	154.900	13.592	2.900	0.121	0.008	0.155	0.009
2454876.890513	1.397	4.302	-137.969	-1.359	-0.889	0.156	162.387	98.244	1.563	0.028	69.021	51.322	1.987	2.381	0.096	0.008	0.131	0.008
2454877.618119	-185.353	4.173	94.044	0.961	-4.401	0.121	87.340	97.493	-0.594	0.023	87.238	223.869	22.386	2.522	-0.041	0.006	0.079	0.007
2454877.769133	-177.671	4.026	-0.666	0.014	-3.533	0.129	84.345	97.463	-1.653	0.024	-3.604	118.801	15.624	2.676	-0.020	0.006	0.047	0.007
2454877.897032	-160.721	3.745	54.556	0.566	-2.488	0.140	-4.616	96.574	-1.384	0.022	6.935	60.988	11.824	2.300	0.002	0.006	0.080	0.006
2454891.703262	-181.749	3.867	-8.089	-0.060	-4.036	0.124	151.296	98.133	6.312	0.028	120.670	76.759	21.121	2.253	0.031	0.006	0.064	0.006
2454891.872272	-152.146	3.814	11.572	0.136	0.213	0.167	131.657	97.936	5.976	0.029	40.862	89.856	-5.006	2.450	-0.064	0.006	-0.012	0.007
2454892.715716	26.934	3.879	52.355	0.544	0.337	0.168	120.268	97.823	5.500	0.030	-11.959	204.055	-2.366	1.676	-0.041	0.006	-0.026	0.007
2454893.702287	152.656	12.048	-9.607	-0.076	1.239	0.177	93.979	97.560	1.885	0.068	-675.122	698.059	3.010	6.076	-0.062	0.019	-0.031	0.020
2454894.784196	-82.500	5.804	174.461	1.765	-0.380	0.161	238.429	99.004	1.772	0.038	-209.410	281.118	1.029	3.358	0.000	0.009	0.038	0.010
2454975.592591	196.143	2.003	–	–	–	–	–	–	-9.980	0.009	-3.368	26.561	14.786	1.241	-0.083	0.003	-0.068	0.003
2454976.501983	25.930	5.967	7.317	0.267	4.664	0.211	-657.882	90.043	-8.915	0.025	20.769	50.785	-18.198	4.529	-0.060	0.010	-0.103	0.011
2454976.688093	-41.259	3.065	9.027	0.200	2.445	0.189	-648.826	90.137	-8.781	0.013	43.205	31.116	-6.965	2.538	-0.023	0.005	-0.071	0.005

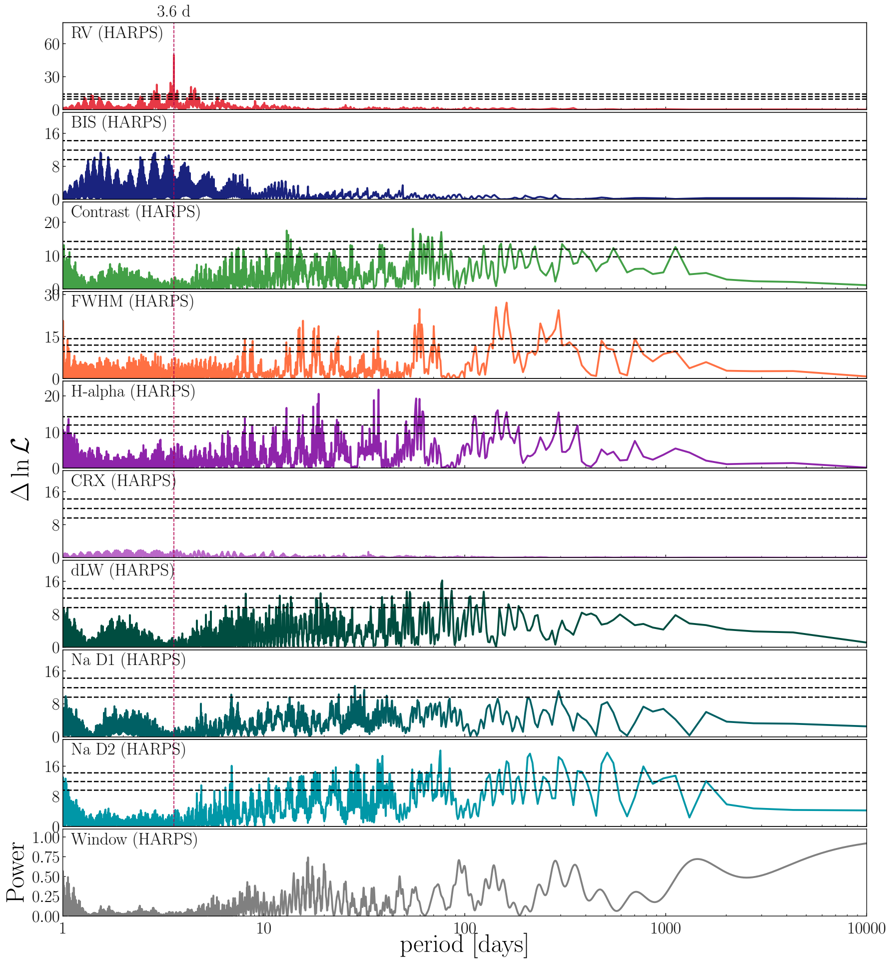

Figure C2: Full set of maximum likelihood periodograms for HARPS radial velocity and activity measurements of TW Hya.

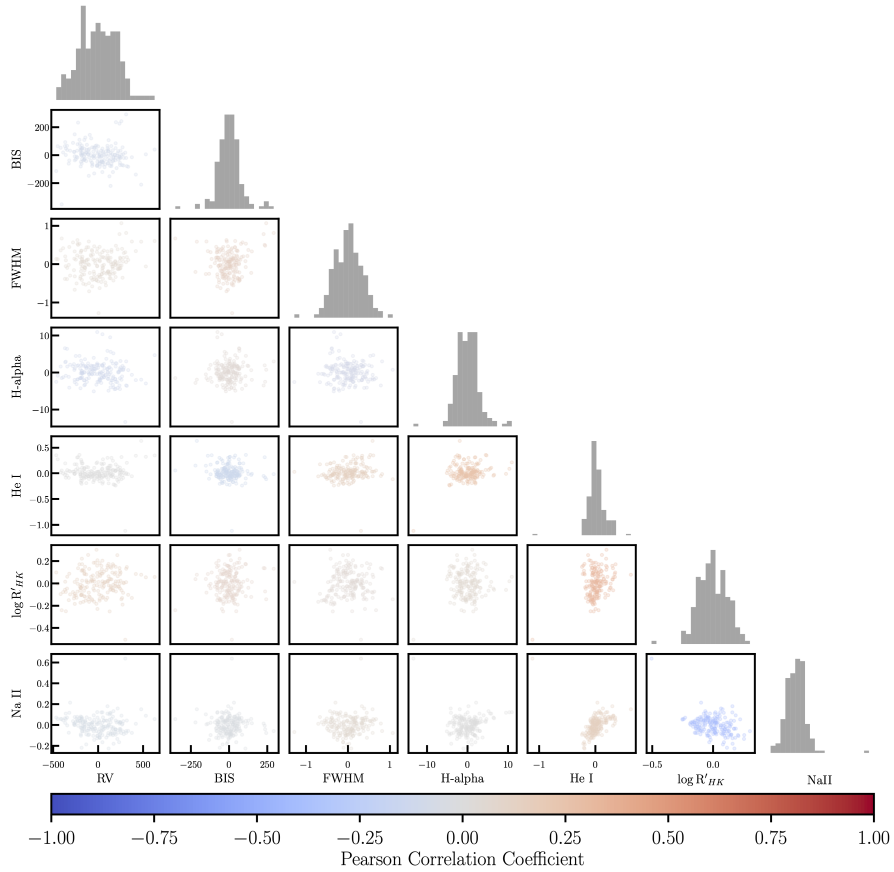

Figure C3: Corner plot showing the correlations between the FEROS RVs and stellar activity data. The individual datasets are colored according to the Pearson correlation coefficients.

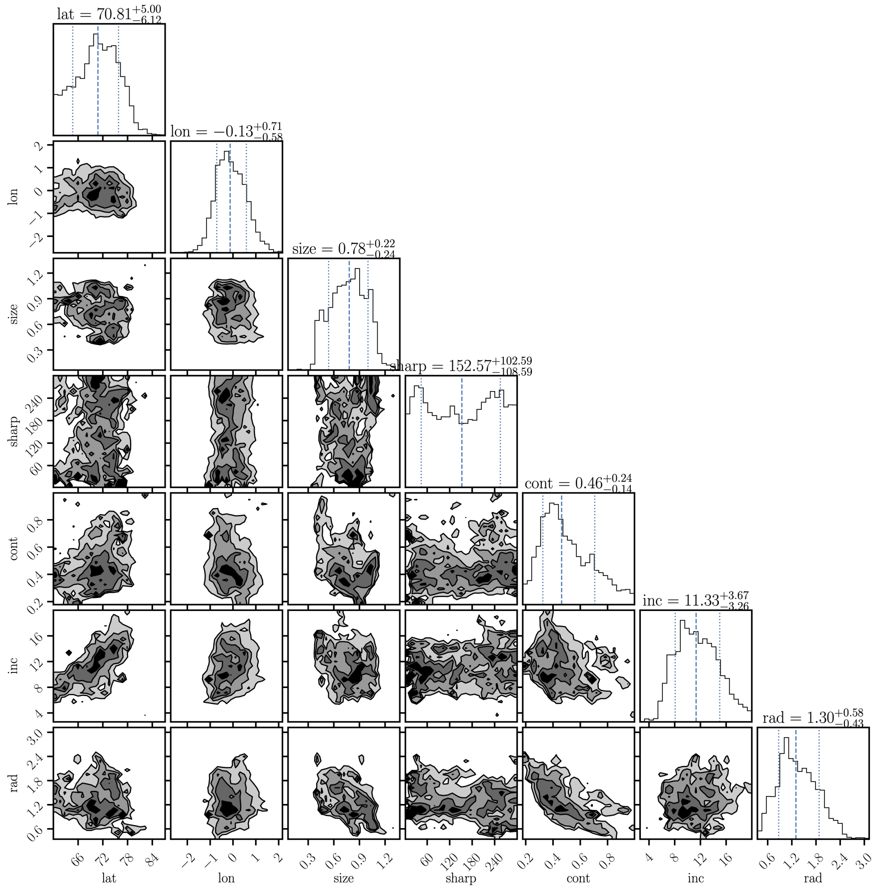

Figure C4: Corner plot showing the posterior sample distributions of our spot-model MCMC.

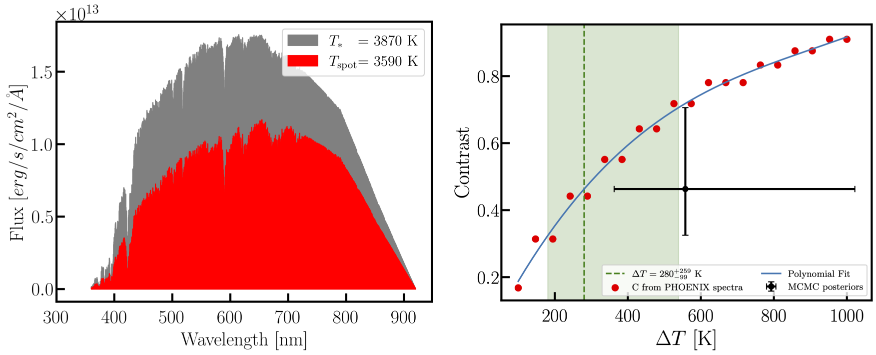

Figure C5: *Left*: Synthetic PHOENIX spectra for a stellar temperature of 3870 K and a spot temperature of 3590 K, modulated with the FEROS response curve. *Right*: Estimation of the temperature difference from a set of synthetic PHOENIX spectra.

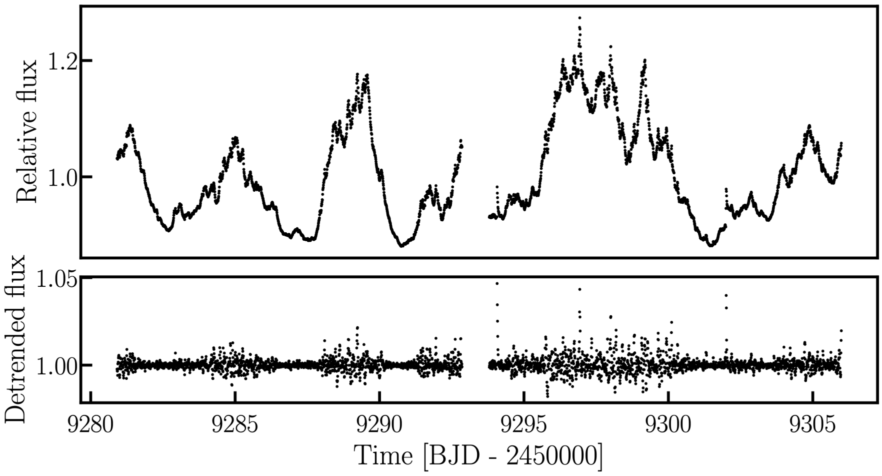

Figure C6: Same as Figure 5.10 but for *TESS* sector 36.

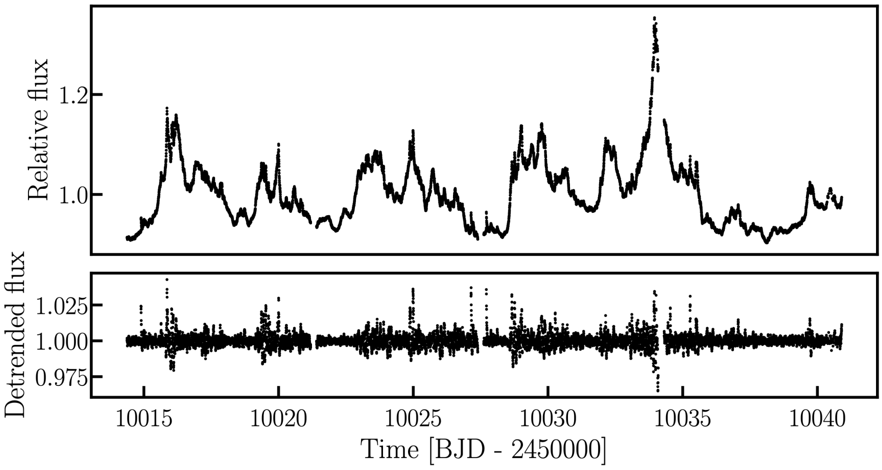

Figure C7: Same as Figure 5.10 but for *TESS* sector 63.

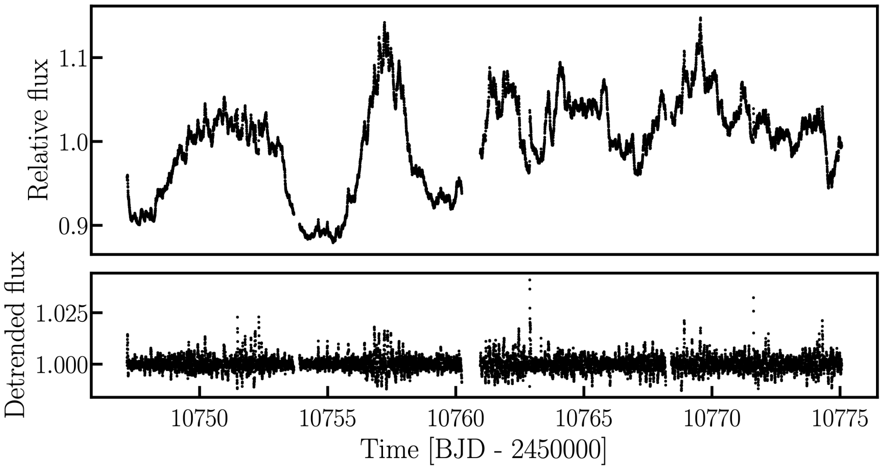

Figure C8: Same as Figure 5.10 but for *TESS* sector 90.

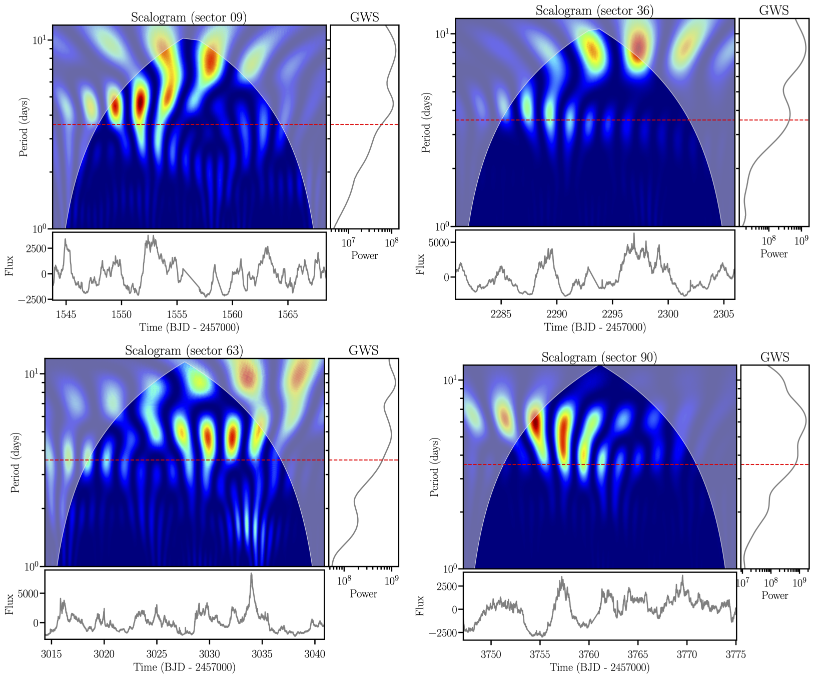

Figure C9: Wavelet analysis of the *TESS* photometry of TW Hya. The main panel shows the scalogram of the Continuous Wavelet Transform (CWT) and the Cone-of-Influence (CoI) as a shaded region. Below the scalogram, the time series are shown and to the right the power of the Global Wavelet Spectrum (GWS). The 3.57 d signal is marked as a red dashed line.

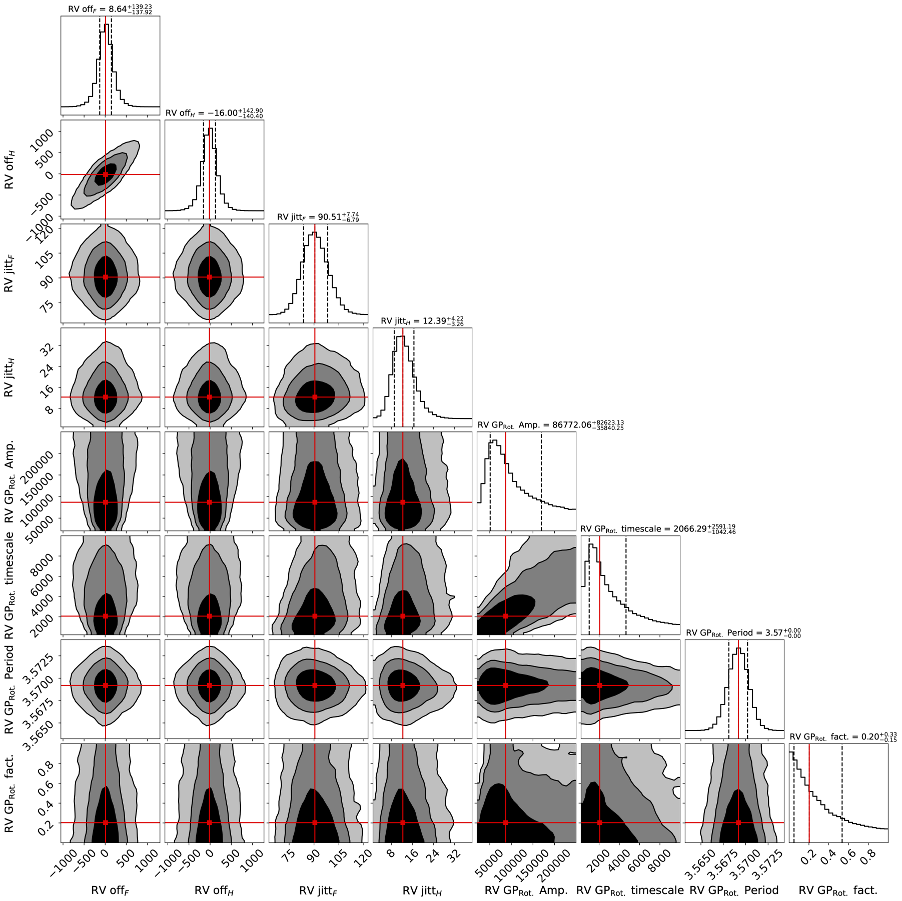

Figure C10: Posterior distribution of the rotational kernel gaussian process hyperparameters and radial velocity offsets and jitters. The shaded contours show the 1−, 2− and 3 − σ uncertainty levels, whereas the red cross marks the median of the distribution.

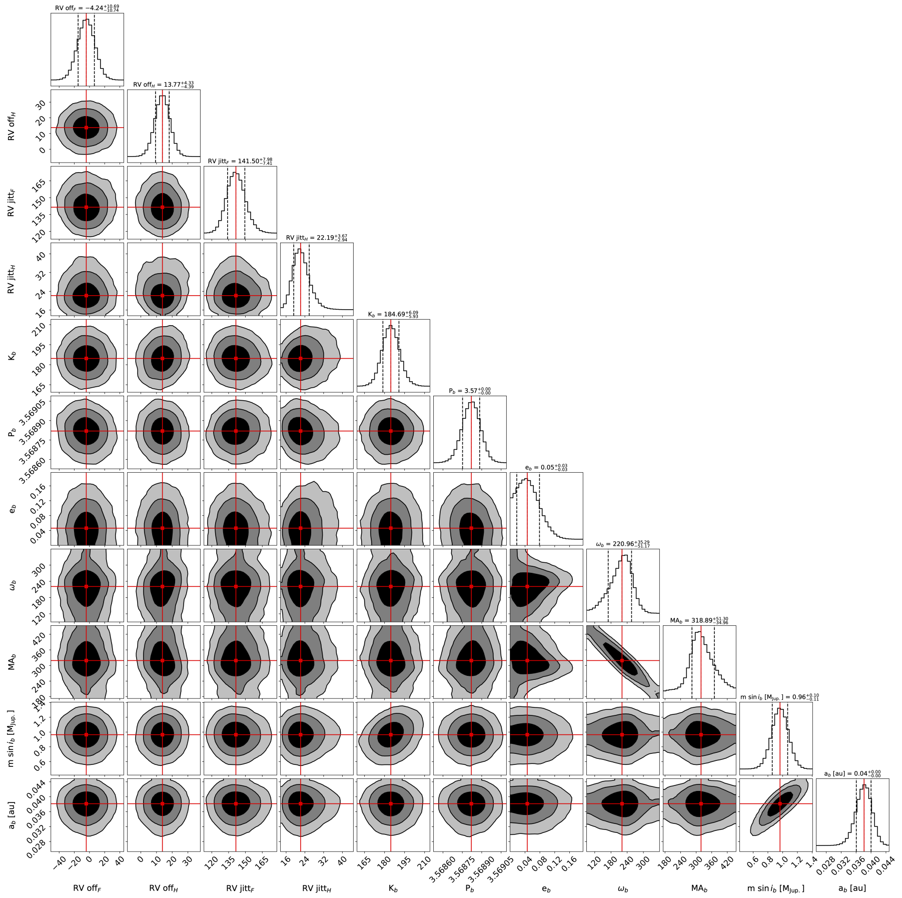

Figure C11: Same as Figure C10, but for the posterior distribution of the Keplerian model.

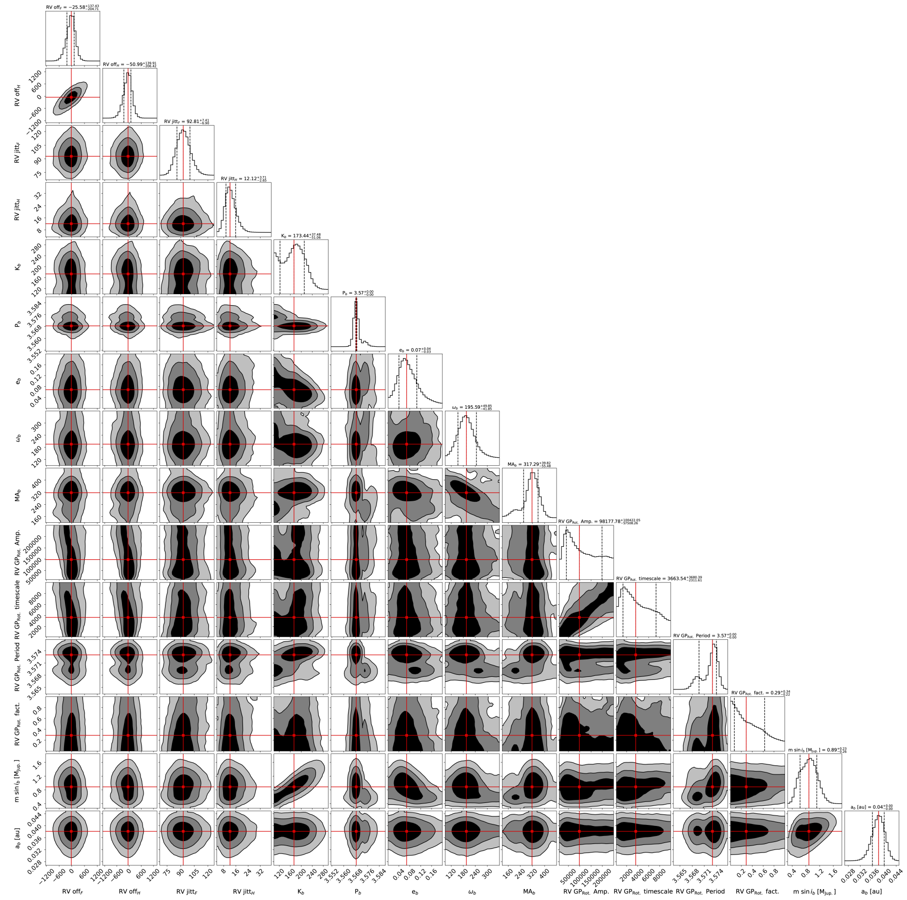

Figure C12: Same as Figure C10, but for the posterior distribution of the combined GP+Keplerian model.

BIBLIOGRAPHY

[1] L. Acuña et al. "GASTLI. An open-source coupled interior-atmosphere model to unveil gas-giant composition." In: *A&A* 688, A60 (Aug. 2024), A60. DOI: 10.1051/0004-6361/202450559. arXiv: 2406.10032 [astro-ph.EP].

[2] Lorena Acuña et al. "Characterisation of the hydrospheres of TRAPPIST-1 planets." In: *A&A* 647, A53 (Mar. 2021), A53. DOI: 10.1051/0004-6361/202039885. arXiv: 2101.08172 [astro-ph.EP].

[3] Simon H Albrecht et al. "Stellar obliquities in exoplanetary systems." In: *Publications of the Astronomical Society of the Pacific* 134.1038 (2022), p. 082001.

[4] Silvia H. P. Alencar et al. "Variability of Southern T Tauri Stars. II. The Spectral Variability of the Classical T Tauri Star TW Hydrae." In: *ApJ* 571.1 (2002), pp. 378–393. DOI: 10.1086/339878.

[5] A. Aller et al. "Planetary nebulae seen with TESS: Discovery of new binary central star candidates from Cycle 1." In: *A&A* 635 (Mar. 2020), A128. ISSN: 0004-6361, 1432-0746. DOI: 10.1051/0004-6361/201937118. URL: https://www.aanda.org/10.1051/0004-6361/201937118 (visited on 06/03/2022).

[6] J. M. Almenara et al. "TOI-3884 b: A rare 6-R_E planet that transits a low-mass star with a giant and likely polar spot." In: *A&A* 667, L11 (Nov. 2022), p. L11. DOI: 10.1051/0004-6361/202244791. arXiv: 2210.10909 [astro-ph.EP].

[7] A. J. Alves et al. "Dynamics of the 3/1 planetary mean-motion resonance: an application to the HD60532 b-c planetary system." In: *Celestial Mechanics and Dynamical Astronomy* 124.3 (Mar. 2016), pp. 311–334. DOI: 10.1007/s10569-015-9664-x. arXiv: 1511.08727 [astro-ph.EP].

[8] Isabel Angelo et al. "Kepler-1656b's Extreme Eccentricity: Signature of a Gentle Giant." In: *AJ* 163.5, 227 (May 2022), p. 227. DOI: 10.3847/1538-3881/ac6094. arXiv: 2204.00019 [astro-ph.EP].

[9] Guillem Anglada-Escudé et al. "The HARPS-TERRA Project. I. Description of the Algorithms, Performance, and New Measurements on a Few Remarkable Stars Observed by HARPS." In: *ApJS* 200.2, 15 (June 2012), p. 15. DOI: 10.1088/0067-0049/200/2/15. arXiv: 1202.2570 [astro-ph.EP].

[10] Étienne Artigau et al. "Line-by-line Velocity Measurements: an Outlier-resistant Method for Precision Velocimetry." In: *AJ* 164.3, 84 (Sept. 2022), p. 84. DOI: `10.3847/1538-3881/ac7ce6`. arXiv: `2207.13524 [astro-ph.IM]`.

[11] Pawel Artymowicz et al. "Dynamics of Binary-Disk Interaction. I. Resonances and Disk Gap Sizes." In: *ApJ* 421 (Feb. 1994), p. 651. DOI: `10.1086/173679`.

[12] N. Astudillo-Defru et al. "The HARPS search for southern extra-solar planets. XXXVI. Planetary systems and stellar activity of the M dwarfs GJ 3293, GJ 3341, and GJ 3543." In: *A&A* 575, A119 (Mar. 2015), A119. DOI: `10.1051/0004-6361/201424253`. arXiv: `1411.7048 [astro-ph.EP]`.

[13] O. Attia et al. "DREAM II. The spin-orbit angle distribution of close-in exoplanets under the lens of tides." In: *arXiv e-prints*, arXiv:2305.00829 (May 2023), arXiv:2305.00829. DOI: `10.48550/arXiv.2305.00829`. arXiv: `2305.00829 [astro-ph.EP]`.

[14] C. A. L. Bailer-Jones et al. "Estimating Distance from Parallaxes. IV. Distances to 1.33 Billion Stars in Gaia Data Release 2." In: *AJ* 156.2, 58 (2018), p. 58. DOI: `10.3847/1538-3881/aacb21`. arXiv: `1804.10121 [astro-ph.SR]`.

[15] Roman V. Baluev. "Detecting non-sinusoidal periodicities in observational data using multiharmonic periodograms." In: *MNRAS* 395.3 (May 2009), pp. 1541–1548. DOI: `10.1111/j.1365-2966.2009.14634.x`. arXiv: `0811.0907 [astro-ph]`.

[16] A. Baranne et al. "ELODIE: A spectrograph for accurate radial velocity measurements." In: *A&AS* 119 (Oct. 1996), pp. 373–390.

[17] J P Beaulieu et al. "Discovery of the distant cool sub-Neptune mass planet OGLE 2005-BLG-390Lb by microlensing." In: *Nature* 439.7075 (Nov. 2005). URL: `https://www.osti.gov/biblio/887282`.

[18] Edwin A. Bergin et al. "An old disk still capable of forming a planetary system." In: *Nature* 493.7434 (2013), pp. 644–646. DOI: `10.1038/nature11805`. arXiv: `1303.1107 [astro-ph.SR]`.

[19] I. Boisse et al. "Stellar activity of planetary host star HD 189 733." In: *A&A* 495.3 (Mar. 2009), pp. 959–966. DOI: `10.1051/0004-6361:200810648`. arXiv: `0811.3923 [astro-ph]`.

[20] X. Bonfils et al. "The HARPS search for southern extra-solar planets. XXXIV. A planetary system around the nearby M dwarf <ASTROBJ>GJ 163</ASTROBJ>, with a super-Earth possibly in the habitable zone." In: *A&A* 556, A110 (Aug. 2013), A110. DOI: `10.1051/0004-6361/201220237`. arXiv: `1306.0904 [astro-ph.EP]`.

[21] L. Borsato et al. "Exploiting timing capabilities of the CHEOPS mission with warm-Jupiter planets." In: *MNRAS* 506.3 (Sept. 2021), pp. 3810–3830. DOI: `10.1093/mnras/stab1782`.

[22] William J. Borucki et al. "Kepler Planet-Detection Mission: Introduction and First Results." In: *Science* 327.5968 (Feb. 2010), p. 977. DOI: `10.1126/science.1185402`.

[23] Vladimir Bozhilov et al. "A 2:1 Mean-motion Resonance Super-Jovian Pair Revealed by TESS, FEROS, and HARPS." In: *ApJL* 946.2, L36 (Apr. 2023), p. L36. DOI: `10.3847/2041-8213/acbd4f`. arXiv: `2302.10838 [astro-ph.EP]`.

[24] Madison T. Brady et al. "Kepler-1656b: A Dense Sub-Saturn with an Extreme Eccentricity." In: *AJ* 156.4, 147 (Oct. 2018), p. 147. DOI: `10.3847/1538-3881/aad773`. arXiv: `1809.08436 [astro-ph.EP]`.

[25] Rafael Brahm et al. "CERES: A Set of Automated Routines for Echelle Spectra." In: *PASP* 129.973 (Mar. 2017), p. 034002. ISSN: 0004-6280, 1538-3873. DOI: `10.1088/1538-3873/aa5455`. URL: `https://iopscience.iop.org/article/10.1088/1538-3873/aa5455` (visited on 06/03/2022).

[26] Rafael Brahm et al. "ZASPE : A Code to Measure Stellar Atmospheric Parameters and their Covariance from Spectra." en. In: *MNRAS* (Jan. 2017), stx144. ISSN: 0035-8711, 1365-2966. DOI: `10.1093/mnras/stx144`. URL: `https://academic.oup.com/mnras/article-lookup/doi/10.1093/mnras/stx144` (visited on 06/03/2022).

[27] Rafael Brahm et al. "HD 1397b: A Transiting Warm Giant Planet Orbiting A $V = 7.8$ mag Subgiant Star Discovered by *TESS*." In: *AJ* 158.1 (July 2019), p. 45. ISSN: 1538-3881. DOI: `10.3847/1538-3881/ab279a`. URL: `https://iopscience.iop.org/article/10.3847/1538-3881/ab279a` (visited on 06/03/2022).

[28] Rafael Brahm et al. "TOI-481 b and TOI-892 b: Two Long-period Hot Jupiters from the Transiting Exoplanet Survey Satellite." In: *AJ* 160.5, 235 (Nov. 2020), p. 235. DOI: `10.3847/1538-3881/abba3b`. arXiv: `2009.08881 [astro-ph.EP]`.

[29] Alessandro Bressan et al. "parsec : stellar tracks and isochrones with the PAdova and TRieste Stellar Evolution Code: parsec : *tracks and isochrones*." en. In: *Monthly Notices of the Royal Astronomical Society* 427.1 (Nov. 2012), pp. 127–145. ISSN: 00358711, 13652966. DOI: `10.1111/j.1365-2966.2012.21948.x`. URL: `https://academic.oup.com/mnras/article-lookup/doi/10.1111/j.1365-2966.2012.21948.x` (visited on 06/07/2022).

[30] T. M. Brown et al. "Las Cumbres Observatory Global Telescope Network." In: *PASP* 125.931 (Sept. 2013), p. 1031. DOI: `10.1086/673168`. arXiv: `1305.2437 [astro-ph.IM]`.

[31] M. A. Burlak et al. "On the causes of brightness variability of the young star BP Tau." In: *arXiv e-prints*, arXiv:2504.09290 (Apr. 2025), arXiv:2504.09290. DOI: `10.48550/arXiv.2504.09290`. arXiv: `2504.09290 [astro-ph.SR]`.

[32] R. Paul Butler et al. "A Planet Orbiting 47 Ursae Majoris." In: *ApJL* 464 (June 1996), p. L153. DOI: `10.1086/310102`.

[33] J. Cabrera et al. "Transiting exoplanets from the CoRoT space mission . XIII. CoRoT-13b: a dense hot Jupiter in transit around a star with solar metallicity and super-solar lithium content." In: *A&A* 522, A110 (Nov. 2010), A110. DOI: `10.1051/0004-6361/201015154`. arXiv: `1007.5481 [astro-ph.EP]`.

[34] F. Castelli et al. *New Grids of ATLAS9 Model Atmospheres*. Tech. rep. arXiv:astro-ph/0405087. arXiv:astro-ph/0405087 type: article. arXiv, May 2004. URL: `http://arxiv.org/abs/astro-ph/0405087` (visited on 06/03/2022).

[35] David Charbonneau et al. "Detection of Planetary Transits Across a Sun-like Star." In: *ApJL* 529.1 (Jan. 2000), pp. L45–L48. DOI: `10.1086/312457`. arXiv: `astro-ph/9911436 [astro-ph]`.

[36] Karen A. Collins et al. "AstroImageJ: Image Processing and Photometric Extraction for Ultra-precise Astronomical Light Curves." In: *AJ* 153.2, 77 (Feb. 2017), p. 77. DOI: `10.3847/1538-3881/153/2/77`. arXiv: `1701.04817 [astro-ph.IM]`.

[37] Jeffrey D. Crane et al. "The Carnegie Planet Finder Spectrograph." In: *Ground-based and Airborne Instrumentation for Astronomy*. Ed. by Ian S. McLean et al. Vol. 6269. Society of Photo-Optical Instrumentation Engineers (SPIE) Conference Series. June 2006, p. 626931. DOI: `10.1117/12.672339`.

[38] Jeffrey D. Crane et al. "The Carnegie Planet Finder Spectrograph: a status report." In: *Ground-based and Airborne Instrumentation for Astronomy II*. Ed. by Ian S. McLean et al. Vol. 7014. Society of Photo-Optical Instrumentation Engineers (SPIE) Conference Series. July 2008, p. 701479. DOI: `10.1117/12.789637`.

[39] Jeffrey D. Crane et al. "The Carnegie Planet Finder Spectrograph: integration and commissioning." In: *Ground-based and Airborne Instrumentation for Astronomy III*. Ed. by Ian S. McLean et al. Vol. 7735. Society of Photo-Optical Instrumentation Engineers (SPIE) Conference Series. July 2010, p. 773553. DOI: `10.1117/12.857792`.

[40] Rebekah I. Dawson et al. “Origins of Hot Jupiters.” In: *ARA&A* 56 (2018), pp. 175–221. DOI: 10.1146/annurev-astro-081817-051853.

[41] Rebekah I. Dawson et al. “Precise Transit and Radial-velocity Characterization of a Resonant Pair: The Warm Jupiter TOI-216c and Eccentric Warm Neptune TOI-216b.” In: *AJ* 161.4, 161 (Apr. 2021), p. 161. DOI: 10.3847/1538-3881/abd8d0. arXiv: 2102.06754 [astro-ph.EP].

[42] John H. Debes et al. “The 0.5-2.22 μm Scattered Light Spectrum of the Disk around TW Hya: Detection of a Partially Filled Disk Gap at 80 AU.” In: *ApJ* 771.1, 45 (July 2013), p. 45. DOI: 10.1088/0004-637X/771/1/45. arXiv: 1306.2969 [astro-ph.EP].

[43] Brice-Olivier Demory et al. “Lack of Inflated Radii for Kepler Giant Planet Candidates Receiving Modest Stellar Irradiation.” In: *ApJS* 197.1, 12 (Nov. 2011), p. 12. DOI: 10.1088/0067-0049/197/1/12. arXiv: 1110.6180 [astro-ph.EP].

[44] J. F. Donati et al. “The large-scale magnetic field and poleward mass accretion of the classical T Tauri star TW Hya.” In: *MNRAS* 417.1 (2011), pp. 472–487. DOI: 10.1111/j.1365-2966.2011.19288.x. arXiv: 1106.4162 [astro-ph.SR].

[45] J. F. Donati et al. “SPIRou spectropolarimetry of the T Tauri star TW Hydrae: magnetic fields, accretion, and planets.” In: *MNRAS* 531.3 (July 2024), pp. 3256–3278. DOI: 10.1093/mnras/stae1227. arXiv: 2405.04461 [astro-ph.SR].

[46] Jean-François Donati et al. “The Large-Scale Axisymmetric Magnetic Topology of a Very-Low-Mass Fully Convective Star.” In: *Science* 311.5761 (Feb. 2006), pp. 633–635. DOI: 10.1126/science.1121102. arXiv: astro-ph/0602069 [astro-ph].

[47] R. J. Dorn et al. “CRIRES+: Exploring the Cold Universe at High Spectral Resolution.” In: *The Messenger* 156 (June 2014), pp. 7–11.

[48] R. J. Dorn et al. “CRIRES$^+$ on sky at the ESO Very Large Telescope. Observing the Universe at infrared wavelengths and high spectral resolution.” In: *A&A* 671, A24 (Mar. 2023), A24. DOI: 10.1051/0004-6361/202245217. arXiv: 2301.08048 [astro-ph.IM].

[49] Georgina Dransfield et al. “Observation scheduling and automatic data reduction for the Antarctic Telescope, ASTEP+.” In: *Observatory Operations: Strategies, Processes, and Systems IX*. Ed. by David S. Adler et al. Vol. 12186. Society of Photo-Optical Instrumentation Engineers (SPIE) Conference Series. Aug. 2022, 121861F. DOI: 10.1117/12.2629920. arXiv: 2208.04501 [astro-ph.EP].

[50] X. Dumusque. “Measuring precise radial velocities on individual spectral lines. I. Validation of the method and application to mitigate stellar activity.” In: *A&A* 620, A47 (Nov. 2018), A47. DOI: 10.1051/0004-6361/201833795. arXiv: 1809.01548 [astro-ph.SR].

[51] Douglas K. Duncan et al. “CA II H and K Measurements Made at Mount Wilson Observatory, 1966–1983.” In: *ApJS* 76 (May 1991), p. 383. DOI: 10.1086/191572.

[52] Jason Eastman et al. “EXOFAST: A Fast Exoplanetary Fitting Suite in IDL.” In: *PASP* 125.923 (Jan. 2013), p. 83. DOI: 10.1086/669497. arXiv: 1206.5798 [astro-ph.IM].

[53] Jan Eberhardt et al. “Three Warm Jupiters around Solar-analog Stars Detected with TESS.” In: *AJ* 166.6, 271 (Dec. 2023), p. 271. DOI: 10.3847/1538-3881/ad06bc. arXiv: 2402.17592 [astro-ph.EP].

[54] Jan Eberhardt et al. “A Massive Spot on the Stellar Surface of TW Hya.” In: *in prep.* (2025).

[55] Jan Eberhardt et al. “TOI-6695: A Pair of Near-resonant Massive Planets Observed with TESS from the WINE Survey.” In: *AJ* 169.6, 298 (June 2025), p. 298. DOI: 10.3847/1538-3881/adc44e.

[56] Mohammed El Mufti et al. “TOI 560: Two Transiting Planets Orbiting a K Dwarf Validated with iSHELL, PFS, and HIRES RVs.” In: *AJ* 165.1, 10 (Jan. 2023), p. 10. DOI: 10.3847/1538-3881/ac9834.

[57] Alexandre Emsenhuber et al. “The New Generation Planetary Population Synthesis (NGPPS). I. Bern global model of planet formation and evolution, model tests, and emerging planetary systems.” In: *A&A* 656, A69 (Dec. 2021), A69. DOI: 10.1051/0004-6361/202038553. arXiv: 2007.05561 [astro-ph.EP].

[58] Alexandre Emsenhuber et al. “The New Generation Planetary Population Synthesis (NGPPS). II. Planetary population of solar-like stars and overview of statistical results.” In: *A&A* 656, A70 (Dec. 2021), A70. DOI: 10.1051/0004-6361/202038863. arXiv: 2007.05562 [astro-ph.EP].

[59] Juan I. Espinoza-Retamal et al. “The Aligned Orbit of the Eccentric Proto Hot Jupiter TOI-3362b.” In: *ApJL* 958.2, L20 (Dec. 2023), p. L20. DOI: 10.3847/2041-8213/ad096d. arXiv: 2309.03306 [astro-ph.EP].

[60] Néstor Espinoza et al. “HD 213885b: a transiting 1-d-period super-Earth with an Earth-like composition around a bright (V = 7.9) star unveiled by TESS.” In: *MNRAS* 491.2 (Jan. 2020), pp. 2982–2999. DOI: 10.1093/mnras/stz3150. arXiv: 1903.07694 [astro-ph.EP].

[61] Néstor Espinoza et al. “juliet: a versatile modelling tool for transiting and non-transiting exoplanetary systems.” en. In: *MNRAS* 490.2 (Dec. 2019), pp. 2262–2283. ISSN: 0035-8711, 1365-2966. DOI: `10.1093/mnras/stz2688`. URL: `https://academic.oup.com/mnras/article/490/2/2262/5583056` (visited on 06/03/2022).

[62] Mark E. Everett et al. “High-Resolution Multi-Band Imaging for Validation and Characterization of Small Kepler Planets.” In: *AJ* 149.2, 55 (Feb. 2015), p. 55. DOI: `10.1088/0004-6256/149/2/55`. arXiv: `1411.3621 [astro-ph.EP]`.

[63] Daniel Foreman-Mackey et al. “emcee: The MCMC Hammer.” In: *PASP* 125.925 (Mar. 2013), p. 306. DOI: `10.1086/670067`. arXiv: `1202.3665 [astro-ph.IM]`.

[64] Gaia Collaboration. *VizieR Online Data Catalog: Gaia EDR3 (Gaia Collaboration, 2020)*. VizieR On-line Data Catalog: I/350. Originally published in: 2021A&A...649A...1G; doi:10.5270/esa-1ug. Nov. 2020. DOI: `10.26093/cds/vizier.1350`.

[65] Gaia Collaboration et al. “The Gaia mission.” In: *A&A* 595, A1 (Nov. 2016), A1. DOI: `10.1051/0004-6361/201629272`. arXiv: `1609.04153 [astro-ph.IM]`.

[66] Gaia Collaboration et al. “Gaia Data Release 2. Summary of the contents and survey properties.” In: *A&A* 616, A1 (2018), A1. DOI: `10.1051/0004-6361/201833051`. arXiv: `1804.09365 [astro-ph.GA]`.

[67] Gaia Collaboration et al. “Gaia Data Release 3. Summary of the content and survey properties.” In: *A&A* 674, A1 (June 2023), A1. DOI: `10.1051/0004-6361/202243940`. arXiv: `2208.00211 [astro-ph.GA]`.

[68] Ronald L. Gilliland et al. “Kepler Mission Stellar and Instrument Noise Properties.” In: *ApJS* 197.1, 6 (Nov. 2011), p. 6. DOI: `10.1088/0067-0049/197/1/6`. arXiv: `1107.5207 [astro-ph.SR]`.

[69] Sivan Ginzburg et al. “Heavy-metal Jupiters by major mergers: metallicity versus mass for giant planets.” In: *MNRAS* 498.1 (Oct. 2020), pp. 680–688. DOI: `10.1093/mnras/staa2500`. arXiv: `2006.12500 [astro-ph.EP]`.

[70] J. Gomes da Silva et al. “Long-term magnetic activity of a sample of M-dwarf stars from the HARPS program. I. Comparison of activity indices.” In: *A&A* 534, A30 (Oct. 2011), A30. DOI: `10.1051/0004-6361/201116971`. arXiv: `1109.0321 [astro-ph.SR]`.

[71] T. Guillot et al. “Thermalizing a telescope in Antarctica - analysis of ASTEP observations.” In: *Astronomische Nachrichten* 336.7 (Sept. 2015), p. 638. DOI: 10.1002/asna.201512174. arXiv: 1506.06009 [astro-ph.IM].

[72] Te Han et al. “TESS-Gaia Light Curve: A PSF-based TESS FFI Light-curve Product.” In: *AJ* 165.2, 71 (Feb. 2023), p. 71. DOI: 10.3847/1538-3881/acaaa7. arXiv: 2301.03704 [astro-ph.IM].

[73] Nathan C. Hara et al. “FENRIR: A statistical model of stellar variability: I. A physics-based, fast Gaussian process model to represent stellar activity and perform statistical Doppler imaging.” In: *A&A* 696, A141 (Apr. 2025), A141. DOI: 10.1051/0004-6361/202346391. arXiv: 2304.08489 [astro-ph.SR].

[74] G. Hébrard et al. “SOPHIE velocimetry of Kepler transit candidates. XIX. The transiting temperate giant planet KOI-3680b.” In: *A&A* 623, A104 (Mar. 2019), A104. DOI: 10.1051/0004-6361/201834333. arXiv: 1811.09580 [astro-ph.EP].

[75] Gregory W. Henry et al. “A Transiting “51 Peg-like” Planet.” In: *ApJL* 529.1 (Jan. 2000), pp. L41–L44. DOI: 10.1086/312458.

[76] Gregory J. Herczeg et al. “Twenty-five Years of Accretion onto the Classical T Tauri Star TW Hya.” In: *ApJ* 956.2, 102 (Oct. 2023), p. 102. DOI: 10.3847/1538-4357/acf468. arXiv: 2308.14590 [astro-ph.SR].

[77] Michael Hippke et al. “Optimized transit detection algorithm to search for periodic transits of small planets.” In: *A&A* 623, A39 (Mar. 2019), A39. DOI: 10.1051/0004-6361/201834672. arXiv: 1901.02015 [astro-ph.EP].

[78] Michael Hippke et al. “Wōtan: Comprehensive Time-series Detrending in Python.” In: *AJ* 158.4, 143 (Oct. 2019), p. 143. DOI: 10.3847/1538-3881/ab3984. arXiv: 1906.00966 [astro-ph.EP].

[79] Melissa J. Hobson et al. “A Transiting Warm Giant Planet around the Young Active Star TOI-201.” In: *AJ* 161.5, 235 (May 2021), p. 235. DOI: 10.3847/1538-3881/abeaa1. arXiv: 2103.02685 [astro-ph.EP].

[80] Melissa J. Hobson et al. “TOI-199 b: A Well-characterized 100 day Transiting Warm Giant Planet with TTVs Seen from Antarctica.” In: *AJ* 166.5, 201 (Nov. 2023), p. 201. DOI: 10.3847/1538-3881/acfc1d. arXiv: 2309.14915 [astro-ph.EP].

[81] Steve B. Howell et al. “Speckle Camera Observations for the NASA Kepler Mission Follow-up Program.” In: *AJ* 142.1, 19 (July 2011), p. 19. DOI: 10.1088/0004-6256/142/1/19.

[82] Steve B. Howell et al. “The K2 Mission: Characterization and Early Results.” In: *PASP* 126.938 (Apr. 2014), p. 398. DOI: 10.1086/676406. arXiv: 1402.5163 [astro-ph.IM].

[83] Chelsea X. Huang et al. “Photometry of 10 Million Stars from the First Two Years of TESS Full Frame Images: Part I.” In: *Research Notes of the American Astronomical Society* 4.11, 204 (Nov. 2020), p. 204. DOI: `10.3847/2515-5172/abca2e`. arXiv: `2011.06459 [astro-ph.EP]`.

[84] Chelsea X. Huang et al. “Photometry of 10 Million Stars from the First Two Years of TESS Full Frame Images: Part II.” In: *Research Notes of the American Astronomical Society* 4.11, 206 (Nov. 2020), p. 206. DOI: `10.3847/2515-5172/abca2d`.

[85] Chelsea Huang et al. “Warm Jupiters Are Less Lonely than Hot Jupiters: Close Neighbors.” In: *ApJ* 825.2, 98 (July 2016), p. 98. DOI: `10.3847/0004-637X/825/2/98`. arXiv: `1601.05095 [astro-ph.EP]`.

[86] N. Huélamo et al. “TW Hydrae: evidence of stellar spots instead of a Hot Jupiter.” In: *A&A* 489.2 (2008), pp. L9–L13. DOI: `10.1051/0004-6361:200810596`. arXiv: `0808.2386 [astro-ph]`.

[87] T. O. Husser et al. “A new extensive library of PHOENIX stellar atmospheres and synthetic spectra.” In: *A&A* 553, A6 (May 2013), A6. DOI: `10.1051/0004-6361/201219058`. arXiv: `1303.5632 [astro-ph.SR]`.

[88] M. Ikoma et al. “On the Origin of HD 149026b.” In: *ApJ* 650.2 (Oct. 2006), pp. 1150–1159. DOI: `10.1086/507088`. arXiv: `astro-ph/0607212 [astro-ph]`.

[89] International Astronomical Union. *IAU 2006 General Assembly: Results of the IAU Resolution Votes*. Accessed: 2025-03-18. 2006. URL: `https://www.iau.org/news/pressreleases/detail/iau0603/`.

[90] J. M. Jenkins et al. “The TESS science processing operations center.” In: *Software and Cyberinfrastructure for Astronomy IV*. Vol. 9913. Proc. SPIE. Aug. 2016, 99133E. DOI: `10.1117/12.2233418`.

[91] Jon M. Jenkins. “The Impact of Solar-like Variability on the Detectability of Transiting Terrestrial Planets.” In: *ApJ* 575.1 (Aug. 2002), pp. 493–505. DOI: `10.1086/341136`.

[92] Jon M. Jenkins et al. “Transiting planet search in the Kepler pipeline.” In: *Software and Cyberinfrastructure for Astronomy*. Ed. by Nicole M. Radziwill et al. Vol. 7740. Society of Photo-Optical Instrumentation Engineers (SPIE) Conference Series. July 2010, p. 77400D. DOI: `10.1117/12.856764`.

[93] Jon M. Jenkins et al. *Kepler Data Processing Handbook: Transiting Planet Search*. Kepler Science Document KSCI-19081-003, id. 9. Edited by Jon M. Jenkins. Mar. 2020.

[94] Jianghui Ji et al. "Could the 55 Cancri Planetary System Really Be in the 3:1 Mean Motion Resonance?" In: *ApJL* 585.2 (Mar. 2003), pp. L139–L142. DOI: `10.1086/374391`. arXiv: `astro-ph/0301636 [astro-ph]`.

[95] Matías I. Jones et al. "HD 2685 b: a hot Jupiter orbiting an early F-type star detected by TESS." In: *A&A* 625, A16 (May 2019), A16. DOI: `10.1051/0004-6361/201834640`. arXiv: `1811.05518 [astro-ph.EP]`.

[96] Matías I. Jones et al. "A long-period transiting substellar companion in the super-Jupiters to brown dwarfs mass regime and a prototypical warm-Jupiter detected by TESS." In: *A&A* 683, A192 (Mar. 2024), A192. DOI: `10.1051/0004-6361/202348147`. arXiv: `2401.09657 [astro-ph.EP]`.

[97] Andrés Jordán et al. "K2-287 b: An Eccentric Warm Saturn Transiting a G-dwarf." In: *AJ* 157.3, 100 (Mar. 2019), p. 100. DOI: `10.3847/1538-3881/aafa79`. arXiv: `1809.08879 [astro-ph.EP]`.

[98] Andrés Jordán et al. "TOI-677b: A Warm Jupiter (P = 11.2 days) on an Eccentric Orbit Transiting a Late F-type Star." In: *AJ* 159.4 (Mar. 2020), p. 145. ISSN: 1538-3881. DOI: `10.3847/1538-3881/ab6f67`. URL: `https://iopscience.iop.org/article/10.3847/1538-3881/ab6f67` (visited on 06/03/2022).

[99] Robert E Kass et al. "Bayes factors." In: *Journal of the american statistical association* 90.430 (1995), pp. 773–795.

[100] A. Kaufer et al. "Commissioning FEROS, the new high-resolution spectrograph at La-Silla." In: *The Messenger* 95 (Mar. 1999), pp. 8–12.

[101] HU Käufl et al. "Good Vibrations: Report from the Commissioning of CRIRES." In: *The Messenger* 126 (2006), pp. 32–36.

[102] Hans Ulrich Käufl. "CRIRES: a high resolution infrared spectrograph for ESO's VLT." In: *Precision Spectroscopy in Astrophysics: Proceedings of the ESO/Lisbon/Aveiro Conference held in Aveiro, Portugal, 11–15 September 2006*. Springer. 2008, pp. 227–230.

[103] Eliza M. R. Kempton et al. "A Framework for Prioritizing the TESS Planetary Candidates Most Amenable to Atmospheric Characterization." In: *PASP* 130.993 (Nov. 2018), p. 114401. DOI: `10.1088/1538-3873/aadf6f`. arXiv: `1805.03671 [astro-ph.EP]`.

[104] Diana Kossakowski et al. "TOI-150b and TOI-163b: two transiting hot Jupiters, one eccentric and one inflated, revealed by TESS near and at the edge of the JWST CVZ." In: *MNRAS* 490.1 (Nov. 2019), pp. 1094–1110. DOI: `10.1093/mnras/stz2433`. arXiv: `1906.09866 [astro-ph.EP]`.

[105] Laura Kreidberg. “batman: BAsic Transit Model cAlculatioN in Python.” In: *PASP* 127.957 (Nov. 2015), p. 1161. DOI: `10.1086/683602`. arXiv: `1507.08285 [astro-ph.EP]`.

[106] Michelle Kunimoto et al. “Quick-look Pipeline Lightcurves for 9.1 Million Stars Observed over the First Year of the TESS Extended Mission.” In: *Research Notes of the American Astronomical Society* 5.10, 234 (Oct. 2021), p. 234. DOI: `10.3847/2515-5172/ac2ef0`. arXiv: `2110.05542 [astro-ph.EP]`.

[107] A. M. Lagrange et al. “A probable giant planet imaged in the β Pictoris disk. VLT/NaCo deep L′-band imaging.” In: *A&A* 493.2 (Jan. 2009), pp. L21–L25. DOI: `10.1051/0004-6361:200811325`. arXiv: `0811.3583 [astro-ph]`.

[108] J. Laskar et al. “HD 60532, a planetary system in a 3:1 mean motion resonance.” In: *A&A* 496.2 (Mar. 2009), pp. L5–L8. DOI: `10.1051/0004-6361/200911689`. arXiv: `0902.0667 [astro-ph.EP]`.

[109] Gregory Laughlin et al. “On the Anomalous Radii of the Transiting Extrasolar Planets.” In: *ApJL* 729.1, L7 (Mar. 2011), p. L7. DOI: `10.1088/2041-8205/729/1/L7`. arXiv: `1101.5827 [astro-ph.EP]`.

[110] A. Lecavelier des Etangs et al. “The IAU working definition of an exoplanet.” In: *NewAR* 94, 101641 (June 2022), p. 101641. DOI: `10.1016/j.newar.2022.101641`. arXiv: `2203.09520 [astro-ph.IM]`.

[111] J. Leconte et al. “Structure and evolution of the first CoRoT exoplanets: probing the brown dwarf/planet overlapping mass regime.” In: *A&A* 506.1 (Oct. 2009), pp. 385–389. DOI: `10.1051/0004-6361/200911896`. arXiv: `0907.2669 [astro-ph.EP]`.

[112] Man Hoi Lee et al. “Secular Evolution of Hierarchical Planetary Systems.” In: *ApJ* 592.2 (Aug. 2003), pp. 1201–1216. DOI: `10.1086/375857`. arXiv: `astro-ph/0304454 [astro-ph]`.

[113] Christian Lehmann et al. “Survey for Distant Solar Twins (SDST) - I. EPIC method for stellar parameter measurement.” In: *MNRAS* 512.1 (May 2022), pp. 11–26. DOI: `10.1093/mnras/stac421`. arXiv: `2202.06469 [astro-ph.SR]`.

[114] Jie Li et al. “Kepler data validation II–transit model fitting and multiple-planet search.” In: *PASP* 131.996 (2019), p. 024506.

[115] John H. Livingston et al. “44 Validated Planets from K2 Campaign 10.” In: *AJ* 156.2, 78 (Aug. 2018), p. 78. DOI: `10.3847/1538-3881/aaccde`. arXiv: `1806.11504 [astro-ph.EP]`.

[116] Geoffrey W. Marcy et al. “Precision Radial Velocities with an Iodine Absorption cell.” In: *PASP* 104 (Apr. 1992), p. 270. DOI: `10.1086/132989`.

[117] F. Masset et al. “Reversing type II migration: resonance trapping of a lighter giant protoplanet.” In: *MNRAS* 320.4 (Feb. 2001), pp. L55–L59. DOI: 10.1046/j.1365-8711.2001.04159.x. arXiv: astro-ph/0003421 [astro-ph].

[118] M. Mayor et al. “Setting New Standards with HARPS.” In: *The Messenger* 114 (Dec. 2003), pp. 20–24.

[119] Michel Mayor et al. “A Jupiter-mass companion to a solar-type star.” In: *Nature* 378.6555 (1995), pp. 355–359. DOI: 10.1038/378355a0.

[120] Curtis McCully et al. “Real-time processing of the imaging data from the network of Las Cumbres Observatory Telescopes using BANZAI.” In: *Software and Cyberinfrastructure for Astronomy V*. Ed. by Juan C. Guzman et al. Vol. 10707. Society of Photo-Optical Instrumentation Engineers (SPIE) Conference Series. July 2018, 107070K. DOI: 10.1117/12.2314340. arXiv: 1811.04163 [astro-ph.IM].

[121] D. B. McLaughlin. “Some results of a spectrographic study of the Algol system.” In: *ApJ* 60 (July 1924), pp. 22–31. DOI: 10.1086/142826.

[122] D. Mékarnia et al. “Transiting planet candidates with ASTEP 400 at Dome C, Antarctica.” In: *MNRAS* 463.1 (Nov. 2016), pp. 45–62. DOI: 10.1093/mnras/stw1934.

[123] J. Menu et al. “On the structure of the transition disk around TW Hydrae.” In: *A&A* 564, A93 (Apr. 2014), A93. DOI: 10.1051/0004-6361/201322961. arXiv: 1402.6597 [astro-ph.SR].

[124] Neil Miller et al. “The Heavy-element Masses of Extrasolar Giant Planets, Revealed.” In: *ApJL* 736.2, L29 (Aug. 2011), p. L29. DOI: 10.1088/2041-8205/736/2/L29. arXiv: 1105.0024 [astro-ph.EP].

[125] A. Morbidelli et al. “In situ enrichment in heavy elements of hot Jupiters.” In: *A&A* 675, A75 (July 2023), A75. DOI: 10.1051/0004-6361/202346868. arXiv: 2306.01653 [astro-ph.EP].

[126] C. Mordasini et al. “Characterization of exoplanets from their formation. II. The planetary mass-radius relationship.” In: *A&A* 547, A112 (Nov. 2012), A112. DOI: 10.1051/0004-6361/201118464. arXiv: 1206.3303 [astro-ph.EP].

[127] J. Morin et al. “Large-scale magnetic topologies of mid M dwarfs.” In: *MNRAS* 390.2 (Oct. 2008), pp. 567–581. DOI: 10.1111/j.1365-2966.2008.13809.x. arXiv: 0808.1423 [astro-ph].

[128] Diego J. Muñoz et al. “Long-lived Eccentric Modes in Circumbinary Disks.” In: *ApJ* 905.2, 106 (Dec. 2020), p. 106. DOI: 10.3847/1538-4357/abc74c. arXiv: 2008.08085 [astro-ph.HE].

[129] R. W. Noyes et al. “Rotation, convection, and magnetic activity in lower main-sequence stars.” In: *ApJ* 279 (Apr. 1984), pp. 763–777. DOI: `10.1086/161945`.

[130] Martin Paegert et al. “TESS Input Catalog versions 8.1 and 8.2: Phantoms in the 8.0 Catalog and How to Handle Them.” In: *arXiv e-prints*, arXiv:2108.04778 (Aug. 2021), arXiv:2108.04778. DOI: `10.48550/arXiv.2108.04778`. arXiv: `2108.04778 [astro-ph.EP]`.

[131] Léna Parc et al. “From super-Earths to sub-Neptunes: Observational constraints and connections to theoretical models.” In: *A&A* 688, A59 (Aug. 2024), A59. DOI: `10.1051/0004-6361/202449911`. arXiv: `2406.04311 [astro-ph.EP]`.

[132] Leonardo A. Paredes et al. “The Solar Neighborhood XLVIII: Nine Giant Planets Orbiting Nearby K Dwarfs, and the CHIRON Spectrograph’s Radial Velocity Performance.” In: *AJ* 162.5, 176 (Nov. 2021), p. 176. DOI: `10.3847/1538-3881/ac082a`. arXiv: `2111.15028 [astro-ph.EP]`.

[133] H. Parviainen et al. “Transiting exoplanets from the CoRoT space mission. XXV. CoRoT-27b: a massive and dense planet on a short-period orbit.” In: *A&A* 562, A140 (Feb. 2014), A140. DOI: `10.1051/0004-6361/201323049`. arXiv: `1401.1122 [astro-ph.EP]`.

[134] Mark J. Pecaut et al. “Intrinsic Colors, Temperatures, and Bolometric Corrections of Pre-main-sequence Stars.” In: *ApJS* 208.1, 9 (Sept. 2013), p. 9. DOI: `10.1088/0067-0049/208/1/9`. arXiv: `1307.2657 [astro-ph.SR]`.

[135] F. Pepe et al. “HARPS: ESO’s coming planet searcher. Chasing exoplanets with the La Silla 3.6-m telescope.” In: *The Messenger* 110 (Dec. 2002), pp. 9–14.

[136] F. Pepe et al. “ESPRESSO at VLT. On-sky performance and first results.” In: *A&A* 645, A96 (Jan. 2021), A96. DOI: `10.1051/0004-6361/202038306`. arXiv: `2010.00316 [astro-ph.IM]`.

[137] Michael Perryman. *The Exoplanet Handbook*. 2014.

[138] J. Pons et al. “Secular evolution of resonant planets in the coplanar case. Application to the systems HD 73526 and HD 31527.” In: *A&A* 685, A105 (May 2024), A105. DOI: `10.1051/0004-6361/202348378`.

[139] D. Queloz et al. “From CORALIE to HARPS. The way towards 1 m s^{-1} precision Doppler measurements.” In: *The Messenger* 105 (Sept. 2001), pp. 1–7.

[140] D. Queloz et al. “No planet for HD 166435.” In: *A&A* 379 (Nov. 2001), pp. 279–287. DOI: `10.1051/0004-6361:20011308`. arXiv: `astro-ph/0109491 [astro-ph]`.

[141] Didier Queloz. “Echelle Spectroscopy with a CCD at Low Signal-To-Noise Ratio.” In: *New Developments in Array Technology and Applications*. Ed. by A. G. Davis Philip et al. Vol. 167. IAU Symposium. Jan. 1995, p. 221.

[142] St Raetz et al. “Transit analysis of the CoRoT-5, CoRoT-8, CoRoT-12, CoRoT-18, CoRoT-20, and CoRoT-27 systems with combined ground- and space-based photometry.” In: *MNRAS* 483.1 (Feb. 2019), pp. 824–839. DOI: `10.1093/mnras/sty3085`. arXiv: `1812.01536 [astro-ph.EP]`.

[143] Enrico Ragusa et al. “The evolution of large cavities and disc eccentricity in circumbinary discs.” In: *MNRAS* 499.3 (Dec. 2020), pp. 3362–3380. DOI: `10.1093/mnras/staa2954`. arXiv: `2009.10738 [astro-ph.EP]`.

[144] J. Rey et al. “Brown dwarf companion with a period of 4.6 yr interacting with the hot Jupiter CoRoT-20 b.” In: *A&A* 619, A115 (Nov. 2018), A115. DOI: `10.1051/0004-6361/201833180`. arXiv: `1807.01229 [astro-ph.EP]`.

[145] Malena Rice et al. “A Tendency Toward Alignment in Single-star Warm-Jupiter Systems.” In: *AJ* 164.3, 104 (Sept. 2022), p. 104. DOI: `10.3847/1538-3881/ac8153`. arXiv: `2207.06511 [astro-ph.EP]`.

[146] George R. Ricker et al. “Transiting Exoplanet Survey Satellite.” en. In: *Journal of Astronomical Telescopes, Instruments, and Systems* 1.1 (Oct. 2014), p. 014003. ISSN: 2329-4124. DOI: `10.1117/1.JATIS.1.1.014003`. URL: `http://astronomicaltelescopes.spiedigitallibrary.org/article.aspx?doi=10.1117/1.JATIS.1.1.014003` (visited on 06/03/2022).

[147] M. M. Romanova et al. “Unstable accretion in TW Hya: 3D simulations and comparisons with observations.” In: *MNRAS* 538.1 (Mar. 2025), pp. 480–502. DOI: `10.1093/mnras/staf148`. arXiv: `2501.13294 [astro-ph.SR]`.

[148] R. A. Rossiter. “On the detection of an effect of rotation during eclipse in the velocity of the brigher component of beta Lyrae, and on the constancy of velocity of this system.” In: *ApJ* 60 (July 1924), pp. 15–21. DOI: `10.1086/142825`.

[149] Jason F. Rowe et al. “Validation of Kepler’s Multiple Planet Candidates. III. Light Curve Analysis and Announcement of Hundreds of New Multi-planet Systems.” In: *ApJ* 784.1, 45 (Mar. 2014), p. 45. DOI: `10.1088/0004-637X/784/1/45`. arXiv: `1402.6534 [astro-ph.EP]`.

[150] P. Sarkis et al. “Evidence of three mechanisms explaining the radius anomaly of hot Jupiters.” In: *A&A* 645, A79 (Jan. 2021), A79. DOI: `10.1051/0004-6361/202038361`. arXiv: `2009.04291 [astro-ph.EP]`.

[151] Kevin C. Schlaufman. “Evidence of an Upper Bound on the Masses of Planets and Its Implications for Giant Planet Formation.” In: *ApJ* 853.1, 37 (Jan. 2018), p. 37. DOI: `10.3847/1538-4357/aa961c`. arXiv: `1801.06185 [astro-ph.EP]`.

[152] Martin Schlecker et al. “A Highly Eccentric Warm Jupiter Orbiting TIC 237913194.” In: *AJ* 160.6, 275 (Dec. 2020), p. 275. DOI: `10.3847/1538-3881/abbe03`. arXiv: `2010.03570 [astro-ph.EP]`.

[153] Aaron David Schneider et al. “No evidence for radius inflation in hot Jupiters from vertical advection of heat.” In: *A&A* 666, L11 (Oct. 2022), p. L11. DOI: `10.1051/0004-6361/202244797`. arXiv: `2210.01466 [astro-ph.EP]`.

[154] Nicholas J. Scott et al. “The NN-explore Exoplanet Stellar Speckle Imager: Instrument Description and Preliminary Results.” In: *PASP* 130.987 (May 2018), p. 054502. DOI: `10.1088/1538-3873/aab484`.

[155] J. Setiawan et al. “A young massive planet in a star-disk system.” In: *Nature* 451.7174 (2008), pp. 38–41. DOI: `10.1038/nature06426`.

[156] S. Shibata et al. “The origin of the high metallicity of close-in giant exoplanets. II. The nature of the sweet spot for accretion.” In: *A&A* 659, A28 (Mar. 2022), A28. DOI: `10.1051/0004-6361/202142180`. arXiv: `2112.12623 [astro-ph.EP]`.

[157] A. Sicilia-Aguilar et al. “Stable accretion in young stars: the cases of EX Lupi and TW Hya.” In: *MNRAS* 526.4 (Dec. 2023), pp. 4885–4907. DOI: `10.1093/mnras/stad3029`. arXiv: `2310.02681 [astro-ph.SR]`.

[158] John Skilling. “Nested Sampling.” In: *American Institute of Physics Conference Series*. Ed. by Rainer Fischer et al. Vol. 735. American Institute of Physics Conference Series. Nov. 2004, pp. 395–405. DOI: `10.1063/1.1835238`.

[159] Jeffrey C. Smith et al. “Kepler Presearch Data Conditioning II - A Bayesian Approach to Systematic Error Correction.” In: *PASP* 124.919 (Sept. 2012), p. 1000. DOI: `10.1086/667697`. arXiv: `1203.1383 [astro-ph.IM]`.

[160] Kimberly R. Sokal et al. “Characterizing TW Hydra.” In: *ApJ* 853.2, 120 (2018), p. 120. DOI: `10.3847/1538-4357/aaa1e4`. arXiv: `1712.04785 [astro-ph.SR]`.

[161] John Southworth. “Homogeneous studies of transiting extrasolar planets - IV. Thirty systems with space-based light curves.” In: *MNRAS* 417.3 (Nov. 2011), pp. 2166–2196. DOI: `10.1111/j.1365-2966.2011.19399.x`. arXiv: `1107.1235 [astro-ph.EP]`.

[162] Joshua S. Speagle. “DYNESTY: a dynamic nested sampling package for estimating Bayesian posteriors and evidences.” In: *MNRAS* 493.3 (Apr. 2020), pp. 3132–3158. DOI: `10.1093/mnras/staa278`. arXiv: `1904.02180 [astro-ph.IM]`.

[163] Keivan G. Stassun et al. “The Revised TESS Input Catalog and Candidate Target List.” In: *AJ* 158.4, 138 (Oct. 2019), p. 138. DOI: `10.3847/1538-3881/ab3467`. arXiv: `1905.10694 [astro-ph.SR]`.

[164] M. C. Stumpe et al. “Multiscale Systematic Error Correction via Wavelet-Based Bandsplitting in Kepler Data.” In: *PASP* 126 (Jan. 2014), p. 100. DOI: `10.1086/674989`.

[165] Martin C. Stumpe et al. “Kepler Presearch Data Conditioning I—Architecture and Algorithms for Error Correction in Kepler Light Curves.” In: *PASP* 124.919 (Sept. 2012), p. 985. DOI: `10.1086/667698`. arXiv: `1203.1382 [astro-ph.IM]`.

[166] John P. Subasavage et al. “SMARTS revealed.” In: *Observatory Operations: Strategies, Processes, and Systems III*. Ed. by David R. Silva et al. Vol. 7737. Society of Photo-Optical Instrumentation Engineers (SPIE) Conference Series. July 2010, p. 77371C. DOI: `10.1117/12.859145`.

[167] Prakruti Sudarshan et al. “How cooling influences circumbinary discs.” In: *A&A* 664, A157 (Aug. 2022), A157. DOI: `10.1051/0004-6361/202243472`. arXiv: `2206.07749 [astro-ph.EP]`.

[168] Marcelo Tala Pinto et al. “Three warm Jupiters orbiting TOI-6628, TOI-3837, and TOI-5027 and one sub-Saturn orbiting TOI-2328.” In: *A&A* 694, A268 (Feb. 2025), A268. DOI: `10.1051/0004-6361/202452517`. arXiv: `2412.02069 [astro-ph.EP]`.

[169] Jamie Tayar et al. “A Guide to Realistic Uncertainties on the Fundamental Properties of Solar-type Exoplanet Host Stars.” In: *ApJ* 927.1, 31 (Mar. 2022), p. 31. DOI: `10.3847/1538-4357/ac4bbc`. arXiv: `2012.07957 [astro-ph.EP]`.

[170] Richard Teague et al. “Spiral Structure in the Gas Disk of TW Hya.” In: *ApJL* 884.2, L56 (Oct. 2019), p. L56. DOI: `10.3847/2041-8213/ab4a83`. arXiv: `1910.01532 [astro-ph.EP]`.

[171] Daniel P. Thorngren et al. “The Mass-Metallicity Relation for Giant Planets.” In: *ApJ* 831.1, 64 (Nov. 2016), p. 64. DOI: `10.3847/0004-637X/831/1/64`. arXiv: `1511.07854 [astro-ph.EP]`.

[172] Daniel P. Thorngren et al. “Bayesian Analysis of Hot-Jupiter Radius Anomalies: Evidence for Ohmic Dissipation?” In: *AJ* 155.5, 214 (May 2018), p. 214. DOI: `10.3847/1538-3881/aaba13`. arXiv: `1709.04539 [astro-ph.EP]`.

[173] Daniel Thorngren et al. "Connecting Giant Planet Atmosphere and Interior Modeling: Constraints on Atmospheric Metal Enrichment." In: *ApJL* 874.2, L31 (Apr. 2019), p. L31. DOI: `10.3847/2041-8213/ab1137`. arXiv: `1811.11859 [astro-ph.EP]`.

[174] Andrei Tokovinin. "Ten Years of Speckle Interferometry at SOAR." In: *PASP* 130.985 (Mar. 2018), p. 035002. ISSN: 0004-6280, 1538-3873. DOI: `10.1088/1538-3873/aaa7d9`. URL: `https://iopscience.iop.org/article/10.1088/1538-3873/aaa7d9` (visited on 06/03/2022).

[175] Andrei Tokovinin et al. "CHIRON—A Fiber Fed Spectrometer for Precise Radial Velocities." In: *PASP* 125.933 (Nov. 2013), p. 1336. DOI: `10.1086/674012`. arXiv: `1309.3971 [astro-ph.IM]`.

[176] Trifon Trifonov. *The Exo-Striker: Transit and radial velocity interactive fitting tool for orbital analysis and N-body simulations*. 2019. ascl: `1906.004`.

[177] Trifon Trifonov et al. "A Pair of Warm Giant Planets near the 2:1 Mean Motion Resonance around the K-dwarf Star TOI-2202." In: *AJ* 162.6, 283 (Dec. 2021), p. 283. DOI: `10.3847/1538-3881/ac1bbe`. arXiv: `2108.05323 [astro-ph.EP]`.

[178] Trifon Trifonov et al. "TOI-2525 b and c: A pair of massive warm giant planets with a strong transit timing variations revealed by TESS." In: *arXiv e-prints*, arXiv:2302.05694 (Feb. 2023), arXiv:2302.05694. arXiv: `2302.05694 [astro-ph.EP]`.

[179] Roberto Trotta. "Bayes in the sky: Bayesian inference and model selection in cosmology." In: *Contemporary Physics* 49.2 (2008), pp. 71–104. DOI: `10.1080/00107510802066753`. arXiv: `0803.4089 [astro-ph]`.

[180] Joseph D. Twicken et al. "Kepler Data Validation I—Architecture, Diagnostic Tests, and Data Products for Vetting Transiting Planet Candidates." In: *PASP* 130.988 (June 2018), p. 064502. DOI: `10.1088/1538-3873/aab694`. arXiv: `1803.04526 [astro-ph.EP]`.

[181] L. Venuti et al. "X-shooter spectroscopy of young stars with disks. The TW Hydrae association as a probe of the final stages of disk accretion." In: *arXiv e-prints*, arXiv:1909.06699 (2019), arXiv:1909.06699. arXiv: `1909.06699 [astro-ph.SR]`.

[182] Michaela Vítková et al. "TOI-4504: Exceptionally Large Transit Timing Variations Induced by Two Resonant Warm Gas Giants in a Three-planet System." In: *ApJL* 978.2, L22 (Jan. 2025), p. L22. DOI: `10.3847/2041-8213/ad9a53`. arXiv: `2412.05609 [astro-ph.EP]`.

[183] Kevin J. Walsh et al. “A low mass for Mars from Jupiter’s early gas-driven migration.” In: *Nature* 475.7355 (July 2011), pp. 206–209. DOI: `10.1038/nature10201`. arXiv: `1201.5177 [astro-ph.EP]`.

[184] Jack Wisdom et al. “Symplectic maps for the N-body problem.” In: *AJ* 102 (Oct. 1991), pp. 1528–1538. DOI: `10.1086/115978`.

[185] Aleksander Wolszczan et al. “A planetary system around the millisecond pulsar PSR1257+ 12.” In: *Nature* 355.6356 (1992), pp. 145–147.

[186] M. Zechmeister et al. “The generalised Lomb-Scargle periodogram. A new formalism for the floating-mean and Keplerian periodograms.” In: *A&A* 496.2 (2009), pp. 577–584. DOI: `10.1051/0004-6361:200811296`. arXiv: `0901.2573 [astro-ph.IM]`.

[187] M. Zechmeister et al. “Spectrum radial velocity analyser (SERVAL). High-precision radial velocities and two alternative spectral indicators.” In: *A&A* 609, A12 (Jan. 2018), A12. DOI: `10.1051/0004-6361/201731483`. arXiv: `1710.10114 [astro-ph.IM]`.

[188] M. Zechmeister et al. “The CARMENES search for exoplanets around M dwarfs. Two temperate Earth-mass planet candidates around Teegarden’s Star.” In: *A&A* 627, A49 (July 2019), A49. DOI: `10.1051/0004-6361/201935460`. arXiv: `1906.07196 [astro-ph.EP]`.

[189] Li Zeng et al. “Growth model interpretation of planet size distribution.” In: *Proceedings of the National Academy of Science* 116.20 (May 2019), pp. 9723–9728. DOI: `10.1073/pnas.1812905116`. arXiv: `1906.04253 [astro-ph.EP]`.

[190] Li-Yong Zhou et al. “Apsidal corotation in mean motion resonance: the 55 Cancri system as an example.” In: *MNRAS* 350.4 (June 2004), pp. 1495–1502. DOI: `10.1111/j.1365-2966.2004.07755.x`. arXiv: `astro-ph/0310121 [astro-ph]`.

[191] Carl Ziegler et al. “SOAR *TESS* Survey. I. Sculpting of *TESS* Planetary Systems by Stellar Companions.” In: *The Astronomical Journal* 159.1 (Dec. 2019), p. 19. ISSN: 1538-3881. DOI: `10.3847/1538-3881/ab55e9`. URL: `https://iopscience.iop.org/article/10.3847/1538-3881/ab55e9` (visited on 06/03/2022).

[192] R. van Boekel et al. “Variable accretion as a mechanism for brightness variations in T Tauri S.” In: *A&A* 517, A16 (July 2010), A16. DOI: `10.1051/0004-6361/200913840`. arXiv: `1004.3502 [astro-ph.EP]`.

[193] R. van Boekel et al. “Three Radial Gaps in the Disk of TW Hydrae Imaged with SPHERE.” In: *ApJ* 837.2, 132 (2017), p. 132. DOI: `10.3847/1538-4357/aa5d68`. arXiv: `1610.08939 [astro-ph.EP]`.